SIMULATIONS AND PROJECTIONS OF MAJOR AIR POLLUTANTS OVER THE UNITED STATES AND UNCERTAINTY ANALYSES, EFFECTS OF NATURAL CHANGE AND HUMAN ACTIVITIES

BY

HANG LEI

DISSERTATION

Submitted in partial fulfillment of the requirements
for the degree of Doctor of Philosophy in Atmospheric Sciences
in the Graduate College of the
University of Illinois at Urbana-Champaign, 2011

Urbana, Illinois

Doctoral Committee:

Professor Donald Wuebbles, Chair
Professor Xin-Zhong Liang
Assistant Professor Nicole Riemer
Assistant Professor Somnath Baidya Roy

ABSTRACT

Changes in global climate and pollutant emissions are very likely to continue in the coming decades driven by the human-related activities and natural fluctuations in the Earth climate system. These potential changes would have very important consequences on regional air quality over the contiguous United States due to their effects on atmospheric chemical and physical processes. To understand these effects, the present studies use the global climate chemistry model, CAM-Chem version 3, to systematically assess potential changes in major air pollutants including surface ozone, particulate matter and mercury from the present (1998–2002) to the 2050 (2048–2052). The projections of future air quality consider changes in global climate, precursor emissions from anthropogenic and biogenic sources, and pollutant transport. Moreover, to evaluate the projection uncertainties resulting from different plausible trends of climate and emissions as a result of unknown human-related activities and climate variations, three IPCC SRES scenarios, A1FI, A1B and B1, are considered and compared to evaluate the resulting uncertainty in projecting future pollutant concentrations. To achieve a better understanding on the effect of mineral dust emissions on changes in future air quality especially the PM concentrations, a physical dust aerosol module is developed and incorporated into the CAM-Chem model. A mercury module is developed for the CAM-Chem model to simulate the atmospheric cycle of mercury and its consequences on the toxicity of U.S. air quality.

For the study of ozone air quality, we focus on the risk of high ozone episodes and the relative contributions from changes in local anthropogenic emissions (LE) versus changes in intercontinental transport (ICT) on 2050 U.S. surface ozone air quality. It is

found that the projected changes in air temperature, precipitation, lighting, planetary boundary layer height and cyclone activities tend to intensify the associated extreme weather conditions that foster the risk of high ozone pollution episodes over many parts of the world. As a result of both changes in climate and emissions, the frequency of hazardous ozone days in the summertime is derived to be 6-73 days for North America. Through analysis of the contributions from changes in domestic and international emissions, we find that projected changes in the U.S. domestic anthropogenic emissions and the changes in long range transport under the A1FI scenario have a comparable contribution in affecting western U.S. ozone air quality in 2050. However, under the A1B and B1 scenarios, contributions from changes in domestic emissions are more significant than that from changes in long range transport. The results indicate that for the United States, pollution control is a domestic issue under low global emission situations, while it becomes an international issue when fossil fuel use is rapidly increasing throughout the world.

For the study of future surface particulate matter (PM) air quality, a physical dust aerosol module is developed and incorporated into the CAM-Chem to better simulate the dust emission over the globe and improve the simulations of PM air quality. This dust module incorporates the wind erosion physics of Shao [2008] and various other improvements necessary for a global modeling. These improvements include the parameterizations of frozen soil effect and snow cover effect on dust emission. The module is tested in reproducing the present dust pollution, through the comparison with available observations. Then, the surface PM concentration under the 2050 climate is projected to increase the levels of particulate matter in 2050 by 0-10 $\mu g/m^3$ for PM2.5

and 0-14 $\mu g/m^3$ for PM10 in the eastern and western U.S., but decrease PM2.5 by 0-6 $\mu g/m^3$ and 10-0 $\mu g/m^3$ for PM10 in the central United States. When considering only the reduced anthropogenic emissions relevant to aerosols, there will be overall decreases in PM2.5 concentrations around 2-18 $\mu g/m^3$ and PM10 concentrations around 2-22 $\mu g/m^3$. Mineral dust and organic compounds are projected to increase in the 2050 U.S. PM composition, but secondary inorganic aerosols will decrease.

For the study of atmospheric mercury, a global mercury scheme is developed and incorporated into the CAM-Chem model. The scheme represents the emission, transport, transformation and deposition of atmospheric mercury (Hg) in three forms: elemental mercury (Hg0), reactive mercury (HgII), and particulate mercury (HgP). It is tested by using the NCEP/DOE AMIP II reanalysis meteorology data. The result shows the model can simulate the spatial and temporal distribution of atmospheric mercury concentrations. Then, the future mercury air quality is projected to 2050 under each IPCC climate and emission change scenario. We find that the U.S. total gaseous mercury (TGM) concentration in 2050 may have a 2.1-4.0 $\mu g/m^2$'s increase on the eastern U.S. and around 1.4-3.0 $\mu g/m^2$'s increase on the western U.S. under the A1FI scenario. The corresponding changes in wet deposition are around 10-14 and 2-4 $\mu g/m^2$, respectively. The increase of HgII in emissions tends to enhance the wet deposition.

For all my teachers that pass me the knowledge

And my family that give me the hope

ACKNOWLEDGMENTS

My deepest gratitude is to my advisor, Professor Donald Wuebbles, for his indispensable and insightful guidance, continuous encouragement and everlasting patience throughout my Ph.D. study and research. His never-ending enthusiasm, meticulous attitude toward the research work, and second-to-none excellence toward scientific achievement have kept me motivated for the last five years. His generous personality and strict requirements in academy also influence my work and living attitude. All these will certainly be carried on to my research and life in the future. I especially would like to express my deepest thanks to him for his patience in teaching me how to write a good paper and helping me finish this thesis. For everything you have done for me, Prof. Wuebbles, I thank you.

Special thank Prof. Xin-Zhong Liang, for his help on my research and writing. I would like to thank Professors, Nicole Remer, Somnath Baidya Roy and Ault Jain for serving on my thesis committee and their comments and critics of my research. Many thanks go to many officemates, especially Seth, Ken, Anne, Huikyo, Dong, Wenjing, and Jintai. Aslo thanks all professors and my friends in Dept. of Atmospheric Sciences.

I would like to acknowledge the United States Environmental Protection Agency Science to Achieve Results (STAR) Program under award number EPA RD-83096301-0 and RD-83337301-0, as well as the supercomputing facilities at DOE/NERSC and NCSA/UIUC.

Finally, my deep gratitude goes to my wife and parents from both sides for their endless and greatest support throughout my life, and my daughter for providing me the passion to work hard.

TABLE OF CONTENTS

CHAPTER 1: INTRODUCTION

1.1 Motivation

Air quality is an important issue that closely affects human life. With the average human adult breathing about 20 cubic meters of air a day, there is a concern about those of us living in urban areas because of the potential exposure to air pollutants coming from automobile traffic, commercial, industrial and manufacturing facilities, as well as other sources. These air pollutants can cause a variety of health problems including breathing problems, asthma, reduced lung function, lung damage, bronchitis, cancer, and brain and nervous system damage [Goldacre et al., 2010]. Air pollution can also irritate the eyes, nose and throat, and reduce resistance to colds and other illnesses [U.S. EPA, 1997]. Air pollution can be especially harmful to the very young, the very old, and those with certain preexisting medical conditions [U.S. EPA, 2008]. Air pollution also causes haze and smog (as in Los Angeles's "Brown Cloud"), reduces visibility, dirties and damages buildings and other landmarks, and harms trees, lakes and animals [Seinfeld et al., 1999]. It is also responsible for thinning the protective ozone layer in the upper atmosphere that protects us from harmful ultraviolet radiation from the Sun [WMO, 2010]. Air pollutants also contribute to changes in the Earth's climate system [IPCC, 2001, 2007]. These air pollutants that may cause environmental problems can be divided into three categories: gases, particulate matter, and heavy metals.

Among various hazardous gases, surface ozone is particularly of concern because it can cause direct health effects. Surface ozone pollution is a major air quality issue for the United States and many other countries around the world. Unlike stratospheric ozone

which protects us from the dangerous levels of ultra-violet (UV) radiation, the existence of ozone near the Earth ‘s surface has significant adverse impacts on both human health and the environment [Heck et al., 1984; Friedman et al., 1988; National Research Council (NRC), 1991; Lippman, 1993; Peden, 2001; Mauzerall and Wang, 2001; Oksanen and Holopainer, 2001; Desqueyroux et al., 2002; Mortimer et al., 2002; Morgan et al., 2003; Morgan et al., 2004; Klumpp et al., 2006]. Surface ozone can trigger a variety of health problems even at very low levels, e.g., tens of parts per billion (ppb), such as lung irritation, breathing difficulties, aggravated asthma, reduced lung capacity, increased susceptibility to respiratory illnesses like pneumonia and bronchitis. It can also cause permanent lung damage after long-term exposure, discouraging outdoor activities in polluted areas. In addition, surface ozone is a threat to agriculture and ecosystems, causing crop and other vegetation to be more susceptible to diseases and insects, damaging vegetation leaves, and thus reducing crop and forest yields.

Particulate matter (PM) is also a hazard to human health. PM includes a verity of materials suspended in the air in the form of minute solid particles or liquid droplets. PM is made up of a number of aerosols from human-related sources such as directly emitted black carbon, industrial gases produced secondary aerosols produced from industrially-emitted gases and metals, and natural sources such as mineral dust aerosol and particles from organic chemicals. In the past decades, many studies highlighted the role of ambient airborne particulate matter as a leading cause of many different cardiopulmonary diseases and lung cancer [Brunekreef et al., 2002; U.S. EPA, 2007]. Numerous epidemiological studies found a strong exposure-response relationship between PM for short-term effects (premature mortality, hospital admissions) and long-term or cumulative health effects

(morbidity, lung cancer, cardiovascular and cardiopulmonary diseases, aggravated asthma, nonfatal heart attacks, etc) [U.S. EPA, 2007; Valavanidis et al., 2008]. In addition, PM is also associated with environmental damages, including reductions in visibility; acidification of lakes and streams; changing the nutrient balance in coastal waters and large river basins; depletion of nutrients in soil; effects on sensitive forests and farm crops; and effects on the diversity of ecosystems [U.S. EPA, 2007].

Heavy metals in the atmosphere usually include lead (Pb) and mercury (Hg). The major sources of lead emissions have historically been from fuels in on-road motor vehicles (such as cars and trucks) and industrial sources. The atmospheric pollution of lead over the United States has been effectively controlled [U.S. EPA, 2007]. However, the processes affecting atmospheric mercury are not yet well understood. Mercury can be emitted into the air from all kinds of surface reservoirs including ocean, soil, vegetation, and industries. The deposition and reemission processes result in accumulation of mercury pollutants in the surface environment [UNEP, 2008]. Global atmospheric mercury pollution is reported to have intensified during recent decades [UNEP, 2008]. Atmospheric mercury compounds have become heavy metal pollutants of most concern [Selin et al., 2007; U.S.EPA, 2007]. Mercury can adversely affect the nervous system, kidney function, immune system, reproductive and developmental systems and the cardiovascular system. Infants and young children are especially sensitive to even low levels of mercury, which may contribute to behavioral problems, learning deficits and lower intelligence.

The United States has been trying to improve the air quality through emission controls and by transitioning to clean energy approaches instead of traditional energy

sources. Congress passed the Clean Air Act in 1970, which set national air quality goals for the protection of human health and welfare. Then the United States Environment Protection Agency (U.S.EPA) established the National Ambient Air Quality Standards (NAAQS) and invested tens of billions of dollars each year to reduce air pollution. The results have been impressive. In the more than three decades since the passage of the Clean Air Act, emissions of air pollutants have declined significantly [http://www.epa.gov]. Despite these efforts and significant progress, the United States still faces challenges in air quality: Almost a third of the population lives in areas where air pollution levels exceed the U.S. EPA's health-based standards for air quality. Tens of thousands of people die each year as a direct result of exposure to high levels of air pollution; many more suffer adverse health impacts. Crop yields and forest productivity are adversely impacted by exposure to air pollution [U.S. EPA, 2008; http://www.oar.noaa.gov]. As of April 21, 2011, of the 474 counties with observations (mainly over the eastern U.S. and California), there are still 242 counties with nonattainment areas of 8-hour maximum ozone standard covering the entire county and 121 counties with nonattainment areas of PM-2.5 standard covering the county [http://www.epa.gov].

One straightforward and critical question is what are the potential changes in U.S. air pollution in the coming decades, especially for these major pollutants. There are many factors that need to be considered to fully address this question. First, atmospheric pollution is affected by climate change. For example, biogenic emissions of ozone and aerosol precursors are affected by climate. Increase in temperature will accelerate ozone production and aerosol formation [Seinfeld, 1999]. Second, changes in emissions will

directly alter the composition of the atmosphere and concentrations of pollutants. These potential changes may affect our lives in the coming decades through effects on health, agriculture, and living environment. Systematic assessment of the potential changes in major hazardous pollutants can guide policy making and help humanity to avoid potential environmental disasters in the near future.

1.2 Background Information and remaining issues

In the past decade there has been much public and scientific focus on current air quality and potential changes in the future. The two air pollutants of most concern are surface ozone and particulate matter (PM), due to their effects on public health. In addition, as toxic air pollutants, mercury compounds also have received more concern in recent several years.

Ozone is formed in the troposphere by photochemical oxidation of carbon monoxide and volatile organic compounds (VOCs) by the hydroxyl radical in the presence of reactive nitrogen oxides (NOx) [references therein Wayne, 2000]. Most nations are highly concerned about damage to air quality caused by increases in surface ozone. Many control strategies have been introduced to reduce the surface ozone concentration by limiting the anthropogenic emissions of ozone precursors [U.S. EPA, 2007]. Despite many attempts at local controls, however, it is clear that intercontinental transport (ICT) is also significant in building up background levels of ozone [Jacob et al. 1999; Lin et al. 2008; Wuebbles et al., 2007]. A critical factor in controlling future regional air quality is the relative contribution of changes in local emissions (LE) on surface ozone versus the changes in background ozone considering the uncertainties in

global climate and emission changes [Wuebbles et al., 2007]. That factor determines whether the control strategy is a domestic issue or an international issue. Regional environmental differences, uncertainties in the effects from climate change, and in the assumptions about the levels of human activities, all add uncertainties to that relationship. Many studies have analyzed the potential changes in future ozone air quality [Wu et al., 2008; Lin et al., 2008], but existing studies are not adequate to address all key questions. A comprehensive study of contributions to changes in future surface ozone concentrations from local emissions or long range transports under all possible climate and emission change scenarios will provide a reliable assessment for future effects in ozone.

Another important issue for future air quality is the risk of hazardous ozone pollution episodes under future climate and emissions projections. Compared to changes in average concentration, the risk of hazardous ozone pollution is of more concern to human health. Recent studies have examined future increases in the background ozone level and increases in average concentrations [Tao et al., 2007; Wu et al., 2008; Lin et al., 2008]. These improved background and average ozone level would likely enhance the risk for extreme or hazardous ozone pollution episodes. The individual ozone pollution episodes depend on specific weather conditions and the strength of precursor emission plumes. Suitable weather conditions expected under the changing climate, including probabilities for high temperature conditions, strong solar radiation, drought, and stable boundary layers, tend to foster higher surface ozone concentrations, even for fixed levels of precursor emissions. Emissions of ozone precursors in the future can be projected through recent studies on climate change [IPCC, 2001; Intergovernmental Panel on

Climate Change (IPCC) Special Report on Emissions Scenarios (SRES), http://sres.ciesin.org/final_data.html, 2004] and its biological impacts [Guenther et al., 1999; U.S. EPA, 2008]. Therefore, a quantitative and comprehensive assessment of the risk of hazardous ozone pollution episodes under future climate and emissions projections is needed.

The principal components of PM are sulfate, nitrate, organic carbon, elemental carbon, mineral dust, and sea salt. The first four are mostly present as fine particles less than 2.5 μm diameter (PM2.5); these are the ones of most concern to human health. Recent studies [Dawson et al., 2007] demonstrate that perturbations to present-day temperature, wind speed, absolute humidity, mixing height, and precipitation can all significantly affect PM2.5. Pye et al. [2009] shows that PM2.5 and its aerosol precursor (sulfate, ammonium and nitrate) concentrations will likely increase by 2050 under the mid-level A1B scenario. As an important contributor to PM levels, intercontinental transport's impact on PM level is also affected by the assumptions of climate and emission changes. Chemical sensitivities of aerosol related chemicals (e.g., the sensitivities of sulfate-ammonia-nitrate reactions on temperature and relative concentration) are other factors which will affect future ICT of aerosols. Most recent modeling studies have investigated the effect of climate and emissions change on U.S. aerosol levels in 2050 under the control A1B scenario [Pye et. al., 2009]. However, due to the sensitivity of aerosol chemistry on ambient air conditions [Seinfeld et al., 1998], uncertainties in climate change and emission change may lead to unexpected changes in ICT and large uncertainties on U.S. surface aerosol levels. Therefore, a broader, more

comprehensive study of future changes and uncertainties of ICT is necessary to understand future air quality change and its uncertainties.

In addition, some interactions between aerosols in the formation processes are not well understood, and these interactions may be very important in determining effects on air quality. For example, the chemical competition between nitrate and sulfate aerosol formation is known through laboratory studies. How this competition occurs in the practical atmosphere and how it will affect future aerosol concentration change have not been adequately studied. Also, as a precursor for ozone as well as a precursor for nitrate aerosols, NOx transformation is highly related to the concentrations of two major air pollutants. The change in transformation rate of NOx may affect future ozone and aerosol levels. How the transformation rate changes with climate and emission perturbations are not well understood and worthy of further analyses.

Mineral dust is a primary component of PM. Around 28 to 35% of PM10 in the USA is mineral dust [Harrison et al., 2004]. Quantifying the mineral dust emission and transport is important for PM estimate. Therefore, scientists have been working on developing mineral dust models to simulate dust emission and transportation processes. However, due to the complexity in natural soil erosion processes, most current dust models are based on parameterization rather than on physical (dynamic) dust emission schemes [Ginoux et al., 2001; Gong et al., 2003b; Liu et al., 2003; Marticorena and Bergametti, 1995; Tegen and Fung, 1994; Uno et al., 2003; Zender et al., 2003]. Shao et al., [2002] developed a physical dust scheme based on soil erosion dynamics [Shao et al, 2001, 2002] that has been evaluated in regional mesoscale models to forecast Asian dust storms [Shao et al., 2003; Lei et al., 2005]. Through the principles of soil erosion theory

[Shao., 2002, 2008] in combination with the NASA global soil information and the Community Land Surface Model (CLM), we have developed a new physical dust module for global dust simulation that is expected to improve PM simulations. This module is incorporated into the CAM-Chem for a better PM concentration prediction.

The toxic effects of mercury (Hg) on human and environment have been seriously regarded by governments and scientific community. Much effort has been put into assessing and monitoring present releases of mercury and their effects on air quality [NADP, 1996; USEPA, 2006; UNEP, 2008]. Controlling mercury air pollution has been a common target for all nations [UNEP, 2008]. The future of mercury air pollution is a key criterion for control strategies. Although many modeling studies have investigated the past and present mercury air pollutions [Bullock et al., 2002; Selin et al., 2008; Lei et al., 2011], potential changes of mercury air pollution in the future are seldom examined. That seriously limits our reorganization of mercury air pollution change in the coming decades and also prevents us from making effective control strategies. Therefore, assessing what the global or regional mercury air pollution level will be and how the compositions of mercury pollutants change in the coming decades has become an urgent research task.

However, assessment of future mercury effects on air quality is complicated because of the potential effects of uncertainties in the extent of climate change and emissions changes. Due to its low vapor point, the atmospheric lifetime and natural emissions of mercury are sensitive to changes in climate. As a result, a major challenge for modeling future atmospheric mercury is to obtain defendable emission estimates. The current emission inventory data are known to contain substantial uncertainties. Many present atmospheric models cannot consider the effects of climate factors on emission

change. Therefore, developing dynamic scheme to consider the impact of climate change on emissions is necessary for future mercury concentration projection. Another challenge for modeling mercury effects on air quality is to determine the mechanism for chemical cycling of mercury in the lower troposphere. Various chemical reactions about atmospheric mercury have been reported and tested in numerical models [Bullock et al., 2002; Calvert and Lindberg, 2005; Holmes et al., 2006; Lin et al., 2006; Selin et al., 2007, 2008] that include gaseous phase, aqueous-phase, and photochemical reactions. Chemical mechanisms in previous numerical models differ extensively. How to select the most significant reactions for use in a model affects the resulting simulations of mercury effects on air quality. In order to achieve an accurate projection of future mercury concentrations, building a well evaluated atmospheric mercury model in CAM-Chem is necessary. This study provides such a model.

1.3 Objectives

The objective of this work is to undertake a holistic study of the effects of climate, surface environment and emission changes on air quality, especially ozone (O_3) particulate matter (PM10 & PM2.5), mineral dust and mercury, and to account for total effects. The result is expected to help air quality planners in designing more effective air quality control strategies for future air quality to meet the National Ambient Air Quality Standards (NAAQS) or regulations under the Clean Air Act. Our studies will focus on four critical issues: (1) Future projections of ozone and PM; (2) Chemical and biochemical processes affecting ozone and aerosol concentration; (3) Mineral dust emission and future change; (4) Present and future effects of mercury compounds on air

quality. Specific objectives of these studies, and their associated uniqueness relative to the existing scientific literature, are summarized as follows:

1. Based on the future background emissions, use climate and multi-scenario ensembles in air quality projections to assess the risk of high ozone episodes.
2. Assess the effects of domestic versus international human activities on future regional ozone air quality change; this has not been well resolved in earlier studies.
3. Develop a 3-D physical (process-based) mineral dust model that extends the capabilities of current models.
4. Evaluate changes in future PM concentrations in the United States with an emphasis on the compositions of major components including sulfate, nitrate, elemental carbon, organic carbon, mineral dust and sea salt; this has not been resolved in earlier studies.
5. Explore the competition affecting the interactions between nitrate-ammonia and sulfate-ammonia reactions in the atmosphere to evaluate nonlinear effects on the nitrate aerosol concentration response to emission changes. The role of this mechanism in aerosol concentration change has not been as completely analyzed in previous study.
6. Develop an atmospheric mercury model including associated homogeneous and heterogeneous reactions and dynamic emissions from land and ocean to better simulate mercury effects on air quality.
7. Project future mercury effects on air quality by considering the effects of changes in climate and emissions, and uncertainty analysis.

These results will help to understand the potential changes in U.S. air quality due to global climate and emissions changes and can be used by others in agriculture and health effects studies to better understand how the agriculture ecosystems and public health will respond to these changes. This information will help inform U.S. EPA in developing effective management strategies for adapting to future change. With the IPCC is currently actively engaged with national level air quality management agencies and governments to ensure that current and future emissions controls strategies will achieve the best effect for air quality and resources, this study will provide information that the IPCC can use in these discussions with regulatory agencies so that effective air management programs are continued.

1.4 Research Methodology and Data

In order to address the issues discussed above I develop physical mineral dust and atmospheric mercury modules for use in the Community Atmospheric Model with Chemistry (CAM-Chem). The updated CAM-Chem model is then used to determine a more comprehensive estimate of air quality change in the future. Projections of future emissions are considered with and without human related emission change to quantify the impacts and uncertainties of climate and emission changes, from present to 2050. Three distinct climate/emission pathways from the Intergovernmental Panel on Climate Change (IPCC) Special Report on Emissions Scenarios are considered, including the A1FI, A1B and B1 scenarios (http://sres.ciesin.org/final_data.html) representing upper, middle and lower emissions estimates over the 21st century, respectively.

Three primary sets of experiments are designed that use the state-of-the-art global climate-chemistry model, CAM-Chem. Historical simulations of climate and air quality are first conducted for model evaluation and for use as a baseline reference for the future projections. Future projections for the 2050 period are then made, where the model incorporates scenarios of global changes in climate and/or emissions to quantify their individual and combined impacts on global air quality. The third set is sensitivity experiments to determine dominant source regions and types (by adding perturbations in the regional or global emission inventories), relative roles of episodic transport versus mean background change, chemical interactions (by modifying the model physics or emissions) as well as uncertainties associated with key conclusions. All experiments are run for 5-10 years so that the model results approximate a relatively steady-state. Diagnostic studies are aimed at further understanding of the results.

Two parallel research experiments address the development of the physical mineral dust module and atmospheric mercury module. Starting from NASA's global soil information and the physical soil erosion theory [Shao et al., 2008], we develop a physical dust aerosol module. This model can simulate the practical wind erosion process from various land surface conditions and consider the effects of soil condition, wind speed, and surface vegetation. The contributions to future PM pollution are analyzed by bin sizes.

1.4.1 **Climate and Emission Change Scenarios: A1FI, A1B and B1**

Changes projected to occur under the IPCC A1FI, A1B and B1 scenarios are compared to evaluate the potential uncertainties in future pathways of global climate and

precursor emissions. These three scenarios are selected for analysis in this research to best represent current knowledge on the range of potential climate changes over the coming century. Since all the IPCC climate scenarios used in previous studies, such as the mid-high A2 [Hogrefe et al., 2004; Racherla and Adams, 2006] and mid-range A1B [Fiore et al., 2002b; Murazaki and Hess, 2006], lie within the range bounded by A1FI and B1, the uncertainty in projections of climate-related pollutant change in future years can be roughly inferred by the differences in pollutant changes between A1FI and B1. Although the future climate change could end up being either greater than A1FI or smaller than B1 depending on policy choices and trends during the next few decades, the results can also interpret the future changes in high and low climate changing situations. Therefore, the mid-range IPCC A1B scenario is also adopted to present an additional emissions case for the future.

It is necessary to note, however, that scenarios can be derived from socio-economic (SE) models that may contain different assumptions regarding precursor emissions from anthropogenic sources not necessarily bounded by the scenario itself. Here, projected anthropogenic (fossil fuel, industrial, transportation, biofuel, etc.) emissions were derived from the socio-economic (SE) models used in IPCC [2001], including the miniCAM model for A1FI, the AIM model for A1B and the IMAGE model for B1, respectively (http://sres.ciesin.org/final_data.html). To generate future emissions, the present-day emissions in each model gridcell were scaled up to match those projected by the SRES scenarios in 2050 (representing the 2048–2052 period) and 2090 (representing the 2095–2099 period). Scaling factors for CO and NOx were used directly to scale emissions of these species, while SRES projected changes in anthropogenic

'NMVOC' emissions were used to scale anthropogenic emissions of acetone, ethene (C_2H_4), ethane (C_2H_6), propene (C_3H_6), propane (C_3H_8), formaldehyde (CH_2O) and NMV (representing the hydrocarbons with four or more carbons in a molecule, except isoprene and terpenes). Other species without significant anthropogenic components (methanol (CH_3OH), isoprene, terpenes) were not altered. Projections of natural emissions are based on the projected meteorology and specialized dynamic approach for each specie.

1.4.2 Description of the CAM-Chem model

For the global model simulations in this study we use the Community Atmosphere Model with Chemistry (CAM-Chem) climate chemistry model [Lamarque et al., 2005; 2011; Heald et al., 2008; Pfister et al., 2008]. CAM-Chem is an integrated system including atmosphere, chemistry, land surface, ocean and ice modules. The model is based on the atmospheric general circulation model CAM3, which is a part of the Community Climate System Model version 3 (CCSM3) [Collins et al., 2006a, 2006b]. CAM-Chem's chemistry module is based on the chemical component of the Model of Ozone and Related Chemical Tracers (MOZART) [Emmons et al., 2010]. The module includes a full representation of the O_3-NOx-CO-VOC and other chemistry affecting ozone, and has been evaluated and used in many previous studies [e.g., Lamarque et al., 2005; Murazaki and Hess, 2006; Lin et al., 2008a]. The chemistry module contains a comprehensive tropospheric gas phase and aerosol chemical mechanism, including 119 species and 300 reactions, together with representation of aerosols using a bulk mass approach for different types of particles. This configuration has been applied to a number

of recent chemistry-climate studies [Heald et al., 2008; Lamarque et al., 2005; Lamarque et al., 2008; Murazaki and Hess, 2006].

The CAM-Chem simulated aerosol mass classes include sulfate from the oxidation of SO_2 (both emitted directly and from dimethyl sulfide (DMS) oxidation), ammonium nitrate, directly emitted carbonaceous aerosols (black carbon (BC), organic carbon (OC)), secondary organic aerosols from the oxidation of biogenic VOCs and aromatics, sea salt (4 size bins), and dust (4 size bins). The standard CAM-Chem aerosol configuration is a mass-based, externally mixed treatment. The model includes the primary inorganic gas-phase nitrogen species (NO_y=NO+NO_2+NO_3+2N_2O_5+HNO_3) as well as organic nitrogen in the form of peroxyacetyl nitrate (PAN) (+ other organic nitrates), ammonia (NH_3), and particulate ammonium nitrate. Dry deposition velocities (V_d) of pollutants are computed in the CAM-Chem using the resistance-based parameterization of Wesely (1989), Walmsley and Wesely (1996), Wesely and Hicks (2000). The calculation of surface resistances uses the vegetation distribution of Bonan et al. (2003). Wet deposition is taken from the formulation of Brasseur et al.(1998). The physical planetary boundary layer (PBL) parameters used in the chemical calculations are provided by the land surface module (Community Land Model) integrated in the CAM-Chem system.

The majority of the anthropogenic emissions used in the CAM-Chem come from the POET (Precursors of Ozone and their Effects in the Troposphere) database for 2000 (Granier et al., 2005; Olivier et al., 2003). Monthly average biomass burning emissions are from the Global Fire Emissions Database, version 2 (GFED-v2), which is currently available for 1997–2007(van der Werf et al., 2006). The natural emissions of VOCs and

mercury are calculated by dynamic schemes in the model. The natural emission module for mercury will be introduced in Chapter 5. The calculation for natural emission of VOCs (isoprene, terpenes, acetone, ethene, ethane, propene, propane, and methanol) is based on atmospheric carbon dioxide (CO_2) concentrations and air temperature, as well as incident solar radiation [Guenther, 1997]. In the current CAM-Chem model, the biogenic emissions and soil emissions formulas following the algorithms presented in Guenther (1999) has been added into the coupled community land surface model. For instance, isoprene emissions were calculated using the equation (Guenther, 1999). The scaling factor, γ_T , considers the effects of temperature perturbations.

$$\gamma_T = \frac{\exp\left(\frac{C_{T1}(T - T_s)}{RT_sT}\right)}{0.961 + \exp\left(\frac{C_{T2}(T - T_M)}{RT_sT}\right)}$$

The variation of isoprene emissions due to perturbations in atmospheric CO_2 concentration were calculated using the relationship (after http://www.face.bnl.gov/ modelling/isoprene.htm):

If $[CO_2] > 600$ ppb then $\delta iso = -0.00041 \bullet [CO_2] + 1.28$; otherwise $\delta iso = 1.0$

1.4.3 Observed Datasets Used in Model Evaluation

Observational data from various sources will be used to evaluate the model results, as summarized in Table 1.1. The AQS dataset, the NADP-NTN observations of aerosols, and the ACE-Asia dataset are used to evaluate current simulations with the CAM-Chem CTM. NASA's soil texture data is used in the dust module development.

Table 1.1. Summary of major observational datasets used in this study

Name	Host Agency	Usage	Range	Information & Reference
AQS	USEPA	Model Test (Chemicals)	USA	In-situ measurements; Hourly observational data for 11 pollutants [USEPA 2007]
CASTNET	USEPA	Model Test (Aerosols)	USA	In-situ measurements; Hourly observational data for particulate aerosols [USEPA 2007]
IMPROVE	NOAA	Model Test (Aerosols, PM)	USA	Aerosol concentration and compositions vista.cira.colostate.edu/improve
UMMAN	Univ. Miami	Model Test (Chemicals)	Global	Long term dust aerosol records [Prespro et al., 1999]
NTN/MDN	NADP	Model Test (Aerosols)	USA	In-situ measurements; Daily wet deposition data for aerosols [NADP 2009]
ACE-ASIA	NCAR	Model Test (Mineral Dust)	Asia	Satellite, ship observation of Asian mineral dust [Zhang et al., 2003]
Global Soil Data	NASA	Model Developing	Global	1-Degree Grid Global soil information in 27 types [Zobler, 1999]

This study also uses historical and future simulations from a suite of atmospheric models to drive the CAM-Chem integrations, as summarized in Table 1.2. The NCEP/DOE AMIP II reanalysis (R2) data is considered as one of the best proxy of observed climate conditions and thus used to drive the CAM-Chem reference run for direct correspondence with air quality observations. The CCSM3 climate outputs are used to drive the CAM-Chem simulations to project future changes of air quality.

Table 1.2. Summary of Key characteristics of model data used

Name	Host Institute	Resolution	Time	Reference
CCSM3	NCAR	T85 (256*128)	1995-2005; A1FI(2048-2052; 2095-2099); A1B(2048-2052; 2095-2099) B1(2048-2052; 2095-2099)	Collins et al., 2006
NCEP-RII	NCAR-DOE	T42 (192*94)	2001-2002	Kanamitsu et al., 2002

1.5 Arrangement of the Chapters

Towards the objectives as stated above, the following chapters are presented to study the related issues one by one. Chapter 2 examines the risk of high ozone episodes by using climate and multi-scenario ensembles in air quality projections. Chapter 3 assesses the effects of domestic human activities versus international human activities on the changes in future regional ozone air quality. Chapter 4 presents the 3-D physical (process-based) mineral dust model developed to extend the capabilities of CAM-Chem model. Chapter 5 evaluates changes in future PM concentrations in the United States with an emphasis on the compositions of major components including sulfate, nitrate, elemental carbon, organic carbon, mineral dust and sea salt. Chapter 6 explores the competition between nitrate-ammonia and sulfate-ammonia formations in the atmosphere and further evaluate its effects on the nitrate aerosol concentration in response to precursor emission changes. Chapter 7 depicts the atmospheric mercury module (including associated homogeneous and heterogeneous reactions and dynamic emissions from land and ocean) developed to better simulate mercury air quality. Chapter 8 analyzes the future changes in concentrations of mercury compounds by considering

effects of changes in climate and emissions, and the uncertainty in the results. Chapter 9 summarizes the findings and provides an analysis of future research needs.

CHAPTER 2: PROJECTING OZONE AIR QUALITY IN 2050: RISK OF HIGH OZONE EPISODES

2.1.Introduction

Surface ozone is a special concern in air quality because of its health effects. Recent studies show that high surface ozone concentrations may cause hazardous effects on lung function, the human respiratory system and on plants and animals [Green Fact, 2011]. High ozone pollution episodes have been observed in many cities [WHO, 2008]. To prevent the adverse effects of ozone on ecosystems and on human health, many countries have established maximum surface ozone concentration limits. For example, the U.S. EPA set both an 8-hour maximum surface ozone standard and a 1-hour maximum ozone standard [U.S. Environmental Protection Agency (EPA), 2008a]. Due to the potential hazards, monitoring and prediction of surface ozone concentration changes have become regular tasks for environment agencies and provide an important guide for public health.

Several recent air quality studies have been focused on the changes in average ozone during the past, present and future associated with climate and emission variation [Murazaki and Hess, 2006; Lin et al., 2008a; Wu et al., 2008a]. Analyses of historical records show that the average surface ozone level is rapidly increasing in developing countries and slowly decreasing in developed countries [Wang et al., 2001; U.S. EPA 2008b]. This change is attributed to the increase of anthropogenic emissions in developing countries and the control on high emissions in developed countries [Streets et al., 2000; 2004]. Despite effective regional emissions controls, ozone pollution in most, if

not all, developed countries, is still a very serious problem [U.S. EPA, 2008b]. In addition, despite decreasing emissions internally, most developed countries will likely face effects to increase pollution levels from climate change and from long range transport of pollutants from developing countries in the coming decades [Jacob et al., 1999; Wuebbles et al., 2007; Lin et al., 2008a]. Chemical-transport modeling studies driven by results from climate models have examined the separate and/or combined effects of climate and emissions changes on future tropospheric background ozone and average condition of surface ozone air quality [Yienger et al. 2000; Fiore et al. 2002a; Fusco and Logan 2003; Mickley et al., 2004; Murazaki and Hess, 2006; Lin et al., 2008a; 2008b]. Changes in anthropogenic emissions is reported to be the largest factor in determining future global and regional ozone air quality with a contribution of 40-90% of total changes [Jacob et al., 1999; Prather et al., 2003; Wu et al., 2008a; Lin et al., 2008a]. These and other analyses also indicate that changes in natural emissions and climate will likely contribute to increase future global ozone change by 10 to 30 % [Brasseur et al. 1998; Stevenson et al. 2000; Hauglustaine and Brasseur 2001; Hogrefe et al. 2004; Leung and Gustafson 2005; Hauglustaine et al., 2005; Lin et al., 2008b]. The combined studies by Tao et al., (2007), Wu et al., (2008a) and Lin et al. (2008a) show that changes in climate and U.S. anthropogenic emissions may cause near-surface ozone concentrations in 2050 either significantly higher under the IPCC A1FI scenario or slightly lower under the A1B and B1 scenarios. Wu et al., (2008b) also show that the 2000–2050 changes in global climate and anthropogenic emissions of ozone precursors under the A1B scenario could increase the tropospheric background ozone burden by as much as 18%.

The possibility of an increase in the background ozone level and increase in average concentrations would likely enhance the risk for extreme or hazardous ozone pollution episodes. However, quantitative and comprehensive assessment of the risks under future climate and emissions projections has not been well established. The individual ozone pollution episodes depend on specific weather conditions and the strength of precursor emission plumes. Suitable weather conditions expected under the changing climate, including probabilities for high temperature conditions, strong solar radiation, drought, and stable boundary layers, tend to foster higher surface ozone concentrations even for fixed levels of precursor emissions. Emissions of ozone precursors from anthropogenic emissions show little seasonality but large spatial diversity, while natural emissions have clear seasonality [Street et al., 2000]. High anthropogenic emissions of ozone precursors usually occur over industrial regions. The natural emissions of ozone precursors (mainly in forms of volatile organic carbon), which contribute more than half of the total emissions [Guenther et al., 1997], peak in summertime. In addition, the production rate of surface ozone peaks in summer due to the strong solar radiation. Thus summertime over industrial regions is where high ozone episodes are likely to occur [U.S. EPA, 2008b; European Environment Agency (EEA), 2010].

To investigate the attainment of the maximum ozone standard and assess the risk of hazardous ozone pollution episodes in 2050 under the global climate and emission change scenarios, this study uses the global climate-chemistry model, Community Atmospheric Model with Chemistry (CAM-Chem), with meteorology derived from the Community Climate System Model 3 (CCSM3), to simulate the effects of changes in climate and emissions on maximum concentrations of surface ozone and to analyze the

effects on 2050 global air quality. To address the effects of uncertainties on the results and to achieve a more comprehensive understanding of possible changes, three distinct climate/emission pathways from the Intergovernmental Panel on Climate Change (IPCC) Special Report on Emissions Scenarios (SRES, http://sres.ciesin.org/final_data.html) are considered, including the A1FI, A1B and B1 scenarios representing upper, middle and lower bounds of future climate change, respectively. To quantify the risk, two types of "hazardous ozone days" are analyzed based on the U.S. EPA's 8-hour maximum ozone standard and 1-hour maximum ozone standard.

Section 2 introduces the associated approach used with the model in this study. The CAM-Chem model is then evaluated for its ability to reproduce maximum ozone concentrations. Thereafter, potential effects of climate change on 2050 ozone air quality, along with uncertainty analysis and statistical analysis on distribution of high daily values, will be discussed in sections 4 and 5. In section 6, risk analysis based on frequencies of hazardous ozone days will be presented using two definitions. Finally, the conclusions are presented in section 7.

2.2. Methods

In this study, CAM-Chem is driven by meteorological fields prescribed by climate system model outputs from the climate system model CCSM3 corresponding to the present climate state and the 2050 climate under different IPCC scenarios. The meteorology fields were archived with 6-hour temporal resolution. Meteorology fields include winds, temperature, pressure, humidity and solar radiation. Simulations are performed with a 30 minute time step and a horizontal resolution of 1.9˚ x 2.5˚ with 26

vertical levels from the surface (1000 hPa) to 3-millibar level (~40 km altitude). Previous tests have shown that a spin-up of about 6 months is needed for CAM-Chem to have small effect from initial conditions. Each case was run for 5 years (2048–2050) following 1 year of model spin-up. Unless noted otherwise, all results presented below are based on the last 5-year averages from hourly outputs.

Emissions of ozone precursors for 2000 are based on the present-day inventory as described by Horowitz et al. [2003]. We use 2050 estimates of anthropogenic emissions of ozone and aerosol precursors from the IPCC Marker scenarios as derived from the economic models used by IPCC [2001], miniCAM for A1FI, AIM for A1B and IMAGE for B1, respectively. Similarly to Fiore et al. [2002b], we derive 2000–2050 growth factors for different categories of anthropogenic emissions for different countries, and then apply these factors to the present-day CAM-Chem emission inventories. The corresponding changes of ozone precursor emissions for different regions are shown in Table 1. The detailed changes in anthropogenic emissions will be discussed together with surface ozone air quality change in the next section. For the purposes of this study, seven masks were created that map the SRES marker reference model regions for each scenario and sensitive experiments onto the CAM-Chem grid [IPCC 2001]. Present (2000) standard emissions of other chemical species in each region are projected to 2050 following the corresponding SRES emissions scenario in order to reproduce the changed atmospheric environment. Emissions from biomass burning sources are fixed at the present-day level for all experiments.

Biogenic emissions of ozone precursors including non-methane VOCs (NMVOCs) from vegetation and CO emitted from soil are computed online based on instantaneous

local meteorological variables and hence vary in response to climate change. Vegetation produces large amounts of NMVOCs through natural processes, with important effects by temperature and ambient CO_2 concentrations. The current CAM-Chem predicts the biogenic and soil emissions using its coupled Community Land Model following the algorithms in Guenther [1997] and Potosnak, [2002]. Changes in soil emissions of carbon monoxide (CO) due to the temperature dependence of net primary production (NPP) were also considered [Adams et al., 2004]. However, soil emissions of NOx and oceanic emissions of all ozone precursors were kept same at the present-day levels in all experiments because of large uncertainties in their estimations and poor understanding of their future changes.

2.3. Ozone Evaluation for the Current Climate

The ozone chemistry module in the CAM-Chem, adopted from the previous MOZART chemical-transport model, has been extensively evaluated against observations of ozone and its precursors, both globally [e.g., Horowitz et al., 2003; Emmons et al., 2010] and regionally [e.g., Tie et al., 2006; Lin et al., 2008a]. These studies have demonstrated the ability of the CAM-Chem ozone chemistry module to reproduce the long-term average, temporal variation and spatial distribution of global tropospheric ozone concentration. Our evaluation below focuses on the CAM-Chem model ability to reproduce the statistics of daily maximum concentrations of surface ozone.

To assess CAM-Chem's ability to simulate the maximum concentrations of surface ozone that occur during the summer months, we compare the model-derived summer averaged D8hM surface ozone concentrations over the continental United States and Europe in 2002 relative to the Environmental Protection Agency (EPA) Air Quality

System (AQS) site measurements and the European Environment Agency (EEA) air quality database AirBase, respectively. The model is driven by NCEP reanalysis II meteorology [Kanamitsu et al., 2002] for 2001-2002. The model result for the second year is used in the comparisons. All measurements at the sites within a given model grid cell are selected through a quality control filter that requires the selected sites have at least a 75% record of valid operations to be able to derive 8-hour averages per day during the whole comparison period. Then the selected measurements are averaged to get a grid cell mean value that can be directly compared with the modeled value for that grid cell.

Figure 2.1 shows the CAM-Chem derived summer mean of daily 8-hour maximum surface ozone concentration over the contiguous U.S. and its difference from U.S. EPA AQS observations. We find that the model is able to reasonably reproduce high ozone concentrations observed over most of the contiguous United States, with biases generally smaller than 20 ppb. The model tends to overpredict observations by 0-25 ppb with the majority in the range of 5-20 ppb over the eastern United States. On the western United States, the biases are within 15 ppb, with the majority within -10 to 5 ppb. Similar patterns and values of biases over the contiguous United States have been reported by Lin et al. using the earlier MOZART-2.4 simulations for 1996-2000 driven by the CCSM3 meteorology [Lin et al., 2008b]. We also compared the annual mean, seasonality and regional diurnal cycles simulated by the CAM-Chem with EPA AQS observations. The biases of these quantities are small. The results are summarized in EPA STAR Project reports [Liang et al., 2009].

Figure 2.2 shows the CAM-Chem derived summer mean of D8HM ozone concentration over western Europe, and the difference relative to EEA Airbase

observations [EEA, 2002]. The model captures the general pattern of hazardous ozone pollution over western Europe. The model tends to over-predict the 8-hour maximum surface ozone concentrations over southern Europe by 0-15 ppb and underestimates it over northern Europe by 0-20 ppb. Such differences may be related to the coarse resolution in the global model. The coarse grid will filter the effects of small weather systems on ozone air quality, which is important to determining the variations of local ozone concentration. The correct pattern that CAM-Chem captures suggests this issue may not affect the climatology of ozone air quality at the regional scale. In addition, we also made comparison with observed maximum one hour ozone concentrations with EEA Airbase observations. The results (https://netfiles.uiuc.edu/hanglei2/shared/) show that CAM-Chem can capture the right spatial pattern and magnitude.

Asia is one of the major ozone pollution regions. However, the continuous monitoring of surface ozone pollutions over a large area has just recently started (March 2011) in China. Therefore, we are not able to systematically evaluate model performance over the Asia region. However, it has been reported from some measurement sites in East Asia that surface ozone has a concentration range from 30-45 ppb in the late 1990s [Tan et al., 2003; Wang et al., 2006; Wang et al., 2009]. CAM-Chem simulations over the same area show 5-10 ppb's higher than these reported values. However, the biases may be less than 5-10 ppb, if the rapid development of industry in East Asia from the late 1990s is considered.

Through these comparisons with observations at various worldwide stations, the CAM-Chem model shows a strong ability to reproduce high surface ozone values over the continents. The model captures the right patterns of summer time daily 8-hour

maximum surface ozone concentrations over the U.S. and Europe. The comparison with limited site observations in Asia also confirms the ability of CAM-Chem model in global surface ozone simulation.

2.4. Potential effects of climate change on surface O_3

Climate change can affect surface ozone air quality through meteorological factors including air temperature, humidity, precipitation, solar radiation, lightning, plenary boundary layer (PBL) mixing, and convection ventilations [Brasseur et al., 1998; Mickley et al., 2004; Murazaki and Hess, 2006; Lin et al., 2008b]. Rapid changes of the global climate system may increase the probability of extreme weather episodes like heat waves and result in higher risk of the occurrence of hazardous ozone pollution. Table 2.2 summarizes these main meteorological variables that affect ozone, their associated extreme weather/climate conditions, possible changes in the trend to 2050, their effects on risk of hazardous pollution, and affecting pathways. The climate change from 2000 to 2050 following the IPCC scenarios A1FI/A1B/B1) result in an increase of 1.9/1.7/1.4 K, respectively, in global annual mean surface air temperature. Warmer air temperatures will enhance ozone production, and also leads to faster thermal decomposition of peroxyacetyl nitrate (PAN) and thus increases the levels of NO_2 and peroxyacetyl radicals [Sillman and Samson 1995; Dawson et al., 2007]. In addition, warmer temperatures will increase the natural emissions of ozone precursors (isoprene, terpenes, etc). Heat waves are likely to increase in frequency and to become more intense in the coming decades [Kunkel et al., 2010; Hayhoe et al., 2010], increasing the likelihood of high ozone pollution episodes in 2050.

Higher air temperature tends to increase the water storage capability of the atmosphere and enhance the land-atmosphere water exchange (accelerate evaporation and precipitations). As a result of the changing climate future atmospheric H_2O content and precipitation are expected to increase by 2050 [IPCC 2007]. Thus, more hydroxyl radicals (OH) are expected to be produced in the atmosphere. Ozone production could either decrease or increase, depending on the relative levels of NO_x versus odd hydrogen in each region [Sillman and Samson, 1995; Racherla and Adams 2006].

For increasing risk of hazardous pollution episodes, the impact from changes in precipitation is likely to be more significant than that from changes in H_2O content. Previous studies on extreme climate events under global change scenarios have shown that the frequencies of flood and drought in 2050 are both likely to increase as the spatial distribution of precipitation become more unbalanced [Dairaku et al., 2008; Rosenberg et al., 2010]. Under this situation, the ozone concentrations will be enhanced when drought occurs. The analysis of CCSM3 meteorology shows that summer precipitation in 2050 over North America, western Europe and East Asia under selected future scenarios decrease on drought regions and increase on the wet regions (https://netfiles.uiuc.edu/hanglei2/shared/), confirming the findings of previous studies.

Changes in cloud cover and cloud depth can alter the transmission of solar radiation through the atmosphere, which can in turns affect the photochemical processes associated with surface ozone formation. Estimates of cloud cover and cloud depth changes in the future are notoriously difficult because of too much uncertainty [Wylie et al., 2005]. However, cloud liquid water content provides a good estimable variable to evaluate the cloud effects on solar radiation. Since the effects of cloud cover and depth on

radiation transfer is based on the absorption and scattering of water droplets, the more liquid water in the cloud, the stronger reduction of solar radiation made by the cloud. In addition, cloud liquid water content also affects the wet removal of nitrogen species. The analysis of CCSM3 meteorology shows that the cloud liquid water content in low-levels increases over the Northeast and Midwest of the U.S., and over western Europe, and East Asia by 2050 during the summer time under the A1Fi and A1B scenarios, while it decreases under the B1 scenario expect for Southeast Asia. The global general change trend is not found. Therefore, the effect of clouds on the possibility of high ozone episodes depends on local changing trends.

Lightning is a natural source of NOx emissions. Potential changes in the strength and frequency of lightning depend on the projection of deep convections. In CAM-Chem, the lightning production of nitric oxide (LNO) is calculated using the scheme by Price et al. [1997] and Pickering et al. [1998]. An increase in the frequency of deep convection is also found in the CCSM3 meteorological data for 2050. As a result of the increasing frequency of deep convection in 2050, summer mean production of LNO increases by 24%, 18% and 11% according to the A1FI, A1B and B1 scenarios respectively.

Physical processes within the planetary boundary layer (PBL) determine the transport of surface ozone. Mixing is the main process, which associated with two physical factors. The first one is the PBL height, which can affect the vertical diffusion of surface ozone. Meteorological factors, including air temperature, humidity, surface winds, soil moisture and temperature, can affect the PBL height. In CAM-Chem, the variation of PBL height is calculated by the PBL parameterization scheme incorporated within the atmospheric model. The derived CAM-Chem change in PBL height for 2050 is

increasing over the major arid and semiarid areas where the drought occurs, but decreasing over the rest. We find that simulated summer mean PBL heights under the A1FI scenario decrease up to 100 m over the wet regions (eastern United States, Southern Europe and eastern China) and increase up to 200 m over arid regions (Southwest United States, Northern China). Similar situations are found under the A1B and B1 scenarios. The changing patterns are similar to that under the A1FI scenario, but with only smaller magnitudes. We also compared our results with the meteorology analysis in previous studies. The simulated PBL change in 2050 generally agrees with the previous analyses by Wu et al. [2008b] and Lin et al. [2008b]. Since all the decreasing regions mentioned above are industrial regions, this changing pattern is expected to decrease the efficiency of vertical transport of produced ozone. Therefore, this change tends to increase the risk of high ozone levels. The second factor is the wind speed in the PBL, which usually affects the horizontal dilution of surface ozone. The most affected areas are coastal regions where the surface ozone level is usually diluted by low-ozone air from the ocean. Previous studies have suggested that future wind fields over the contiguous U.S. will be intensified due to the increased thermal contrast between land and ocean under a warming climate [Bueh et al., 2003; Murazaki, and Hess, 2006]. In the CCSM meteorology, the surface wind field over U.S. is strengthened under all three scenarios. The wind systems affecting major ozone polluted areas (such as: low-level jet from Gulf of Mexico for the eastern U.S.; Westerly winds from the Atlantic for Europe; summer monsoon for eastern Asia) are all intensified in 2050. Therefore, it is expected that the average changes in PBL wind filed reduce the risk of high ozone episodes. However, the wind field change within the PBL is altered by local and regional thermodynamic factors.

Although the risks of high ozone are weakened by the intensified average winds, low wind episodes are still possible.

In major ozone polluted regions such as the Midwest and eastern U.S., western Europe and eastern Asia, surface ozone concentrations are affected by cyclonic behavior and associated frontal passages. Mickley et al. [2004] point out that changes in future years will have implications for regional pollution levels. Previous studies on climate change have shown a potential decreasing trend in the frequency of over-land cyclones. In CCSM3 meteorology, the projected changes in summer time show a decrease in the number of cyclone passages under all three scenarios. For the eastern United States, we find a 7%-19% decrease in the number of cyclones passing over the Midwest to southeastern Canada. For western Europe, north Atlantic cyclones show a frequency decrease and an intensity enhanced trend. For eastern Asia, there is a 5%- 21% decrease in the number of Mongolia cyclones that may affect the pollution ventilation from Central China to Japan. This is consistent relative to previous projections of future meteorology. Mickley et al., [2004] found an increase in the frequency of stagnation episodes and a decrease in frequency for the 2050 eastern U.S. cyclone activities. Lionello et al., [2010] studied the future changes in cyclone tracks over Europe and show a significant reduction in storm track intensity. Zhu et al., [2008] point out that the frequency of occurrence and the intensity of the Mongolian cyclones are likely to decrease.

In conclusion, significant changes in major climate factors that can affect ozone air quality have been found in projected meteorology following IPCC future change scenarios. Changes in most extreme weather conditions associated with these factors tend

to increase the possibility of high ozone pollution episodes during the period from 2000 to 2050, although the increase in PBL wind field may decrease these effects in heavy polluted regions. In addition, effects of changes in some factors such as cloud liquid water content and atmospheric H_2O content on ozone depends on the magnitudes of changes. In order to improve our understanding on the total effect and uncertainties, it is necessary to conduct a modeling study on projections of the frequency of hazardous ozone pollution episodes in 2050.

2.5. Summer surface ozone air quality in 2050

The summer average daily 8-hour maximum surface ozone concentration for 2000 and projections under the IPCC climate and emissions change scenarios for 2050 are shown on Figure 2.3. The simulation for 2000 (present) driven by the CCSM3 meteorology shows a similar pattern to the results driven by the NCEP reanalysis II meteorology. The projection to 2050 considers the effects of changes in climate, natural emissions and anthropogenic emissions under different climate and emission change scenarios. Among these scenarios, the A1FI scenario emphasizes the continued intensive use of fossil fuels, and results in more severe air pollution than the other cases examined. The A1B scenario emphasizes the balanced use of fossil fuels and renewable fuels, with resulting smaller changes in pollution amounts. The B1 Scenario assumes much lower consumption of fossil fuel and puts emphasis on global solutions to economic, social and environmental stability, and gives a relatively clean developing pathway. These three scenarios together represent the likely range of situations for future emission changes without much larger policy driven changes in emissions. The following paragraphs

discuss the summer average D8HM ozone concentration change in 2050 to see the general pollution situation over the major polluted regions.

The 2050 D8HM ozone concentrations under the A1FI scenario show an increase up to 40 ppb over land areas throughout much of the world. Of particular significance in the simulated changes in major ozone pollution regions is the increase in peak values. The increase over the eastern U.S. region is up to 20 ppb. Considering the fact that the present ozone pollution level over the eastern U.S. is high, the risk of hazardous ozone pollution in 2050 under the A1FI scenario will continue to be high. Although the increase over Europe and the Mideast is up to 36 ppb, the summer average of D8HM ozone level over Europe in 2050 is below that over the U.S. due to lower pollution levels in 2000. The large increase is mainly caused by the projected anthropogenic emissions increase over the Mideast and its transport to Europe. The potential increase in eastern Asia under the A1FI scenario is up to 28 ppb, which results in the D8HM ozone over eastern Asia by 2050 being on the same level as that over the eastern U.S. The increase of summertime D8HM ozone concentrations in 2050 compares well with the earlier study by Hogrefe et al. [2004], except that our findings are larger due to the differences in climate and emissions changes between the A1FI and A2 scenarios.

Under the A1B scenario, the major characteristic of changes in global D8HM surface ozone concentration by 2050 is the increase over Europe, Asia and Africa and the decrease over North America. The decrease up to 13 ppb over North America is mainly caused by the significant reduction in anthropogenic emissions of ozone precursors. Previous studies on D8HM ozone change under the A1B scenario by Wu et al. [2008b] gave a decrease of as much as 15ppb over the northeast U.S., similar to this study. the

small difference may be related to the estimates of biogenic emissions response to global climate change used in each study. The D8HM ozone concentration increase over Europe is mainly caused by the dispersion and emissions increase in eastern Europe and the Mideast. The increase in Europe is around 0-10 ppb with a slight decrease up 4 ppb near the coastal areas of western Europe. The increase/decrease trend of Europe ozone in 2050 in this study agrees with other studies of future surface ozone under the A1B scenario [Koffi et al., 2010; Katragkou et al., 2010]. Increases of D8HM ozone concentration over the eastern Asia and the Mideast is up to 33 ppb, which leads to a high risk of hazardous ozone pollution on both regions in 2050. Asian anthropogenic emissions of ozone precursors keep on growing under the A1B scenario. This situation in 2050 also makes Asia a strong source for global tropospheric ozone pollution. A similar study by Wang et al., [2011] for the A1B scenario shows a similar result on 2050 summer surface ozone pollution over China.

The 2050 summer D8HM surface ozone concentration under the B1 scenario shows a decrease over North America and Europe, and an increase over the Mideast and the eastern Asia. As a background, the global average temperature rises about 1.4 C by 2050 under the B1 scenario versus 1.7 C under the A1B scenario, which results in a relatively stronger increase in biogenic emission of ozone precursor under the A1B scenario. Disregarding the biogenic emission change, the net reduction of anthropogenic emission of ozone precursors under the B1 scenario is larger than that under the A1B scenario. Therefore, the decrease of D8HM ozone concentration under the B1 scenario is larger than the change under the A1B scenario over North American, while the increase over Asia is smaller. Specifically, the decrease over North America is up to 18 ppb, the

high value bound of which is larger than the previous estimate of 13% by Kunkel et al., [2008]. For Europe, the transport of increased emissions of ozone precursors over Asia is not enough to compensate the summer D8HM ozone decrease caused by the local anthropogenic emission reduction. Therefore, the summertime D8HM surface ozone concentration shows a slightly decrease of 0-6 ppb. The increase of D8HM ozone over Asia is between 0-17 pbb due to the continuous increasing of ozone precursors from 2000 to 2050. The peak increase occurs over eastern Asia.

2.6. Day to day distributions of D8HM ozone concentrations

Important aspects in assessing the hazard of future ozone pollution is how high the daily pollution can reach and how often it reaches the high values in the summer season. Here we investigate changes in the number of heavy pollution days during June-August from 1998-2002 to 2048-2052 on three major ozone polluted areas. As shown in Figure 4, we examine the red rectangular three areas including eastern U.S., Europe and East Asia. In each region, projected changes in regional mean day to day accumulative frequency distribution (CFD) of the simulated D8HM ozone during the 1998-2002 summers are compared.

Including both the climate and emissions changes, projected future ozone changes are generally less than 15 ppb over the entire CFDs in all three regions (Figure 2.4) and few are statistically significant at the 95% confidence level based on the two-sample quantile test. Over the eastern U.S., there is no statistically significant ozone change under the lower emissions (B1 and A1B) scenario, but there is a significant increase under the higher emissions (A1FI) scenario. Ozone concentrations decrease around 15 ppb at most of the CFD above the 96^{th} percentile and 5 ppb at the lower concentration

part of the CFD under the B1 scenario. Under the A1FI scenario, there is statistically significant ozone increase at the higher concentration part of the CFD, while the increase magnitude at the lower concentration part is small. Over Europe, ozone concentrations increase up to 15 ppb at the 1st quantile of the CFD under the A1FI scenario. Under the B1 and A1B scenarios, there is no statistically significant ozone change except the significant decrease above the 50th percentile. Over East Asia, there is a statistically significant ozone increase under the A1FI, A1B and B1 scenarios. Overall we find that the ozone changes from 1998–2002 to 2048–2052 over Europe and Asia are significant in the entire CFDs.

We also examine the changes in the ozone CFD for individual model grid cells within each region and find similar results. Similarly, Wu et al., [2008b] studied the cumulative probability change over the eastern U.S. by 2050 under the A1B scenario also shows that the ozone concentration decrease is more significant in the higher concentration part of the CFD than in the lower concentration part. Murazaki and Hess [2006] constructed the CFDs of daily mean ozone for regional maximum, median, and minimum, respectively, over a region in the central and eastern United States (35°–45°N, 96°– 80°W) as well as the CFDs for individual model grid cells within the region. They also found that ozone concentrations increased throughout the CFD from the 1990s to the 2090s under the midrange A1B scenario. In contrast, using a global model to study climate change effects on black carbon and CO (no changes in biogenic emissions), Mickley et al. (2004) found that changes in pollutant concentrations from 1995–2002 to 2045–52 under the A1B scenario were significant at and only at the higher concentration part of the CFDs over the Northeast and Midwest. The differences between our and their

findings can be explained by the differences in climate and chemistry models as well as climate scenarios. For example, the spatial resolution here (2.9° latitude 2.8° longitude with 18 vertical layers) is much higher than that in Mickley et al. (2004) (4° latitude 5° longitude with nine vertical layers).

When changes in both climate and anthropogenic emissions are incorporated, surface ozone concentrations significantly increase from 1998–2002 to 2048-2052 under the A1FI scenario primarily because of global wide increases in anthropogenic emissions. Under all three scenarios, ozone concentrations over East Asia increase throughout the CFDs, although increases tend to be greater toward the higher concentration part of the CFDs over most regions. By comparison, Hogrefe et al. (2004), who also considered climate and anthropogenic emissions perturbations using a regional modeling framework, found little ozone change at the lower concentration part of the CFDs over the Northeast and Midwest with changes in climate and biogenic emissions as projected under the mid–high A2 scenario. Again, in addition to the distinctive climate–emission scenarios used, the differences between model formulations may also play a role.

2.7. Frequency of days with hazardous ozone pollution episodes

As shown in previous sections, the average conditions of summertime daily 8-hour maximum surface ozone concentration in 2050 will likely be affected by both climate and emission changes under the three global change scenarios examined. To quantify the risk of hazardous ozone pollution, we examine the use of frequency of days with hazardous ozone pollution episodes as a variable in the analysis. However, it should be noted that the definition of hazardous ozone pollution episode varies in different countries. The

latest surface ozone regulation in the U.S. National Ambient Air Quality Standards (NAAQS) has set 75 ppb of daily 8-hour maximum average ozone concentration as a controlling target. The Europe Environment Association (EEA) has set an alert threshold value of 56 ppb of daily 8-hour maximum average ozone concentration as the long term objective for ambient air quality. Here we use the U.S. NAAQS standard 75 ppb as a threshold value to determine the hazardous ozone pollution episode. The daily 8-hour maximum ozone concentration above 75 ppb will be counted as a hazardous ozone pollution day.

The average frequency of summertime (JJA) hazardous ozone pollution episodes for present and 2050 under the B1, A1B and A1FI scenarios are shown on Figure 5. Present simulation results show that the highest frequency of hazardous ozone pollution episodes over North America is up to 38 days per summer. The eastern United States and southern California, eastern China, Europe and mid-Africa are the major hazardous regions. Compared with the present, the 2050 evaluation results under the B1 scenario show a significant reduction in hazardous ozone pollution episodes over the eastern U.S. region. Western Europe did not show any hazardous episodes as a result of precursor emissions reduction. However, as areas of emissions increase, eastern Europe and the Mideast show significant increases in hazardous ozone pollution episodes. The peak value over the Mideast is around 16 days per summer. On the other emission increasing area, East Asia, the peak value increased to 47 days per summer by 2050. The pollution situation of 2050 under the A1B scenario keeps the similar pattern to that under the B1 scenario, but with a higher frequency of hazardous ozone pollution episodes. The frequency over the North American is 19 days per summer. The frequency on western

Europe is 1 day per summer, while on the Mideast and eastern Europe it raise up to 52 days per summer. The frequency on East Asia rises up to 71 days per summer. Under the A1FI scenario, the global ozone pollution in 2050 is intensified due to the increasing use of fossil fuel. The frequency of hazardous ozone pollution episodes over North America, East Asia and the Mideast are all above 70 days/ summer. The frequency over western Europe rises up to 39 days per summer. Detailed frequency of summer hazardous ozone pollution episodes under each case are summarized in table 3. From the socioeconomic view point, the developed area, North America and western Europe, has the potential to improve their ozone air quality, while developing area, Asia and eastern Europe, are facing a potential increasing risk of hazardous ozone pollution. Based on three IPCC scenarios, it is shown that the uncertain in the assessment of risk is large. Although the variation range is estimated here, what the practical change will be still depend on the energy use and energy type on each region.

As a comparison with the definition based on D8HM ozone standard, we also make an analysis of hazardous pollution episodes in 2050 based on the second highest 1-hour average ozone concentration. We set the threshold for a hazardous ozone day as 120 ppb following the U.S. EPA 1-hour surface ozone standard. The results are summarized in Table 2.3. Generally, the frequency of a hazardous day under this definition decreased. The frequency represents the probability of more serious short period pollution episodes. It is reasonable that possibility of occurrence of higher values is lower than that of lower values. For the variation under different scenarios, a similar trend in the changes of frequencies is found to that using D8HM ozone definition. However, under the 1-hour threshold definition for corresponding scenarios, the frequency of hazardous ozone days

increased relative to the present value. According to CFDs analysis, the changes of ozone concentrations response to climate and emission change are more sensitive on the higher concentration part.

2.8. Conclusion

We have investigated the effects of possible changes in climate and emissions by 2050 on the frequency of hazardous ozone pollution episodes by using a global climate chemistry model (CAM-Chem) with meteorological input from a climate system model (CCSM3). We considered the total effects of changes in climate, associated biogenic emissions and anthropogenic emissions of ozone precursors under the IPCC [2001] A1FI, A1B and B1 scenarios. Our focus was to determine the possibility of future extreme and hazardous ozone pollution episodes and analyze the uncertainty. Based on previous studies on future ozone air quality those mainly focus on changes in background or average conditions, this study provide a comprehensive understanding on the future risk of high ozone episodes those may cause hazardous effects.

The evaluation of CAM-Chem model on summertime D8HM ozone concentration against available measurements worldwide shows that the biases over the western U.S. is generally below 14%, while the biases over the eastern U.S. is below 20%. In addition, the examination on the 2000-2050 changes of major climate factors in CCSM3 meteorology shows that the projected changes in air temperature, precipitation, lighting, planetary boundary layer height and cyclone activities tend to intensify the associated extreme weather conditions that foster the risk of high ozone pollution episodes over many parts of the world. This indicate that climate change will aggravate the hazard of

surface ozone in the future and pose further difficulty to mitigate ozone pollution after considering the changes in anthropogenic emissions in the future. However, some factors such as the PBL wind strength, atmospheric H_2O content and cloud conditions are sensitive to the magnitude of changes or changes in other environmental factors, bringing uncertainty to the resulting sensitivity. Therefore, further studies on climate changes are needed to reduce the uncertainty from projections of meteorology factors. On the other hand, sensitivity studies of ozone changes response to meteorological perturbations may also help our understanding of this uncertainty.

By defining the "hazardous ozone days" as the daily D8HM ozone concentration lying above 75 ppb, we examined the model simulated frequency of hazardous surface ozone episodes in 2050. Analysis on the CCSM3 meteorology used in this study shows that major climate factors under projected climate change trends tend to increase the possibility of hazardous ozone pollution events and the potential increase of anthropogenic emissions of ozone precursors in developing countries may raise the risk of hazardous pollution events. The frequency of hazardous ozone pollution episodes in 2050 for North America increases under the A1FI scenario but decreases under the A1B and B1 scenarios as a result of the sharp decrease of anthropogenic emission. The change in frequency for western Europe follows a trend similar to that of North America because of the similar energy structure. However, Asia (both East Asia and the Middle East) shows an increased frequency under all three scenarios. The projected changes in frequency under the B1 scenario show up to 84% reduction in frequency of high ozone days over the eastern U.S. and no more hazardous episodes over the western Europe, but an increase of three times over Asia. Under the A1B scenario, the frequency of hazardous

ozone days decreases to 19 days/summer over the eastern U.S., and 1 day/summer over Europe. The Asia from the Mideast to East Asia shows a higher increase of 59 days in frequency than that under the B1 scenario. The change under the A1FI scenario is the most serious case. The number of hazardous ozone days all increase on three main ozone pollution regions. The eastern U.S., the Mideast and East Asia are main high risky areas with hazardous ozone pollution. The frequencies of hazardous ozone days for these three areas are all above 70 days/summer. In addition, we also make an analysis of the second highest 1-hour average ozone concentration in 2050. We set the threshold for a hazardous ozone day as 120 ppb following the U.S. EPA 1-hour surface ozone standard. The analysis shows relatively lower frequencies than that using D8HM ozone definition. It is reasonable that the probability of extreme values is lower than that of lower values. However, a similar trend in the changes of summertime hazardous ozone days is found to that under D8HM definition. The rate of change based on present value for the frequency of hazardous ozone days under 1-hour threshold definition for corresponding scenarios increased. The increase can be understood through statistical analysis of cumulative frequency distribution of daily peak ozone concentrations, which shows that the changes of ozone level are relatively more significant on the high value part. For human health, this result also means that any increase in ozone pollution is able to cause hazardous effects. Conversely, it provides the public and governments a substantial proof that any investment on air quality control will save the expense on medical bills.

In closing, it is important to recognize that there remain many uncertainties in projections of future global climate and emissions that affect our results. Reduction and assessment of these uncertainties will be a long term requirement for climate and air

quality studies. The previous studies may only address one scenario and often lower emissions scenarios. We did at least three scenarios from low, medium to high emissions, giving a more likely range of the feasible trends. In addition, this study focuses on high ozone episodes (days with surface ozone concentration that exceed the high ozone standard), which is different from the extreme ozone episodes (days with surface ozone concentrations that near or over the historical extreme record). The extreme ozone episodes are special cases associated with extreme meteorological conditions and/or extreme emission episodes, and may need to be explored further in future studies to determine their relationship to climate change.

Table 2.1. Projected global summer emissions budgets of ozone precursors for present (1998–2002) and their fractional changes by 2050 (2048-2050)

Species	*Years*	*Anthropogenic*	*Biomass*	*Biogenic*	*Total*
NO_x	2000	7.58 TgN	1.74 TgN	3.14 TgN	12.5 TgN
	2050	226% /84.2%/ 36% [a]	-10% /25%/83%	0% /0%/0%	136% /54.2%/34%
CO	2000	171 Tg	162 Tg	52.7 Tg	386 Tg
	2050	224% /-5%/-29%	-14% /63%/117%	2% /1.4%/1%	93% /24.3%/36%
NMVOC	2000	17.9 TgC	4.43 TgC	228 TgC	250 TgC
	2050	170% /130%/18%	-15% /66%/125%	32% /20%/16%	41% /28.8%/18%
Isoprene	2000	—	—	145 TgC	145 TgC
	2050	—	—	41% /25%/ 20%	41% /25%/ 20%

[a]: The numbers before and after '/' denote projected fractional emissions changes under the A1FI, A1B and B1 scenarios, respectively, relative to present budgets.

Table 2.2. Main meteorological conditions associated with hazardous ozone change in 2050.

Variables	***Associated Extreme weather conditions***	***Changes in frequency of extremes in 2050***	***Frequency of Hazardous O_3 Pollution Episodes***	***Effects on surface ozone***
Air Temperature	Heat Waves	Increase	increase	Emissions, reaction rates, PAN
H_2O Content	High Humidity	Increase	Depends [a]	OH production
Precipitation	Flood/ Drought	Both increase	increase	pollutant deposition
Cloudiness	Strong Solar Radiation	Depends [b]	Depends [c]	Solar radiation
Lighting	Deep convection	increase	increase	NOx production
PBL Height	Low mixing depth	decrease	increase	Vertical transport
PBL Wind Field	Strong wind	increase	decrease	Horizontal transport
Cyclone/fronts	Stagnation	increase	increase	Transport

[a] The effect of change in atmospheric H_2O content depends on the relative levels of NOx versus odd hydrogen in each region [Sillman and Samson, 1995; Racherla and Adams 2006].
[b] The future change in cloudiness depends on regional climate change. Due to the regional diversity, the estimate on future global cloudiness contains large uncertainty.
[c] As a result of uncertainty in future cloudiness, the effect of change in cloudiness on surface ozone also depends on specific regional change.

Table 2.3. Frequency of summer hazardous ozone pollution episodes in four global regions (Unit: days/summer).

	North America		*Western Europe*		*Eastern Europe & Mideast*		*East Asia*	
	8-hour	1-hour	8-hour	1-hour	8-hour	1-hour	8-hour	1-hour
Present	38	23	5	0	0	0	12	4
B1 2050	6	0	0	0	16	12	47	14
A1B 2050	19	8	1	0	52	27	71	31
A1FI 2050	73	57	39	17	76	51	79	59

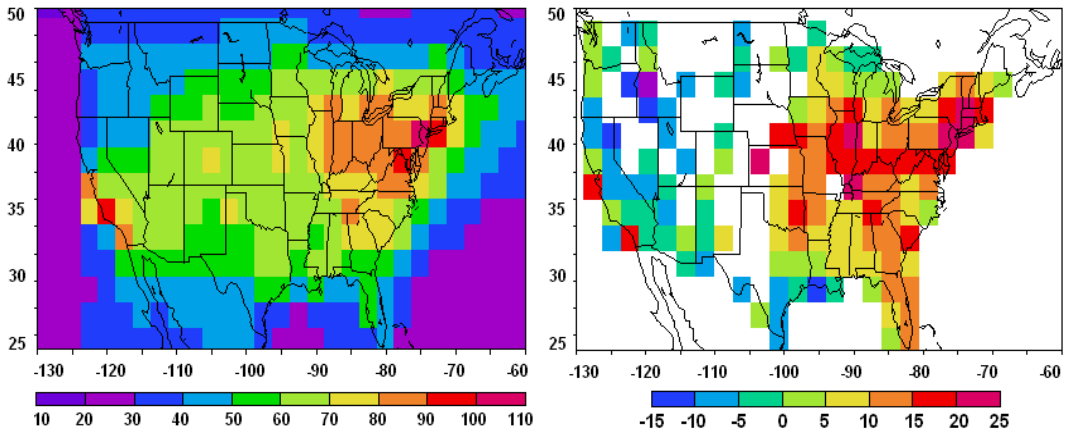

Figure 2.1. Summer average daily 8-hour maximum surface ozone concentration over the contiguous United States for 2002. The CAM-Chem simulated results (Left) and the comparison with the U.S. EPA AQS site measurements (Right). (Unit: ppb)

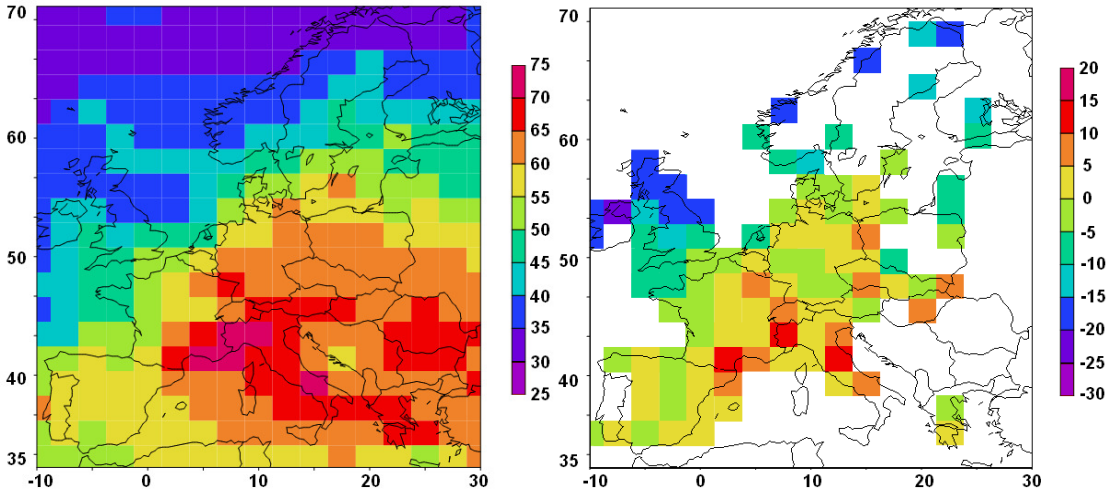

Figure 2.2. Summer average daily 8-hour maximum surface ozone concentrations over Europe for 2002. The CAM-Chem simulated results (Left) and the comparison with the Europe Environment Agency AirBase site measurements (Right). (Unit: ppb)

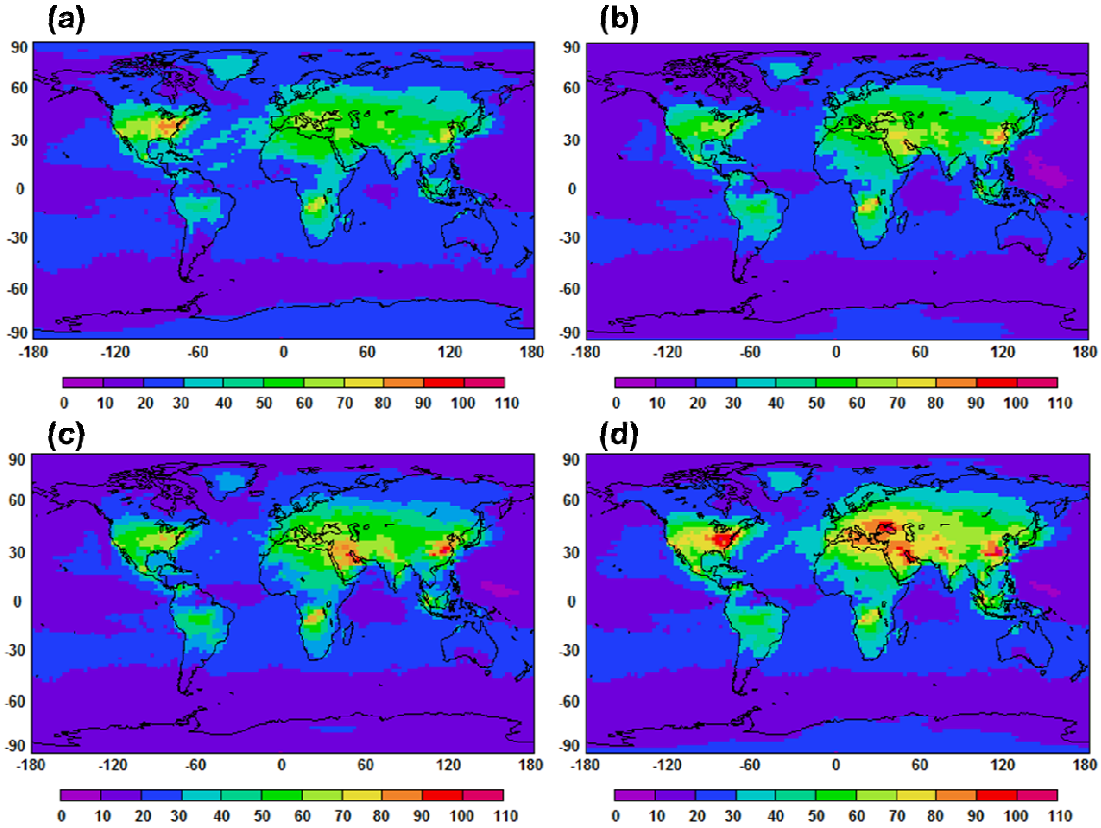

Figure 2.3. CAM-Chem simulated summertime (June-August) average daily 8-hour maximum surface ozone concentrations (ppb) for 2000 and projections under IPCC climate and emission change scenarios for 2050; (a) 2000; (b) 2050 under the B1 scenario; (c) 2050 under the A1B scenario; (d) 2050 under the A1FI scenario.

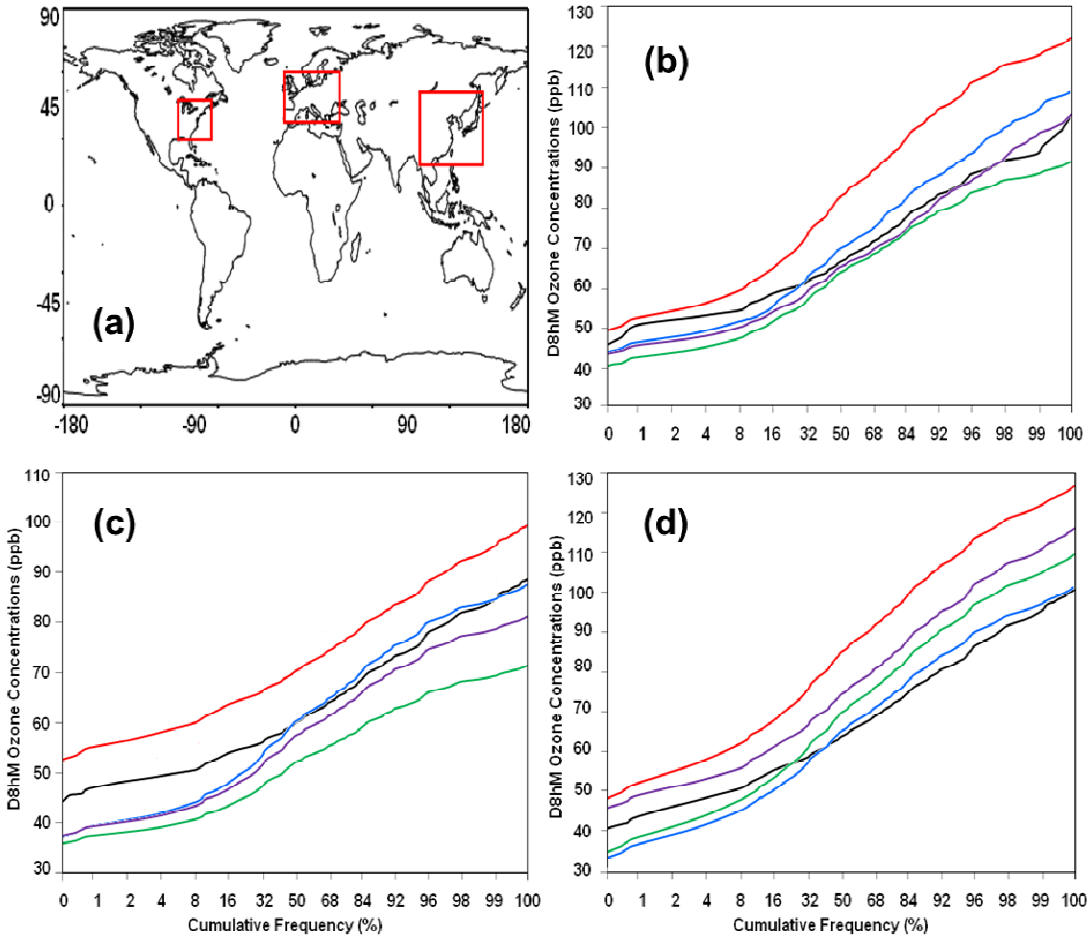

Figure 2.4. June–August Cumulative Frequency Distributions (CFDs) of regional mean daily 8-h maximum ozone concentrations during 1998–2002 and 2048–2052 over three major ozone pollution regions as shown: (a) Regional boundary specifications; (b) The eastern United States (30N-48N; 90W-70W); (c) Europe (35N-60N; 10W-30E); (d) East Asia (20N-50N; 100E-140E). In each region, the black line depicts the observed CFD during 1998–2002 (after adding the difference in the ozone median concentrations between the simulations and observations during 1998–2002), the blue line depicts the modeled CFD during 1998–2002, the red line depicts the modeled CFD during 2048–2052 under the A1FI scenario, the purple line depicts the modeled CFD during 2048–2052 under the A1B scenario, the green line depicts the modeled CFD during 2048–2052 under the B1 scenario.

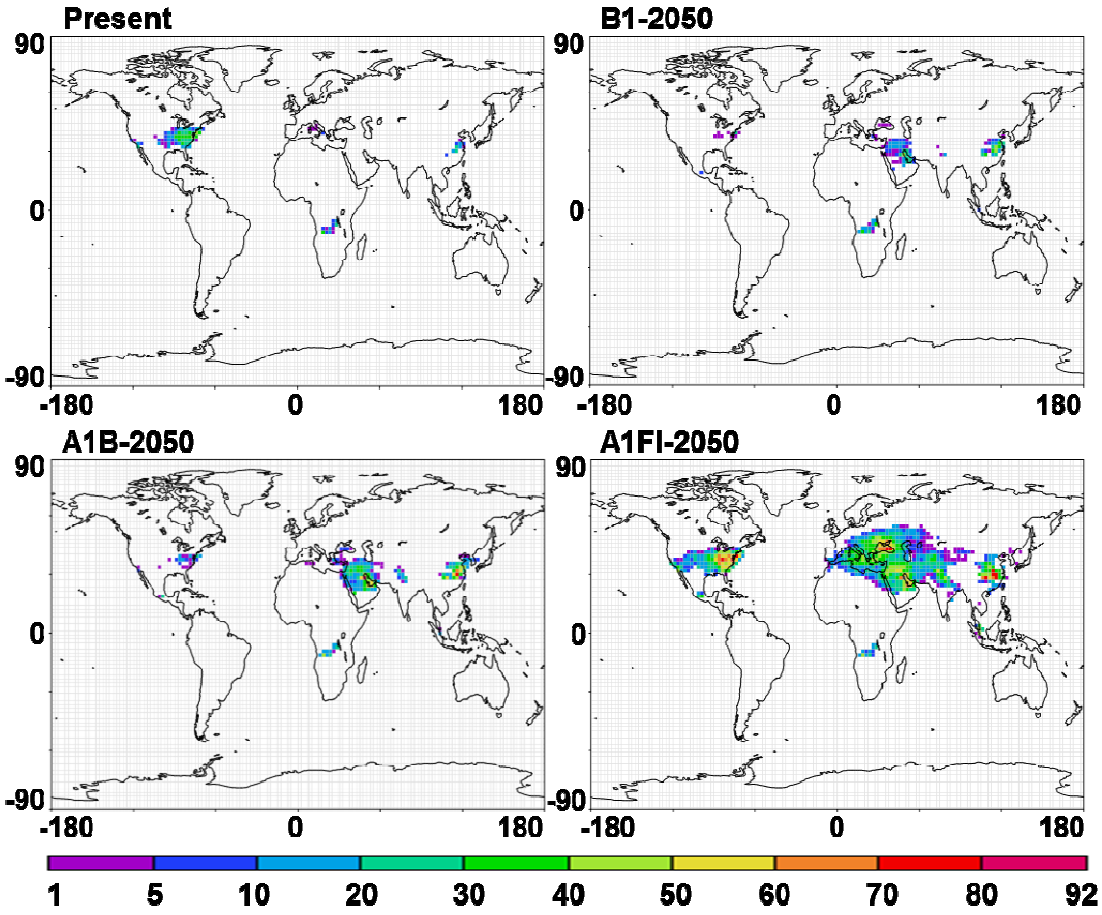

Figure 2.5. Frequency of high ozone days in summer for 2000 and projections under IPCC climate and emission change scenarios for 2050, based on daily 8-hour maximum standard. The results are all 5 years average with unit of days/summer.

CHAPTER 3: DOMESTIC VERSUS INTERNATIONAL CONTRIBUTIONS ON 2050 OZONE AIR QUALITY: HOW MUCH IS CONVERTIBLE BY REGIONAL CONTROL?

3.1 Introduction

Ozone near ground is an air pollutant with harmful effects on the respiratory systems of human. It forms from the reaction of sunlight on ozone precursors: volatile organic compounds and nitrogen oxides. Human activities contribute a large part of ozone precursors to the atmosphere, particularly as fossil fuel combustions. Previous studies have shown that the anthropogenic emission of ozone precursors is the dominant part of total precursors in surface ozone production [Solberg., et al., 2005; Godowitch et al., 2008]. As well as the most controllable part, reduction of anthropogenic emissions of ozone precursors becomes an effective way to improve air quality. Therefore, many countries have made control strategies to reduce the surface ozone concentration by limiting the anthropogenic emissions of ozone precursors [U.S. Environmental Protection Agency (EPA), 2008].

However, not all countries are only affected by emissions from themselves. For the north hemisphere middle latitude, air resource over major industrial regions, U.S., Europe and Asia, is connected by the westerly flow. Previous studies have shown that pollutants from upwind remote areas can affect air quality in downwind area [Fiore et al., 2002, 2005; Lin et al., 2008; Wuebbles et al., 2007]. In particular, the transpacific transport is the primary process for bringing Asian pollutants to the U.S.. Various ground-level observation analyses, field campaigns, and model simulations have been

conducted to investigate the current pathways and characteristics of transpacific transport, as well as their influence on U.S. air quality [e.g., Jacob et al., 1999; Wilkening et al., 2000; Yienger et al., 2000; Jaeglé et al., 2003; Hudman et al., 2004; Parrish et al., 2004; Bertschi and Jaffe, 2005; Heald et al., 2006]. For Europe, transatlantic transport of U.S. pollutants is the primary process contributing to European surface ozone [Li et al., 2002]. Observation and modeling studies have confirmed that its strong impact has been made in the free troposphere above Europe [Stohl and Trickl, 1999; Stohl et al., 2003]. In addition, a few studies have examined the transport of European pollution to Asia [Newell and Evans, 2000; Pochanart et al., 2003; Wild et al., 2004; Duncan and Bey, 2004]. Newell and Evans [2000] estimated that some 25% of the air parcels arriving over Central Asia have previously crossed over Europe, and some 4% have originated in the European boundary layer. Asian pollution can also reach Europe via westward transport with the monsoon circulation from India to Africa and the Mediterranean [Lawrence et al., 2003]. These studies have confirmed the interaction relationship among U.S., Europe, and Asia and the significance of effects of long range transports on them.

Several studies have projected the average and hazardous (extreme) conditions of surface ozone air quality in the coming decades under the climate and emission change background [Racherla and Adams 2006; Murazaki and Hess 2006; Tao et al. 2007; Hogrefe et al. 2004; Kunkel et al. 2008]. Hogrefe et al. [2004] studied the effect of climate change during 1990–2050 under the A2 scenario by using a regional model, and found an increase by 2050 of about 4.2 ppb in the summertime daily maximum 8-hour average ozone in the eastern U.S. A similar study with a global model by Racherla and Adams [2006] found that ozone decreases over most of the United States but slight

increases over the mid-Atlantic region and a large increase in the southeast by 2050. Studies by Tao et al., [2007], Wu et al., [2008a] and Lin et al. [2008a] found that changes in climate and U.S. anthropogenic emissions may cause near-surface ozone concentrations in 2050 either significantly higher under the A1FI scenario or slightly lower under the A1B, and B1 scenarios than the present level. Wu et al., [2008b] also show the 2000–2050 change in global climate and anthropogenic emissions of ozone precursors increases the tropospheric background ozone burden by 18%. As a companion study to that study, the study on the risk and uncertainty of hazardous ozone pollution in 2050 shows that peak frequency in summertime can be 6-73 days for North America, 0-39 days for Europe, and 47-79 days for Asia under the 8-hour maximum ozone standard, while it can be 0-57 for North America, 0-17 for Europe, and 4-59 for Asia under the 1-hour maximum ozone standard.

Of particular interest is how much of the future change in major ozone polluted regions is convertible by regional emission control activities. To understand it in each region, the critical issue is the relative contribution of local anthropogenic emission (LE) perturbations versus that of remote anthropogenic emission (RE) perturbations to average and hazardous (extreme) conditions in major ozone polluted regions and its uncertainty. In the coming decades, Changes in regional anthropogenic emission are likely to affect local air quality and downwind regions after transport. As a result, the ozone air quality change over each region contains large uncertainty. For instance, if U.S. anthropogenic emissions increase (decrease) and Asia anthropogenic emissions decrease (increase) in the future, there will probably be no reduction in pollution over the U.S. as a result of a greatly enhanced (reduced) RE. On the other hand, the LE decrease (increase) in U.S.

will affect European air quality through transatlantic transport. Affected by the uncertainties in climate and emission projections, the conclusions from analysis may vary under different scenarios as well. Previously, Lin et al [2008b] studied the future effects of intercontinental transport on the average condition of surface ozone air quality in 2050 over the U.S. under the A1FI and B1 scenarios. However, the discussion on future intercontinental transport changes was under the current background emissions [Lin et al., 2008b]. Considering the mass exchange with surroundings, a study with future background emissions would be more relavent for showing the changes under different scenarios. In addition, future changes in long range transport processes and their relative impacts on hazardous ozone air quality have not been examined. Comprehensive understanding on possible future contributions of changes in LE and RE for major industrial regions will be useful to air quality control strategies and emissions policies.

In this study, the Community Atmospheric Model with chemistry (CAM-Chem) is employed to investigate the relative contributions of changes in local anthropogenic emissions (LE) versus remote anthropogenic emissions (RE) to global hazardous ozone air quality in 2050. The model was driven by projected meteorology for 2050 from the Community Climate System Model version 3 (CCSM3). Three distinct climate/emission pathways from the Intergovernmental Panel on Climate Change (IPCC) Special Report on Emissions Scenarios (SRES, http://sres.ciesin.org/final_data.html) are considered, including the A1FI, A1B and B1 scenarios representing upper, middle and lower bounds of climate warming over the 21st century, respectively. Analyses will focus on changes in the summer months (June–August), when the risk of hazardous ozone episodes typically maximizes.

3.2 Methods

This study includes 15 experiments for the years of 2050, as listed in Table 1. These experiments were conducted with CAM-Chem driven by meteorological fields prescribed by climate system model outputs from the Community Climate System Model (CCSM3) which corresponds to the climate state of present or 2050 for different IPCC scenarios. The meteorology fields were archived with 6-hour temporal resolution. The main meteorology factors include wind, temperature, pressure, humidity and long/short wave radiation which have been prescribed to 2050 following the corresponding IPCC scenario in the climate system model; others are calculated in the model based these prescribed ones. Simulations are performed here with a 30 minute time step and a horizontal resolution of 1.9˚ x 2.5˚ with 26 vertical levels from the surface (1000 hPa) to 3-millibar level (~40 km altitude). Previous tests have shown that roughly a 6 months' spin-up calculation is enough for CAM-Chem to get rid of the effect of initial conditions. In this study, each case was run for 5 years (2048–2050) following 1 year of model spin-up. Unless noted otherwise, all the results discussed in this paper are 5-year averages. The modeled ozone concentrations were outputted at 1-hour interval to save storage.

Emissions of ozone precursors for 2000 are based on the present-day inventory as described by Horowitz et al. [2003]. We use 2050 estimates of anthropogenic emissions of ozone and aerosol precursors from the IPCC Marker scenarios as derived from the economic models used by IPCC [2001], miniCAM for A1FI, AIM for A1B and IMAGE for B1, respectively. Similarly to Fiore et al. [2002], we derive 2000–2050 growth factors for different categories of anthropogenic emissions for different countries, and then apply these factors to the present-day CAM-Chem emission inventories. The corresponding

changes of ozone precursor emissions for different regions are shown in Figure 3.1. The detailed changes in anthropogenic emissions will be discussed together with surface ozone air quality change in the next section. For the purposes of this study, seven masks were created that map the SRES marker reference model regions for each scenario and sensitive experiments onto a CAM-Chem grid (1.9°×2.5°) [IPCC 2001]. Current (2000) standard emissions of other chemical species in each region were projected to 2050 following the corresponding SRES emissions scenario in order to reproduce the changed atmospheric environment. Emissions from biomass burning sources are fixed at the present-day level for all experiments.

Biogenic emissions of ozone precursors including nonmethane VOCs (NMVOCs) from vegetation and CO emitted from soil are computed locally within the model on the basis of meteorological variables and hence allowed to change in response to climate change. Vegetation produce large amounts of NMVOCs through natural processes, many of which are affected by temperature and ambient CO2 concentrations. In the current CAM-Chem model, the biogenic emissions and soil emissions are calculated using the coupled community land surface model following the algorithms presented in Guenther (1999) and Potosnak (2002). Changes in soil emissions of carbon monoxide (CO) due to the temperature dependence of net primary production (NPP) were also considered [Adams et al., 2004]. However, soil emissions of NOx and oceanic emissions of all ozone precursors were kept at the same present-day levels in all experiments because of the large uncertainties in emissions estimations and the poor understanding of future changes. Biogenic emission changes were calculated for each experiment.

3.3 Surface Ozone air quality Change in 2050 due to human activities

To identify the relative effects of anthropogenic emission changes on future air quality, we first project the 2050 U.S. air quality in response to changes in climate and biogenic precursor emissions under the A1FI, A1B, and B1 scenarios. For these specific studies, the future anthropogenic precursor emissions are kept unchanged at present-day levels. In a second series of studies, the anthropogenic emission changes were considered in the projection together with climate and biogenic precursor emission changes. The results from all of these studies are then compared to see the contributions from anthropogenic emission changes under different scenarios.

For ozone pollution, what really matters to human life are hazardous levels of ozone pollution rather than the average level. Understanding the effect of changes in regional emissions on hazardous ozone pollution is the objective of this study. The U.S. EPA has been using the metric of daily maximum 8-hour average ozone for the ozone air quality standard, which provides a reference to quantify the hazard of ozone pollution. In addition, summer is the most productive season for surface ozone formation and natural precursor emission [Guenther et al., 1997]. The risk of hazardous ozone episodes typically maximizes in summer. Therefore, summertime daily 8-hour maximum (D8hM) surface ozone concentration is used here to examine the changes in future hazardous ozone air quality. Figure 3.2 shows the simulated daily maximum 8-hour average surface ozone concentration perturbations averaged over June–August for 2050 anthropogenic emissions changes. Results under the A1FI scenario are shown in Figure 3.2a. The A1FI scenario emphasizes continuing heavy use of fossil fuels. It is seen that surface ozone concentration increases all over the world due to emission change in 2050. The most

intense areas are current industrial developed regions. For the United States area, the maximum increase is around 10 to 15 ppb, which occurs on the eastern United States and in the southwest near California. The overall surface ozone increase is more than 5 ppb in the contiguous U.S. For western Europe, the situation is similar to U.S. with a maximum increase around 10 to 15 ppb. The largest increase in ozone occurs in Asia with a maximum increase around 30 to 35 ppb. Our result on each region is consistent with previous results and the change in emissions of ozone precursors. According to previous studies by Tao et al., [2007], the U.S. surface ozone by 2050 will increase around 2-15 % under the A1FI scenario. Generally, the increase magnitude in the Northern Hemisphere is larger than that in the Southern Hemisphere, simply because the major anthropogenic emission sources are located in the Northern Hemisphere. The similar changes in trends spreading over the whole hemisphere shows the significant impacts of intercontinental transports.

Figure 3.2b shows the results for the A1B scenario. The A1B scenario emphasizes a balanced reliance on all energy sources. Either increases or decreases in surface ozone concentrations occur due to emissions changes in 2050 under the A1B scenario. For the U.S. region, the most decreased areas are current industry developed areas, such as the eastern United States and in southern California. The maximum decrease is around 10 to 15 ppb. The ozone change found here is similar to the finding by Wu et al., [2008b]. In their study, changes in anthropogenic emissions reduce the U.S. summer daily 8-hour maximum ozone by 2-15 ppb under the A1B scenario. Similar change trend also occurs in Europe with a decrease of 0-10 ppb over the continental Europe and an increase of 0-6 ppb on coastal area. Other parts of the world show clear increase of D8HM surface ozone

in 2050. The maximum increase is in Asia, because of the rapid increase of anthropogenic emission there (e.g., 2050 NOx emission in Asia increase by about 110% relative to the 2000 value). In contrast, the anthropogenic emission of NOx in the contiguous U.S. and Europe decreased to half its current emission by 2050. Therefore, the anthropogenic emission is the major force for estimating future ozone air quality change.

Figure 3.2c shows the results under the B1 scenario. The B1 scenario describes a world more integrated, and more ecologically friendly. It emphasizes the introduction of clean and resource efficient technologies. Therefore, the anthropogenic emissions do not increase much in developing countries and decrease a lot in developed countries. As a result, the surface ozone concentrations over the world increase in south hemisphere, in which most countries are developing countries, and decrease in north hemisphere, in which most developed countries located. By the year 2050, the NOx emission of U.S. goes down to less than half of current emission. The resulting surface ozone concentrations in U.S. region decrease about 15 to 20 ppb. This estimate is close to the estimate by Lin et al., [2008a, 2008b]. However, in Asia, the emissions increase is significant but not the biggest increase. The maximum increase of emissions occurs in Africa and Latin America. Therefore, the increase of D8HM surface ozone concentration in Asia is up to 23 ppb, while the increase over Africa and Latin America is up to 28 ppb.

3.4 Global Pathways of Intercontinental Pollution Transport

Through the analysis of effects of anthropogenic emission changes on future summer time daily 8-hours maximum ozone concentration, significant contributions from

anthropogenic emission changes under different scenarios have been shown. But how much of the changes in ozone concentration is contributed by the change in local emission and how much is the consequence of changed intercontinental transport of remote emissions? To answer this question, it is necessary to find out the possible pathways of intercontinental transport over the world and their functions in connecting different areas.

Long range transport of surface pollutants associates with wind above the boundary layer. The wind on the pressure layers between 850 HPa and 500 HPa are usually used in transport analysis. Figure 3.3 shows the CAM-Chem simulated summer daily 8-hours maximum ozone concentration and the summer mean wind field on 850 HPa pressure level. In the summer, the oceans are controlled by high pressure systems, while continents are controlled by low pressure systems. In the northwest Pacific Ocean, the winds at 30° to 50° N are blowing from the high ozone concentration area of Asia to the west coast of the United States, while the easterly winds at 20° to 30° N bring air from the tropical Pacific region to East Asia. In the north Atlantic, winds at 30° to 50° N middle latitudes are blowing from eastern U.S. to Europe, while the winds at low latitudes bring the air from tropical regions to the south U.S. The wind field over the Euro-Asia continents is mainly affected by terrain. Blocked by mountains in the middle and western Asia, the direction of averaged winds at 850 HPa pressure surface are indistinct over central Euro-Asia. According to previous studies on pollutant transport, the CAM-Chem simulated summer wind fields capture the main characteristics of global wind distribution and transport associated wind flows [HTAP, 2007].

From the pattern of simulated summer wind fields and the summertime surface ozone distribution, major ozone polluted regions affected by long range transport are North American, Europe and Asia. This result is also found by previous studies of intercontinental transport of air pollution in the Northern Hemisphere research project [HTAP, 2007]. In addition, Wuebbles et al. [2007] summarize the major global transport pathways for long range transport from previous studies and show that major pathways of long range transport include transpacific transport, transatlantic transport and transport by easterly wind on tropical regions. Studies by Newell and Evans [2000] and Lawrence et al. [2003] show that pollutant exchange exists in surface air pollution between Europe and Asia. Therefore, we are going to examine the effect of changes in remote emissions among North American, Europe and Asia connected by the transpacific transport, the transatlantic transport and the Euro-Asia transport.

3.5 Contributions analysis

3.5.1 Surface Ozone Change due to local emissions change

Projected changes in local anthropogenic emissions can have significant impacts on the future ozone air quality. Over the coming half century, anthropogenic emissions of ozone precursors over the world are projected to change greatly, strongly varying under the A1FI, A1B and B1 scenarios. As a result, from 2000 to 2050, increases in U.S. anthropogenic emissions under the A1FI scenario lead to increases in U.S. daily 8-hour maximum surface ozone concentrations by 1–4 ppb over the west and 4–8 ppb over the east (Figure 3.4a). Under the A1B scenario, the effect of local emission change is conversed, i.e., by decrease 1-6 ppb over the western U.S. and 12-18 ppb over the eastern

U.S. (Figure 3.4d). Similarly for the B1 scenario, the local emissions change result in a decrease of 6-12 ppb over the west and 12-19 ppb over the east (Figure 3.4g). Overall, under the A1FI scenario, U.S. local emissions change makes positive contribution to future ozone air quality, due to the rapid increasing trend for NOx and VOCs emissions. Conversely, the effects of U.S. local emissions changes under the A1B and B1 scenarios show negative contributions to surface ozone concentration as a result of emissions decreases.

For Europe, from 2000 to 2050, increases in anthropogenic emissions under the A1FI scenario lead to an increase in summer daily 8-hour maximum ozone concentration by 3–9 ppb over continental Europe (Figure 3.4b). Under the A1B scenario, the anthropogenic emission change in Europe leads to a decrease of 5-10 ppb (Figure 3.4e). Similarly under the B1 scenario, the local emission change result in a decrease of 7-10 ppb (Figure 3.4h). The change trend is similar to that for the U.S., because of similar emission projection rates and close current emission levels.

For Asia, anthropogenic emissions have increasing trends under all three scenarios. Increases in Asian anthropogenic emissions under the A1FI scenario lead to a 10-30 ppb increase in summer daily 8-hour maximum ozone concentration in 2050 (Figure 3.4c). Under the A1B scenario, the local anthropogenic emission change in Asia leads to a 1-12 ppb increase (Figure 3.4f). Under the B1 scenario, the local anthropogenic emission change contributes an increase of 1-4 ppb to summer daily 8-hour maximum ozone concentration in 2050 (Figure 3.4i). Relatively, contributions of Asian local anthropogenic emissions change are the largest to local ozone in the three major industrial regions.

3.5.2 Surface Ozone Change due to remote emissions change

Changes in long range transport of remote emissions can affect the regional air quality. Many factors other than local activities can affect the long range transport. Relatively, source emissions are a more significant factor in determining the effect of long range transport by directly changing the source-receptor relationship [HTAP, 2007]. Emission control activities in the remote (/source) region directly affect the flux of pollutant in transport. Therefore, the region under strong remote emissions impact could have difficulty in solving its pollution issues. To investigate the possible changes in future long range transport impacts over major industrial regions, sensitivity experiments with/without considering source emissions change under future climate and emission change scenarios were analyzed. The meteorology field and surrounding emissions are projected to 2050 in order to approach the practical future environment.

The United States (North America) is affected by remote emissions from Asia and Europe. Projected changes in Asia anthropogenic emissions can have significant impacts on the transpacific transport. Over the coming century, anthropogenic emissions of ozone precursors over Asia are projected to change greatly under the A1FI, A1B and B1 scenarios relative to present-day levels (Figure 3.1). As a result, by 2050, increases in Asia anthropogenic emissions under the A1FI scenario lead to an increase of 5–9 ppb in summertime D8HM ozone concentration over the western U.S. and an increase of 2–5 ppb over the eastern U.S. (Figure 3.5j). Compared with the results for 2050 by Lin et al., [2008b], the effect of changes in Asian emissions under the A1FI scenario is estimated to be larger in this study. The primary reason appears to be associated with the increase in

future Asian emissions. Under the A1B scenario, the 2050 effect of RE change in Asia is slightly reduced, i.e., with no more than a 3 ppb effect on the continental U.S. (Figure 3.5p). Under the B1 scenario, the effect is greatly reduced, i.e., with an impact of no more than 0.5 ppb (Figure 3.5v). The effects of changes in transatlantic transport on the U.S. ozone concentrations are small under all three scenarios due to the small changes in emission gradient between North America and Europe (Figures 3.5m 3.5s and 3.5y). Due to the same reason that U.S. surrounding emission decrease by 2050 in this study, this result under the B1 scenario is smaller than the estimate by Lin et al. [2008]. Under the A1FI scenario, total Europe anthropogenic emission change contribute 0.1-0.6 ppb's increase in summertime D8HM ozone to the contiguous U.S. The impact on the northern U.S. is larger than that on the southern states because of the position of transport flow. Under the A1B and B1 scenarios, contributions of total Europe anthropogenic emissions change lead to decreases in D8HM ozone concentration within the range of 0-1.5 ppb. The decrease magnitude under the A1B scenario is slightly less than that under the B1 scenario, because the anthropogenic emissions decrease in Europe under the B1 scenario is greater than that under the A1B scenario.

Europe is affected by remote emissions from the United States and Asia. Over the coming 50 years, it is more likely that anthropogenic emissions over the United States will be reduced as a result of a series of pollution control activities while Asian emissions will likely grow, at least for the coming decades as a result of the fast on-going industrialization and economic/population growth; in the longer term, these emissions may also be reduced under stronger control policies. Since there are clear pathways for transport pollutants from U.S. and Asia to Europe, it is of interest to investigate the

effects of the likely changes in emissions on future air quality over Europe through transatlantic and Asia-Euro transports. In this regard, we find that, by 2050, the summer D8HM ozone concentrations in Europe will increase 1–6 ppb due to the increasing U.S. anthropogenic emissions following the A1FI scenario (Figure 3.5k). If the changes follow the A1B or B1 scenarios, both corresponding effects by 2050 show decreases in D8HM ozone concentration over Europe of 0.5-0.7 ppb (Figures 3.5q and 3.5w). This suggests that the projected changes in Asian emissions under the A1B and B1 scenarios have similar effects on Europe ozone air quality. In addition, projected future changes in Asian anthropogenic emissions affect the air quality over Europe as well. Relatively, the Eastern Europe, closest to Asia, is more affected by Asian emissions. Under the A1Fi scenario, there is an increase of 1-3 ppb in (Figure 3.5n) summertime D8HM ozone concentration due to the large increase in emissions of ozone precursors in Asia (Figure 3.1). Unlike the world wide increase of emissions under the A1FI scenario, the emission change under the A1B and B1 scenarios are more affected by control activities, which results in small impacts of change in Asian remote emission. The result under the A1B scenario shows an increase up to 0.5 ppb (Figure 3.5t) in summertime D8HM ozone concentration over eastern Europe, while the impact on western Europe is small. The increase under the B1 scenario is around 0-0.05 ppb (Figure 3.5z). Compared with the impacts of transatlantic transport, the Asia-Euro transport has less contribution to ozone air quality in Europe, even though Asia has far greater increase in emissions than U.S. under the A1FI scenario. The blocking effect of terrain affects the transport flow between Europe and Asia.

Asian ozone air quality is under the impacts of remote emissions from Europe and the United States. Under the A1FI scenario, increases in European anthropogenic emissions lead to an increase of 0.1-0.6 ppb in summertime D8HM ozone concentration over Asia. Since the emissions in Europe has a trend similar to that in U.S., the small impacts on Asia and large impacts on Europe demonstrate that transpacific transport is much stronger than Euro-Asia transport. The A1B scenario gives a decrease of 0.1-0.4 ppb in summer D8HM ozone over Asia from European sources. Under the B1 scenario, projected changes cause a decrease of 0.1-1.0 ppb in Asian summertime D8HM ozone concentration. The weak transport rate of Euro-Asian transport is mainly attributed to the terrain effects of high altitude terrain in the west and middle Asia. Since most of pollutants go follow the jet stream in the lower and middle troposphere, pollutants emitted in Europe is difficult to get to Asia. In addition, the effects of transpacific transport on Asia surface ozone tend to be a passive process changes in the transport rate from Asia rather than directly transport pollutants from North America. Under the A1FI scenario, the summer D8HM ozone concentration over Asia in 2050 does not show a clear increase or decrease trend from increasing U.S. anthropogenic emissions (Figure 3.5k). The effect under the A1FI scenario is an increase of 0-1.0 ppb on the continent, but a decrease up to 1.0 ppb near the coast. If the changes follow the A1B or B1 scenario, the corresponding effects in 2050 are both decreases in Asian D8HM ozone concentration with a range of 0.1-0.6 ppb under the A1B scenario or 0.1-0.7 ppb under the B1 scenario (Figures 3.5q and 3.5w). These results suggest that the transpacific transport rate under the A1B or B1 scenario decreases due to the emission decreases in the U.S.

3.6 Discussions on how much is convertible by regional effort?

Anthropogenic emission control is the primary way that people can act on future air quality change. Although climate change also affects the future air quality, the effects of human activities on global warming by 2050 are estimated between 1.0 □ C and 2.5 □ C [IPCC, 2001]. Previous studies have shown that the change in climate may contribute to ozone air quality change in 2050 by 8-13% [Tao et al., 2007; Wu et al., 2008; Engardt et al., 2009], while the ozone air quality change caused by change in anthropogenic emissions is around 87-92%. Therefore, control on anthropogenic emissions of ozone precursors is likely the practical way to affect the future air quality.

The argument for anthropogenic emission control is that each country may (/may not) improve air quality through its own control action. The effect of anthropogenic emissions control on each region depends on local emissions and remote emissions which is relatively inconvertible by regional effort. As summarized in Table 2, we find that the major factor (local emission or intercontinental transport of remote emissions) to determine future surface ozone air quality change on each region differs due to the differences in general circulation, climate change and emissions trends. The specific characteristics affecting major ozone polluted regions are discussed below.

(1) The United States: The transpacific transport of ozone precursors from Asia is an important issue for future U.S. ozone air quality. Therefore there is a concern that regional control strategies for air pollution may be insufficient. Under the A1FI scenario, the D8HM ozone concentration increase due to the rapid rising emissions of ozone precursors in Asia is equivalent to that caused by local anthropogenic emission rise. For the low anthropogenic emission changes in Asia under the A1B and B1 scenarios, the

impacts of transpacific transport changes are much smaller than that of local emissions changes. However, under all scenarios, the effects from transatlantic transport of European emissions are relatively small. This reveals that the success of U.S. ozone mitigation not only depends on the country-wide emission reductions but also depends on what happens to air pollution in Asia.

(2) Europe: For 2050 ozone air quality over Europe, the analysis under the three scenarios shows greatly different results. Under the A1FI scenario, both the local emissions changes and the intercontinental transports changes can make similar contributions to the 2050 Europe surface ozone air quality. Although the increase in transatlantic transport has a major role in future intercontinental transport effects on ozone, the Asia-Euro transport also affects European ozone. Therefore, for air quality control strategies in Europe, controlling local emissions can only have a limited effect unless emissions are also reduced in the United States and Asia. For the A1B or B1 scenarios, the effects from transatlantic transport changes and Asia-Euro transport changes counteract each other. Then controlling local emissions can effectively improve Europe ozone air quality.

(3) Asia: The transport of pollutants from Europe to Asia seems to be very weak. Rapid industrialization in Asian countries and resulting increase in emissions in the coming decades will likely dominate the Asian air quality change. Under all three scenarios, the surface ozone air quality change by 2050 due to local emissions changes is much larger than that caused by intercontinental transport changes. Although the remote emission changes in the United States and Europe together contribute a decrease up to 1.7 ppb to Asian ozone air quality, the local emission change dominates the increasing local

trend with a contribution up to 4ppb. So, local emission control is a crucial strategy for future Asian ozone air quality.

To better understand our results, it is noted that the simulations of intercontinental transports are affected by (1) meteorological data, and (2) nonlinear processes in chemical reactions and physical transport. For instance, we use the meteorological data from climate system model output, for which a 5 years' average is used to represent the climatology in 2050. Therefore our findings here are largely climatological. On the other hand, chemical nonlinear characteristic in surface ozone production is mainly attributed to the NOx-VOCs relationship. Physical nonlinear behaviors result from the transport of pollutants. These nonlinear processes can affect the projected changes in surface ozone in response to the changes in emissions over source regions [HTAP, 2007].

In addition, there are several limitations in this study. Because of the coarse resolution of model and data, the detailed projections of changes at urban or smaller scales are unavailable. To achieve a better understanding on regional air quality change, an integrated modeling system with CMAQ regional Chemical transport model nested has been developed and the results on the U.S. will be published soon. Also, in the projections of peak ozone concentration, we did not consider the effects of interactions between plants and hazardous ozone levels as a feedback on ozone concentrations. High ozone concentrations can be hazardous for plants, causing death in cells, which in turn may decrease the biogenic emissions of ozone precursors. As a possible consequence, the change in D8HM ozone concentrations may be lower than our estimate. Despite these limitations, however, the results of this study allow us to draw several important conclusions regarding future ozone concentration changes over major polluted regions.

3.7 Summary

We investigated the effects of 2000–2050 global anthropogenic emission change on global surface ozone air quality by using a climate chemistry model (CAM-Chem CTM) driven by meteorological output from the community climate system model (CCSM3). We examined the total and then separate effects of changes in regional anthropogenic emissions on 2050 surface ozone air quality over major polluted regions, in order to find out how much of change is convertible by the regional emission control effort under future climate and emission situations. The result is expected to be scientific reference in making air quality control strategies or emission policies.

We find that the contributions from local emission change and remote emission change on 2050 ozone air quality under the IPCC A1FI scenario are comparable for the United States and Europe, but changes in Asian ozone air quality largely depend on local emission changes. The summertime daily 8 hour maximum (D8HM) surface ozone concentration over the United States increase of 5-14 ppb by 2050, 48% of which is contributed by changes in local anthropogenic emissions and 52% of which is contributed by changes in long range transport of remote emissions. For Europe, the changes in local emissions contributes 62% of the surface ozone increase in the 2050 summer, while 38% of the increase is attributed to remote emission changes. For Asia, local anthropogenic emissions change dominate the 2050 surface ozone changes with increases of 10-30 ppb on summertime D8HM surface ozone concentrations.

Under the A1B scenario, Asian ozone air quality change is still dominated by the changes in local anthropogenic emissions, while the relative contribution from the changes in remote anthropogenic emissions to the air quality changes over the United

States and Europe become less important. The contribution from the changes in local anthropogenic emissions takes up around 83% of the total summertime D8HM ozone changes in 2050 over the United States. The rest is due to the effect of changes in remote emissions from other regions. For the summertime D8HM ozone change in Europe, the small decrease caused by change in remote emission from North America cancels the small increase caused by change in Asian remote emissions. As a result, the change in local anthropogenic emissions dominates the 2050 ozone air quality change in Europe. For Asia, the increase in summertime D8HM ozone concentration contributed by change in local emissions is 12 times as much as the contributions from remote emissions.

Change in Asian ozone air quality under the B1 scenario will be affected by changes in both local emissions and long range transport effects, while effects of changes in remote emissions on ozone air quality changes in the United States and Europe are negligible. For the 2050 summertime D8HM ozone changes in Asia, the changes in local anthropogenic emissions tend to increase the concentration with a contribution of 69% in the total change. The changes in remote emissions tend to decrease the Asian ozone concentration with a contribution of 31% in the total change. For the U.S. and European ozone air quality change, the local emissions changes contribute more than 90 % of the total changes. The effects of changes in long range transport effects are small and of opposite sign, with the net effect being negligible.

In summary, the results indicate that for the United States and Europe, pollution control is a local issue under the low global emissions scenarios examined, while air quality becomes an international issue under the A1FI scenario. Due to the weak Euro-Asia transport, local emission increase seems to be the main problem for Asian ozone air

quality changes under all scenarios, although the effect of remote emission change is comparable under the low emissions scenario B1.

Table 3.1. Experimental Design Design for study of climate and ozone precursor emissions.

Experiment	*Climate*[a]	*Anthropogenic Emissions*[b]
(1) A1FI2050	A1FI 2050	F / F / F /F[c]
(2) A1B2050	A1B 2050	F / F / F /F
(3) B12050	B1 2050	F / F / F /F
(4) A1FI2050_noAEC	A1FI 2050	C /C /C /C
(5) A1B2050_noAEC	A1B 2050	C /C /C /C
(6) B12050_noAEC	B1 2050	C /C /C /C
(7) A1FI_2050_noEUR	A1FI 2050	C / F / F /F
(8) A1FI_2050_noUS	A1FI 2050	F / C / F /F
(9) A1FI_2050_noASIA	A1FI 2050	F / F / C /F
(10) A1B_2050_noEUR	A1B 2050	C / F / F /F
(11) A1B_2050_noUS	A1B 2050	F / C / F /F
(12) A1B_2050_noASIA	A1B 2050	F / F / C /F
(13) B1_2050_noEUR	B1 2050	C / F / F /F
(14) B1_2050_noUS	B1 2050	F / C / F /F
(15) B1_2050_noASIA	B1 2050	F / F / C /F

[a] Physical environment of the troposphere, including temperature, water vapor, etc.
[b] Including emissions from fossil fuel, industrial, transportation, biofuel etc.
[c] The four symbols separated by '/' denote the emission over Europe, the United States, Asia and rest of the world. Symbol 'C' denotes current emissions; 'F' denotes future emissions projected under each scenario.

Table 3.2. Summary of local emissions impact and remote emissions impact under the A1FI, A1B and B1 scenarios

		Emissions Region		
		U.S.	Europe	Asia
Impact Region	U.S.	1-8 /-1--18 / -6--19 [a]	0.1-0.6 /0--1.5/0--1.5	2-9 /0-3 / 0-0.5
	Europe	1-6 /-0.5--0.7/-0.5--0.7	3-6 /-5--10 / -7--10	1-3 /0-0.5/0-0.05
	Asia	-1-1/-0.1--0.6/-0.1--0.7	0.1-0.6 /-0.1--0.4 /-0.1--1	10-30 /1-12 / 1-4

[a]: The numbers before and after '/' denote projected fractional emissions changes under the A1FI, A1B and B1 scenarios, respectively, relative to present budgets.

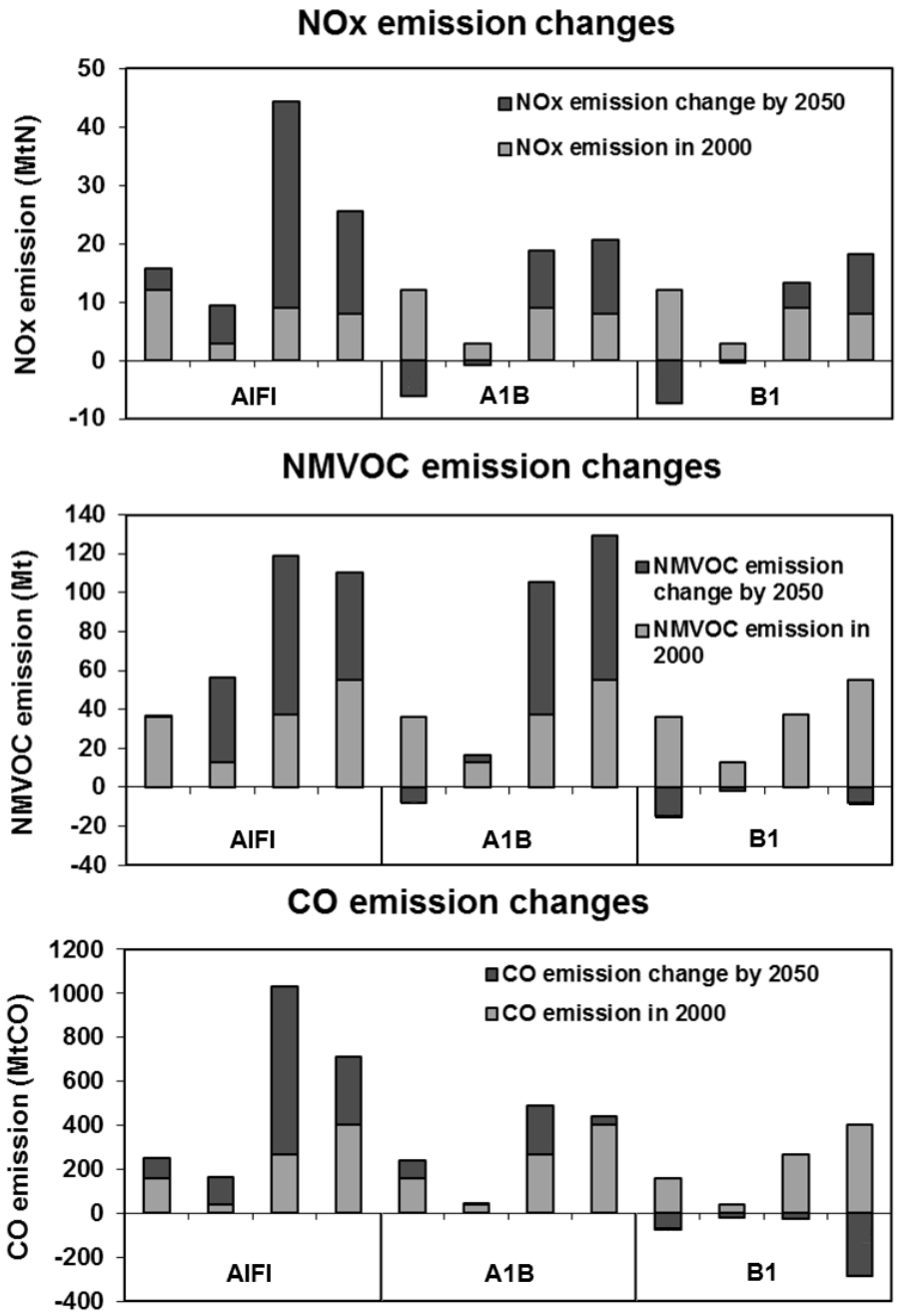

Figure 3.1. Projected annual anthropogenic emission budgets of ozone precursors (NOx, nonmethane VOCs, and CO) over the world for 2000 and their changes by 2050 under the IPCC A1FI, A1B and B1 scenarios. (1: OECD90 REGION; 2: REF REGION; 3: ASIA REGION; 4: ALM REGION)

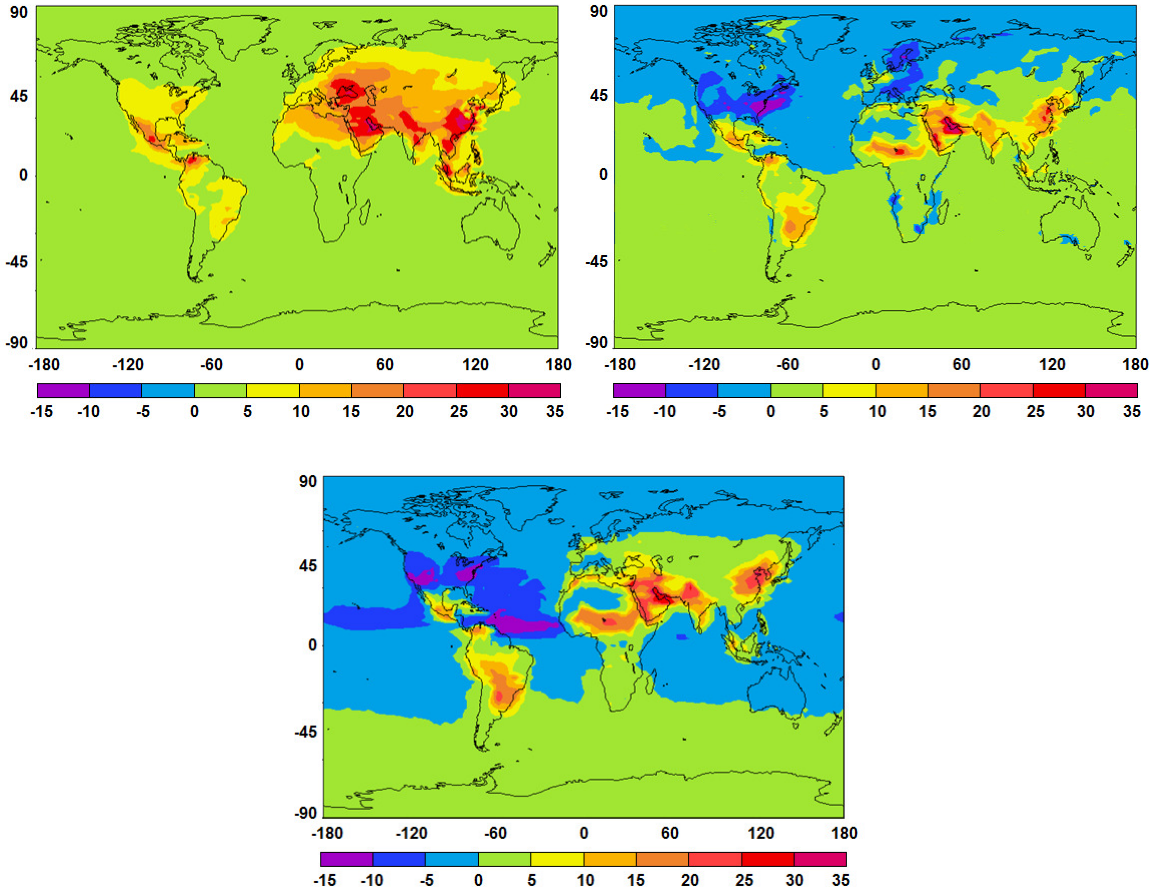

Figure 3.2. Contributions (in ppb) of anthropogenic emissions change to 2050 summer daily 8-hour maximum surface ozone concentrations under the A1FI (a: top), A1B (b: middle) and B1 (c: bottom) scenarios.

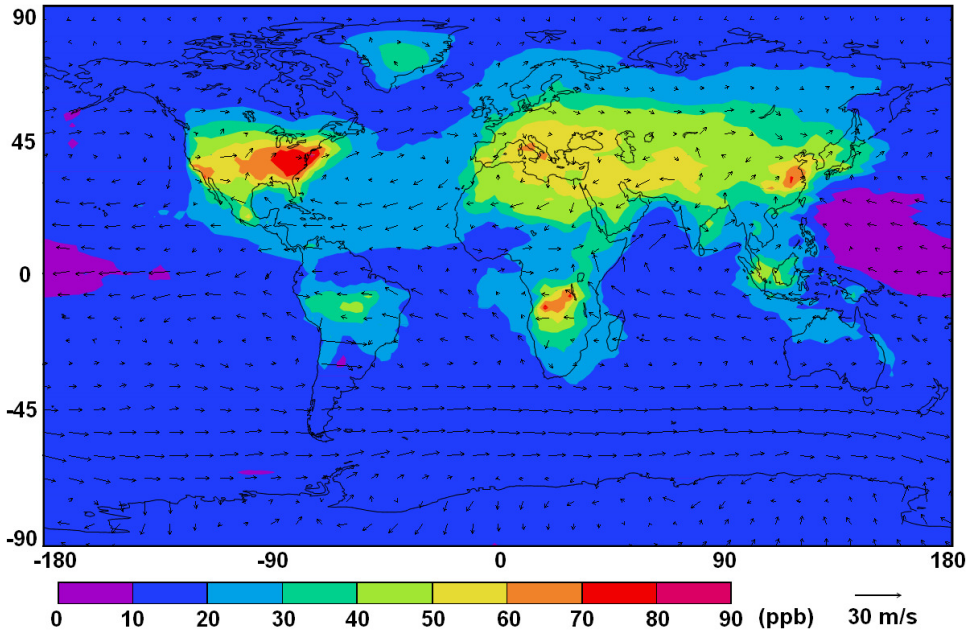

Figure 3.3. CAM-Chem simulated summer daily 8-hours maximum surface ozone concentration and averaged winds at the 850 HPa pressure level. The results represent the average of the simulations during the years 1998-2002.

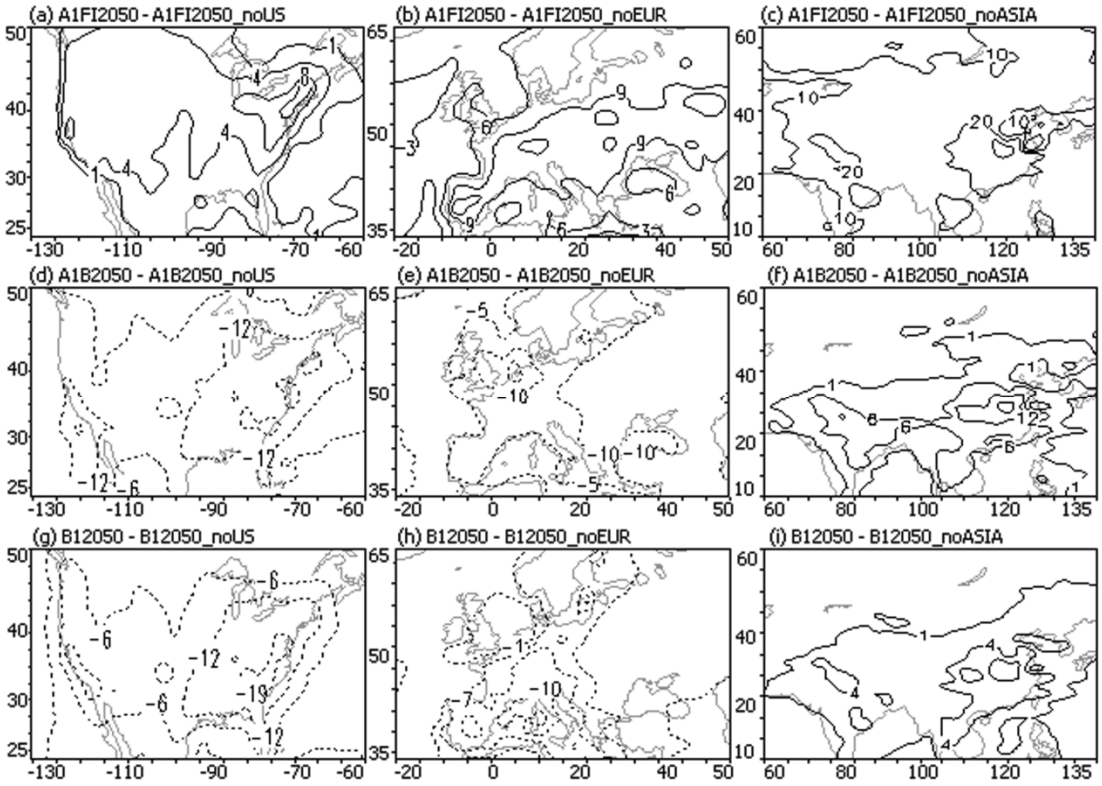

Figure 3.4. Contributions (in ppb) of local anthropogenic emissions change to 2050 summer daily 8-hour maximum surface ozone concentrations over the United States, Europe, and Asia (left, middle, right) under the A1FI, A1B and B1 scenarios (top, middle, bottom).

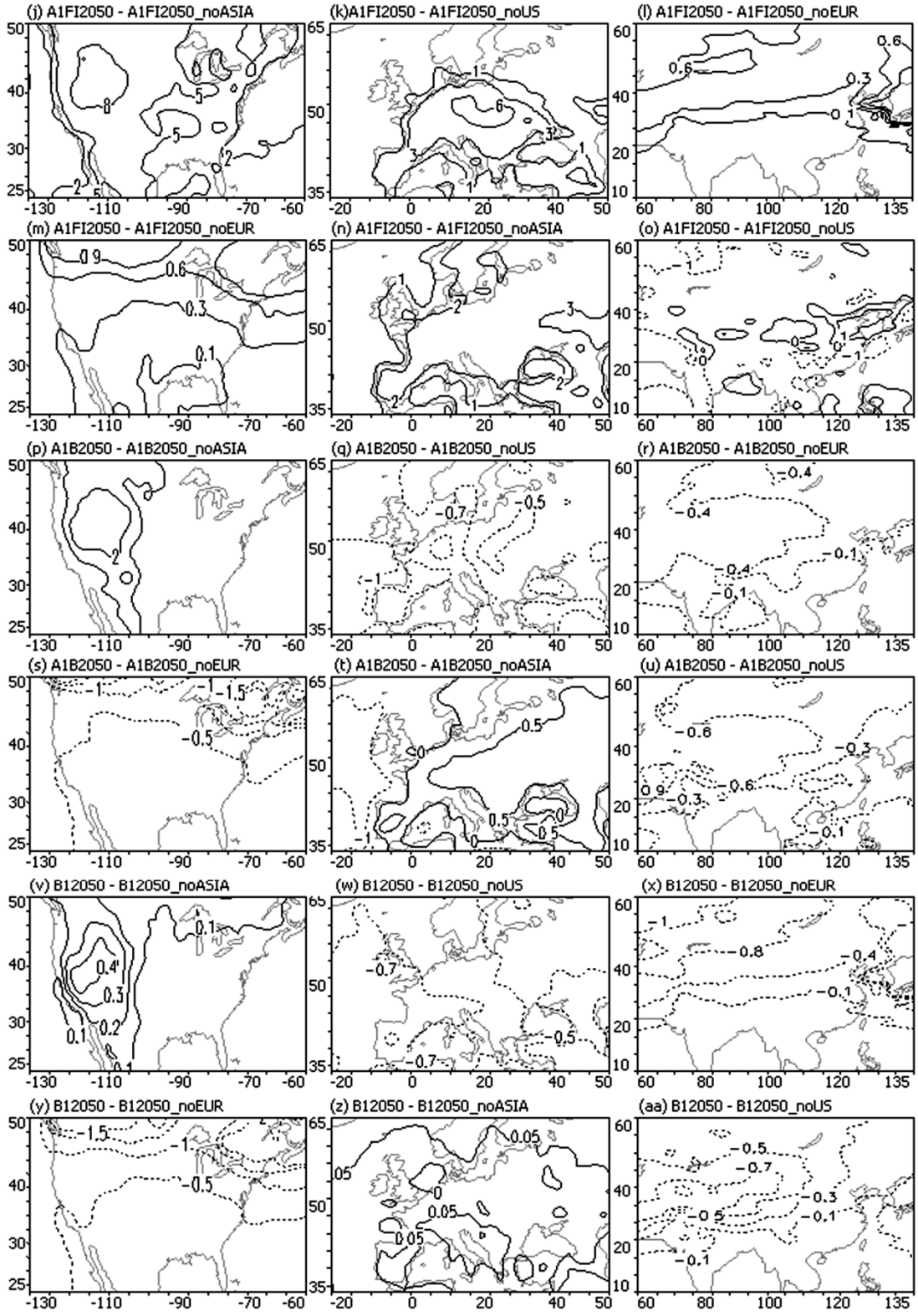

Figure 3.5. Contributions (in ppb) of intercontinental transport changes to 2050 summer daily 8-hour maximum surface ozone concentrations over the United States, Europe, and Asia (left, middle, right) under the A1FI, A1B and B1 scenarios (top 2 rows, middle 2

rows, bottom 2 rows). The sub-title of each plot shows its name. The name is composed of two experiment results. The rest of each name includes the name of remote region, which indicates the contributions of intercontinental transport from that region. Detailed information about each experiment is included in Table 3.1.

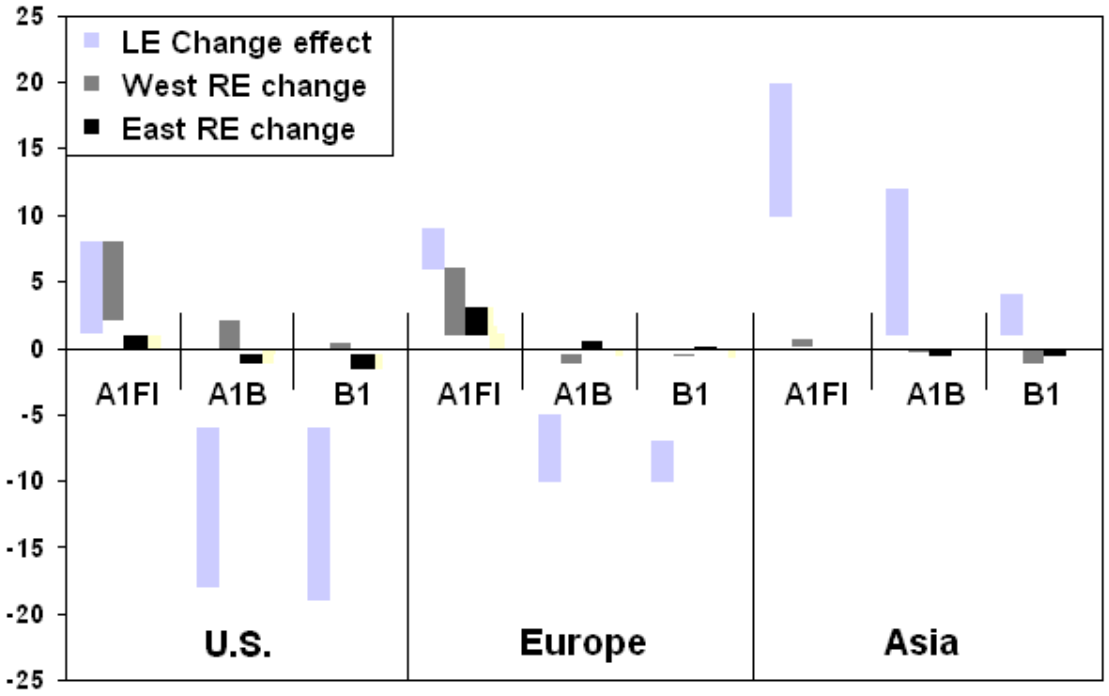

Figure 3.6. Effects (in ppb) of local anthropogenic emissions changes versus intercontinental transport changes on 2050 summer daily 8-hour maximum surface ozone concentrations. From the left, 1: The United States under the A1FI scenario, 2: The United States under the A1B scenario, 3: The United States under the B1 scenario, 4: Europe under the A1FI scenario, 5: Europe under the A1B scenario, 6: Europe under the B1 scenario, 7: Asia under the A1FI scenario, 8: Asia under the A1B scenario, and 9: Asia under the B1 scenario.

CHAPTER 4: PHYSICAL DUST AEROSOL MODELING BY CAM-CHEM: MODEL FORMULATION AND EVALUATION

4.1. Introduction

Mineral dust is a major component of atmospheric aerosols. The emission, transport, and chemical reactions of mineral dust particles in the atmosphere seriously affect air quality and weather processes [Prospero, 1999; Ansmann, et al. 2008]. Their impacts on radiation transfer, ecological and biogeochemical processes can deeply affect the climate system [Woodward, 2001; Werner et al., 2002; Bauer et al., 2007]. Mineral dust is reported as a major pollutant in air quality standards [Harrison et al., 2004]. Serious dust storms occur in Asia, Africa, Australia, North and South America [Shao et al., 2002; Tulet et al., 2008]. Dust particles can induce changes in the formation of clouds and precipitation as nuclei [Wiacek and Peter, 2009], which further impacts the regional climate [Yin et al., 2002]. Mineral dust also affects the acid equilibrium [Rastogi and Sarin 2006] and oxidant power of the troposphere [Bian et al., 2004]. In addition, deposited mineral dust affects the Earth's biogeochemistry by joining the phosphorous cycle of terrestrial ecosystems and phytoplankton processes over the surface ocean [Okin et al., 2004].

A challenge in mineral dust aerosol studies is to accurately estimate the emission rate of dust particles in all size ranges for natural land surfaces. There have been several attempts already at representing these processes. Wind erosion schemes for dust emission and sediment drift have been developed on the basis of the microphysics of wind erosion [Marticorena and Bergametti, 1995; Shao et al., 1996; Marticorena et al., 1997; Lu and

Shao, 1999; Wang et al., 2000; Alfaro and Gomes, 2001; Shao, 2002; Zender et al., 2003; Wang et al., 2000; Gong et al., 2006; Yue et al., 2009]. However, most of these dust emission schemes are based on empirical formulation for dust emissions processes. Dust source regions and the erosion characteristics of each region are pre-determined in empirical dust emission models. The model results are highly depended on these pre-determined parameters rather than the climate and environmental conditions.

However, the area of dust source regions on the surface of the Earth is highly variable. Climate and environmental factors such as soil type, moisture, snow cover as well as vegetation type, coverage, and height, can affect the soil erodibility in a given region. Therefore, pre-determined parameters disregard the natural variability of some critical factors for dust emission, which cannot adequately describe characteristics that respond to environmental changes. As a result, the empirical models have problems in simulating the inter-annual variability of dust emissions and occasional dust emission episodes (dust storms) in response to distinct variations in climate and associated surface condition or severe changes in local weather and surface conditions.

To capture the natural variability of dust emissions and improve the predictions of occasional dust storm episodes, Shao et al., [2007] developed a systematic physical theory for dust emissions based on a large number of wind tunnel experiments. Instead of using parameterizations, Shao's theory calculates major factors for the dust emission by using climate and surface environmental variables that are essential to the natural dust emission process. Physical dust models based on this theory has been coupled into many mesoscale weather models and successfully tested in forecasting dust storms in many parts of the world [Shao et al., 2003; Sun et al., 2002; Lei et al., 2005]. Shao's theory has

not been used in global dust climate simulations. The physical principles in Shao's theory are mainly prepared for short term dust emissions in tropical and middle latitude regions. Some important physical processes that are critical for high latitude regions or long term climate change have not been considered, which prevent using Shao's theory in studies of the global dust aerosol climatology.

In this study, a new Physical Dust Aerosol Model (PDAM) is developed for global dust climate simulations by incorporating the wind erosion physics of Shao [2008] along with various improvements including adding new physical processes, redistributing particle size groups, using dynamic vegetation, and updating transport and deposition schemes. The resulting scheme is incorporated into the Community Atmospheric Model with Chemistry (CAM-Chem). The coupled system is used to simulate the present dust climatology, including the surface concentration and deposition. The results are compared with both ground-based and satellite observations.

The following section describes the detailed structure and physics of the dust model and the integrated modeling system. Physical data used in the dust model are discussed within the model description. Experimental design and resulting analyses are discussed thereafter.

4.2. Modeling System Description

The dust model is developed for incorporation into a climate chemistry model, namely the Community Atmosphere Model with Chemistry version 3 (CAM-Chem). As introduced in Chapter one, the advanced numeric core for atmospheric dynamics and sophisticated treatments for atmospheric physical processes, including radiation, convection, turbulent diffusion, ice, ocean and the atmospheric boundary layer in CAM-

Chem can be used to support the simulations of mineral dust. The atmospheric dynamic module provides meteorological data for simulations of dust emissions, chemical transport, and land surface process.

The land surface module integrated in this system is the Community Land surface Model (CLM) with special update for biogenic emissions [Lamarque et al., 2011]. The CLM simulates energy, momentum and mass exchanges between the atmosphere, soil and vegetation. The soil and vegetation information in the CLM is not tested and may have bias for the simulation of dust emissions. Since the dust emission is very sensitive to soil and vegetation characteristics, the soil data in CLM were updated based on the NASA soil database [Zobler et al., 1999]. The vegetation parameters in CLM are updated with the ISLSCP II Vegetation Data [Hall et al., 2005], which is an inversion of latest satellite observations. In the dust emission modeling, CLM produces friction velocity, soil moisture, and dynamic vegetation information as inputs to the PDAM.

The physical dust model obtains dynamic vegetation, soil moisture information from the land surface scheme and other spatially distributed parameters associated with soil type, and then project dust emission fluxes for different particle size groups. The dust transport and deposition modules calculate the concentration, dry deposition and wet deposition by using wind fields, turbulent diffusivities and precipitation obtained from the atmospheric model. The dust concentration is directly introduced into the modeled distribution of aerosols by size bins. Then, the optical depth of total aerosols (including dust) is calculated.

4.3. Physical Dust Aerosol Model

A crucial task for process-based modeling is to divide the complex process into small coherent stages and find out the essential factors that control each stage. Shao's soil erosion theory divides the whole process of dust emission into several stages and parameterizes each stage using physical equations deduced from wind tunnel experiments [Shao et al., 2008]. Regional dust models based on this theory have shown strong ability in dust storm weather analyses and forecasting [Shao et al., 2002, 2003; Sun et al., 2003; Lei et al., 2005]. However, all of those experiments have been performed over mid-latitudes or tropical regions in spring or summer time. The abilities in those studies to simulate the dust emissions over high latitude regions and on winter-time mid-latitude regions are highly uncertain. Some important physical processes including snow cover and frozen soil have not been previously been considered in Shao's theory. This affects the ability to use Shao's theory in a simulation of global dust climate, where the seasonal cycle and effects at high latitudes may also have an important role. In this study, we further develop the Shao's dust erosion theory to fit the requirements of a global simulation under all possible soil/meteorology conditions.

As discussed above, more physical processes are necessary to consider in completing Shao's theory. The effect of snow cover on dust emissions is the first process that we have to consider for a long term simulation. This effect is significant for simulating the dust emission in different seasons. The frozen soil effect is also important, which is significant on high latitude regions and at mid latitude winter. The seasonal cycle of land surface conditions and climate effects on it can be considered by introducing the dynamic vegetation information simulated by the land surface model into the dust emission process. Then the impacts of climate change and human activities on a

long term simulation can be fully considered in the model. In addition, the new transport scheme and dry/wet deposition scheme are used to achieve better simulations over the globe. The following sections will introduce the main principles of the PDAM.

4.3.1. Particle Size Distribution

We distinguish two particle-size distributions: the minimally disturbed soil particle-size distribution, $p_m(d)$, and the fully disturbed soil particle-size distribution, $p_f(d)$. Dust is divided into 4 size ranges according to air quality standard. They are 0.1-1.0 μm, 1.0-2.5 μm, 2.5-10.0 μm and 10.0-40 μm. The ideal case is that soil samples have been collected and analyzed to estimate $p_m(d)$and $p_f(d)$ for each soil class. However, this type of data is not yet available over the world. Currently, $p_m(d)$ and $p_f(d)$ are regarded as a composite of several lognormal distributions [Gomes et al., 1990; Chatenet et al., 1996]. Depending on soil type and its related erodibility, soil particle saltation and aggregation calculation in PDAM follows Shao's simplified scheme [Shao et al., 2004].

4.3.2. Dust Emission Scheme

Many factors may affect the dust emission process; these factors can be divided into internal factors and environmental factors. Soil type and texture are major internal factors that determine the soil erodibility. The vegetation growth, soil hydrological cycle, and weather condition are major environmental factors that affecting the dust emission process. Figure 4.1 shows how the PDAM model deals with these factors in the dust emission simulation. Important factors and relationships associated with the dust emission process are shown on the diagram.

Vegetation growth is a first order factor that affects the dust emission. Wind tunnel experiments show that vegetation cover effectively can reduce the intensity of dust emission [Shao et al., 2008]. The main characteristics of vegetation involved in dust emission include vegetation height and coverage. The reduction rate of dust saltation process and surface roughness associate with the vegetation height. Vegetation coverage directly affects the erodibility of surface soil. Roughness length is the physical parameter that describes the surface roughness caused by vegetation and topography. Roughness length is considered in calculation of friction related items in dust emission. Accurate representations of these parameters are significant for simulations. Therefore, GIS data are used in Shao's dust emission model [Shao et al., 2002, 2003]. As mentioned before, instead of using high resolution GIS vegetation data, the CLM is used in PDAM to provide dynamic vegetation information. The ability for producing land surface information by the CLM used in this study has previously been tested [Levis et al., 2003]. Compared with static GIS data, data from the land surface model has its merit in describing the changes in vegetation growth for long time periods. In the integrated system Frontal Leaf Area Index (LAI) and roughness length are updated each time step. In addition, soil moisture and soil temperature is also provided by CLM. They are important factors to determining the erodibility of soil, frozen-soil and snow cover effects on dust emissions. Wind tunnel experiments show that the dust emission process is sensitive to the condition of the soil in the top soil layer [Shao, 2008]. 50 mm is suggested to be a good reference depth for the top soil layer in simulations. In this model we use the simulations of soil variables on the depth of 25 mm to represent the averaged

conditions for the whole layer. These CLM output variables are used together with global soil type and texture information to calculate each physical variable in the dust emission.

4.3.2.1. Threshold Friction Velocity

The threshold friction velocity for the surface u_{*t}, is an important factor for dust mobilization and is depends on size of soil particle d_s , soil texture, and several factors including roughness frontal area index, λ, soil moisture, w, salt concentration in soil, s_c, etc. [Shao, 2000]. The calculation of u_{*t} proposed by Shao et al., [2001] is used in this study as the following form

$$u_{*tf}(d_s, \lambda, w, s_c, \ldots) = u_{*t0}(d_s) f_\lambda(\lambda) f_w(w) f_{sc}(s_c) f_{cr}(c_r) \ldots$$

where $u_{*t0}(d_s)$ is the threshold friction velocity for sand particle of size ds in the idealized situation when soil is dry, bare and free of salt and crust. In this study, $u_{*t0}(d_s)$ is calculated using the expression given by Shao and Lu [2000]:

$$u_{*t0}(d_s) = \sqrt{a_1\left(\sigma_p g d_s + \frac{a_2}{\rho d_s}\right)}$$

where σ_p is particle-to-air density ratio. The coefficients $a_1 = 0.0123$ and $a_2 = 3 \times 10^{-4}$ kg s^{-2} are empirical coefficients obtained from fitting the above expression to wind tunnel observations.

The factor f_λ, f_w, f_{sc} and f_{cr} are correction functions for surface roughness elements, soil moisture, salt concentration and crust, respectively. The first correction function has been derived by Raupach [1992] and Raupach et al. [1993] based on conceptual analysis and wind tunnel data

$$f_\lambda = \left(1 - m_r \sigma_r \lambda\right)^{1/2} \left(1 + m_r \beta_r \lambda\right)^{1/2}$$

According to Wyatt and Nickling [1997], β_r, σ_r and m_r are respectively 202, 1.45 and 0.16. The correction function f_w follows Fecan et al. [1999]:

$$f_w = \left[1 + A(\theta - \theta_r)^b\right]^{1/2}$$

where θ is volumetric soil moisture. The air-dry soil moisture θ_r and the empirical coefficients A and b are soil type dependent [Shao, 2008]. According to Nickling [1984], the correction function f_{sc} is set to 1.

4.3.2.2. Frozen soil factor

Studies on the effects of frozen soil indicate that it has a significant influence on land surface [Luo et al., 2002]. Freezing and thawing cause changes in soil tightness, affect the cycle of water on and below the land surface, and regulate soil particle structure [Zhang et al., 1999], which has direct effects on soil erodibility. Therefore, considering the frozen soil effect on dust erodibility is important in cold regions.

On the other hand, the timing, duration, thickness and distribution of frozen soils are primarily controlled by heat exchanges between the atmosphere and land surface. In the polar region, soil is frozen all years around without considering potential changes in climate. Many higher latitude regions have seasonal frozen soil. Thus, whether there is frozen soil needs to be determined before considering the resulting effect on dust emissions. Previous studies show that frozen soil is determined by water content in the soil and by soil temperature [Zhang et al., 1999; Khaladoune et al., 2008]. In PDAM, we set the soil moisture above 1% and soil temperature below 0 °C as the threshold to determine frozen soil. Foster et al., [1984, 1995] studied the erodibility of frozen soil and

point out the relationship between water content and shear stress. Based on this relationship, we define the frozen soil effect factor as:

$$f_z = \begin{cases} 1 & w < 0.01 \\ k(0.22 - w) & 0.22 \geq w \geq 0.01 \\ 0 & w > 0.22 \end{cases}$$

where f_z is the dust emission reduction ratio for frozen soil effect, k=8.33 is the erodibility factor, w is the water content of frozen soil. For frozen soil, the soil water content below 1% is regarded as not affecting erosion and above 22% is regarded as non-erodible soil. The threshold values are fitted from model runs.

4.3.2.3. Snow cover effect

Among land surface conditions, the effect of snow cover has not been discussed in detail, except in studies on dust in the ice ages [Lunt and Valdes, 2002a, 2002b]. This is probably because snow cover has been thought to have little effect on global dust distribution [Woodward, 2001; Lunt and Valdes, 2002b] and dust emission on lower latitude regions. However, snow cover affects dust outbreaks in high latitude regions where there is snow cover during winter and spring. For instance, in East Asia, arid and/or semiarid regions are frequently covered by snow in the season of dust events. Dust sources in East Asia are located at relatively high latitudes (around 35°N–50°N), and dust outbreaks frequently occur from March to May [Kurosaki and Mikami, 2003]. The areas of snow cover differ every year, especially in high latitudes and early in the dust season (March and April). Yasunori et al., [2004] studied the snow cover effect on dust outbreaks from measurements and tried to include the effect into the threshold wind velocity.

In PDAM, snow cover effect is considered as:

$$f_s = \begin{cases} 0 & D_s > D_0 \\ (D_0 - D_s)/D_0 & D_s \leq D_0 \end{cases}$$

where f_s is the snow cover coefficient, which is determined by the snow depth D_s. The threshold snow depth (D_0) to block dust outbreak is set to 5 cm. When snow depth is over 5 cm, dust emission is blocked. When snow depth is below 5 cm, fraction of snow is likely to occur. Therefore, a linear equation is used to consider the snow fraction. Since the CLM is coupled in the system, the snow depth is easily estimated from surface temperature, precipitation type and precipitation amount. The simple physical fact is that no dust will be emitted when there is snow cover.

4.3.2.4. Streamwise Sand Flux

In PDAM, soil particles are separated into sand and dust categories. This is done by introducing a critical particle size, d_c, which is determined by

$$w_t(d_c) = \alpha_d \kappa u_*$$

where w_t is the particle terminal velocity, $\kappa = 0.4$ is the von Karman constant and α_d is an empirical parameter, commonly set to 0.5 to 1. The meaning of d_c is that particles smaller than d_c are easily dispersed in the atmosphere while particles larger than d_c are not. For $\alpha_d = 0.5$ and $u_* = 0.5$ ms^{-1}, d_c is 35 μm.

The saltation of sand sized particles plays a critical role in the process of dust emission. For a given particle size, d_s, the streamwise saltation flux □ can be calculated using the Owen model [Owen, 1964]

$$\tilde{Q}(d_s) = \begin{cases} \frac{c_o \rho u_*^3}{g}\left(1 - \frac{u_{*t}^2}{u_*^2}\right) * fz * fs & u_* \geq u_{*t} \\ 0 & u_* < u_{*t} \end{cases}$$

where c_o is a coefficient of order one, ρ is air density, g is acceleration due to gravity, u_* is friction velocity and u_{*t} is threshold friction velocity, a function of d_s. f_z and f_s are frozen soil effect coefficient and snow cover coefficient. The calculation of u_{*t} will be described later. The streamwise saltation flux for all particle sizes can be estimated using

$$Q = \int_{d_1}^{d_2} \tilde{Q} p_s(d) \delta d$$

where d_1 and d_2 are the lower and upper size limits of particles in saltation. In the wind erosion scheme used in this study, u_{*t} is allowed to vary with surface conditions and hence, the supply-limited saltation has been considered.

4.3.2.5. Dust Emission

Three dust emission mechanisms are considered in the model:

1. Aerodynamic entrainment: Dust particles can be lifted from the surface directly by aerodynamic forces [Loosmore and Hunt, 2000]. However, as the importance of gravity and aerodynamic forces diminishes for smaller particles and the interparticle cohesion becomes important, dust emission arising from direct aerodynamic lift is small in general;

2. Saltation bombardment: As saltating particles (sand or aggregates) strike the surface, they cause localized impacts which are often strong enough to overcome the binding forces acting upon dust particles, leading to dust emission [Gillette, 1981; Gomes et al., 1990a; Alfaro et al., 1997].The wind tunnel experiments of Shao et al. [1993] show

that the dust emission rate caused by this mechanism is an order of magnitude larger than the aerodynamic entrainment; and

3. Aggregates disintegration: Under natural conditions, dust particles often exist as dustcoats attached to sand grains in sandy soils or as aggregates in soils with high clay content. During a weak wind erosion event, sand particles coated with dusts and clay aggregates behave as individuals and dust particles may not be released, while during a strong wind erosion event, dustcoats and soil aggregates may disintegrate resulting in increased dust emission. The importance of this mechanism is similar to that of saltation bombardment.

The dust emission rate related to these three mechanisms is formally expressed as

$$F = F_a + F_b + F_c$$

In calculating F, we distinguish the dust emission in the absence of saltation from that in the presence of saltation, namely,

$$F = \begin{cases} F_a & \text{weak wind, no saltation} \\ F_b + F_c & \text{strong wind, with saltation} \end{cases}$$

In modeling dust storms, the latter expression is used.

We divide dust particles into I size intervals, each with a mean value d_i (I = 1, … I) and an increment Δd_i. As derived by Shao [2001], the emission of dust in the ith group generated by saltation bombardment and aggregates disintegration of particles of size d_s is given by

$$\tilde{F}(d_i, d_s) = c_Y \left[(1-\gamma) + \gamma \frac{p_m(d_i)}{p_f(d_i)} \right] \frac{\tilde{Q}g}{u_*^2 m} \left(\rho_b \eta_{fi} \Omega + \eta_{ci} m \right) * Ev * Es$$

where c_Y = 1/7 co is set to 0.05, ρb is soil bulk density, ηfi is the dust fraction and ηci is the dust fraction in aggregation. E_s and E_v are roughness factor and vegetation factor to describe the reduction of vertical dust flux. Ω is the volume removal (abrasion) caused by saltation and m is dust particle mass. Detailed calculation of Ω is described by Lu and Shao [1999].

The emission of dust particles of size d_i caused by the saltation of all sand particles (sand plus aggregates) can be estimated as a weighted average,

$$\breve{F}(d_i) = \int_{d_1}^{d_2} \tilde{F}(d_i, d)\, p_s(d)\, \delta d.$$

Note the integration is over the particle size range of saltating particles.

4.3.3. Dust Transport

The transport scheme in the CAM-Chem model follows the method by Zender et al., [2003]. Summarizing the physical processes described in the preceding sections, the total vertical mass flux of dust $F_{d,j}$ into transport bin j is

$$F_{d,j} = \varepsilon * F(d_i, d_s)$$

where the summation is over four size groups. A global tuning factor, ε, is chosen to give a reasonable climatological simulation.

4.3.4. Dry Deposition

The dry deposition scheme in this study directly uses the scheme for aerosols in CAM-Chem. The dry process is the most significant sink for mineral dust cycle. The simulation of dry deposition of mineral aerosol particles requires accurate specification of the gravitational settling and turbulent mix-out of particles ranging from $0.1 < D_p < 40.0$ μm. V_d is the dry deposition velocity.

$$Vd = Vg + Vt$$

where V_g is the gravitational settling velocity and V_t is the turbulent mix-out velocity. Particles are assumed to settle gravitationally at their terminal velocity vg and to reach this velocity instantaneously.

$$v_g = \left(\frac{4gDC_c\rho_p}{3C_D\rho} \right)^{1/2}$$

where the slip correction factor C_c and the drag coefficient C_D are given by Seinfeld and Pandis [1997]. $Re_t = V_g\ d/v$ is particle Reynolds number at settling velocity (v is kinematic viscosity) and the drag coefficient, C_d, is approximated following Durst et al. [1984] by

$$C_d(Re_t) = \frac{24}{Re_t}\left(1 + 0.15 Re_t^{0.687}\right).$$

Cc is the Cunningham correction factor defined as:

$$C_c = 1 + \frac{\lambda}{r_e}\left[1.257 + 0.4\exp\left(-\frac{1.1 r_e}{\lambda}\right)\right]$$

Turbulent mix-out is only significant in the lowest layer. Turbulent deposition is calculated by using the resistance-in-series method [e.g., Wesely, 1989]. The turbulent deposition velocity v_t

$$v_t = \frac{1}{r_a + r_b + r_a r_b v_g}$$

where the aerodynamic resistance through the constant flux layer ra accounts for local stability effects using similarity theory [Bonan, 1996]. While r_a is independent of particle size, the quasi-laminar layer resistance r_b depends on a particle's microphysical characteristics [Slinn et al., 1978]. The rate-limiting resistance for turbulent mix-out of accumulation mode particles is r_b for all wind speeds. For coarser particles (D greater

than or similar to 2 μm), r_b is the limiting resistance for weak wind speeds, but r_a becomes the limiting resistance as U increases above about 5 m s^{-1}.

4.3.5. Wet Deposition

For the wet deposition for dust, CAM-Chem use the scheme introduced in the DEAD model by Zender et al., [2003]. Wet deposition or scavenging of particles by water is the dominant deposition process for small dust particles because dry deposition processes are very inefficient for D < 2 μm, i.e., the accumulation mode [e.g., Seinfeld and Pandis, 1997]. Cloud aerosol interaction and scavenging are treated using the method of Rasch et al. [2000] with modifications. Wet scavenging processes are treated with mass mean, path-normalized scavenging coefficients $\overline{\Lambda}_M$m2 kg-1 defined such that

$$\frac{dM_p}{dt} = AP_M\overline{\Lambda}_M M_p$$

where M_p kg m^{-2} is the grid cell aerosol mass path, A is the horizontal fraction of the grid cell over which the scavenging process occurs, and P_M kg m^{-2} s^{-1} is the rate of interaction with the scavenging droplets. Nucleation scavenging occurs through the entire vertical domain of the fraction of the grid cell occupied by the appropriate (convective or stratiform) cloud type. For nucleation scavenging, P_M is the local rate of conversion of water vapor to droplets (condensation) and inline equation for all size classes for both stratiform and convective rain. This is identical to the sulfate nucleation scavenging representation of Rasch et al. [2000], except that we allow dust nucleation scavenging in frozen clouds. The present simple formulation of nucleation scavenging must be viewed as a temporary procedure while more microphysically based methods involving aerosol

composition and CCN activation suitable for large-scale models are investigated [e.g., Zhang et al., 2000].

4.4. Present-Day Dust Evaluation

The resulting integrated CAM-Chem system is driven by the CCSM3 meteorology and CAM-Chem standard emissions to simulate the present global dust climatology. The meteorology fields were archived with 6-hour temporal resolution. In this study, each case was run for 5 years (1998–2002) following 1 year of model spin-up. Unless noted otherwise, all results discussed in this paper are based on 5-year averages. The modeled dust concentrations were outputted at 1-hour interval to save storage.

4.4.1 Surface dust concentration and long range transport

Surface observations at sites managed by the University of Miami provide a unique long-term record and climatology of surface dust concentrations [e.g., Prospero and Nees, 1986; Prospero, 1996a]. Previous global dust simulations have been evaluated against these University of Miami station observations [Tegen and Fung, 1994; Tegen et al., 1996; Mahowald et al., 1999; Ginoux et al., 2001; Perlwitz et al., 2001; Luo et al., submitted manuscript, 2003; Penner et al., 2001; Zender et al., 2003; Liao et al., 2004; Tanaka and Chiba, 2006; Li et al., 2008; Yue et al., 2009]. Station locations [Ginoux et al., 2001; Woodward, 2001] are shown as signs on Figure 4.2. The sampling length [Savoie et al., 1992; Maring et al., 2000] are discussed in the Table 4.1. It should be noted that not all the stations record dust concentrations continuously, and some do not have complete year-round records. Most of the sites have been operating for less than 10

years, which indicates that the natural temporal variability may reduce the accuracy of the data set as a representative climatology.

The observational surface dust concentrations from the 16 sites are used to evaluate the simulated climatology of surface dust concentrations in Figure 4.3. The 16 sites are roughly distributed evenly over the world. The site values in each region are averaged to represent the concentration of that area. Modeled results on the grid where the sites located are also averaged to match the observation. Figure 4.2 shows simulated mineral dust concentration on surface level and the contributions from all size bins. The concentration is plotted in mixing ratio of dust mass over air mass. The impact of mineral dust on air quality varies from over 500 μg/kg (μg of dust in kg of dry air) in source region to near 0.01 μg/kg over the West Wind Drift (or called Antarctic Circumpolar Current (ACC)). The observational values on all sites include a lowest value of 0.17 μg/kg over the Pacific Ocean and a high value up to 400 μg/kg near the coast of North Africa.

The first two stations, Miami and Bermuda, are off the eastern coast of the United States. The averaged concentrations on these two sites are used to present the North American dust pollution. In this region the dust concentration is mainly affected by dust from the Sahara desert. The peak concentration occurs in July and August in both observed and model results, but the modeled amplitude appears to be weak in summer. In general the phasing and amplitude of the surface concentration is within the monthly variance in this region. The mean bias is -0.95 $\mu g/m^3$. The correlation coefficient is 0.85.

In the South America region, also affected by the Sahara dust, the observation at Barbados shows a peak value in June and low values in winter months. The model result

shows a converse seasonal variance in this area. The simulated concentrations are lower than observations. The mean bias is -7.1 $\mu g/m^3$. The negative correlation coefficient is -0.42.

Two sites, Izania and Sal Island, near the west coast of North Africa are more directly affected by Sahara dust than any other sites. The observation shows peak concentrations in February and March. The model result reproduces this trend with a correlation coefficient of 0.31. Although the simulations on summer months are lower than observations, the general bias is 1.67 $\mu g/m^3$ that is around 4% of the annual mean concentration.

The observations at Mace head site present the dust concentrations over Europe. The observed annual mean concentration is 0.8 $\mu g/m^3$, which shows that Europe is slightly polluted by mineral dust. The simulated dust concentration is close to the observation with a bias of -0.17 $\mu g/m^3$. The seasonality of dust variance is not clear. The model result shows seasonality with peaks in spring and fall months. The correlation coefficient is 0.09 between the observations and simulations.

The observations at Cape point are not continuous. The available observations include records of March, April, May, June and July. The presented seasonality seems peak concentrations in summertime. The simulated results show the dust concentrations peak in summer and fall seasons. Compared with the limited observations, the mean bias is around -0.26 $\mu g/m^3$, and the correlation coefficient is 0.86.

Kaashidhoo is the only site in south Asia and Indian Ocean. The dust concentration on this area is affected by dust from the Mideast. The observation shows the peak dust concentrations occur from March to June. The model results capture the main

characteristic of seasonal variance. The correlation coefficient is 0.54 between the observations and simulations. However, the simulated mean concentration is 2.0 $\mu g/m^3$ lower than the mean of observations.

East Asia is a typical dust polluted region. Two sites at Cheju and Okinawa locates in the downwind area of East Asia dust plume. The observations from these two sites present a typical seasonality of East Asia dust activity, which peaks in Spring season [Shao et al., 2002; Ding et al., 2004]. The model result captures this trend with a correlation coefficient of 0.80. However, the simulated dust concentration is lower than the observations. The mean bias is -5.1 $\mu g/m^3$.

Four sites in the central Pacific Ocean (Enewetak, Nauru, Funafuti and American Samoa) represent the dust concentration in this region. The main characteristic of the observations on these sites is low concentration. The average monthly dust concentration is below 0.5 µg/m3. The modeled concentration has a mean bias of 0.04 µg/m3. The weak seasonality presented by observations is captured by simulation, which shows a peak in late winter and spring time. The correlation coefficient between observations and simulations is 0.43.

Australia is a dust emission region. The observations at Cape Grim represent the pollution in this area. The result shows that dust in this area peaks from November to May when is the summer for the Southern Hemisphere. The monthly mean dust concentration is 1.5 µg/m3. The mean bias from model simulations is 0.27 µg/m3. The seasonality is also captured by the CAM-Chem model. The correlation coefficient is 0.56.

Observations from the site at King George Island represent the dust pollution in Antarctic. Due to the location where the atmospheric circulation is highly affected by the

Antarctic Circumpolar Current, the dust concentration in this region is very low and seasonality is not clear. The monthly mean concentration is 0.5 μg/m3. The mean bias in simulations is 0.08 μg/m3. The observation shows high concentration in January and April, while the modeled peaks occur from March to August. The correlation coefficient is 0.07.

Generally, the model captures the monthly climatology of global surface dust concentrations. The overall simulation results show close values to the mean concentrations on the corresponding sites. The relative biases are small. However, the model result shows small negative biases on most of sites. That indicates the CAM-Chem may underestimate the dust emissions. In this comparison, we assume the inter-annual variability of surface dust concentrations is negligible between the 1980s and 1990s, which may bring errors into the analysis. The seasonality is well captured by the CAM-Chem model at these sites with stable seasonal variability. Some sites show unstable seasonal variability including those in the source regions that are more affected by terrain and small scale gust of wind or those with low levels of dust concentrations that are more determined by turbulent diffusion. Variability at unstable sites is a challenge for the CAM-Chem model to capture because sites near the source region may be more affected by the unstable local low-level meteorology and contributions from large size particles. For example, the sites on the west coast of the Sahara desert did not show a stable seasonality. Low dust concentration sites are usually far away from the source and many weather systems may influence the transport of dust, which result in the total meteorology force become complicate and unstable. For example, the Antarctic dust is

influenced by many meteorology systems including the ITCZ, the West Wind Drift and Hadley circulations resulting in unclear seasonality in surface concentrations.

4.4.2 Vertical distribution and transport of dust concentration

Global dust transport is affected by the atmospheric circulation. Major transport processes are associated with mid-latitude westerly zonal winds and tropical easterly winds. Both zonal winds show maximum speed in the middle and upper troposphere [Houghton et al., 2004]. Dust particles can be transported further in the upper layers. Therefore, vertical transport of dust particles influence the transport distance of dust particles.

PADM can simulate the dust long range transport as well as transport in the vertical direction. Figure 4.4 shows the latitude-vertical distribution of mineral dust. Different size bins for the dust are shown to see the characteristics of vertical transport. It can be seen that fine dust can be transported to the height of 200 HPa, while dust particles from 1 μm to 2.5 μm ranges can be transported to roughly 400 HPa. Most of dust particles larger than 2.5 μm cannot be transported over 600 HPa. Therefore, the effect of long range transport of dust particles is mostly associated with the smaller sizes. This finding is similar to those in the dust vertical distribution measured by the CALIPSO (Cloud Aerosol Lidar with Orthogonal Polarization) satellite in its 1064-nm channel attenuated aerosol backscatter results [Young et al., 2011].

Figure 4.4 also shows the contribution of mineral dust at different latitude. Strong dust emissions at about 15 °N latitude show the contribution of the Sahara desert. Dust concentrations peak over 30 to 60 °N is mainly associated with Asian deserts. South

America, Australia and South Africa also contribute to global dust emissions. The PDAM result for latitude-vertical distributions of dust in the Southern Hemisphere is also comparable to the CALIPSO measurement of a single dust event over Australia [Young et al., 2011].

4.4.3 Dry and Wet deposition of mineral dust

Figure 4.5 shows the simulated annual mean wet and dry deposition fluxes for dust particles over the global region. The major characteristic from the comparison of the wet deposition and dry deposition effects is that the dry deposition flux is generally larger than that of wet deposition. In general, the pattern of dry deposition is mainly determined by the emission source and transport. The highest deposition occurs near the source region. The strength of wet deposition is not only affected by the source emission but also results from precipitation. In the Antarctic region, the strength of the wet deposition flux of mineral dust is near zero because of the low dust concentration there. Not surprisingly, the maximum deposition occurs near source regions where dust concentrations are much larger.

Comparisons with measurements of deposition fluxes are valuable to model evaluation. Ginoux et al. [2001] compiled observations previously reported in the literature from 16 locations spanning both hemispheres and approximately 90-station-years of measurements from the 1950s to the present. The majority of the stations were most active in the 1980s, before our simulation period. Figure 4.6 compares simulated mean projections with 16 stations in this observed climatology. A model low bias is readily apparent at land locations in Asia and at most ocean locations. Mean deposition

appears high at the French Alps, somewhat low at Spain, and good in Miami. Mean deposition is under-projected by more than a factor of 2 at both Asian land stations, Taklimakan and Tel Aviv. Since these stations are near active source regions, under-projections there, similar to Ginoux et al. [2001], could result from neglecting transport of particles with diameters larger than 10 μm or missing small but nearby sources. Comparisons at Pacific stations are mixed but a low bias is evident. Mean deposition appears significantly low at Midway and Oahu in the North Pacific, although Shemya in the western Aleutians is well simulated. Simulated deposition is also low in the equatorial Pacific at Enewetak, Nauru, and Samoa, but not at Fanning. Finally in the South Pacific simulated deposition appears too low at Rarotonga, New Caledonia, and Norfolk, but not at New Zealand. The Pacific stations are generally far from emissions and so integrate deposition fluxes over large regions. Low model deposition fluxes there indicate a bias in transport and removal of smaller particles. This low bias is consistent with excessive wet scavenging upstream and/or insufficient turbulent mix-out at the surface. However, the mismatch between simulation and observation periods may contribute significantly to the apparent magnitude of the low bias.

4.5. Summary

A physical dust aerosol model has been developed and incorporated into the CAM-Chem to reproduce the dust pollution over the globe. We developed the model based on previous wind erosion theory, by considering important physical processes including snow cover and frozen soil that have not previously been considered. With these enhancements, the new dust model fits the requirements by simulations under all possible global soil/meteorology conditions. We also used the dynamic soil and vegetation

information provided by a state-of-the-art community land surface model to consider the effect of climate change on surface environment and its projection of dust emissions. Transport of dust is treated by size bins as aerosols. Deposition is determined by size resolved particle and precipitation aerodynamics. As a result, this model has been developed into a state of art process-based atmospheric dust aerosol model that has better representative of natural dust processes than previous dust models. It includes the emission, deposition, and transport processes for four groups of mineral dust aerosols. The group is divided by size as group 1 with dust sizes of 0.1 to 1 μm), group 2 with dust sizes of 1 to 2.5μm, group 3 with dust sizes of 2.5-10 μm, and group 4 with dust sizes of 10-40 μm.

The main features of a model climatology generated from a 1998–2002 simulation were presented. The spatial and temporal patterns of the simulated atmospheric dust are then evaluated against the best available global measurements. The evaluation includes both surface dust concentrations and annual total dust depositions. Surface concentrations are compared with observations from 16 sites in University of Miami Ocean Aerosol Network. Then the simulated mean annual dust deposition is compared with the reported observations of deposition from publications. For both quantities, the model captures the major characteristics of their geographic distributions and seasonal variations. The latitude-vertical distribution is comparable to some published satellite results.

Therefore, the CAM-Chem dust model can be used as a basic modeling tool to better understand the physical processes that govern the emission, transport, and deposition of atmospheric dust aerosols. Meanwhile, further improvements in model formulations for source emissions, depositions and chemical mechanisms are warranted

along with finer model resolutions. In particular, improvements are needed to reduce the large underestimations of wet depositions near the coastal regions.

Table 4.1. Information about observation in University of Miami Ocean Aerosol Network.

Region	Sites	Data Length
North America	Miami; Bermuda	1989-1998
South America	Barbados	1984-1998
North Africa	Izania; Sal Island	1987-1998;1996-1997
Europe	Mace Head	1988-1994
South Africa	Cape Point	1992-1996
South Asia	Kaashidhoo	1998-1999
East Asia	Cheju; Okinawa	1991-1995;1991-1994
Equator Pacific	Enewetak; Nauru; Funafuti; American Samoa	1981-1987;1983-1987; 1983-1987;1982-1999
Austrila	Cape Grim	1983-1996
Antarctic	King George Island	1990-1996

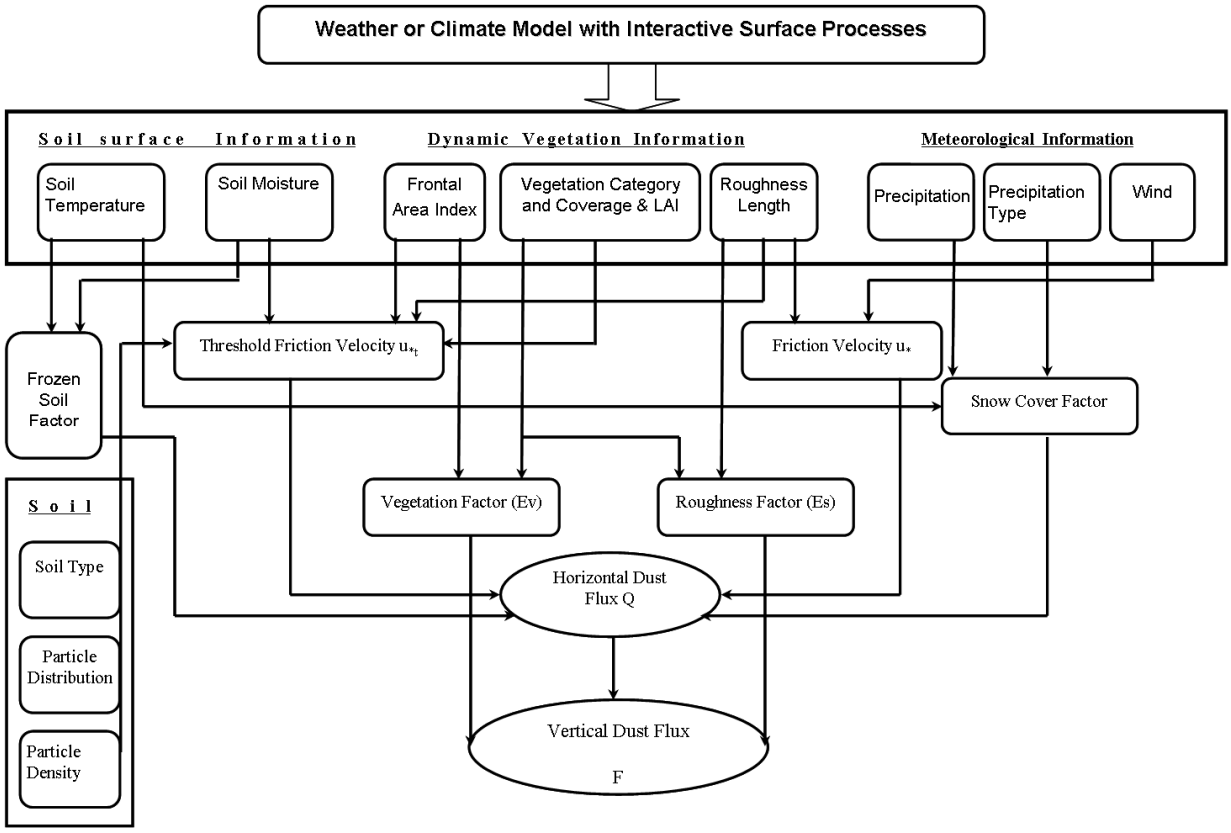

Figure 4.1. Structure of the physical dust emission model (PDAM) developed in this study.

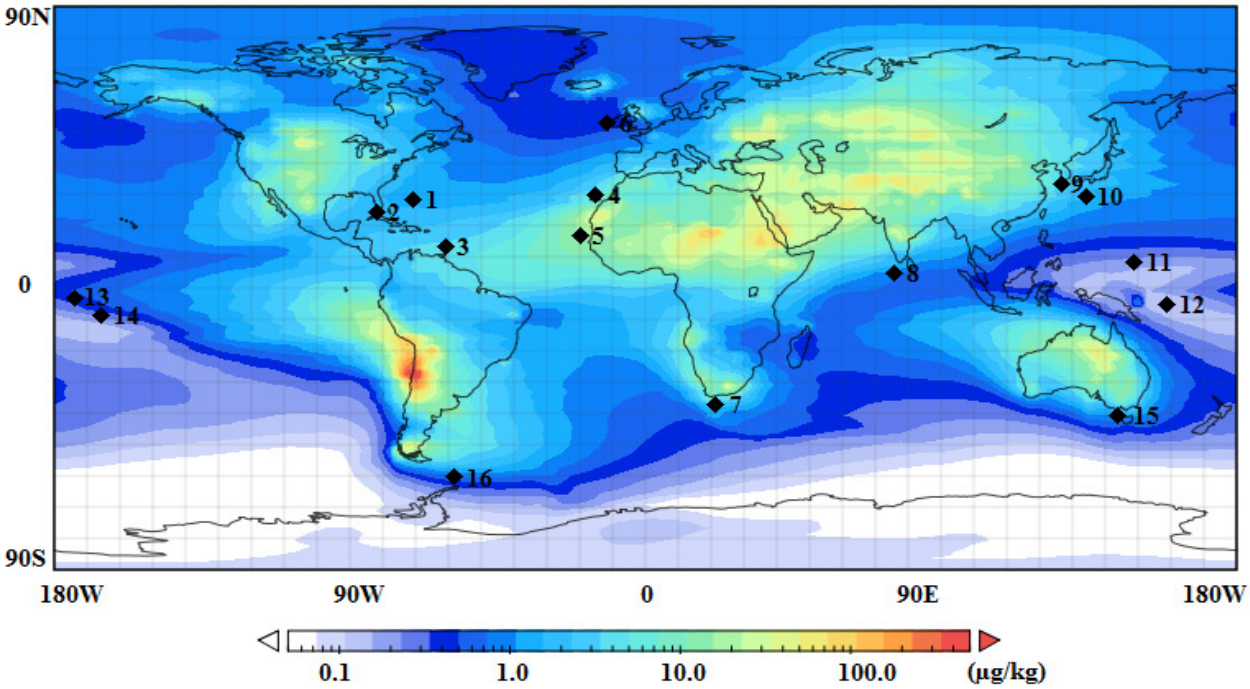

Figure 4.2. Simulated global surface total dust aerosol concentration. Shown also are the observation sites in the University of Miami Ocean Aerosol Network. 1: Bermuda; 2: Miami; 3: Barbados; 4: Izania; 5: Sal Island; 6: Mace Head; 7: Cape Point; 8: Kaashidhoo; 9: Cheju; 10: Okinawa; 11: Enewetak; 12: Nauru; 13: Funafuti; 14: American Samoa; 15: Cape Grim; 16: King George Island.

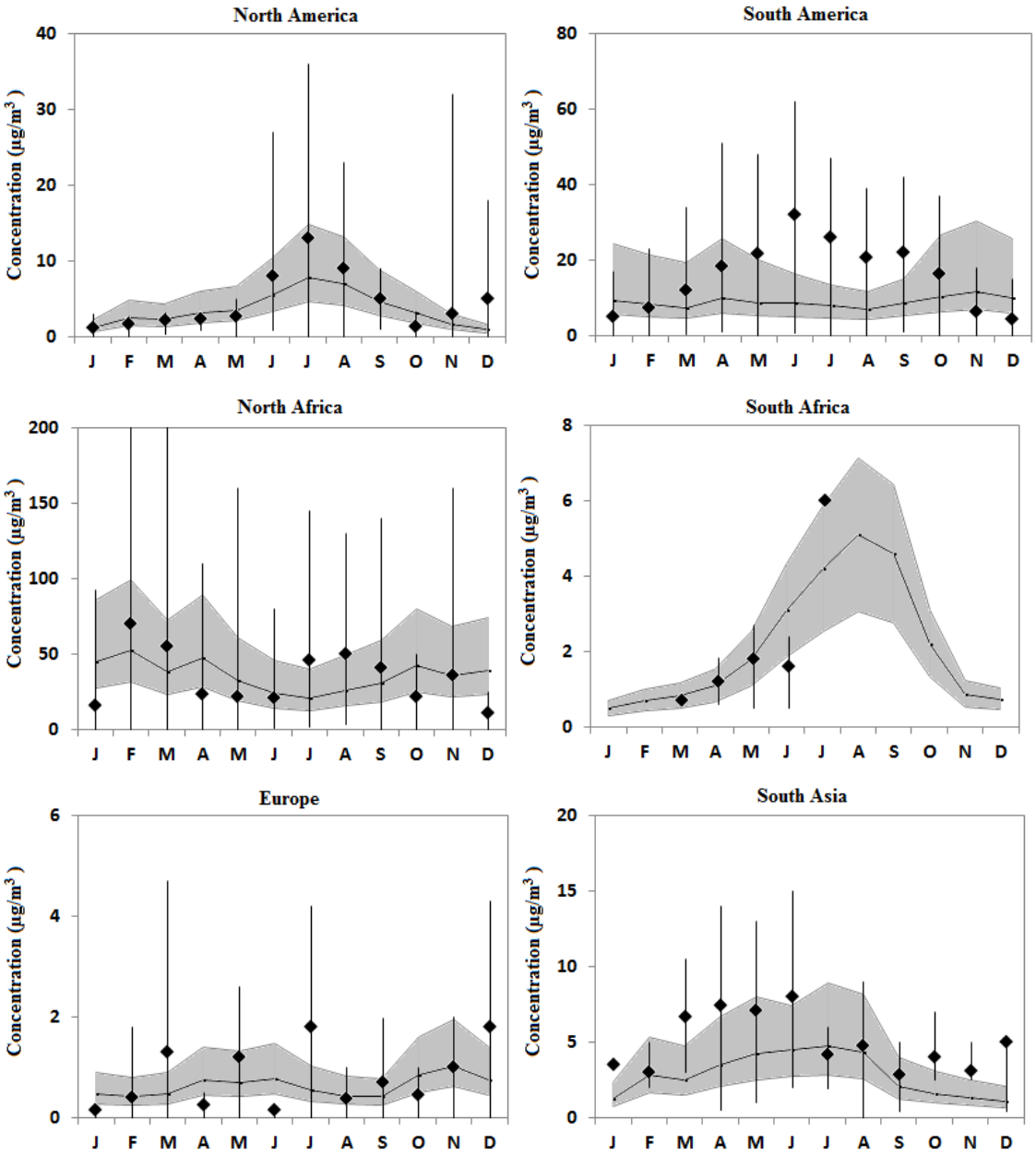

Figure 4.3. Comparison of the monthly time series of dust concentrations at 18 measurement sites relative to the model simulations. Solid lines represent simulated monthly means with one standard deviation denoted by shadings. Dots are observed monthly means. Error bars indicate one standard deviation. Units of vertical coordinate: μg m^{-3}.

Figure 4.3 continue

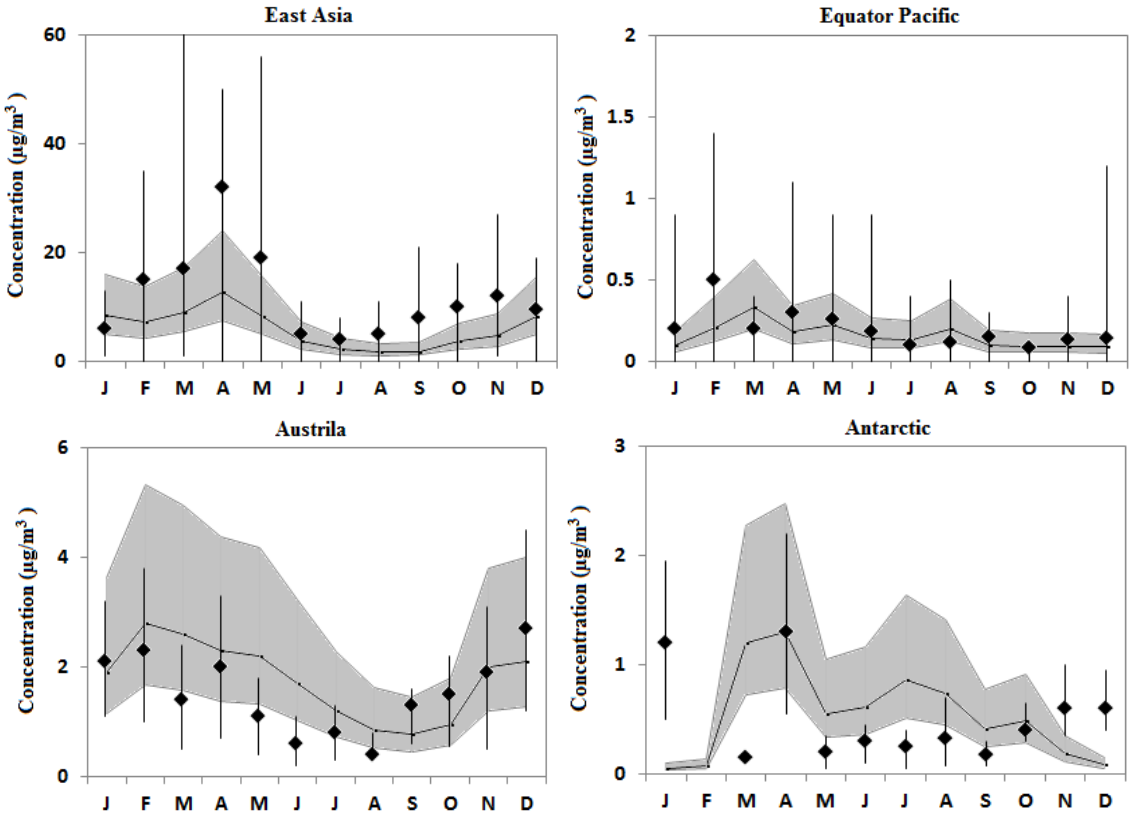

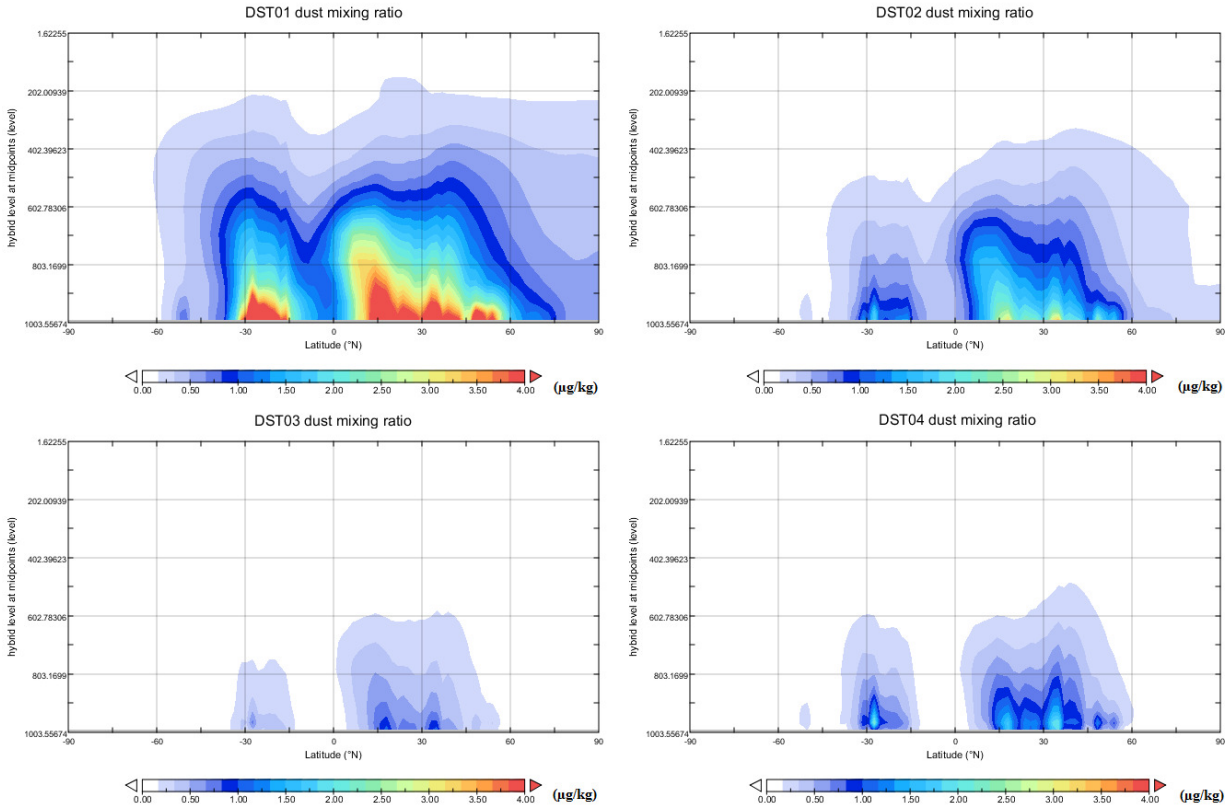

Figure 4.4. Vertical distribution of mineral dust in different size bins as a function of latitude. (Upper left: latitude-vertical distribution of fine dust (0.1-1 µm); Upper right: latitude-vertical distribution of dust (1-2.5µm); Lower left: latitude-vertical distribution of dust (2.5-10µm); Lower right: latitude-vertical distribution of dust (10-40µm).)

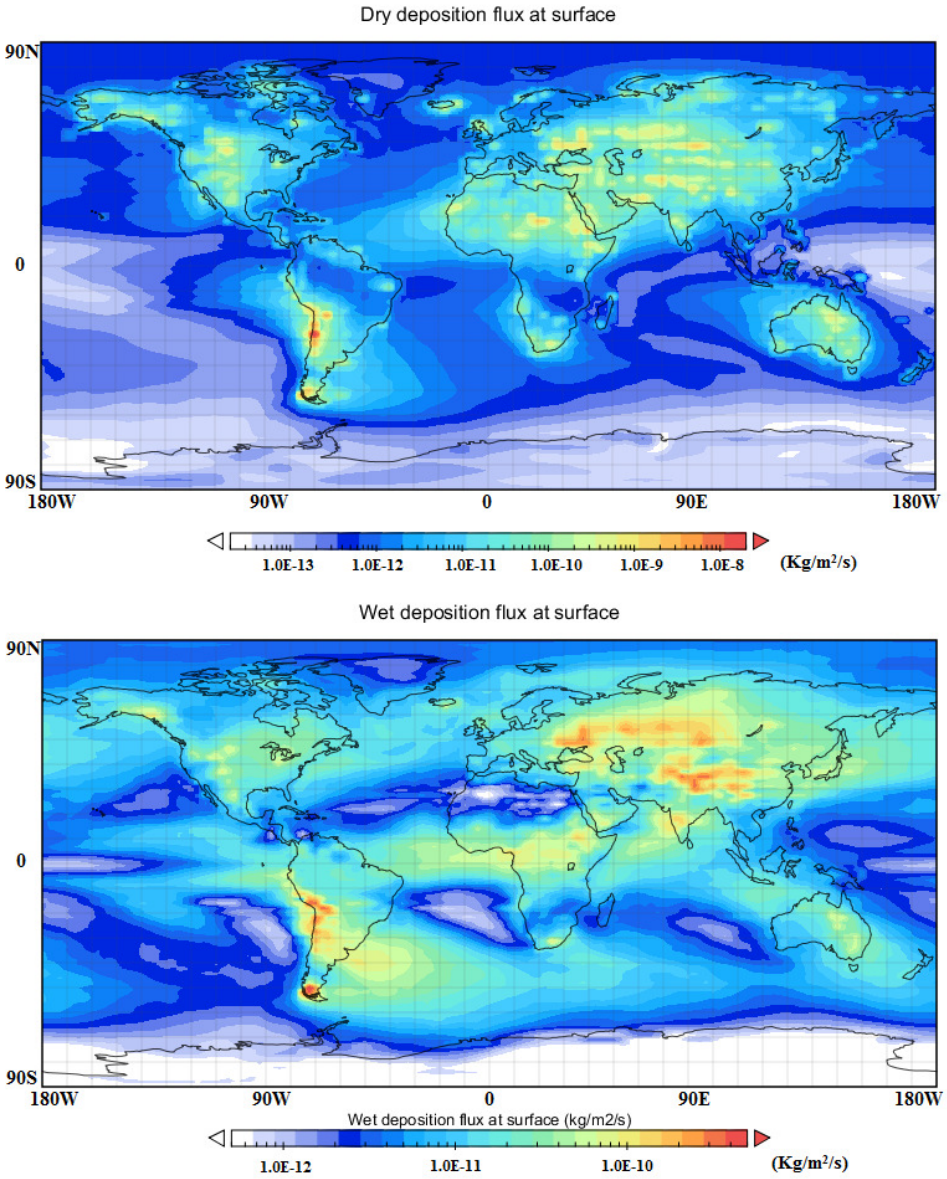

Figure 4.5. Model-derived wet (bottom) and dry (top) deposition fluxes of mineral dust over the global surface. ($Kg/m^2/s$)

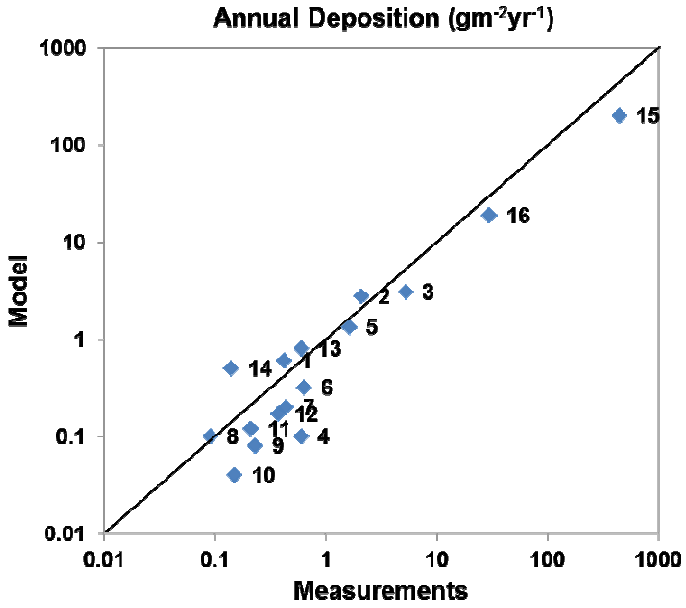

Figure 4.6. Comparison of model derived and observed annual total deposition flux at 16 sites. Site numbers are 1. Shemya (52.92N, 147.06E), 2. French Alps (45.5N, 6.5E), 3. Spain (41.8N, 2.3E), 4. Midway (28.2N, 177.35W), 5. Miami (25.75N, 80.25W), 6. Oahu (21.3N, 157.6W), 7. Enewetak (11.3N, 162.3E), 8. Fanning (3.9N, 159.3W), 9. Nauru (0.53S, 166.95W), 10. Samoa (14.25S, 170.6W), 11. New Caledonia (22.15S, 167W), 12. Rarotonga (21.25S, 159.75W), 13. Norfolk Island (29.08S, 167.98W), 14. New Zealand (34.5S, 172.75E), 15. Taklimakan (40.0N, 85.0E), 16. Tel Aviv (32.0N, 34.5E).

CHAPTER 5: EFFECTS OF CHANGES IN CLIMATE AND EMISSIONS ON FUTURE PARTICULATE MATTER LEVELS AND COMPOSITION IN THE UNITED STATES

5.1. Introduction

Particulate matter (PM) is an important pollutant in the atmosphere with negative effects on human health. Controlling the surface concentrations of PM2.5 (particulate matter with diameter <2.5 μm) and PM10 (particulate matter with diameter <10 μm) has been a basic aim of the U.S. Clean Air Act [U.S. EPA et al., 1994]. In addition, the chemical composition of airborne particulate matter also affects its effects on health [Harrison and Yin, 2000; Laden et al., 2000; Katsouyanni et al., 2001]. The ratios and variation of major components of PM including sulfate, nitrate, elemental carbon, organic carbon, mineral dust, and sea salt [Seinfeld et al., 1999; Jacob et al., 2008] have been emphasized in recent studies [Bell et al., 2007]. Atmospheric concentrations and composition of particulate matter are expected to change in the future as climate and aerosol precursor emissions change.

Even without considering changes in precursor emissions, changes in climate alone will likely influence future PM levels and composition. Changes in meteorology can affect the transport and deposition of pollutants [Murazaki and Hess, 2006; Wuebbles et al., 2007; Jacob et al., 2008]. For example, Dawson et al. [2007] demonstrated that perturbations to present-day temperature, wind speed, absolute humidity, mixing height, and precipitation can all significantly affect the deposition of particulate matter. Mickley et al. [2004] and Wu et al., [2008] have shown that a decrease in the number of Midwest cyclones in 2050 could affect the transport of pollutants and increase the severity of

summertime pollution in the Midwest and northeast U.S. Changes in some environmental factors can directly act on the chemical reactions that produce PM associated secondary aerosols. For instance, productivity and composition ratio in the formation of nitrate and sulfate aerosols are affected by humidity and temperature [Seinfeld et al., 1999]. The study by Racherla and Adams [2006] shows that surface ozone and fine particulate matter concentrations will decrease as a response to the increase of water vapor under the A2 climate change scenario.

Climate change significantly affects PM concentrations and composition through its effects on natural precursor emissions. Firstly, changes in climate act on biosphere may result in the changes in biogenic emissions of aerosol precursors. For example, higher temperatures tend to increase the biogenic emission of volatile organic carbon, which is an organic component of PM [Guenther et al., 1999]. Secondly, emissions of mineral dust and sea salt are directly affected by climate change. Surface winds are the main driver for emissions of mineral dust and sea salt. Previous studies have suggested that future wind fields will be intensified due to the increased thermal contrast between land and ocean under a warming climate [Bueh et al., 2003; Murazaki and Hess, 2006]. As a result, natural emissions of mineral dust and sea salt are expected to increase under a strong wind shear [Shao et al., 2008].

Changes in anthropogenic emissions will directly result in changes in future PM levels and composition. Anthropogenic emissions are responsible for the major part of sulfate, nitrate, and elemental carbon entering the atmosphere. The changes in emissions of aerosol precursors from anthropogenic sources will be very large by 2050 [IPCC SRES, 2004]. For instance, NOx emissions, as a precursor for nitrate aerosols, tend to

drop to 46% of present level in the United States by 2050 under the A1B scenario, while SO_2 emissions, the precursor for sulfate aerosols, are projected at 27% of present levels. Under the A1B scenario, Pye et al., [2009] has evaluated the effect on U.S. secondary inorganic aerosol concentrations, and Tagaris et al., [2007] examined the effect on ozone and fine PM concentrations. They both found that net effect of climate change alone is to increase the total concentration of secondary inorganic aerosols in the eastern U.S. but to decrease it in the western U.S.

Future PM concentrations and composition in the U.S. are affected not only by changes in domestic emissions but also by changes in emissions from other countries as well. Previous studies have shown that pollutants from upwind remote areas can affect air quality in downwind areas [Fiore et al., 2002, 2005; Wuebbles et al., 2007; Lin et al., 2008]. Transpacific transport is likely to be the primary process for bringing Asian pollutants to the U.S. Various ground-level observational analyses, field campaigns, and model simulations have confirmed the current pathways and characteristics of transpacific transport, as well as their influence on U.S. air quality [e.g., Jacob et al., 1999; Wilkening et al., 2000; Yienger et al., 2000; Jaeglé et al., 2003; Hudman et al., 2004; Parrish et al., 2004; Bertschi and Jaffe, 2005; Heald et al., 2006].

As we discussed above, concentrations of major PM components are sensitive to global climate and emission changes. However, previous studies on future PM concentration change only focus on part of the PM components. No one has examined the future changes in all six major components together. The major reason for that are the limitations in modeling tools that have not incorporated all components together. In addition, in previous studies of future PM components, the projection of future changes is

usually based on single scenario. Future changes in climate and emissions contain large uncertainties and may not follow any certain scenario. Therefore, any single scenario study may not provide a comprehensive understanding of changes in future PM concentration and composition.

To achieve a better understanding on the effects of changes in climate and emissions on 2050 concentrations and composition of particulate matter in the United States, this study uses the Community Atmospheric Model with chemistry (CAM-Chem) version 3 by considering various climate change scenarios and emission changes. The model, including representatives of all major PM components, is driven by meteorological fields from the Community Climate System Model (CCSM3) to simulate the levels of various PM components for the year of 2000 and project their changes from 2000 to 2050 due to changes in global climate and emissions. However, future changes in climate and emissions are determined by both natural variability and human activities, projections of which contain large uncertainties. Therefore three distinct climate / emission pathways from the Intergovernmental Panel on Climate Change (IPCC) Special Report on Emissions Scenarios (SRES, http://sres.ciesin.org/final_data.html) are considered, including the A1FI, A1B and B1 scenarios representing upper, middle and lower bounds of climate warming over the 21st century, respectively. The analyses will be based on PM2.5 (fine) and PM10 (coarse), focusing on changes in four seasons (Spring (March, April, May); Summer (June, July, August); Fall (September, October, November) and Winter (December, January, February)), because both the surface emissions and meteorology typically have clear seasonal variability, e.g., some aerosol

precursor emissions usually maximize in summer, but intercontinental transport may be strongest in spring due to the cycle of atmospheric general circulations.

5.2. Methods

5.2.1. Emissions

Emissions of ozone and aerosol precursors from anthropogenic sources for 2000 are based on the present-day inventory as described by Horowitz et al. [2003]. We use 2050 estimates of anthropogenic emissions of ozone and aerosol precursors from the IPCC Marker scenarios as derived from the economic models used by IPCC [2001], miniCAM for A1FI, AIM for A1B and IMAGE for B1, respectively. We derive 2000–2050 growth factors for different categories of anthropogenic emissions for different countries, and then apply these factors to the present-day CAM-Chem emission inventories. The corresponding changes of PM related aerosol precursor emissions for different regions are shown in Table 5.1. For the purposes of this study, seven masks were created that map the SRES marker reference model regions for each scenario and sensitivity experiments onto the CAM-Chem grid [IPCC, 2001]. Present (2000) standard emissions of other chemical species in each region were projected to 2050 following the corresponding SRES emissions scenario in order to reproduce the changed atmospheric environment. Effects of climate change on biomass burning are not considered for all experiments.

Natural emissions of non-methane VOCs (NMVOCs) from vegetation and aerosol precursors emitted from soil are computed locally within the model on the basis of meteorological variables and hence allowed to change in response to climate change.

Vegetation produces large amounts of NMVOCs as aerosol precursors, many of which are affected by temperature and ambient CO_2 concentrations. In the current CAM-Chem model, the biogenic emissions and soil emissions are calculated using the coupled community land surface model following the algorithms presented in Guenther (1997) and Potosnak, (2002). Changes in soil emissions of CO due to the temperature dependence of net primary production (NPP) are also considered [Adams et al., 2004]. However, soil emissions of NOx and oceanic emissions of all aerosol precursors are kept at the same present-day levels in all experiments because of the large uncertainties in emissions estimations and the poor understanding of future changes. Biogenic emission changes are calculated in each experiment. Natural emissions of sea salt are calculated interactively in the CAM-Chem, following the schemes of [Gong et al., 1997]. In this version of CAM-Chem, the emission of mineral dust is calculated in a physical dust emission model [Lei et al., 2011].

5.2.2. Experiments

This study conducts 8 experiments for the years of 2000 and 2050. The detailed experimental design is described in Table 5.2. These experiments were conducted with the CAM-Chem model driven by meteorological data derived from the Community Climate System Model (CCSM3) outputs. The meteorology fields were archived with 6-hour temporal resolution. Meteorology fields include winds, temperature, pressure, humidity, short wave and long wave radiation. Simulations are performed with a 30 minute time step and a horizontal resolution of 1.9˚ x 2.5˚ with 26 vertical levels from the surface (1000 hPa) to 3-millibar level (~40 km altitude). Previous tests have shown that a

6 months' spin-up time is sufficient for CAM-Chem to overcome the effect of initial conditions. In this study, each case was run for a 5 year period (2048–2052) following one year of model spin-up. Unless noted otherwise, all results discussed in this paper are based on 5-year averages. The modeled PM concentrations were output at 1-hour intervals.

5.3. Model Evaluation

The aerosol chemistry module in CAM-Chem has been extensively evaluated in previous studies [e.g., Lamarque et al., 2005; Tie et al., 2005; Heald et al., 2006]. These studies show that the CAM-Chem ozone-aerosol chemistry module reproduces the temporal variations and spatial distribution found in observations of global tropospheric aerosol concentrations. We present here a more focused evaluation of the ability of CAM-Chem model to reproduce the total concentrations of surface particulate matter over the contiguous U.S.

To assess CAM-Chem's ability to simulate the total concentrations of surface particulate matter, we compare the modeled total concentrations of surface PM over the continental United States in 2002 relative to the Environmental Protection Agency (EPA) Air Quality System (AQS) site measurements [http://www.epa.gov/ttn/airs/airsaqs/]. The model is driven by NCEP reanalysis II meteorology [Kanamitsu et al., 2002] for 2001-2002. Since not all EPA AQS sites have continuous records, a quality control is needed to select the records that best fit our model results. To ensure a reliable comparison, all observations at the EPA sites within a given model grid cell are selected through a quality control filter that requires the selected sites have at least 75% record of valid running 24-

hour averages per day during the whole comparison period. Then the selected measurements are averaged to get a grid cell mean value that can be directly compared with the modeled value for that grid cell in order to reduce the influence of the site distribution.

5.3.1. Present-day PM2.5 concentration and seasonality

Present-day PM2.5 concentrations across the United States vary seasonally, as governed by changes in natural emissions, photochemistry/temperature sensitive chemistry, and wet removal processes. Figure 5.1 compares model-derived seasonal-mean PM2.5 at the surface and EPA-AQS observed concentrations over the contiguous United States. The observations show the spatial and temporal patterns of surface PM2.5 concentrations over the contiguous U.S. According to previous observations of PM composition in the United States [Harrison et al., 2004], main component of PM2.5 in present days is anthropogenic aerosols which result from the chemical transformations of anthropogenic emissions. Anthropogenic emissions of aerosol precursors exhibit little seasonality with the highest emissions in the eastern United States. PM2.5 concentrations for the eastern U.S. are generally between 10 $\mu g/m^3$ and 23 $\mu g/m^3$, but a lower concentration down to 5 μg/m3 occurs for the western United States. Oxidation and photochemistry associated with the sulfate, nitrate aerosol productions are strong in the summer months, but weak in the winter. For the AQS observations, the PM2.5 concentrations over the eastern U.S. are high in the summer and fall but very low in the winter. This seasonality is clearly presented in the area of 77-90 °W at latitudes from 34-42 °N. The distribution pattern also suggests a sensitive region for the analysis of PM2.5

pollution over eastern U.S. In the AQS measurements, the seasonality of PM2.5 concentrations over the western U.S. is just the reverse of that over the eastern U.S. Although it is not very strong, there are clearly higher concentrations in winter and spring, and low concentrations in summer and fall are over the western U.S. Similar to that of the eastern U.S., a sensitive area at 122-105 °W and 34-46 °N is suggested to represent the variation of PM2.5 over the western US. The reversed patterns of seasonal variations of PM2.5 concentration over the eastern and western U.S. are produced by different pollution types.

The simulated present day PM2.5 concentrations for each season are close to the U.S. EPA AQS observations. The simulated spatial pattern and peak concentrations over the eastern U.S. match well with the observations. Although the simulated concentrations over the western United States are very close to the observations, the simulations near the west coast area are lower than that presented in AQS dataset. One of the possible reasons for the bias may be the underestimate of sea salt, which is an important component of PM over ocean and coastal regions. Another possible reason could be due to inadequacies in the simulation of wet removal processes, where precipitation near coastal regions is difficult to capture in coarse resolution numerical models. Basic seasonality is captured by model simulations in figure 5.1. The simulated spatial distribution and trend for each season are very similar to observations, except in the industrial region of southern California. The model simulated seasonality is more likely to peak in summer, while the observation peaks in winter. Pollution source in this area is similar to that in eastern U.S. where industrial emission dominates the air quality change. However, previous studies suggested that the combined effect of a lower boundary layer in winter and the terrain

(valley) in this area may result in weak transport of pollutants, and thus higher pollution in the winter season [Bell et al., 2007].

5.3.2 Present-day PM10 concentration and seasonality

Present-day PM10 concentrations across the United States vary seasonally, but not as strongly as PM2.5. Figure 5.2 compares model-derived seasonal-mean PM10 and the EPA-AQS observed concentration over the contiguous United States. PM10 concentrations in the East are generally between 15 $\mu g/m^3$ and 40 $\mu g/m^3$. The eastern PM10 seasonality is rather pronounced, with winter concentrations (December-March) of 24 g/m^3, and July-August peak of 35 g/m3. The amplitude of the PM10 seasonal concentrations is about 30%. PM10 concentrations on the western U.S. extend from 10 $\mu g/m^3$ to 36 $\mu g/m^3$. The western U.S. PM10 seasonality is also rather pronounced, having about 30% amplitude. However, for the western U.S., the lowest concentrations (26 g/m^3) are reported in the late spring (April-June), while the highest values occur in late fall (October-January), distinctly different from the summer-peaked eastern U.S. Similar spatial and temporal patterns of present PM10 concentrations over the contiguous U.S. have been reported in previous studies [Harrison et al., 2004; Peng et al., 2005]. The simulated present day PM10 concentrations in each season reproduces the pollution pattern and seasonality as presented in the EPA AQS observations. Similar to the PM2.5 findings, the CAM-Chem model also slightly underestimates the PM10 concentrations over the U.S. The relative biases in the averaged PM10 concentrations are below 20% in the western and 10% in eastern United States. The reproduced PM10 concentrations and seasonality are more affected by the simulation of transpacific transport from Asia than

that of PM2.5. The main region under the influence of Asian pollution is the western U.S. The CAM-Chem result includes a high concentration area along the coast of California that varies with both Asia emissions and meteorology. The influence usually peaks in late spring and early summer when both Asian dust emission and middle latitude winds are strong.

5.3.3 Sensitivity areas

Through the analysis of EPA AQS air quality data and the comparison with CAM-Chem simulations, both observations and model results show clear spatial patterns of surface PM concentrations in each season. The basic pattern indicates that there is distinct difference in the surface PM levels between the eastern and western U.S., but the surface PM within each region shows uniform seasonal variation and close pollution levels. These findings confirm the western and eastern patterns for the U.S. PM found in previous studies [Harrison, et al., 2004; Park et al., 2007; Bell, et al., 2007]. On the other hand, definitions of the sensitivity regions that can best represent the basic patterns of PM pollution in the western and eastern United States will benefit the quantitive discussion.

Figure 5.3 shows the detailed locations and exact boundaries of two sensitivity regions. The sensitivity area for western U.S. is in longitude of 122-105 °W and in latitude of 34-46 °N; the sensitivity area for eastern U.S. is in longitude of 90-77 °W and in latitude of 34-42 °N. To achieve stable information about the spatial average of changes in PM related pollutants over the western and eastern United States, the average concentrations of pollutants in the two sensitivity regions are used in following analysis.

5.3.4 Particulate Chemicals

For evaluation of the model-derived present day concentrations of secondary inorganic particulates (Sulfate, nitrate and ammonium), the monthly mean model results are compared to the Clean Air Status and Trends Network (CASTNET, http://www.epa.gov/castnet/) measurements. Sulfate, nitrate and ammonium particles together make up about a third of the total air mass of PM in the U.S. They are highly variable in response to changes in anthropogenic emissions and meteorology. Therefore, the uncertainty in the simulations of these particulates will affect the overall reproduction of PM concentration changes. CASTNET provides a continuous record of daily particulate sulfate, particulate nitrate, and particulate ammonium concentrations. The measurements are chosen here for comparison because of their more complete spatial coverage over the eastern U. S. where the highest sulfate and nitrate aerosol concentrations occur. Although CASTNET has a variety of sites covering the contiguous U.S., there are still some model grids that do not contain any sites. Therefore, the monthly data are first distributed on the model grid cells. Then the observations are averaged in each grid cell and interpolated to no-observation grid cells. To be used as reference concentrations over the western and eastern U.S., both the observations and simulations over the sensitivity regions are totally added up and averaged.

Figure 5.4 shows the linear fit and the correlation coefficient between simulated and measured concentrations. Generally, the model captures the variation of particulates over the contiguous U.S. The temporal correlation coefficients between modeled and measured particulate sulfate and nitrate over the eastern U.S. are high (above 0.9), suggesting that the CAM-Chem model basically captures the observed variations. The

correlation coefficients over the western U.S. are lower with a value above 0.65, but the relationship is still fairly linear. The correlation coefficient for ammonium in the western U.S. is also above 0.6 with a good linear relationship. However, the simulations of ammonium concentration in the eastern U.S. show a very weak correlation to observations. The uncertainty in the ammonia emissions may be the primary cause of this discrepancy. Bouwman et al. [1997] found a global uncertainty of $\pm$25% in present NH_3 emissions, and individual seasonal and regional uncertainties may be considerably higher. Another possible reason could be the simulations of nitrate aerosols. Karydis et al. [2007] noted that modest errors in ammonium concentrations can be associated with significant errors in nitrate projections. Although the nitrate concentration appears to be reproduced correctly in the simulation, there remain significant uncertainty. For example, errors in the nitrate concentration may result, at least in part, from a lack of adequate representation of some processes that reduce the nitrate acid from the air before forming nitrate ammonium in the model, i.e., because of interactions with dust and organics [Ansari and Pandis, 2000] not accurately accounted for in the model.

5.3.5. Aerosol Composition

For evaluating the composition of particulate matter, the annual averaged daily model results are compared to the annual averaged observations for the year 2002 from Interagency Monitoring of Protected Visual Environments (IMPROVE, http://vista.cira.colostate.edu/improve/) dataset. Major aerosol composition content including ammonium sulfate, ammonium nitrate, elemental carbon, organic carbon and soil dust are analyzed. IMPROVE provides a continuous record of annual averaged data

for these major components on sites over the contiguous U.S. The IMPROVE data are first distributed on the model grid cells. The observations are then averaged in each grid cell and interpolated onto no-observation grid cells to compare to the model results. To be used as reference concentrations over the western and eastern U.S., both the observations and simulations are averaged for the sensitivity areas.

Figure 5.5 shows the CAM-Chem and IMPROVE percentages for annual averaged PM composition for each component. For PM2.5 composition in the eastern U.S., observations show that ammonium sulfate aerosols, ammonium nitrate aerosols and organic carbon are the dominant components of PM2.5. This characteristic is also captured by the CAM-Chem simulations. However, CAM-Chem overestimates the fraction of organic carbon and underestimates the fractions of secondary aerosols in the eastern U.S. The simulated fractions of each component over the western U.S. are close to the observation, although the fraction of organic carbon is overestimated about 10%. Major difference in the PM2.5 composition between the western and eastern U.S. are captured. First, the fractions of secondary aerosols are larger in the eastern than that in the western U.S. Second, the fraction of organic carbon is larger in the western than that in the eastern United States. Third, the fraction of mineral dust is large in the western U.S. For PM10, CAM-Chem captures the fractions of major PM10 components in the western but overestimates the fraction of secondary aerosols in the eastern United States. The major characteristic for compositions of PM10 is the increase in fraction of mineral dust aerosols. Compared with the PM2.5 composition, the fractions of secondary aerosols in PM10 decreased. The differences in compositions between the western and the eastern United States show the following: (1) For mineral dust in PM10, the fraction in the

eastern is smaller than that in the western United States; and (2) For anthropogenic emitted aerosols in PM10, the fraction is larger in the eastern than that in the western U.S. Overall, CAM-Chem basically captures the major variations of PM composition over the contiguous U.S..

5.4. Projections of Future (2050) PM Levels

Changes in particulate matter concentrations in 2050 due to changes in climate and anthropogenic emissions are examined in this section. The first part will address how the projected changes in meteorology from 2000 to 2050 and its associated natural responses from the environment affect PM concentrations with anthropogenic emissions kept at 2000 levels. The second part will analyze the effect of meteorology change together with anthropogenic emissions change from 2000 to 2050.

5.4.1. Effect of changes in climate

Climate change can affect the future PM concentrations through its effects on natural emissions, chemical reactions, and removal and transport processes. Its effects on natural emissions include changes in mineral dust, NOx and biogenic hydrocarbons. Mineral dust is a major component of particulate matter, and is emitted into the atmosphere through wind erosion on surface soils. Climate change includes changes in surface wind and soil moisture. Dryer surface soil will promote the erodibility of surface soil, and a stronger wind will directly increase wind erosion. In the future, surface winds in the United States are expected to be stronger than that in present and soil moisture in the western U.S. is expected to decrease from present level. Both of these expected changes tend to increase the mineral dust emission. NOx is emitted from natural sources

including soil, lightning and nitrogen fixing plants. Temperature and atmospheric moisture in 2050 are projected to increase (Figure 5.6). As a result, NOx emissions from soil are expected to increase [Wang et al., 1998; Delon et al., 2007]. In addition, higher temperatures also tend to increase the vegetation emissions by accelerating the growth of plants [Guenther et al., 1997; Potosnak, 2002].

Climate change influences PM associated chemical reactions by modifying reaction rates, changing concentrations of reactants and affecting the reaction environment. Many chemical reactions related to PM production are sensitive to temperature, such as reactions for sulfate and nitrate formation. As a result, some reactions may appear to dominate the variation in a certain season, but are less active when the next season comes. In addition, heterogeneous reactions are very important for PM formation and are sensitive to the reaction environment. Changes in humidity and temperature can affect the productivity of heterogeneous reactions. For example, humidity and temperature determine the phase in producing particulate ammonium nitrate. Whether the reaction will start at certain pollution levels depends on temperature. Decreasing atmospheric moisture would result in more products in the solid phase, while increasing it would lead to more in the aqueous phase. On the physical side of climate change impacts, concentrations of reactants can also be altered because of changes in meteorology. Changes in the planetary boundary layer height (PBL) will affect the transport and diffusion of air pollutants. In previous examinations of 2050 meteorology, it is found that the height of the PBL tends to increase with rising temperature [Lin et al., 2008]. The consequence will be decreased concentrations of pollutants in the surface air, which in turn reduce the chance of reactions in forming particulate chemicals.

The deposition / removal processes of PM are closely associated with meteorology conditions. Precipitation is the most important factor that determines the wet removal of particulate matter. However, not all areas of the United States will have the same trend of changes in precipitation from 2000 to 2050. In the future some areas may experience more droughts while others may experience increased precipitation. Projecting future rainfall over the mid-latitudes is notoriously difficult, as it involves two competing factors 1) increased specific humidity in a warmer climate, which increases rainfall and 2) increased atmospheric stability due to heating aloft which decreases rainfall. Precipitation is projected to generally increase, especially for DJF and MAM over the eastern U.S., reflecting changes in both large-scale and convective precipitation [Pye et al., 2009]. Precipitation in the western U.S. is projected to be slightly reduced in CCSM3 meteorology [http://www.earthsystemgrid.org/dataset]. Changes in convective precipitation may be more important than changes in large-scale precipitation as convective storms are generally short-lived and do not necessarily completely wash out aerosols and their precursors [Dawson et al., 2007].

Transport of pollutants is also affected by climate change. Stronger zonal winds can accelerate the long range transport of pollutants and increase the mixing of pollutants at smaller scales by increasing the shear between the free atmosphere and the ground. For the 2050 meteorology, the fall season are projected to experience a particularly strong increase in zonal winds across the contiguous U.S. [IPCC 2007]. This change will effectively reduce the pollution in heavy polluted areas, but worsen the air quality in low polluted areas. In the following paragraphs, the effects of climate change alone on PM concentrations in 2050 and uncertainty in the result will be examined in each season.

5.4.1.1 Climate change impact on PM2.5

Figure 5.7 shows the projected seasonal changes in U.S. surface-level PM2.5 concentrations due to changes in climate alone from the present day (1998-2002) to the future (2048-2052) following the IPCC A1FI, A1B, and B1 scenarios. Anthropogenic emissions are held at present-day values, but natural emission may change in response to climate change.

In the Spring, PM2.5 concentrations are projected to increase in the Southeast, the west coast, the Midwest and the Northeast and decrease in the central region (eastern part of the Mountain region) (Figure 5.7). Under the A1FI scenario, most areas of the contiguous U.S. have increases in PM2.5 concentrations. The most significant increases occur in the Southeast and the Southwest. These increases are contributed to by enhanced long range transport from North Africa along the equator by easterly flow and from East Asia by middle latitude zonal winds. Under the climate change only scenarios, changes in natural emissions are the largest factor affecting PM concentration changes. In Spring when the vegetation in middle latitude has not recovered and meanwhile the surface ground has thawed, soil is suitable for wind erosion. It is the maximum time for Asian dust storms. With the strongest westerly flow, the effect of Asian dust on North America is the strongest. This seasonal characteristic is also characteristic of the dust emissions over the western U.S. where occasional dust storm events occur in the Spring and Fall. Future climate brings higher temperatures which will result in an earlier thaw for soil, and thus stronger dust emissions from Asia and the western U.S. For the African dust, the easterly wind zone is stronger and the ITCZ moves northward in the future. As a result of

climate change under the A1FI scenario, easterly flow becomes stronger under future climate. Therefore, the effect of Africa dust on U.S. becomes stronger. In addition, the increased temperatures have been shown to increase the total concentrations of secondary aerosols over the northeast and decrease the concentrations over the central contiguous U.S. [Pye et al., 2009]; this process also contributes to the PM2.5 change in Figure 5.7. The impacts are similar for the A1B scenario. Increases with smaller magnitudes in PM2.5 concentrations occur in the eastern and western US, while decreases with larger magnitudes occur in the central U.S. region. Under the B1 scenario, small increases in PM2.5 concentrations occur in the northeast, while significant decreases occur over the central region, largely resulting from changes in secondary aerosols rather than changes in natural emissions.

Projected changes in concentrations during the Summer are the result of multiple factors. In summer, the effect of Asian transport is not as significant as that in spring because of increased vegetation recover and a reduction in zonal wind. The transport of Africa dust becomes the strongest of the year due to the ITCZ moving into the northern hemisphere. As a result of climate change in 2050, contributions of Africa dust will increase and the increases under corresponding scenarios are larger than these in spring. Biogenic emissions of organic carbon aerosols are expected to increase more in summer over all of the contiguous U.S. [Heald et al., 2006]. This increase together with increases in dust concentrations can partly compensate for the decrease in secondary aerosols over the central U.S. The concentrations of particulate secondary aerosols increase in source regions and decrease in non-emission regions because the enhancement of reactions in source regions for the projected future climate. Similar to Spring time, the changes under

the A1FI scenario are the largest of all scenarios. Transport from the equator along easterly flow dominates the PM2.5 change and the decrease in the central U.S. is not significant. The changes under the A1B scenario show a relatively weak influence from the transport of African dust relative to that under the A1FI scenario and only a small decrease over the central U.S. The changes under the B1 scenario are largely driven by changes in the amounts of secondary aerosols. The contribution from long-range transport is only minor.

The effect from climate change in the Fall season is close to that in Spring season. It is because the climate in Spring is similar to that in Fall. The main difference between the Fall and Spring seasons is the change in the effect of transpacific transport from Asia. In the Fall season, the middle latitude zonal winds and dust emissions in Asian are not as strong as in the Spring and the Asian pollutant flow arriving at the west coast is not as large. Therefore, the response to climate change in the Fall is not as sensitive as that in the sSpring. Changes in other aspects are very similar to that in Spring. The contribution of transport from the easterly flow in the Fall season has decreased to the level in Spring under the A1FI scenario. The changes under the A1B scenario show the same spatial pattern but a smaller magnitude to that in Spring. Because of the weak transport from Asia, a decrease about 2-6 $\mu g/m^3$ in PM2.5 concentration occurs along the west coast near southern California. The change under the B1 scenario shows a decrease over the central U.S. about the same magnitude to that in Spring, and stronger contributions through transport of Asian and Sahara dust on the east and west coasts.

In winter, changes in precipitation and convective flux may not contribute significantly to changes in PM2.5 concentrations. Changes in PBL height can play an

important role in determining surface concentration changes since the lower PBL height in winter can have a high concentration of pollutants as the boundary layer is compressed. Changes in the strength of the wintertime westerly winds and meridional winds across the United States are expected to affect the transport of inorganic aerosols. The changes caused by climate change alone are projected to show decrease over the central and eastern U.S. under the A1B and B1 scenarios. The possible decrease is up to 10 $\mu g/m^3$. The decreases are mainly related to the decrease in production of secondary aerosols. A weak increase in PM2.5 concentration is shown along the west coast of California, which may be related to enhanced dust emissions over Asia. Under the A1FI scenario, a decrease in PM2.5 concentration is found in the central U.S. and a weak increase occurs in the eastern and northern U.S. The increase near the U.S.-Canada boundary is probably a result of dust emissions from bare farm land.

In this analysis of changes in surface PM2.5 concentrations due to climate change alone, we found that projected changes are between -10 $\mu g/m^3$ and +14 $\mu g/m^3$. As discussed in the previous sections, many factors in climate change contribute to changes in PM concentrations. The results show that the largest increase occurs in the Summer under the A1FI scenario, while the largest decrease occurs in Winter season under the B1 scenario. This result under the A1FI scenario is very close to the result of future PM2.5 change by climate change alone under the A2 scenario as studied by Racherla et al. [2010].

5.4.1.2 Climate change impacts on PM10

Figure 5.8 shows the projected seasonal changes in U.S. surface-level PM10 concentrations due to changes in climate alone from the present day (1998-2002) to the future (2048-2052) following the IPCC A1FI, A1B, and B1 scenarios. Anthropogenic emissions are held at present-day values, but natural emission may change in response to climate change.

Changes in PM10 concentrations by climate change alone have similar patterns to the changes in PM2.5 in each season. This is because the physical processes that contribute to changes in PM2.5 and PM10 are similar. However, the small difference in changes is caused by the difference in relative importance of components. For example sea salt is a dominant component of PM10 near coastal regions, but its relative contribution to PM2.5 is smaller [Manders, et al., 2009]. Therefore, the climate change induced sea salt concentration change is clearly visible in the derived PM10 concentrations, but not in the changes to PM2.5 concentrations. However, the total ratio of particulate sulfate and nitrate in PM2.5 is higher than that in PM10. As a result, the changes in PM2.5 concentration is more affected by changes in chemical reactions associated with secondary aerosols. In addition, the carbonaceous PM increase with temperature increase in the future climate is also a main contributor for the PM10 change. This process is mainly associated with biogenic emissions. Different from secondary aerosols emitted from industrial regions, the biogenic emissions are mainly from farm regions and forests. Therefore, these may affect the pattern of the changes in PM10. Below, the major difference between changes in PM10 concentration and changes in PM2.5 concentration are discussed for each season. The detailed analysis of the patterns

of change in PM2.5 and the associated processes refer to the discussion in the previous section.

In Spring, PM10 concentrations are projected to increase in the Southeast, the west coast, the Midwest and the Northeast and decrease in the central U.S. (eastern part of Mountain region) (Figure 5.8). These characteristics are very similar to those for PM2.5 changes. Same to PM2.5, these changes are contributed by enhanced zonal wind, natural emissions and changed aerosol chemistry. The major difference is the magnitude of changes and change patterns near coastal regions. Note that PM2.5 is counted in PM10 concentrations. Near the coastal regions, the PM10 has a significant sea salt component. Sea salt in the surface air is in the range of PM10 but are too large for PM2.5. As a result, there are differences between patterns of PM10 and PM2.5 near coastal regions. In spring, the difference is also significant under the A1B and B1 scenarios. Over the land or ocean near coastal regions, there are clear decreases in PM10 concentrations. The reduction of sea salt may be caused by precipitation increase or weak boundary layer wind in the future climate. Precipitation will enhance the removal process for sea salt aerosols. Small boundary layer wind speed will reduce the shear and thus less emissions of sea salt.

The pattern of changes in PM10 concentrations in Summer is similar to that of PM2.5. Under the A1FI scenario, an increase of up to 14 $\mu g/m^3$ in PM10 concentration over the contiguous U.S. The dominant factor is transport of mineral dust from North Africa. Under the A1B scenario, the changes in PM10 are very close to that of PM2.5 over land with the only extra decrease up to 6 $\mu g/m^3$ over the ocean. A similar result is

found for the changes under the B1 scenario. The decreases and increases are in the mountain region and eastern U.S., respectively, with a magnitude less than 6 $\mu g/m^3$.

In Fall, the changes in PM10 concentrations over the contiguous U.S. are very close to the changes in PM2.5 concentrations. Under the A1FI scenario, the increases in concentration magnitude are mainly over the oceans; the coarse dust particles have a shorter lifetime in the atmosphere than smaller particles. Most of the coarse particles being transported are deposited on ocean surface before reaching the land of the United States. The changes under the A1B scenario show a decrease over the western and an increase over the eastern United States. A decrease in PM10 concentration are found under the B1 scenario over the entire contiguous U.S.

In Winter, natural processes over land including biogenic emissions and mineral dust emissions are weak and less variable. Anthropogenic emissions are assumed to be the same strength year around. As a result, the changes in PM10 concentration resulting from projected effects of climate change are very close to changes in PM2.5 under all three scenarios. The only difference is on the oceans where sea salt mainly contributes to PM10. There is a weak decrease in sea salt concentrations. A possible reason could be the effect on dilution of pollutants from the PBL height increase under future climate conditions.

In summary, changes in surface PM10 concentrations resulting from climate change alone are projected between -14 $\mu g/m^3$ and 18 $\mu g/m^3$. Many factors in climate change may contribute to changes in PM concentration. Unlike the effects on PM2.5, the additional factor affecting PM10 change near coastal regions is sea salt. The main difference between changes in PM2.5 and PM10 are caused by sea salt emissions. The

change in biogenic emissions of carbonaceous is also a major factor that contributes to the changes in PM10. Due to the emission peaks in farm regions, biogenic emission change may compensate for changes in PM10 caused by anthropogenic aerosol change in the western United States.

5.4.2. Effect of changes in both climate and climate emissions

In addition to climate change, changes in anthropogenic emissions have direct effects on future PM concentrations. Anthropogenic emissions mainly affect the concentrations of particulate chemicals (sulfate, nitrate and ammonium) in PM composition. The future anthropogenic emissions assumed are listed in table 5.1. The changes from present emissions not only change the amount of reactants for aerosol production but also affect the probability of chemical reactions through nonlinear relationships among sulfate-ammonium-nitrate chemistry. For example, the reduction of sulfate precursors results in more ammonia available to react with nitrate, and thus lead to more production of nitrate aerosols. Changes in climate factors including temperature, and humidity may be involved in the nonlinear relationships. This section addresses the extent to which changes in anthropogenic emissions of aerosol precursors between the present-day and 2050 would influence PM concentrations with future climate.

5.4.2.1 Climate change and anthropogenic emissions change impacts on PM2.5

Figure 5.9 shows projected changes in U.S. surface-level PM2.5 concentrations due to changes in climate and emissions together relative to the present day (1998-2002) for the future (2048-2052) following the IPCC A1FI, A1B, and B1 scenarios. Both climate

and anthropogenic emissions are projected into the future. Since changes in anthropogenic emissions are equal to all seasons, the discussion on effect of climate and emission change together will follow the order of scenario cases.

5.4.2.1.1 The A1FI scenario case

The A1FI scenario assumes continued heavy use of fossil fuels worldwide. As a result, the global average temperature rises by about 1.9 °C by 2050. NOx emissions are projected to increase by 136% globally compared to the present-day, but increase in the United States by only about 25% (Table 5.1). Ammonia emissions are projected to increase globally and domestically by 108% and 40%, respectively. SO_2 emissions are projected to increase 16% globally but decrease 70% in the United States. With the precursor emission change, the concentrations of total particulate chemicals decrease over most part of the contiguous U.S.

The largest decreases in PM2.5 concentrations are projected to occur over the northeast in Summer and Fall. The maximum decrease is around 14 $\mu g/m^3$. The changes in natural emissions also contribute to PM2.5 in the central region in the form of increase in dust aerosols concentrations transported from Canada and North Africa. As a major component of PM2.5, particulate sulfate concentrations in the U.S. are projected to decrease in all seasons due to domestic reductions in SO_2 emissions. As a competitor to sulfate aerosols, future nitrate aerosol concentrations are projected to increases due to the increases in both precursor emissions and available ammonia concentrations. Because the decreased sulfate levels coupled with increased ammonia emissions result in more ammonia available to react with nitrate. Although the concentration of nitrate may

increase, the increase in mass concentration of nitrate aerosols is less than the decrease in sulfate aerosols.

5.4.2.1.2 The A1B scenario case

Under the more central A1B scenario, anthropogenic NOx emissions are projected to increase 78% globally compared to the present-day but decrease approximately 35% in the United States (Table 5.1). Ammonia emissions are projected to increase globally and domestically by 32% and 40%, respectively. SO_2 emissions are projected to increase 31% globally but decrease 74% in the United States. With decreases in precursor emissions for both nitrate and sulfate, the contribution of total particulate chemicals to changes in PM2.5 concentration is expected to be a larger decrease than that under the A1FI scenario.

As shown in Figure 5.9, the total effect of changes in climate and anthropogenic emissions under the A1B scenario is to decrease the PM2.5 concentrations over all of the contiguous U.S.. The largest decreases in PM2.5 concentrations are projected to occur over the northeast in summer with a maximum decrease of up to 18 $\mu g/m^3$. Sulfate concentrations in the U.S. are projected to decrease in all seasons due to domestic reductions in SO_2 emissions. Although the decreased sulfate levels coupled with increased ammonia emissions lead to more ammonia available to react with nitrate, the combination of the increased reduction of SO_2 emissions, the small magnitude of increase in ammonia emission, and the decrease in nitrate precursors together result in a lower concentration for total particulate chemicals than that under the A1FI scenario. Compared

with the contribution by climate change induced natural emissions change, the changes caused by anthropogenic emissions are dominant.

5.4.2.1.3 The B1 scenario case

As under the low B1 scenario, anthropogenic NOx emissions are projected to increase 36% globally compared to the present-day but decrease approximately 58% in the United States (Table 5.1). Ammonia emissions are projected to increase globally and domestically by 22% and 30%, respectively. SO_2 emissions are projected to decrease 37% globally but decrease 85% in the United States. With the large decreases in precursor emissions for both nitrate and sulfate, the PM2.5 concentration is expected to show a decrease under the B1 scenario.

As shown in Figure 5.9, the total effect of changes in climate and anthropogenic emissions under the B1 scenario is to decrease the PM2.5 concentrations all over the contiguous U.S. with the largest decrease over 18 $\mu g/m^3$. The largest decreases in PM2.5 concentrations are projected in each season over the northeast.. The insignificant seasonality for changes in PM2.5 concentration indicates that the changes caused by anthropogenic emissions are dominant.

5.4.2.2 PM10

Figure 5.10 shows the projected change in U.S. surface-level PM10 concentrations due to changes in climate and emissions together from the present day (1998-2002) to the future (2048-2052) following the IPCC A1FI, A1B, and B1 scenarios. Both climate and anthropogenic emissions are projected for the future.

The A1FI scenario case

The changes in PM10 concentrations under the A1FI scenario include a significant decrease over the eastern U.S. and weak decrease or increase over the western U.S. The findings indicate that the contributions from climate change and emission change are both important. The largest decreases in PM10 concentrations are projected to occur over the northeast in summer with the maximum decrease of 14 $\mu g/m^3$. In summer time, both transports of North Africa dust from easterly flow and pollutants from Mexico contribute to the PM10 over the southwest, and cause an increase up to 10 $\mu g/m^3$. In winter, the mineral dust aerosols transported from Canada also increases the PM10 concentration on the northwest.

The A1B scenario case

As shown in Figure 5.10, the total effect of changes in climate and anthropogenic emissions under the A1B scenario is to decrease the PM10 concentrations all over the contiguous U.S. The largest decreases in PM10 concentrations are projected to occur over the northeast in summer. The maximum decrease is up to 18 $\mu g/m^3$. The pattern of change is very close to that for PM2.5, which indicates that natural emissions including mineral dust and organic aerosols may not change much with the climate and emissions conditions under the A1B scenario.

The B1 scenario case

For the B1 scenario (in Figure 5.10), the total effect of changes in climate and anthropogenic emissions is to decrease the PM10 concentrations all over the contiguous U.S. with the largest decrease over 18 $\mu g/m^3$. The largest decreases in PM10 concentrations are projected over the northeast. The peak change values are found in all

seasons, but the range in summer season is the largest due to the effect of temperature on aerosol chemistry. The decrease over large areas indicates that total changes in particulate chemicals dominate the changes in future PM10 concentration.

5.5. Changes in Future PM composition

In this section, the effect of changes in climate and emissions on the composition of particulate matter in 2050 in the western and eastern United States is examined. The annual averaged percentage for each component over the sensitivity region is calculated.

Figure 5.11 shows the composition of PM2.5 and PM10 in 2050 under the A1FI scenario. The major characteristic for PM2.5 composition in 2050 is that the percentage of organic carbon increases in both the western and eastern U.S. The percentage of mineral dust in PM2.5 also increases. The increase in the western U.S. is around 40%. The relative increases of organic carbon and mineral dust are the result of climate change and reduction in sulfate concentration. Compared with the CAM-Chem simulated present composition (in Figure 5.5), the mass percentage of sulfate aerosols in the total PM2.5 decreases due to the reduction in emissions of PM precursors under the A1FI scenario. As discussed in previous section, changes in climate foster the increase in emissions of organic carbon and mineral dust. The effect is also presented in the composition change in PM10. The percentage of mineral dust in PM10 increases about 10 percent over both the western and eastern U.S. As shown in Figure 5.8, the increases in local mineral dust emissions and enhanced transport of dust from Africa and Asia dominate the increase in PM10 concentration under the A1FI scenario. Additionally, changes in climate and emissions also significantly changes the ratios of secondary aerosols in PM10. The trend

is that the total ratio of secondary aerosols decreases in 2050. Although the percentage of nitrate aerosols increases resulted from the reduction in emissions of sulfate precursor and increase in emissions of NOx and ammonia, the total mass of secondary aerosols decreases.

Figure 5.12 shows the composition of PM2.5 and PM10 in 2050 under the A1B scenario. The major characteristic for PM composition in 2050 is that percentages of secondary aerosols and elemental carbons decrease in both the western and eastern United States. It is a result of reduction of anthropogenic emissions over the contiguous U.S.. The percentages of natural emissions including mineral dust and organic carbon increase due to the effect of climate change under the A1B scenario, but the magnitude is not much. Specifically, the PM2.5 will include less sulfate and more nitrate per unit mass. Contribution from dust will increase as discussed in Figures 5.7 and 5.8, but will be more presented on changes in composition of PM10. That means the relative contribution to coarse particles is larger than that to fine particles. The difference between the western and eastern United States is mainly due to dust, with dust playing a more important role in the composition of PM over the western United States.

Figure 5.13 shows the composition of PM2.5 and PM10 in 2050 under the B1 scenario. The changes in 2050 PM composition is relatively small. As discussed in section 5.4, the major factor that driving PM change under the B1 scenario is reductions in anthropogenic emissions. It can be seen from Figure 12 that the ratio of total secondary aerosols decreases in both the western and eastern United States. The percentage of sulfate decrease around 10% in the western and 20% in the eastern United States. The induced increase in nitrate percentage is less than 10% for all cases.

In summary, the total ratio of secondary aerosols is expected to decrease under all scenarios as a result of anthropogenic emission change. More affected by climate change, mineral dust may be a significantly increased component of PM under the A1FI scenario. Organic carbons show a slight increase under all three scenarios. Significant composition change occurs under the A1FI scenario when the effects from climate change and anthropogenic emissions change are both considered. The change under the A1B scenario is of smaller magnitude than that under the A1FI scenario. Changes under the B1 scenario is mainly derived by anthropogenic emission change, with small percentage changes in other components.

5.6. Summary and Discussion

Changes in both climate and emissions will influence future particulate matter concentrations and composition. The climate chemistry model, CAM-Chem, which had incorporated all modules for simulations of major PM components, was used to examine the separate effect of climate change and the combined effect of changes in climate and anthropogenic emissions on the concentrations and composition of PM in 2050 over the contiguous United States. Different from previous studies on future PM levels that only consider changes in a part of PM components, this study projects the future changes in all major components including sulfate, nitrate, elemental carbon, organic carbon, mineral dust and sea salt and considers the effects of climate and emission changes on their productions.

CAM-Chem provides a good representative of present-day PM levels in the United States. CAM-Chem simulations of PM2.5 and PM10 concentrations for 2002 capture the

major spatial patterns and seasonality present in the U.S.EPA air quality observations. The simulated monthly variations of inorganic aerosol (sulfate, nitrate, and ammonium) concentrations have linear correlations to the CASTNET measurements over the western and eastern U.S. In addition, the simulations of PM composition over the western and eastern U.S. reproduce the characteristics in size difference and spatial distribution compared with IMPROVE observations.

The changes in climate alone are projected to affect the levels of particulate matter in 2050 by 0-10 $\mu g/m^3$ for PM2.5 and 0-14 $\mu g/m^3$ for PM10 in the eastern and western U.S., but -6-0 $\mu g/m^3$ for PM2.5 and -10-0 $\mu g/m^3$ for PM10 in the central United States. The seasonal variability of climate change alone effects is distinct. The effect on biogenic aerosol emissions and productions of secondary aerosols is strong in summer season, but weak in winter season. Under the A1FI scenario, the climate change induced mineral dust increases both the PM2.5 and PM10 over the United States, due to the combined effects of increases in locally emitted dust, transport of Asian dust, and dust in tropical easterly flow from northern Africa along with changes in inorganic aerosols. The effect of climate change alone under the A1B scenario is relatively small. Changes in natural processes and effects on anthropogenic pollutants result in the decrease of PM concentrations over the central U.S. and the increase over the coast and eastern U.S. Changes under the B1 scenario are presented as decreases over the central and increases over the eastern U.S. with the smallest magnitudes in the three scenarios. Compared with other studies on future PM concentrations, the projected effect of climate change in this study also considered the additional contribution from mineral dust emissions. The projections

under the three IPCC scenarios show large differences among the projected changes in mineral dust. Therefore, this could be the significant uncertainty affecting future PM.

Simulations based on 2050 climate and anthropogenic emissions show that the changes in anthropogenic emissions decreases PM2.5 by 2-18 $\mu g/m^3$ and PM10 by 2=22 $\mu g/m^3$ relative to climate change alone results. The seasonality of the changes in PM concentrations caused by changes in anthropogenic emissions is indistinct. The combined effect of climate and anthropogenic emissions changes shows the smallest decrease in summer and the largest decrease in winter. The decrease mainly peaks in industrial regions including the Midwest and northeast United States. The western U.S. where the mineral dust is one of the major contributors to PM, the decrease is not distinct. Under the three IPCC scenarios, the strongest decrease in PM concentrations occurs under the B1 scenario, while the decrease under the A1FI scenario is relatively weak or even showing weak increases over the western U.S. The magnitude of decrease under the A1B scenarios is in between. In summary, this result shows that the effect in projected anthropogenic emission change is opposite to the effect of climate change on future PM levels in most areas. Relatively, the effect of anthropogenic emissions has a larger magnitude than that of climate change. The changes in future PM concentrations in industrial regions are dominated by changes in anthropogenic emissions. The changes in future PM concentrations in non-industrial and coastal regions are mainly dominated by changes in climate.

The PM compositions are affected both by the changes in climate and emissions. As a result of changes in anthropogenic emissions, the percentages of inorganic aerosols and elemental carbons decrease in both PM2.5 and PM10 by 2050 due to the decrease in

anthropogenic emissions. The ratio of organic aerosols in PM increases by 8-46% following all three IPCC scenarios. Under the A1FI scenario, the percentages of mineral dust mass in total PM over the United States increased by 10-20%, and the increases over the western U.S. are larger n a relative sense. The ratio of mineral dust in PM10 is larger than that in PM2.5. Smaller magnitudes of increase in mineral dust ratios are shown under the A1B scenario, and a weak increase under the B1 scenario. The projected changes in 2050 PM composition indicates that increases in mineral dust and organic aerosols may affect concerns in PM pollution. The significance of industrial emissions decreases. Sulfates, traditionally the main component, will largely decrease in future PM.

In closing, it is important to note that there remain at present many uncertainties in PM modeling that remain difficult to quantify. For example, the land use change is an important factor affecting future emissions of mineral dust. Projections of land use change caused by human activities are not considered in this study, which may affect the analysis of dust emissions. In addition, the biogenic emissions of organic carbon are also seriously affected by land use change. Many uncertain factors including various human activities, changes in agriculture, ecological transition etc. can affect land use change. Therefore, the effect of land use change on future PM concentrations is an interesting topic for future research. There are also large uncertainties in the projection of anthropogenic emissions. For example, the anthropogenic ammonia, unlike the NOx and SO_2, are mainly emitted from fertilizer use and domesticated animals. Both sources are difficult to project for the future. Recent studies [Park et al., 2006; Pye et al., 2009] also argue that there is an underestimate of ammonia emissions in the present inventory. Considering the significance of ammonia in production of secondary inorganic aerosols,

the effects of such a bias may be large. Fully addressing these uncertainties will require additional research. In addition, the current study neglected the detailed microphysics processes being used in the latest version of CAM version 5; further investigation of these effects is needed.

Table 5.1. Projected global summer emissions budgets of aerosol precursors for present (1998–2002) and their fractional changes by 2050 (2048-2050).

Species	*Years*	*Anthropogenic*	*Biomass*	*natural*	*Total*
NO_x	2000	24.9 TgN	5.71 TgN	10.32 TgN	40.93 TgN
	2050	226% /84.2%/ 36% [a]	-10% /25%/83%	0% /0%/0%	136% /54.2%/34%
NH_3	2000	33.3 TgN	5.9 TgN	14.2 TgN	52.5 TgN
	2050	108% / 51.6%/22%	2.7% /3.4%/11%	0% /0%/ 0%	67% /34%/15%
SO_2	2000	61.2 TgS	1.2 TgS	5.8 TgS	68.2 TgS
	2050	16% /33.6%/-37%	43% /66%/83%	0% /0%/0%	15% /31%/-32%
DMS	2000	—	—	16.0 TgS	16.0 TgS
	2050	—	—	0% / 0%/0%	0% /0%/ 0%
$BioHC_s$	2000	—	—	622.0 TgC	622.0 TgC
	2050	—	—	41% /25%/ 20%	41% /25%/ 20%

[a] The numbers before and after '/' denote projected fractional emissions changes under the A1FI, A1B and B1 scenarios, respectively, relative to present budgets.

Table 5.2. Experiments using CAM-Chem for PM projections.

Experiment	*Climate*[a]	*Anthropogenic Emissions*[b]
(1) Evaluation	NCEP R2 2002	2000
(2) Present	CCSM3 2000	2000
(3) A1FI2050_C	CCSM3 A1FI 2050	2000
(4) A1B2050_C	CCSM3 A1B 2050	2000
(5) B12050_C	CCSM3 B1 2050	2000
(6) A1FI2050	CCSM3 A1FI 2050	2050
(7) A1B2050	CCSM3 A1B 2050	2050
(8) B12050	CCSM3 B1 2050	2050

[a] Physical environment of the troposphere, including wind, temperature, water vapor, etc.

[b] Including emissions from anthropogenic and natural sources.

Spring

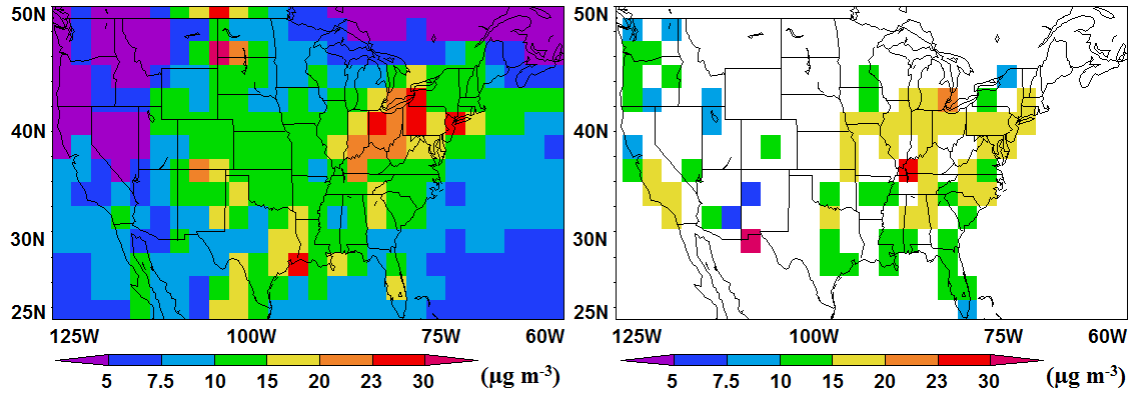

Summer

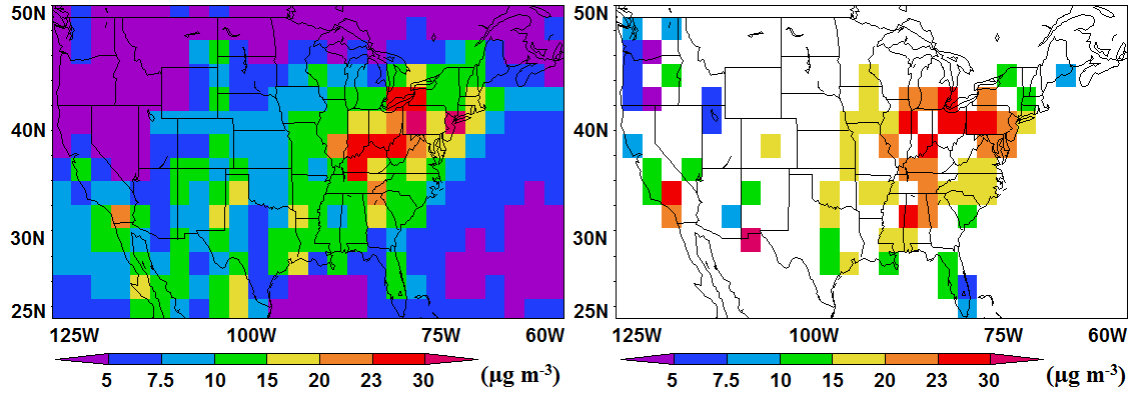

Fall

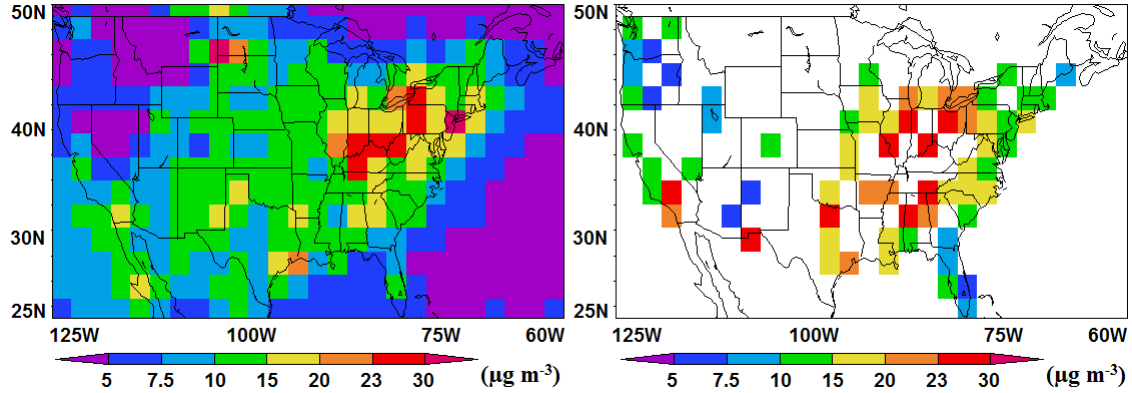

Figure 5.1. CAM-Chem simulated surface concentrations of PM2.5 in 2002 over the contiguous U.S. (left) versus U.S. EPA AQS observations (right).

Figure 5.1 continue
Winter

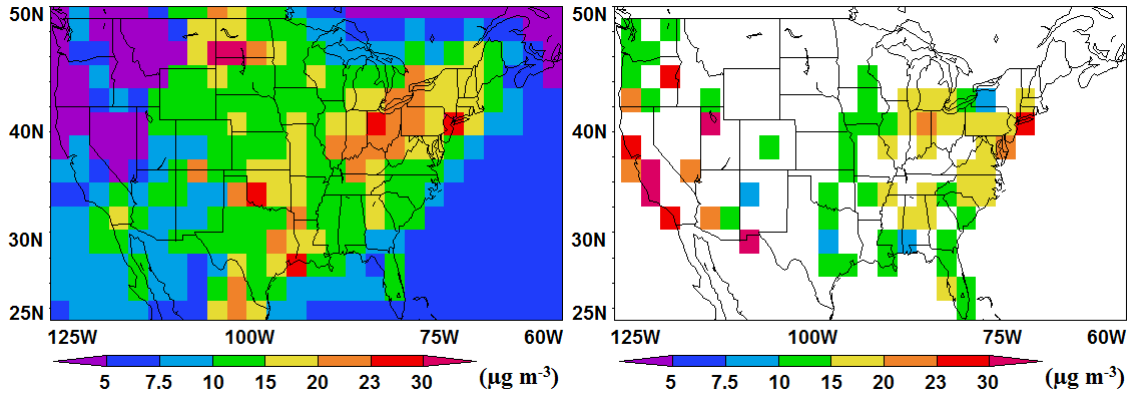

Spring

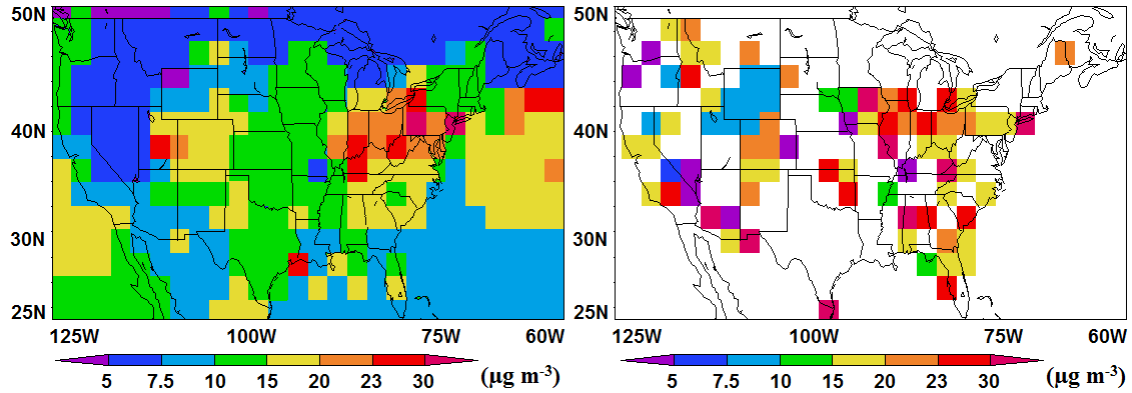

Summer

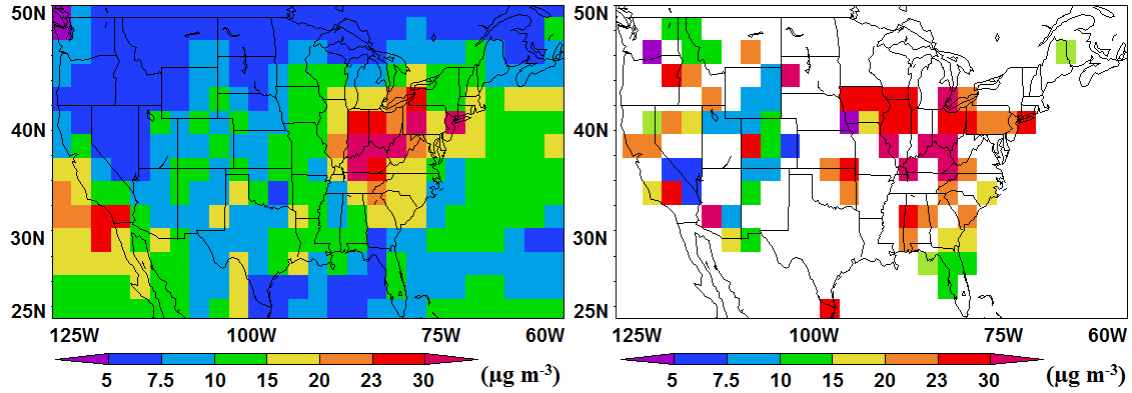

Fall

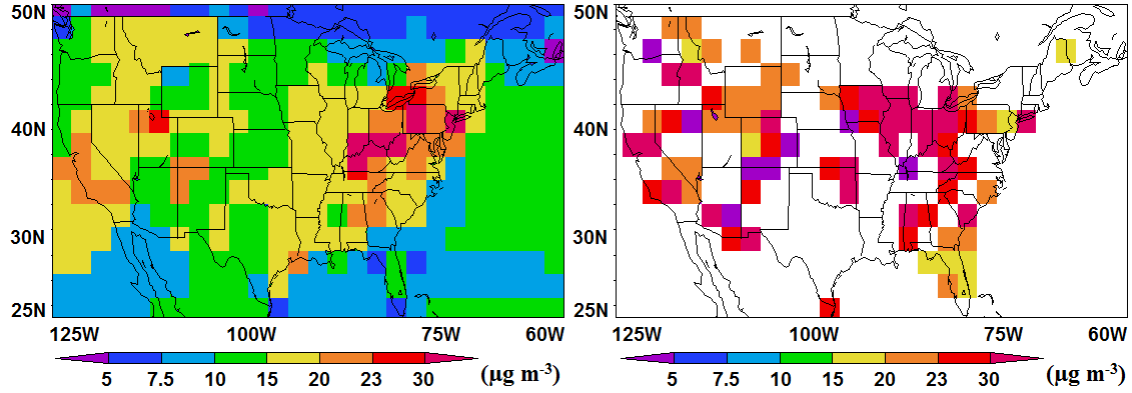

Figure 5.2. CAM-Chem simulated surface concentrations of PM10 in 2002 over the contiguous U.S. (left) versus U.S. EPA AQS observations (right).

Figure 5.2 continue

Winter

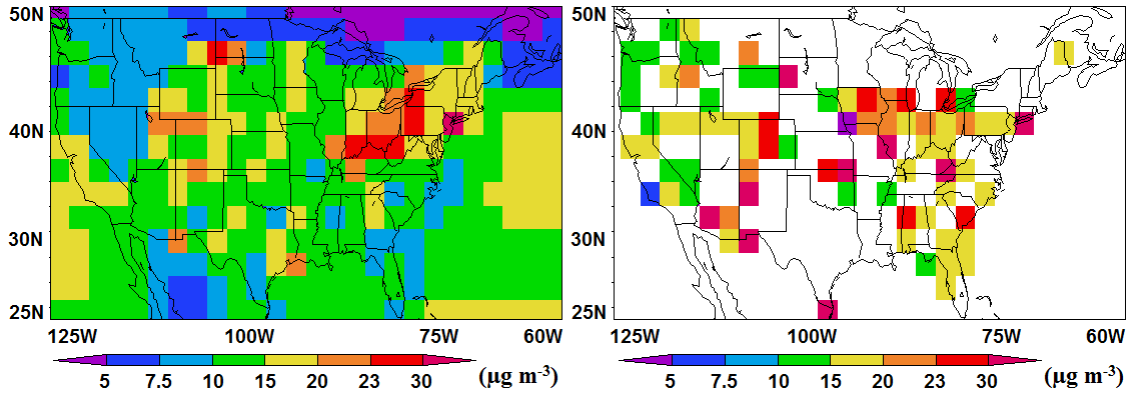

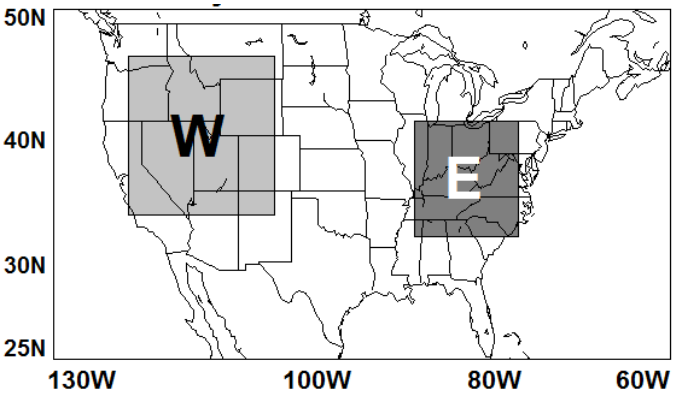

Figure 5.3. Specifications of sensitivity areas that represent typical surface PM pollution over western and eastern U.S.. The sensitivity area for western U.S. is in longitude of 122W-105W and in latitude of 34N-46N; the sensitivity area for eastern U.S. is in longitude of 90W-77W and in latitude of 34N-42N.

Eastern U.S.

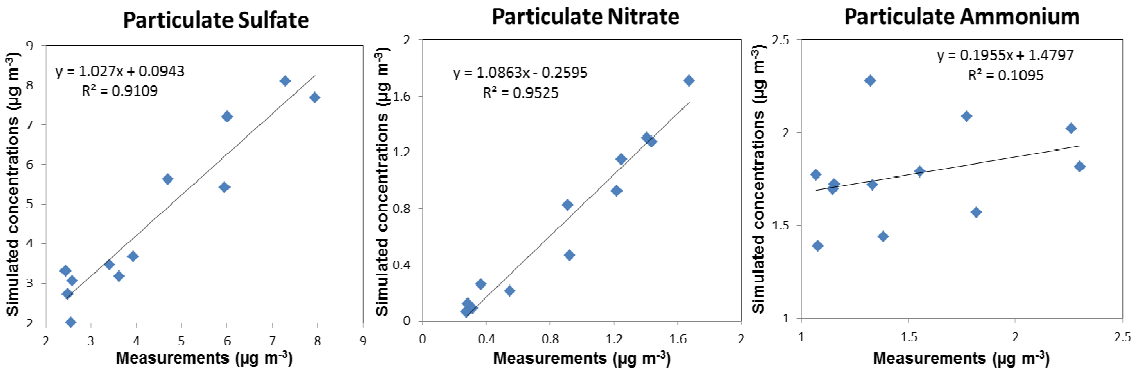

Western U.S.

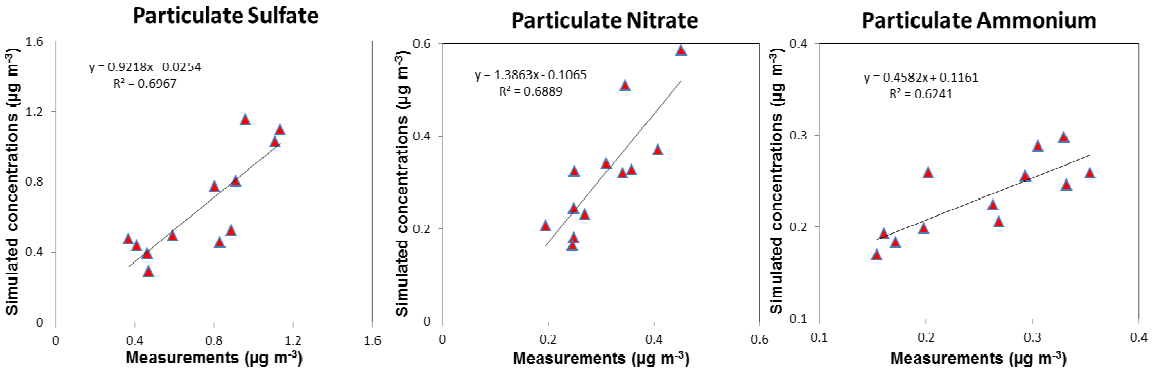

Figure 5.4. CAM-Chem simulated particulate sulfate, nitrate, and ammonium aerosols compared to CASTNET observations. Simulated surface concentrations are monthly averages in 2002 over sensitivity areas specified before. CASTNET measured values are converted to model resolution for comparison and are monthly averaged over the same sensitivity areas. Blue squares represent eastern U.S. sites and red triangles represent eastern U.S. sites. Also shown are the linear least squares fit and the correlation coefficient between simulated and measured concentrations.

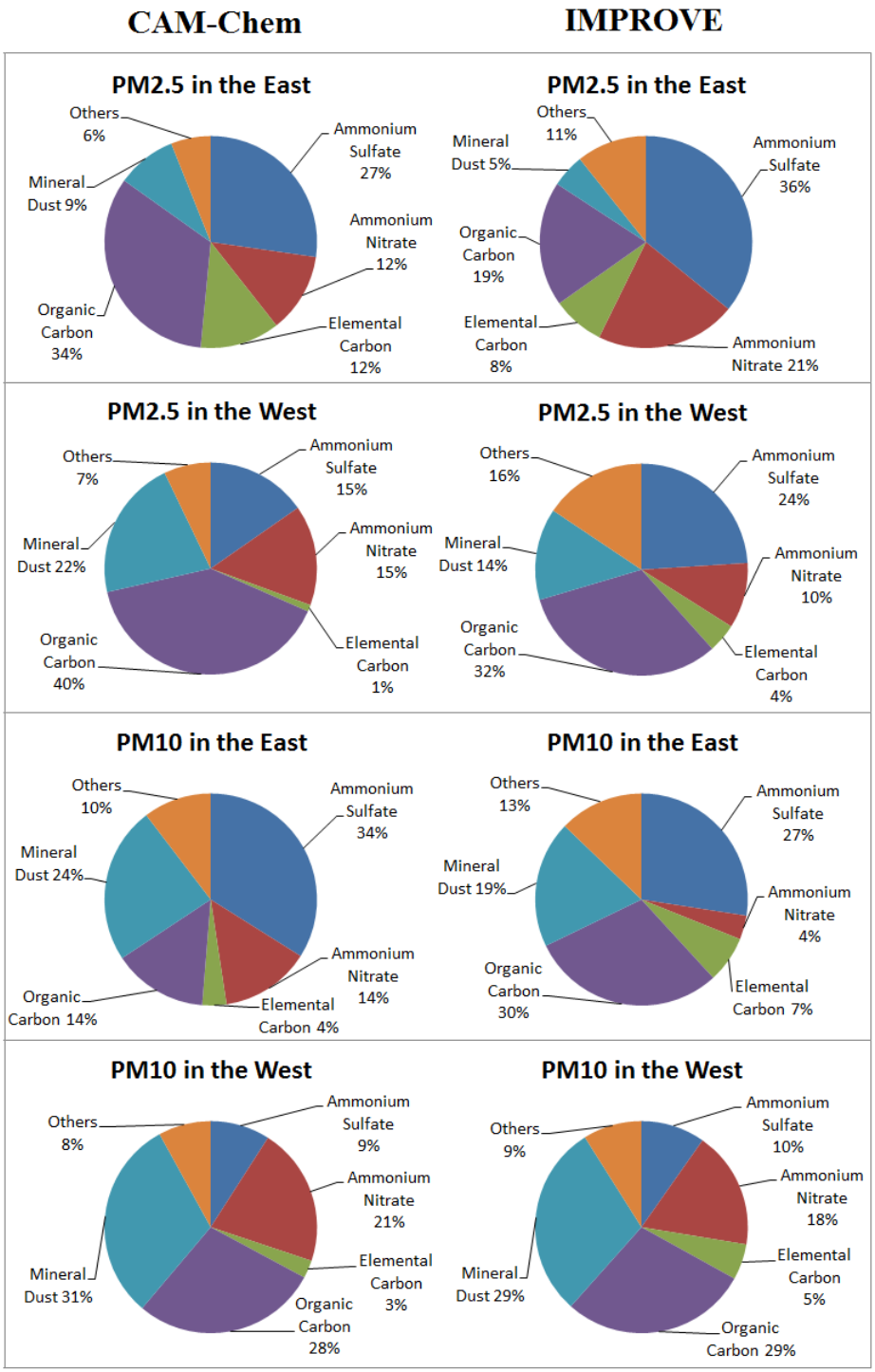

Figure 5.5. CAM-Chem simulated percent of particulate matter composition by components compared to IMPROVE observations. Simulated values are annual averages in 2002 over sensitivity areas specified before. IMPROVE measured values are converted

to model resolution for comparison and are yearly averaged over the same sensitivity areas.

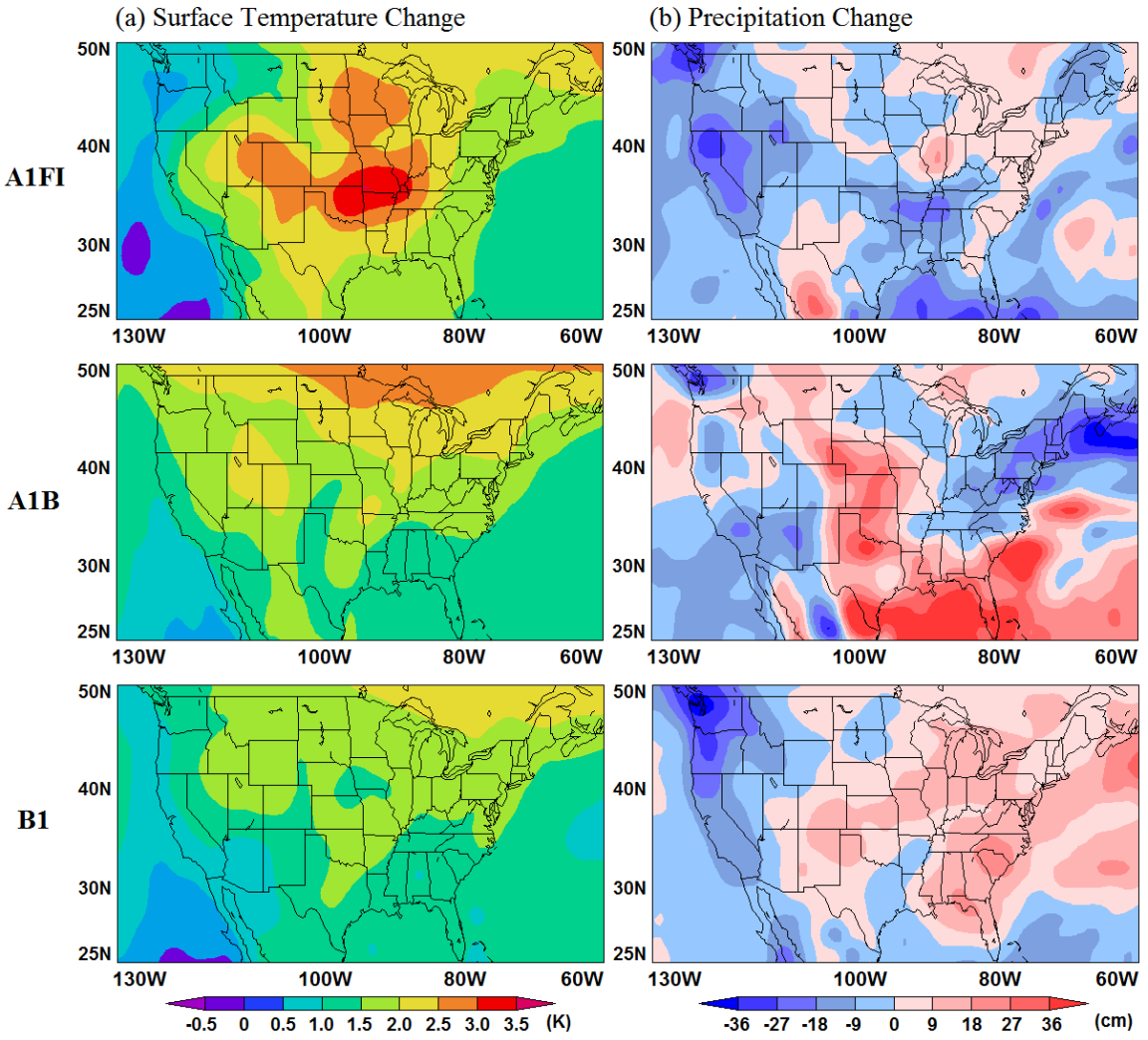

Figure 5.6. Projected change in annual averaged surface temperature and accumulated annual precipitation between the present day (1998-2002) and future (2048-2052).

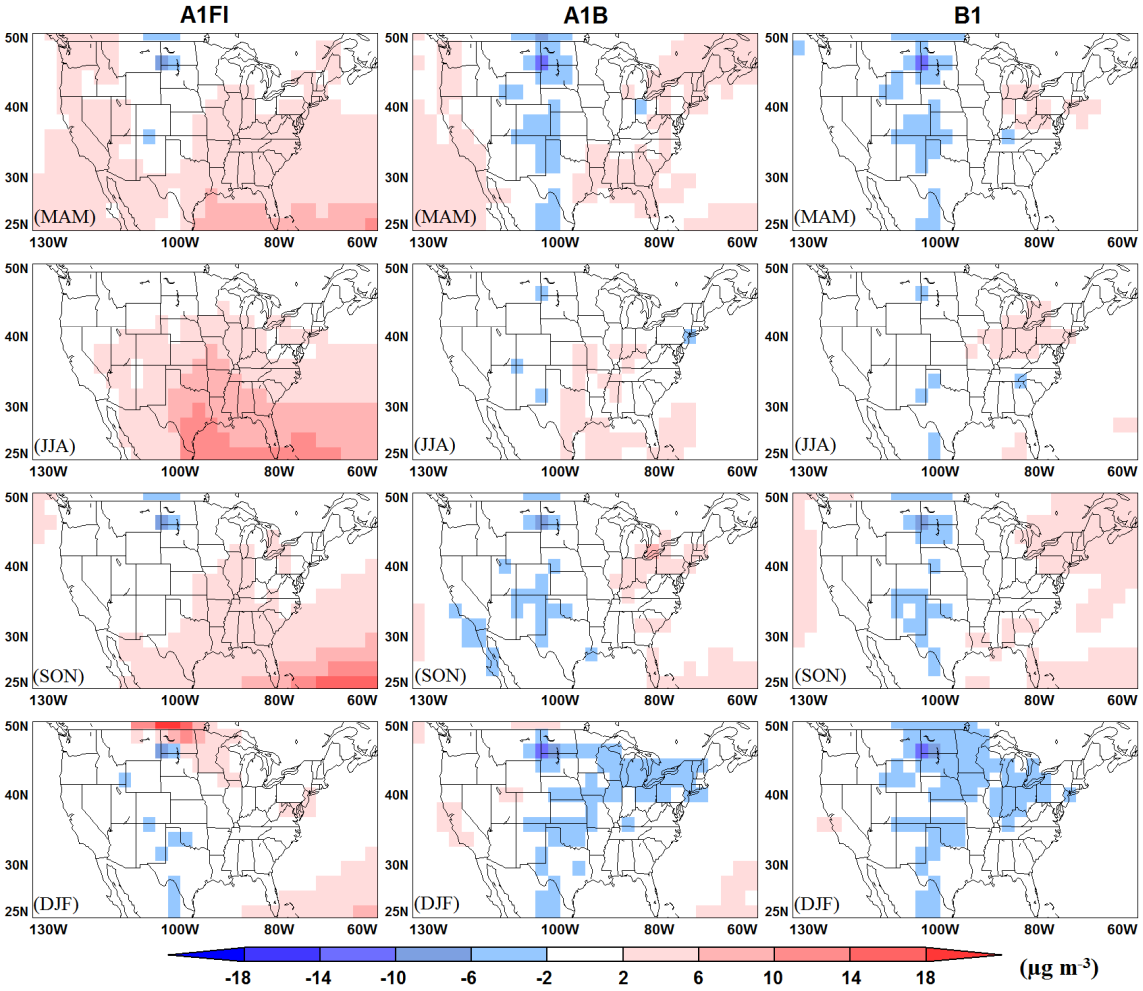

Figure 5.7. Projected change in U.S. surface-level PM2.5 concentrations due to changes in climate from the present day (1998-2002) to the future (2048-2052) following the IPCC A1FI, A1B, and B1 scenarios. Anthropogenic emissions are held at present-day values, but natural emission may change in response to climate change.

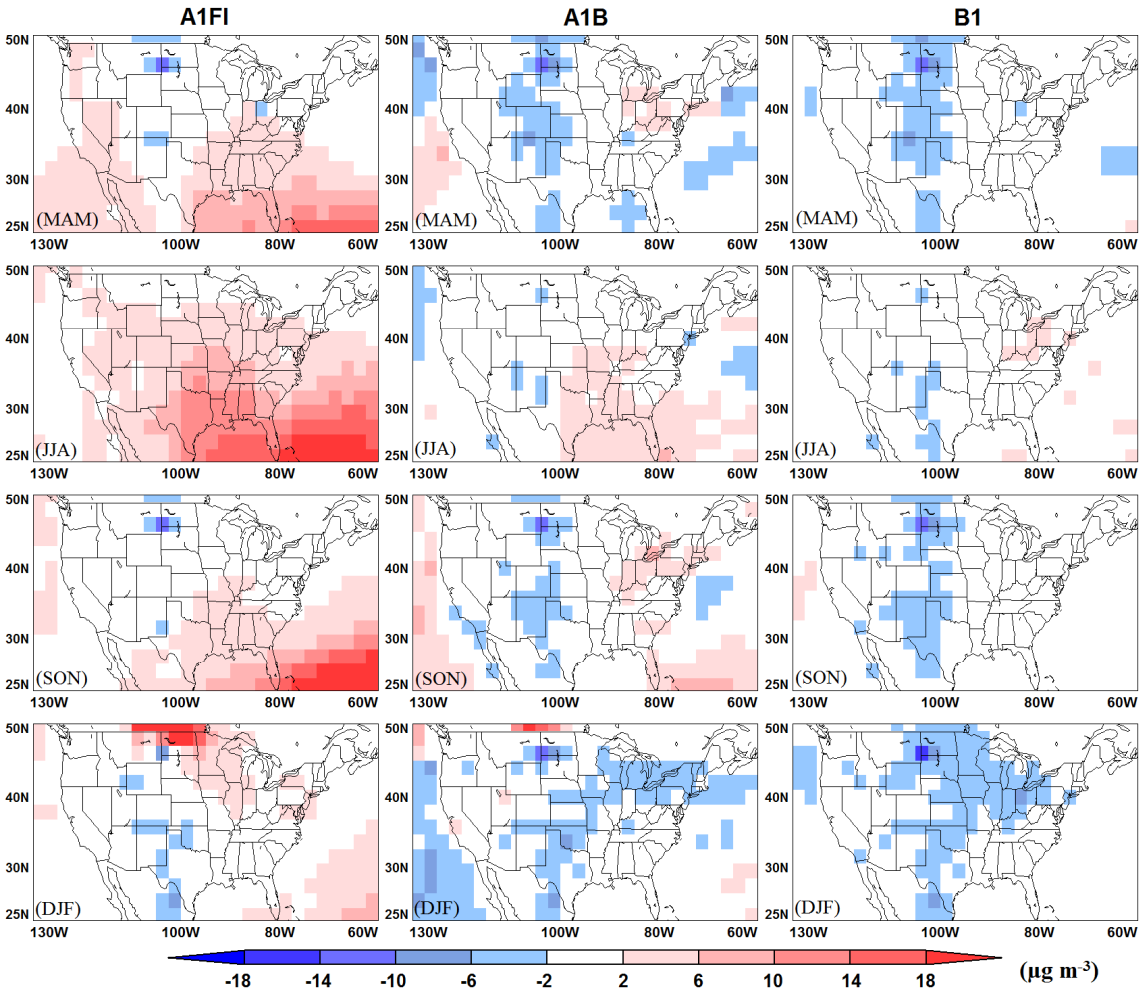

Figure 5.8. Projected change in U.S. surface-level PM10 concentrations due to changes in climate alone from the present day (1998-2002) to the future (2048-2052) following the IPCC A1FI, A1B, and B1 scenarios. Anthropogenic emissions are held at present-day values, but natural emission may change in response to climate change.

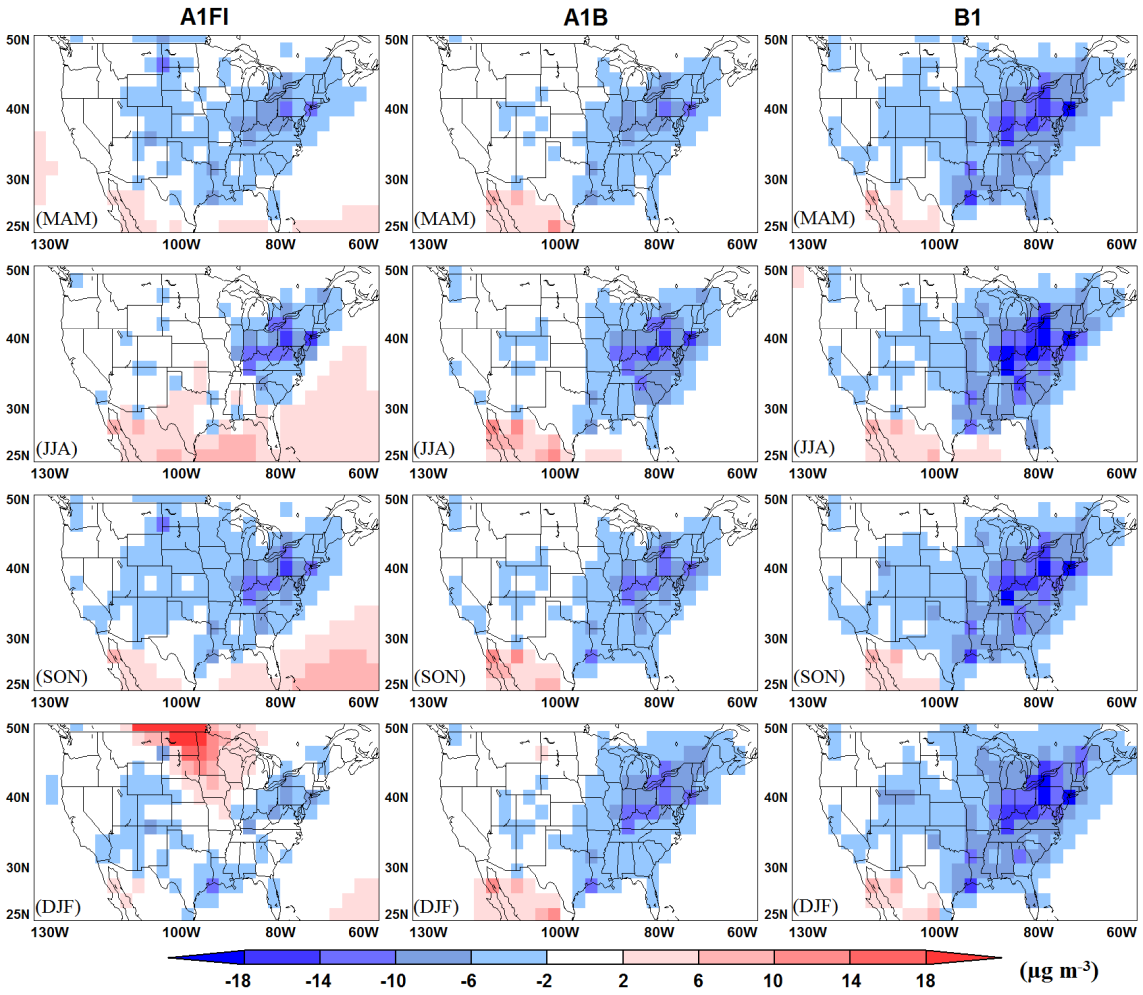

Figure 5.9. Projected change in U.S. surface-level PM2.5 concentrations due to changes in climate and emissions together from the present day (1998-2002) to the future (2048-2052) following the IPCC A1FI, A1B, and B1 scenarios. Both climate and anthropogenic emissions are projected for the future.

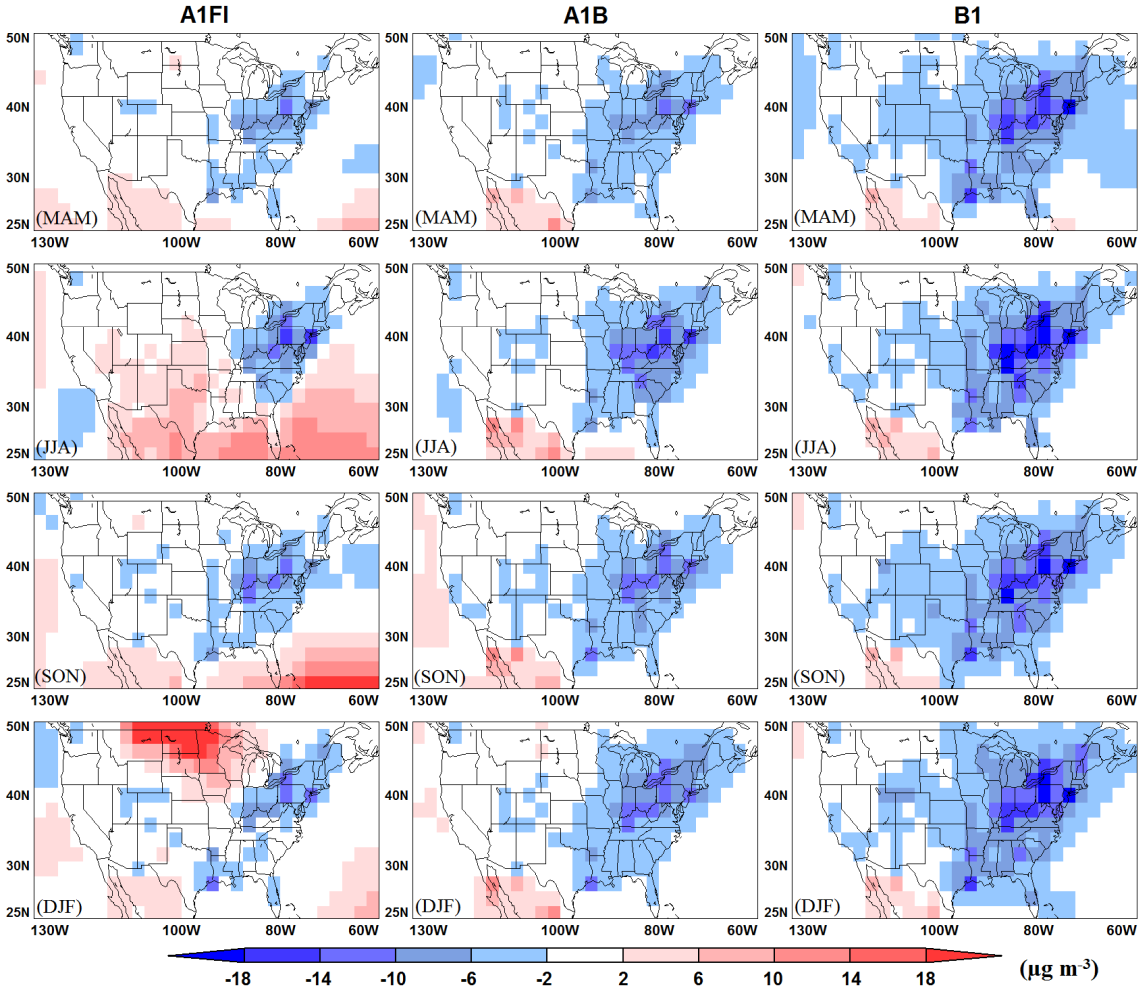

Figure 5.10. Projected change in U.S. surface-level PM10 concentrations due to changes in climate and emissions together from the present day (1998-2002) to the future (2048-2052) following the IPCC A1FI, A1B, and B1 scenarios. Both climate and anthropogenic emissions are projected for the future.

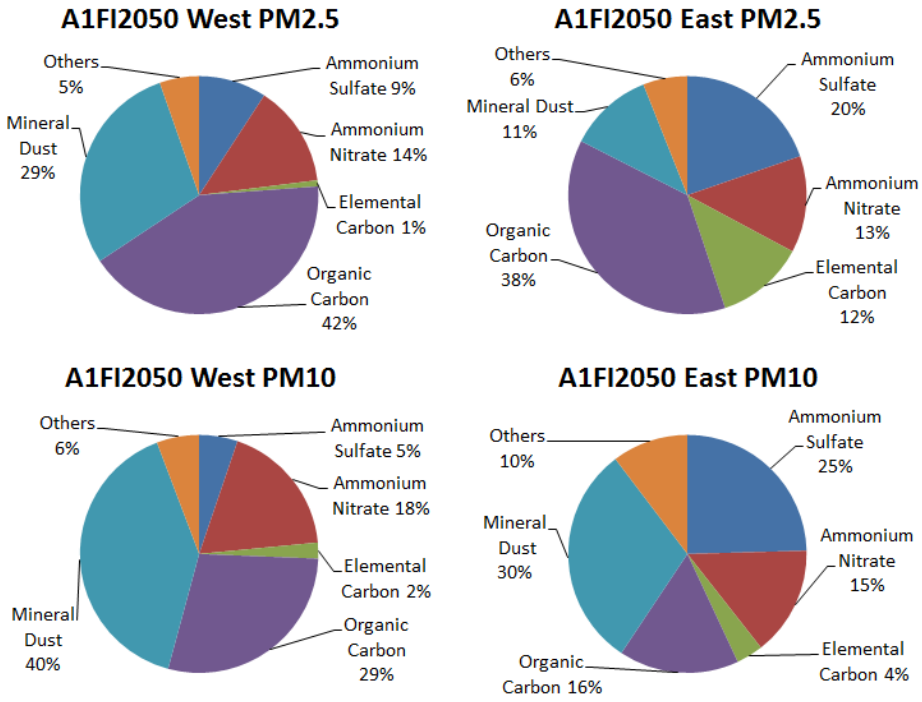

Figure 5.11. Annual averaged percentage of PM composition by component over the western and eastern United States regions for 2050 under the A1FI scenario.

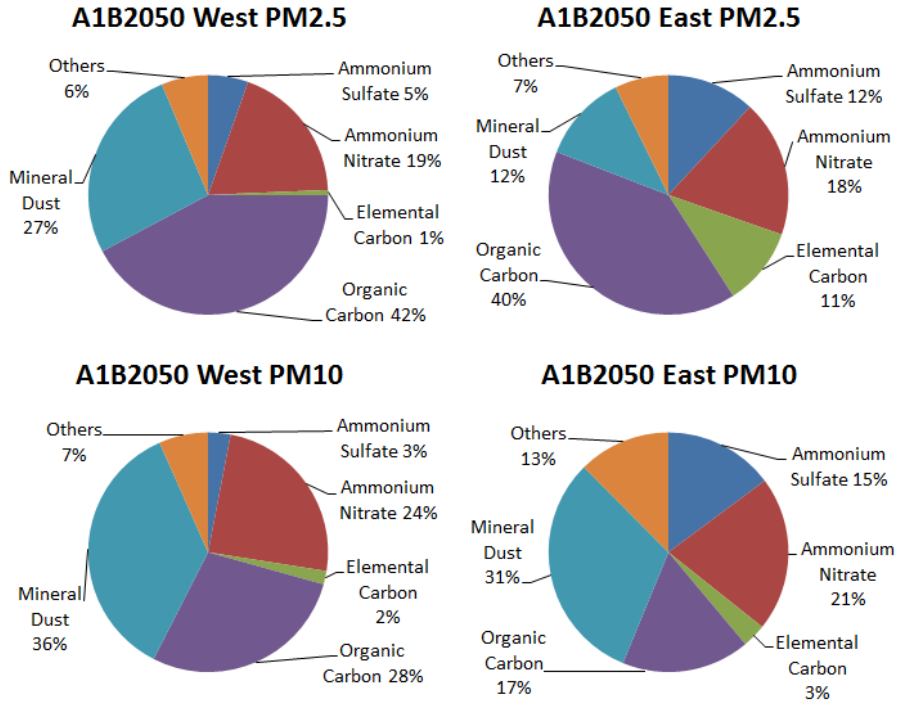

Figure 5.12. Annual averaged percentage of PM compositions by component over the western and eastern United States for 2050 under the A1B scenario.

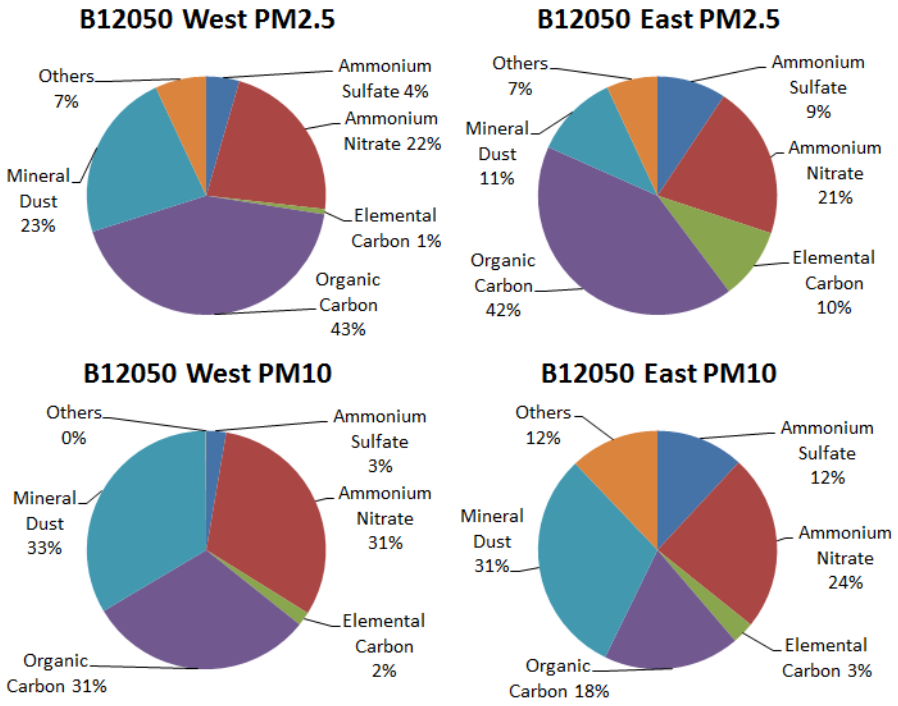

Figure 5.13. Annual averaged percentage of PM compositions by component over the western and eastern United States for 2050 under the B1 scenario.

CHAPTER 6: CHEMICAL COMPETITION BETWEEN NITRATE AND SULFATE

6.1. Introduction

Nitrate (NO_3^-), ammonium (NH_4^+), and sulfate (SO_4^{2-}) are important constituents of particulate matter (PM). As secondary inorganic aerosols (SIA), they form mainly from gas-phase precursors which are mostly industrial emissions. Secondary inorganic aerosols have been listed as the major pollutants in air quality standard [EPA, 2008]. The direct strategy to reduce the level of SIA is to control the industrial emissions of precursors. This may be an effective method overall to reduce pollution, but it may not work for nitrate aerosols. Future projections of global sulfate-ammonium-nitrate level under the IPCC AIFI, A1B and B1 scenarios show that changes in nitrate aerosol levels do not follow a linear relationship with changes in precursor emissions [Liang et al., 2009]. Some opposite relationships between concentration and precursor emissions are also found (e.g., nitrate increase in response to emission reduction) [Pye et al, 2009].

A hypothesis to explain these results is that nitrate aerosol levels are not only determined by its precursors, but are also affected by sulfate aerosol levels. Nitrate and sulfate aerosol concentrations are also connected by ammonia (NH_3) in aerosol production. Most nitrate and sulfate aerosols form from reactions of their precursors but are influenced by the presence of ammonia [Dawson et al., 2007; Liao et al., 2006; Aw and Kleeman, 2003; Rae et al., 2007]. In the real atmosphere, the ammonia concentration is not abundant enough to react with all precursors. As a result, nitrate and sulfate precursors compete for ammonia. Under ambient atmospheric conditions, ammonia gas

reacts with sulfuric acid in preference to nitric acid [Seinfeld et al., 1998]. On the aerosol chemistry, the equilibrium constant in sulfate aerosol formation ($(2NH_3(g)+H_2SO_4(g)\leftrightarrow(NH_4)_2SO_4(s)$; $k_1=4.29\times10^{37}atm^{-2}$) is much larger than that in nitrate aerosol formation ($(NH_3(g)+HNO_3(g)\leftrightarrow NH_4NO_3(s)$; $k_2=3.35\times10^{16}\ atm^{-2}$). The amount of available ammonia for ammonium nitrate formation is affected by the consumption in sulfate production. Therefore, projections of future aerosol level change under different emissions scenarios cannot be linearly extrapolated.

In this study, to test the hypothesis and evaluate its function in the atmosphere, a series of sensitivity experiments using the Community Atmospheric Model with chemistry version 3 (CAM-Chem) to analyze the changes of nitrate aerosol levels in response to changes of precursor emissions. The significance and effect of this mechanism on air quality projections are also discussed.

6.2. Method

The chemical competition between nitrate and sulfate formation can be seen from Table 1, which include the major reactions and their equilibrium constants for nitrate and sulfate aerosol formations. Whether the formation of aerosols is in solid or aqueous phase, the equilibrium constants for sulfate formation are larger than that for nitrate. That implies that the reactions between sulfate precursors and ammonia are preferred in a mixing environment including nitrate precursors. This simple fact results in both sulfate and nitrate precursors competing for ammonia that is usually limited in the atmosphere. If only the chemistry is considered, the result for the competition is always that the available ammonia for nitrate formation is equal to the concentration of total ammonia

minus the doubled concentrations of sulfate precursors. However, the formation of nitrate and sulfate aerosols is also affected by environmental factors including temperature, humidity, and solar radiation. Therefore, the competition becomes complicated and the resulting effect on nitrate aerosol concentrations can be very significant.

In order to examine the effect of competition between nitrate and sulfate on nitrate particle concentrations, a series of sensitivity experiments are designed to test the sensitivity of aerosol levels to sulfate precursor emission change. The three runs include a 50% reduction, a 80% reduction and a 90% reduction of SOx emission runs. The U.S. air quality in 2050 is projected using the present climate and 2050 emissions in order to examine the nitrate concentration change in response to precursor emission changes.

Since the hypothesis is supposed to be effective in industrial regions, a sensitivity area in the industrial region of the eastern United States is defined to analyze the changes in aerosol levels. Detailed definitions are given in Figure 6.1. The reductions of the precursor emissions in sensitivity experiments are made over the whole global area, which will prevent the changes in the relative emission gradient among each region and it caused changes in relative contributions to the sensitivity region. For example, if the reduction were not uniform over the globe, the gradients of aerosol precursors among remote regions would change. The relative contributions to precursor concentrations over a given area would then change as a result of changes in long range transport.

The meteorology data for driving the CAM-Chem model are from the Community Climate System Model version 3 (CCSM3) for the model period approximating 1999 to 2001. For the future air quality projections, the present CCSM3 meteorology and projected anthropogenic emissions in 2050 under the IPCC A1B scenario are used. The

6-hours interval meteorology fields are interpolated to a horizontal resolution of 1.9° latitude by 2.5° longitude and 26 vertical levels extending up to 0.01 hPa to meet the model requiremtns. All of the sensitivity experiments and simulations are performed following a 1-year spin up. The results used in the following analysis are for an average over the three years.

6.3. Nitrate concentration change in response to SOx emission

Figure 6.2 shows the average monthly variation of sulfate/nitrate/ammonium concentrations over the eastern region for the three sensitivity experiments. The time series of changes in monthly concentrations reflect the seasonality in the concentration-emission correlation. The sulfate concentrations show a gradually increasing trend as a response to SOx emissions increase. The sulfate concentrations in summer for the three experiments have good linearity compared to the SOx emissions. As air temperature decreases, the linearity in sulfate concentrations compared to precursor emission levels becomes less distinct in the Fall and Spring. In winter, sulfate concentrations almost do not change. That means sulfate aerosol production is largely affected by air temperature. This is caused by the chemical process of converting sulfides into sulfate acid, a process which requires sunlight and water vapor. These elements are more prevalent in the North American Summer, and so we see peak levels in June, July, and August. The trend shows that the average monthly sulfate concentrations have a positive correlation with SOx emissions. But the average monthly nitrate concentrations and changes in SOx emissions are anti-correlated. In Winter, the sulfate concentrations decrease and still have a positive correlation with SOx emissions. Monthly ammonium concentrations show a similar trend

to sulfate variations found in Summer, indicating that sulfate is the main consumer for ammonia in the Summer. However, the changes in nitrate concentrations are not clearly understood from Figure 6.2 due to the large difference between changes in nitrate and sulfate. The change in nitrate is sizeable in the Summer, but the change in Winter is relatively small. The relatively small change in nitrate concentrations is mainly caused by low sulfate concentrations in Winter.

To better examine the competing mechanisms, changes in nitrate and sulfate concentrations are scaled in Figure 6.3 assuming a linear relationship. If the changes in sulfate or nitrate concentration are only caused by reducing SOx emissions, the changes in concentrations must be linearly parallel to the emissions reduction. To test the assumption, the decrease in sulfate concentration and increase in nitrate concentration are scaled to have the same emission reduction level. If the scaled results are the same, the linear relationship is proved to be very good. Figure 6.3 shows the resulting scaled decrease in monthly mean surface sulfate concentrations and increase in monthly mean nitrate concentrations over the industrial area from the three experiments. The increase in sulfate concentrations shows a near linearity correlation with emission reductions during the whole year. Although the scaled changes in Summer do not match as well as in other seasons, a difference of 0.2 $\mu g/m^3$ does not affect the linear assumption if considering the model bias. The largest sulfate concentration decrease occurs in Summer. That indicates that the maximum sulfate conversion rate occurs in the summer. In Wnter, the nitrate concentration change shows a strong linear correlation to SOx emissions change. The linear correlation indicates that sulfate chemistry has direct effects on the nitrate aerosol formation in Winter. However, the increase in nitrate concentration shows a small

conversion rate for nitrate precursors during Summer and a nonlinear correlation in response to sulfate precursor emissions change.

According to the equilibrium constant values, the production of sulfate aerosols (much larger equilibrium constant) is higher than that of nitrate in all seasons. However, the equilibrium dissociation constant of ammonium nitrate aerosols changes with the fraction of sulfate [Seinfeld et al., 1999]. The less sulfuric acid is included, the more ammonium nitrate that is present. Moreover, humidity is also an important factor that affects the dissociation. The higher the environmental humidity, the easier that nitrate forms [Seinfeld et a., 1999]. As a result, the most abundant amounts of nitrate aerosols are produced when the sulfate precursors have a 90% reduction, and the least are produced for the 50% reduction case. This effect is found in Summer when the humidity is larger than it is in Winter.

We also conduct sensitivity experiments with 50% and 25% reduction in NOx emissions to evaluate the response on the concentrations of sulfate and nitrate (not shown). Neither the nitrate nor the sulfate shows a linear response to the NOx emission perturbation. The reason is that the sulfate aerosol production is not affected by the changes in nitrate precursor emissions because of the priority in reactions with ammonia. For nitrate aerosols, the NOx is the precursor for nitrate as well as for ozone. So, the conversion from changes in NOx emissions to changes in nitrate aerosols is affected by the production of ozone. As a result of all these effects, the change in nitrate concentration may present a high nonlinear characteristic in response to precursor emission perturbations.

6.4. Nitrate concentration change in 2050

In order to examine the effect of competition on future aerosol concentration projection, two experiments both using present day meteorology, and separately using either present day aerosol precursor emissions or projected emissions for 2050 under the IPCC SRES A1B scenario are employed. Keeping the same meteorology is to remove the effect of climate change.

Figure 6.4 shows the surface nitrate concentration change in Winter and Summer by changing the anthropogenic emissions for present day to the projected emission for 2050 following the IPCC SRES A1B scenario. A small nitrate concentration decrease is determined over the central United States. This means that nitrate/sulfate/ammonium chemistry there is not the ammonia limited type. There is a large increase in nitrate concentrations over the eastern United States in Winter. The nitrate concentrations in Summer slightly increase over this region, the main industrial region of the United States and major anthropogenic emissions of nitrate and sulfate precursors occur in this area. Table 6.1 shows the anthropogenic emissions projection for the United States in 2050 following the IPCC A1B scenario. The anthropogenic emissions of nitrate precursors (NOx) is reduced by around 37%. However, the nitrate concentration increased as a response to this reduction. This is caused by the competition between nitrate and sulfate formation. It is noted that the anthropogenic emission of sulfate precursors over the United States is reduced by around 75%, and the ammonia emission increases by about 57%, resulting in more ammonia being available for nitrate aerosol formation.

6.5. Summary and Discussion

The competition for ammonia between nitrate and sulfate aerosol formations significantly changes the concentration-precursor emission relationship for nitrate. Sensitivity experiments with reductions in sulfate precursor emissions in CAM-Chem show that changes in nitrate concentration linearly correlate to sulfate precursor reductions in Winter. Therefore, the nitrate concentration in Winter shows a nonlinear correlation to precursor emissions. Nitrate concentration changes in Summer shows a weak linear response to changes in sulfate precursor emissions because of the effect of humidity and sulfate concentrations on nitrate aerosol formation.

The concentration-precursor emission relationship for sulfate is not significantly affected by the competition with nitrate. Changes in sulfate concentrations show very good linear correlation with changes in precursor emissions in SOx emission reduction experiments and little correlation with changes in nitrate precursor emissions in NOx emission reduction experiments.

The emission change experiment following the IPCC A1B emission change scenario shows that surface nitrate concentration in the major industrial region will increase by 2050, although the nitrate precursor emission will reduce to 63% of present-day level. The reduction in sulfate precursor emissions and increase in ammonia emissions lead to the converse change in nitrate concentrations in response to its precursor emissions perturbations through this competition mechanism. That indicates the future emission control strategy may not effective to reduce the aerosol pollution in industrial regions.

Nitrate production is affected by many processes, including the sulfate aerosol production, ozone production and processes that affect the atmospheric ammonia. In

addition, environmental factors can also affect nitrate production. Therefore, the nitrate concentration changes can be very complicated, likely requiring further study.

Table 6.1. Equilibrium constants for formation of nitrate-sulfate aerosols at 298K [Seinfeld et al., 1999].

Reactions	***Equilibrium Constants***
1. $2NH_3(g)+H_2SO_4(g)\leftrightarrow(NH_4)_2SO_4(s)$	$k_1=4.29\times10^{37}atm^{-2}$
2. $NH_3(g)+HNO_3(g)\leftrightarrow NH_4NO_3(s)$	$k_2=3.35\times10^{16}\ atm^{-2}$
3. $2NH_3(g)+H_2SO_4(g)\leftrightarrow(NH_4)_2SO_4(aq)$	$k_3=3.82\times10^{37}atm^{-2}$
4. $NH_3(g)+HNO_3(g)\leftrightarrow NH_4NO_3(aq)$	$k_4=3.69\times10^{17}\ atm^{-2}$

Table 6.2. Present-day and 2050 projected (A1B) global emissions of aerosol precursors used in this study.

Species		**2000**	**2050**
NO_x (Tg N/yr)	Anthropogenic	6.11	3.88
	Natural	0.11	0.15
NH_3 (Tg N/yr)	Anthropogenic	2.11	3.31
	Natural	0.81	0.79
SO_2 (Tg S/yr)	Anthropogenic	9.24	2.35
	Natural	0.09	0.11
SO_4 (Tg S/yr)	Anthropogenic	0.16	0.04

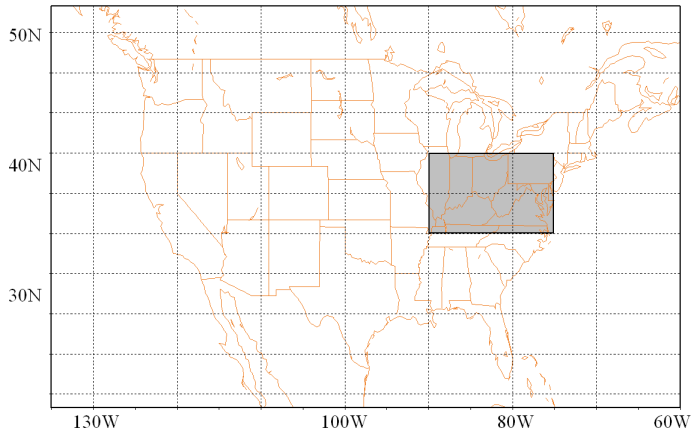

Figure 6.1. The shaded rectangle region is the sensitive region used for analysis. Surface aerosol concentrations are averaged over this area.

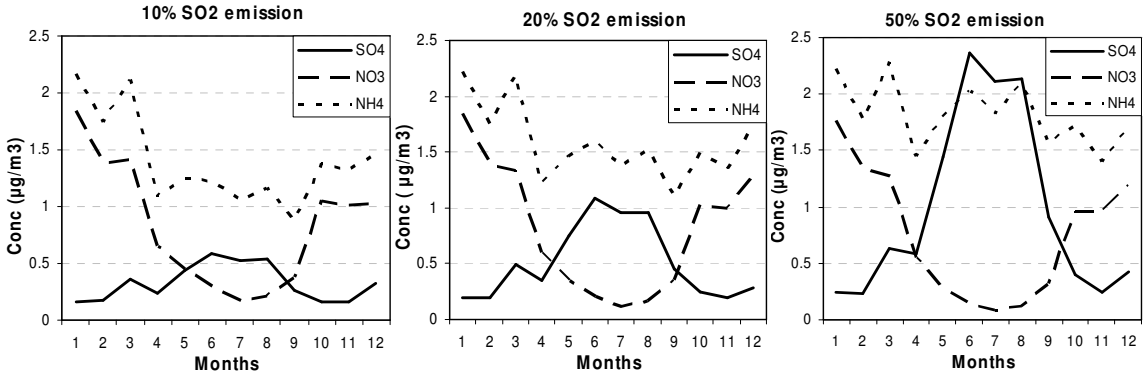

Figure 6.2. Monthly change in average SO_4^{-2}, NO_3^-, NH_4^+ level in sensitivity study area

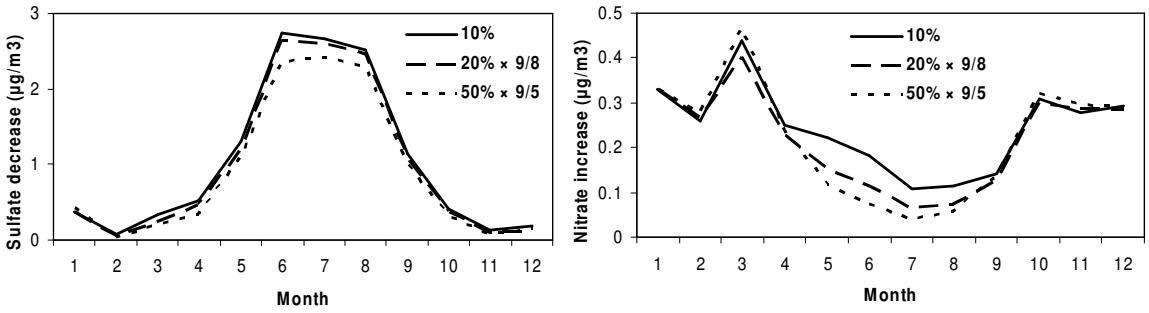

Figure 6.3. Decrease of sulfate and increase of nitrate in monthly mean surface nitrate/sulfate concentrations over sensitivity region resulting from reductions in emissions of SOx. (Solid line denotes the perturbations due to 10% of the present day's emission, long dashed lines represent 9/8 times the perturbations due to 20% of the present day's emission, dot dashed lines represent 9/5 times the perturbations due to 50% of the present day's emission.)

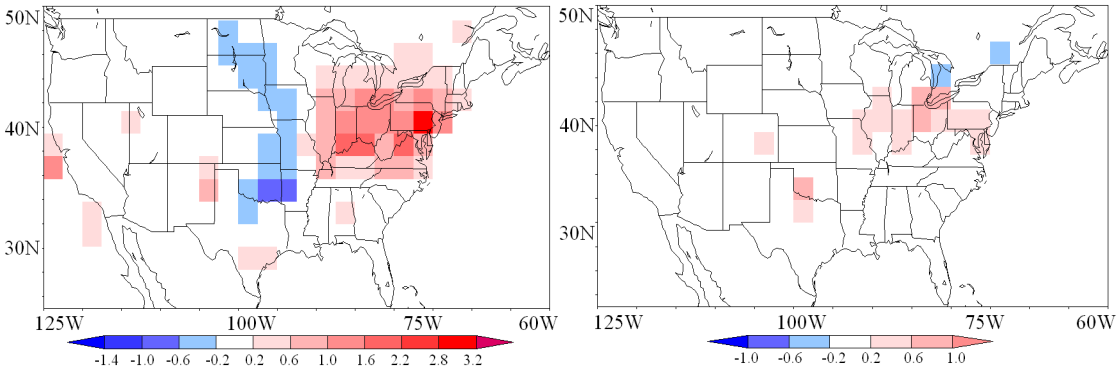

Figure 6.4. Change in surface nitrate aerosol concentration caused by the anthropogenic emission change from present day level to 2050 level projected following IPCC SRES A1B scenario. Winter (left); Summer (right) (Unit: $\mu g/m^3$)

CHAPTER 7: MODEL ANALYSES OF ATMOSPHERIC MERCURY: PRESENT AIR QUALITY AND EFFECTS OF TRANSPACIFIC TRANSPORT ON U.S.

7.1. Introduction

Mercury is a toxic pollutant, having harmful effects on human health and ecosystems. United States and many other countries have listed mercury as a major air pollutant that requires regulatory control (e.g., U.S. Clean Air Act, 1994; EMEP, 2001). Mercury is emitted into the air in forms of elemental mercury (Hg0), reactive mercury (HgII) and particulate mercury (HgP). Elemental mercury accounts for more than 90% of total atmospheric mercury and is the dominant form [Schroeder and Munthe, 1998]. Its atmospheric lifetime (several months) is long enough for global-scale transport. As such, mercury is a global air pollutant and it is difficult to attribute the relative importance of its local and/or remote emissions sources. To facilitate the attribution and project the life cycle of mercury, it is imperative to develop a credible model that incorporates the relevant global emission, transport, and deposition processes as well as represents the key atmospheric chemistry.

The NCAR Community Atmospheric Model with Chemistry (CAM-Chem) has been developed with advanced representations of dynamical, physical, and chemical processes; it serves as a powerful tool for investigating global air quality and climate interactions [Lamarque et al., 2005; 2011; Heald et al., 2006; Pfister et al., 2008]. The CAM-Chem model, however, does not normally include the chemical and physical processes necessary to simulating the atmospheric and surface mercury distributions. Therefore, this study is aimed at developing and incorporating into the CAM-Chem

model an advanced mercury module based on the best available numerical representations of all processes essential to the mercury lifecycle.

The mercury chemistry used in the model is discussed in the next section; this mechanism is based on well understood and tested reactions found in the peer-reviewed literature. Ozone and OH are the main global oxidants for elemental mercury [Lin et al., 2006]. This mechanism and reaction rates have been examined in many air quality studies [Bullock et al., 2002; Calvert and Lindberg, 2005; Selin et al., 2006, 2007]. Halogens are another important oxidant for Hg in both the gaseous and aqueous phases [Holmes et al., 2006; Lin et al., 2006]. Reactions with these oxidants transform Hg into a form subject to deposition through both wet and dry processes. Aqueous-phase reduction of Hg(II) has been observed to be important for mercury transformation [Pehkonen and Lin, 1998] and has been verified through testing in recent modeling studies [Bullock et al., 2002; Selin et al., 2007]. All of these and other well-understood redox reactions with mercury are incorporated and coupled with the corresponding physical processes in the CAM-Chem.

A major challenge for modeling mercury is to obtain a well characterized evaluation of global emissions. The current emission inventory datasets are known to contain substantial uncertainties [Pacyna et al., 2005; Street et al., 2009]. Anthropogenic sources take up a quarter of the current mercury emissions. These include coal-fired power production, metal smelting, and waste incineration [Pacyna et al., 2005; Streets et al., 2005; Mason and Sheu, 2002]. All of these sources are highly variable and total source rates are not well known, causing large uncertainties in estimating their emission inventories. Natural sources include fluxes from water bodies, soil, terrestrial vegetation, volcanic eruptions, and biomass burning. The difficulty in estimating natural emissions is

to represent the surface fluxes in response to meteorological and physical conditions [Poissant and Casimir, 1998; Zhang et al., 2001]. We account for spatial and temporal variability of all three types of mercury (Hg0, HgII, HgP) emitted and re-emitted from various sources over both land and oceans by modifying two dynamic parameterization models [Liss and Slater, 1974; Zhang et al., 2001; Wängberg et al., 2001].

The expanded CAM-Chem with the mercury mechanism simulates the atmospheric pathways of all forms of mercury from their source emissions to eventual deposition back to land and water surfaces through both wet and dry atmospheric processes across a wide range of spatial and temporal scales. The viability of the model, hereafter called CAM-Chem/Hg, is carefully evaluated. Recent intercomparison studies have shown that large differences in modeled results over North America are caused mainly by inconsistent treatments of meteorological and physical processes affecting Hg transport and transformation [Bullock et al., 2008, 2009]. Here we evaluate the CAM-Chem/Hg model performance based on multi-year simulations driven by representative meteorological conditions from global observational reanalysis. The results are compared against the best-available observations for surface mercury concentration and wet deposition, including data from the National Atmospheric Deposition Program (NADP) [Lindberg and Vermette, 1995; Vermette et al., 1995], major networks in Europe (EMEP) and Canada (CAMNet), as well others from the published literature [Friedli et al., 2004; Kock et al., 2005]. The CAM-Chem/Hg model is then used to evaluate the contributions of transpacific transport and domestic anthropogenic emissions to U.S. mercury concentrations.

7.2. Model Formulation

7.2.1. Method

This study adopts anthropogenic emissions mostly from the POET (Precursors of Ozone and their Effects in the Troposphere) database for 2000 [Granier et al., 2005; Olivier et al., 2003], including those of fossil fuel and biofuel combustion based on the EDGAR-3 inventory [Olivier and Berdowski, 2001]. Biogenic emissions of isoprene and monoterpenes, and NO emissions from soil and lightning, are calculated online using the Model of Emissions of Gases and Aerosols from Nature (MEGAN) [Guenther et al., 2006] as implemented by Pfister et al. [2008]. Biomass burning emissions are taken from the Global Fire Emissions Database version 2 (GFED-v2), with monthly average data available for 1997–2007 [van der Werf et al., 2006].

For evaluation relative to observations, the CAM-Chem simulation for the period 1998–2001 is driven by meteorological fields from the NCEP/DOE AMIP II reanalysis [Kanamitsu et al., 2002], including winds, mixed-layer depths, temperature, precipitation, and convective mass fluxes. These data are available at a 6-hour interval and a grid spacing of 1.9° × 2.5° and 26 hybrid sigma-pressure levels. The initial year 1998 is considered as a spin-up. The subsequent analyses focus mainly on the statistics for 2000, and also the average of 1999-2001, to compare against respective observations.

7.2.2. Mercury Chemistry

The mercury chemistry considers major pathways in both gas and aqueous phases. The gas-phase reactions include the oxidation of Hg0 to HgII by OH, ozone and chlorine [Hall, 1995; Sommar et al., 2001; Calhoun and Prestbo, 2001; Pal and Ariya, 2004].

Table 7.1 lists the detailed Hg chemical reactions and their rate constants. These reactions have been used in other mercury simulations and tested in laboratories [Lin and Pehkonen, 1997; Van Loon et al., 2000; Gbor et al., 2006]. The gaseous reactions produce reactive gaseous mercury (RGM, gaseous HgII compounds) that is very soluble in water (with a Henry's Law constant of 1.4×10^{6} M atm^{-1}), and thus dissolves to Hg^{2+} in aqueous aerosols and clouds [Pleijel and Munthe, 1995; Schroeder and Munthe, 1998]. In the aqueous phase, the reduction of Hg^{2+} into Hg^{0} has been proved to be important in laboratory studies [Pehkonen and Lin, 1998; Lin et al, 2003]. The transformation from Hg^{2+} to Hg^{0} can be achieved through photochemical reactions or reactions with SO_3^{2-} /HO_2. Since the solubility of Hg^{0} is relatively low (with a Henry's Law constant of 1.1×10^{-1} M atm^{-1}), the oxidation of Hg^{0} based on the dissolution of gaseous elemental mercury may not be significant. However, the main aqueous oxidation mechanisms included in Table 7.1 can be important for the mercury chemical equilibrium when considering the reduction of Hg^{2+}.

7.2.3. Mercury Deposition

The treatment for wet deposition of Hg0, RGM and HgP follows that for all other aqueous pollutants resolved in the standard CAM-Chem. It is based on the formulation of Brasseur et al. [1998], considering the solution scavenging and incorporating the main parameterization introduced by Giorgi and Chameides [1985]. The wet deposition treatment includes rainout and washout from resolvable and convective precipitation, and scavenging in convective updrafts [Liu et al., 2001]. The aqueous concentration of Hg^{0} is

low relative to the total dissolved Hg^{2+}, and thus its wet deposition is minor compared to that of HgII and HgP.

The treatment for dry deposition of mercury species also follows that for other chemicals in the standard CAM-Chem. Some previous studies neglected dry deposition of Hg0 due to the rapid reemission from the ground [Bullock et al., 2002; Selin et al., 2008]. In CAM-Chem, the rapid reemission of mercury from the land has been considered into the land emission inventory and does not need to be compensated for by dry deposition. Therefore, we determine the dry deposition velocities of Hg0 online in the model, based on the resistance-based parameterization of Wesely [Walmsley and Wesely, 1996; Wesely and Hicks, 2000]. Dry deposition of HgII and HgP is simulated with the scheme based on local surface type and turbulence [Wang et al., 1998; Wesely, 1989].

7.2.4. Mercury Emissions

Anthropogenic sources contribute about a quarter of the current mercury emissions. These include major industrial emitters from coal-fired power production, mining, metal smelting, and waste incineration [Streets et al., 2005; Mason and Sheu, 2002]. Here we adopt the anthropogenic emissions in 2000 from the Global Emission Inventory Activity (GEIA) [Pacyna et al., 2006].

Land sources include emissions from soil and vegetation, plus rapid reemissions of deposited mercury. Soil and vegetation contribute about 500-1800 Mg yr^{-1} [Lindqvist, 1991; Seigneur et al, 2001; Selin et al., 2007], while reemissions range in 260-1500 Mg yr^{-1} [Selin et al., 2008; Nicole et al., 2010], with their total estimate of 1100-3000 Mg yr^{-1}. Land emissions depend on both soil temperature [Lindberg et al., 1995; Poissant and Casimir, 1998] and surface solar radiation [Carpi and Lindberg, 1998; Zhang et al. 2001;

Gustin et al., 2002]. Land mercury emissions are calculated using local temperature, solar flux, and estimated source distribution. The emission flux (F_1) is distributed over the globe according to the locations of mercury industries [Frank, 1999]. It is then adjusted using the relationship suggested by Zhang et al. [2001] and Poissant and Casimir [1998]:

$$F_2 = F_1 \exp[-1.1\times10^4 (1/T_s - 1/T_0)] \exp[1.1\times10^3 (R_s - R_0)]$$

where F_2 is the calculated land emission flux. R_s is the surface solar radiation flux and T_s is the local surface skin temperature. The reference value is 340 Wm^{-2} for R_0 and 288 K for T_0. The parameterization is subject to calibration using the 1995-2005 monthly mean R_s and T_s distributions from the NECP reanalysis to constrain the global annual total emission of 2900 Mg yr^{-1} estimated for 2000 [Nicole et al., 2010].

Ocean emissions are determined by a simplified air-sea exchange scheme that has been tested through field campaigns for good agreement with observations [Liss and Slater, 1974; Wängberg et al., 2001]. We estimate monthly mean mercury concentrations in surface oceans through the following scheme that also removes the dependence on the mercury storage in deep oceans:

$$F = K_w (C_w - C_a / H')$$

where F is the ocean emission flux of mercury, H'=[Hg]g/[Hg]aq is the dimensionless Henry's-Law constant calculated at water temperatures (T_w) [Clever et al., 1985], K_w is the gas transfer velocity of a species in the water-air interface based on the empirical relation of Wanninkhof [1992], and C_w and C_a are respectively the Hg0 concentration in the mixed-layer ocean (pg/L) and in the surface atmosphere (ng/m^3). C_w is simplified by using the monthly mean concentration data [Soerensen et al., 2010], while C_a is determined by the atmospheric model.

Biomass burning emissions are specified as monthly means from the IPCC estimate of biomass burned and the IMAGE projection of managed forests for a typical year. The approach and emission factors depending on vegetation types are adopted from Streets et al. [2009].

Volcanic emissions of mercury are based on those of sulfur in the GEIA inventory. The method uses a typical ratio of Hg relative to SO_2 volcanic emissions to estimate mercury from sulfur emissions. A similar method has been used in previous studies [Ferrara et al., 2000; Nriagu et al., 2003; Pyle and Mather, 2003]. Here we adopt a Hg/SO_2 ratio of 1.5×10^{-7} for all volcanic eruptions.

7.2.5 Global Budget

Figure 7.1 summarizes the partitions of global mercury emissions in 2000 among different sources. The total human-related emission assumed is 2270 Mg yr^{-1}, where Hg0, HgII, and HgP account for respectively 1300, 720, and 250 Mg yr^{-1}. The total natural emission source is 2900 Mg yr^{-1} over land (soil and vegetation), and 3400 Mg yr^{-1} over the oceans. The total emission estimate from biomass burning is 602 Mg yr^{-1}, and 500 Mg yr^{-1} from volcanic eruptions. Thus, the oceans are the largest contributor, followed by natural land emissions and the human-related emissions. However, the oceanic flux per unit area is small as the total emissions are distributed over 72% of the Earth's surface. In contrast, the average emission flux over land is much larger when counting the natural, anthropogenic, and biomass burning emissions together.

Our estimate of global total emissions from all sources is about 9680 Mg yr^{-1}. This falls in the middle between the values of 6200 and 11200 Mg yr^{-1} reported for the GEOS-Chem model [Selin et al., 2007, 2008]. However, our estimate for the ocean emissions is

notably larger than previously published values (3400 versus 2600 $\pm$ 300 Mg yr^{-1}). This reflects our inclusion of emissions from the mixed-layer ocean storage and the rapid reemissions from deposited mercury.

Dry and wet deposition of mercury are calculated separately, in contrast to the net removal rate (evasion) considered in some studies [e.g., Bullock et al., 2008, 2009]. In the Earth's surface, total deposition is around 8800 Mg yr^{-1}. About 61% of the total deposition occurs over the ocean, and 39% over the land. Dry deposition accounts for 70% of the total. Over land, total deposition is 1800 Mg yr^{-1} for HgII, 1600 Mg yr^{-1} for Hg0, and 600 Mg yr^{-1} for HgP. The oceans are a net sink for atmospheric mercury, taking up approximate 2000 Mg yr^{-1}, balancing a portion of the human-related and volcanic sources.

Mercury in the CAM-Chem/Hg model has a lifetime of 0.69 years in the atmosphere against deposition. All mercury species are considered together, and deposition is the only sink for total mercury in the model. Our derived lifetime of mercury agrees well with the estimated lifetime of 0.5 to 0.79 years determined in the GEOS-Chem model studies [Selin et al., 2007, 2008]. Previous studies had estimated the lifetime at 1.0 to 1.7 years [Bergan et al., 1999; Shia et al., 1999; Seigneur et al., 2001; and Lamborg et al., 2002]. The shorter lifetime in the more recent studies may result from modeling approaches where the processes of deposition and reemission are treated separately.

7.3. Global Mercury Distribution

Figure 7.2 shows the annual mean surface air concentrations of total gaseous mercury (TGM) averaged over the 1999-2001 time period as simulated by the CAM-Chem/Hg model using the emission estimates for 2000. The TGM is taken as the sum of gaseous Hg0 and gaseous HgII. The major characteristic is that the mercury concentrations are greatest over land and coastal regions. The most-polluted area occurs in Asia, where strong surface TGM concentrations are derived along the continent boundaries. In particular, the concentrations across the Middle East, India, China, and Japan are above 3 ng/m^3. The second most-polluted area is southern Africa, where high mercury emissions result from intensive development of mercury-related industries, especially mining. Mining in Australia also results in a heavy polluted area along the southeast coast. These areas of heavy mercury pollution are identified with high human-related emissions over land. In contrast, the Antarctic pollution is low because of little human-related emissions. On the other hand, the high concentrations along Chile and the eastern coast of the South Pacific are associated with large natural emissions from the oceans that are accelerated by warm sea surface temperatures in those locations. The high concentrations over the eastern coast of the South Atlantic are likely caused by transport of inland pollutants from South Africa under the prevailing easterly to northeasterly winds near the surface.

The derived CAM-Chem/Hg model results share a general similarity with previous modeling studies. For example, the interhemispheric TGM concentration ratios (Total integrated concentration in the northern hemisphere relative to that in the southern hemisphere) for surface air were estimated to range between 1.2 and 1.8 [Lamborg et al., 2002], without considering the heavy polluted East Asia. The CAM-Chem/Hg model

derived value is 1.68. The spatial pattern of TGM in our study also compares well with that from the GEOS-Chem model over the globe [Selin et al., 2007; Selin et al., 2008]. In particular, the concentrations over land are very close between the GEOS-Chem and CAM-Chem/Hg models, while their differences over oceans are largest in the Arctic, at around a difference of 0.2 ng/m^3. This disagreement may partially result from the use of different driving meteorological conditions that are important to mercury reactions and transport.

Table 7.2 compares the modeled 1999-2001 mean surface TGM concentrations with measurements at 19 nonurban land sites worldwide with varying periods between 1995 and 2007 [Selin et al., 2007]. The model captures the general spatial pattern of global mercury air pollution. The TGM concentrations agree well with observations at 16 out of the total 19 sites, where model biases are smaller than 0.2 ng/m^3. Larger biases occur at the Cape Point site in South Africa, where mining industry development dominates the regional mercury emissions, accounting for a quarter of the total global anthropogenic emissions [Pacyna et al., 2006]. The latest measurements indicate that the TGM concentration at the Cape point site is up to 1.51 ng/m^3, with its variability similar to that over the tropical Atlantic [Witt et al., 2010]. Our analyses show that the prevailing strong westerly winds in near surface layers bring cleaner marine air rather than inland polluted air to the Cape Point. Thus, this site is representative of pollution conditions more over the Southwest Atlantic than South Africa. On the other hand, the model simulates high TGM concentrations over East Asia, where mercury emissions are significant due to intensive industrial activities. The model using the 2000 emissions tends to underestimate the TGM concentrations at 4 Asian sites, as compared with more recent published

measurements. The model biases at these sites are less than 20% relative to the observations [Sakata and Marumoto, 2002; Kim et al., 2006; Wang et al., 2007; Yang et al., 2008].

Figure 7.3 illustrates the CAM-Chem/Hg model simulated zonally- and annually-averaged surface air TGM concentration variations for 1999-2001 compared to observations at various locations worldwide, including land stations [Ebinghaus et al., 2002; Baker et al., 2002; Sakata and Marumoto, 2002; Kellerhals et al., 2003; Weiss-Penzias et al., 2003; Environmental Canada 2003; Han et al., 2004; EMEP 2005; Kim et al., 2006; Wang et al., 2007; Liu et al., 2007; Yang et al., 2008] and ocean cruises [Selin et al., 2007; Temme et al., 2003; Laurier et al., 2003; Lamborg et al., 1999]. Note that these measurements are not necessarily representative of zonally- and annually-averaged conditions, but are used to depict the available variations with latitude. All of the land station data and corresponding CAM-Chem/Hg model values listed in Table 7.2 are also shown in Figure 7.3. In general, the model captures the major TGM characteristic variation with latitude, following the variation of mercury emission sources. In particular, two peak values occur in the northern and southern middle latitudes that correspond to the intensive sources from industrial and mining activities. Due to the scattered distribution pattern of mercury-emitting industries, the variations of zonally averaged TGM concentrations are very clear along the latitude with land fraction, but not significant around the latitude taken by oceans.

In comparison, the GEOS-Chem model simulates a range between 1.25 and 1.75 for zonal mean surface air TGM concentrations [Selin et al., 2007] with latitude. The CAM-Chem/Hg model values are larger than this at lower and middle latitudes, but smaller at

high latitudes. As explained by Selin et al. [2007], the Artic concentrations may be overestimated by the GEOS-Chem model due to missing halogen chemistry. The larger CAM-Chem/Hg model values in the northern middle latitudes are mainly attributed to high surface concentrations over East Asia as confirmed from observations. In contrast, the results for the southern middle latitudes may be overestimated by the CAM-Chem/Hg model due to uncertainties in the southern African emissions.

Figure 7.4 compares the CAM-Chem/Hg modeled Hg0 vertical distribution with that measured in the ACE-Asia aircraft campaign during April-May 2001 over Ontario, Japan [Friedli et al., 2004]. The measurements show a decrease of the mixing ratio from 2 ng m^{-3} near the surface to 1.25 ng m^{-3} at 2.5 km, a relatively small change from there to 6.5 km, and a sharper decrease to 0.6 ng m^{-3} at 7.5 km. The model result is close to observations within the boundary layer below 1.5 km and at 7.5 km. However, large discrepancies exist in middle layers between 2 and 7 km, where the model simulates a monotonic fast reduction to a constant 0.55 ng m^{-3} above 4.5 km. The observed enrichment in the middle layers may result from an occasional pollution influence [Friedli et al., 2004], or the enhanced high-altitude recycling of HgII by photolysis [Selin et al., 2007]. At present, the CAM-Chem/Hg model only considers the photochemical reduction of Hg(II) in the aqueous phase, which is mostly confined to the lower troposphere. This may partially explain the model underestimation.

Figure 7.5 compares the CAM-Chem/Hg modeled and observed seasonal variations of surface TGM concentrations at two coastal monitoring sites, Mace Head, Ireland and Zingst, Germany (see the location information in Table 7.2). These two sites have made continuous measurements, with well characterized accuracy and precision [Kock et al.,

2005]. The monthly means are averaged in 1998-2004 for the observations and in 1999-2001 for the model result. Both sites were observed to have TGM levels higher in winter than summer. This seasonality is captured by the CAM-Chem/Hg model. At Zingst, the model result is realistic during February-August, but underestimates observations by approximately 10% (0.2 ng m^{-3}) for the other months. Model underestimations of a similar magnitude occur at Mace Head throughout the year. Note that air pollution at coastal sites in midlatitudes can be strongly affected by land or sea breezes. In summer, warmer land than ocean temperatures causes prevailing winds toward inland. As such, measurements at coastal sites may be affected more by oceanic than inland mercury levels. The winter conditions generally reverse. This effect is challenging to simulate, especially using a relatively coarse resolution model like CAM-Chem that cannot accurately represent local circulation patterns. On the other hand, the wet deposition measurements suggest that the atmospheric mercury concentration peaks in summer at all non-coastal sites over the contiguous U.S. [NADP, 2008]. At this time, it is not known whether the above disagreements are caused by differences in local source emissions or meteorological conditions.

7.4. U.S. Mercury Wet Deposition

Figure 7.6 illustrates the geographic distribution of wet deposition for annually-averaged total mercury for 1999-2001 over the U.S. as derived by the CAM-Chem/Hg model. The spatial pattern of mercury wet deposition follows closely that of precipitation (Liang et al. 2004) than it does the atmospheric mercury concentration. In general, the

largest wet deposition occurs in the eastern U.S., where the peaks correspond to the annual precipitation centers over the Southeast, but are located on the south flank of the TGM concentration maxima. This is because the TGM concentration has much smaller spatial variations than precipitation amount. The secondary peaks of annual total mercury wet depositions are simulated over the Northwest, where precipitation prevails during cold seasons centered in winter.

Table 7.3 compares the modeled annually-averaged wet depositions for total mercury with the measurements at 26 monitoring sites of the U.S. National Atmospheric Deposition Program (NADP) Mercury Deposition Network (MDN). These sites are marked with letters of the alphabet on Figure 7.6. The model values are averaged over 1999-2001, while observations are given as the means of all measurements during the most closely matched data periods. The results show that the CAM-Chem/Hg simulation is realistic at 18 of the total 26 sites, where differences from observations are within ±20%. However, at some coastal sites (FL11, WA18), model biases are as large as 6 μg m^{-2}. These differences are likely caused by errors in simulating precipitation near the coast by the CAM-Chem model with its coarse resolution. In addition, relative biases are larger at some sites (CA72) with low wet depositions. The differences in data periods may partially explain the model-observation discrepancies.

Figure 7.7 presents scatter diagrams comparing modeled monthly total mercury wet deposition during 1999-2001 at the four MDN sites with continuous records, representing the Southeast (FL11), eastern coast (NC42), Midwest (WI08), and Southwest (TX21). The temporal correlation coefficients between modeled and measured depositions are reasonably high, suggesting that the CAM-Chem/Hg model largely captures

observational variations at each site. The best result is obtained in the Midwest, where the correlation reaches 0.67 at WI08. The result is also good for the Southeast and fair for the Southwest, with a respective correlation of 0.45 at FL11 and 0.32 at TX21. As discussed above, the simulation is worse for the east coast, with a low correlation of 0.19 at NC42.

Wet deposition is mainly determined by the distribution of precipitation amount and air pollutant concentration. Previous regional modeling studies suggested that mercury wet deposition over the U.S. also depends on the mercury emissions used [Bullock et al., 2002; Gbor et al., 2005]. The CAM-Chem/Hg model result may be more accurate than earlier studies (e.g., from the CAMQ model [Gbor et al., 2005]) because it incorporates an improved estimate for natural emissions. The CMAQ considers natural emissions from land, but not from oceans, which may lead to large underestimation of mercury deposition.

7.5. Domestic versus transpacific contributions to U.S. mercury

The transpacific transport is the primary process for bringing Asian pollutants to the U.S. Various ground-level observation analyses, field campaigns, and model simulations have been conducted to investigate the current pathways and characteristics of transpacific transport, as well as their influence on U.S. air quality [e.g., Jacob et al., 1999; Wilkening et al., 2000; Yienger et al., 2000; Jaeglé et al., 2003; Hudman et al., 2004; Parrish et al., 2004; Bertschi and Jaffe, 2005; Heald et al., 2006; Wuebbles et al., 2007; Lin et al., 2008]. Previous sections have shown that the mercury pollution in East Asia is the strongest in the world. Therefore, analysis of the contributions from transpacific transport on U.S. mercury effects on air quality is worth investigating.

Here two sensitivity experiments are conducted to examine the domestic versus international contributions to U.S. mercury concentrations. The first sensitivity experiment (EXP1) assumes no anthropogenic emissions over the United States and use the same meteorology and model setting to previous simulations of global mercury effects on air quality. The second sensitivity experiment (EXP2) assumes no anthropogenic emissions over Asia and keep same setting on others. Simulations of global mercury concentrations in previous section are used as the control run (CtrRun) to present the practical mercury effects on air quality.

Figure 7.8 shows the CAM-Chem simulated TGM concentrations (from CtrRun) on latitude-pressure cross sections over the northern Pacific Ocean between 80°E and 80°W. The cross sections are provided from 20°N to 60°N in the north hemisphere with an interval of 5°. High concentration of TGM occurs on the longitude from 100°E to 130°E, which indicates the strong emissions from East Asia. The red rectangle circles a sharp concentration decrease on the cross sections near 120°W, which suggested a possible strong deposition on the western U.S. The changes in low-level concentrations on these cross sections also suggested that the transpacific transport of mercury is strong between 30°N and 55°N.

Surface TGM concentrations are directly affected by transpacific transport. The top plots in figure 7.9 show the contributions to TGM concentrations from domestic (CtrRun-EXP1 (TGM)) and transpacific transported (CtrRun-EXP2 (TGM)) anthropogenic sources respectively. Domestic anthropogenic emissions contribute 0.2-0.9 ng/m^3 to the total surface TGM over the western and 0.2-1.1 ng/m^3 over the eastern United States. Contributions from transpacific transport mainly focus on the western U.S. with a

magnitude of 0.16-0.32 ng/m^3. However, the contributions to the eastern U.S. are below 0.16 ng/m^3. This pattern is close to the effect of transpacific transport on ozone [Lin et al., 2008]. Relatively, domestic anthropogenic emissions are the dominant anthropogenic sources that contribute around 25% of total gaseous mercury concentrations on a national basis.

The two plots on the bottom of Figure 7.9 show the contributions to total annual mercury deposition (dry and wet) by domestic (CtrRun-EXP1 (Deposition)) versus transpacific transported (CtrRun-EXP2 (Deposition)) anthropogenic emissions. Domestic anthropogenic emissions contribute 6-12 μg/m^2 to the total surface TGM deposition over the eastern and generally below 7 μg/m^2 over the western United States. The highest contributions are over the Midwest. The domestic anthropogenic emissions contribute on average 22% to total deposition in the United States, but near 50% in the industrial regions. This result is consistent with previous modeling studies by Seigner et al., [2004] and Selin et al., [2008]. Contributions from transpacific transport to total mercury deposition in the U.S. are 1-4 μg/m^2 over the western, but below 2 μg/m^2 over the eastern United States. The pattern is consistent with the contributions to TGM concentrations. In addition, it is noted that the contributions by transpacific transported anthropogenic emissions to total mercury deposition on the western United States is comparable to that by domestic anthropogenic emissions. However, for contributions to TGM concentrations, the domestic is much larger than the transpacific.

7.6. Summary and Discussion

A tropospheric mercury chemistry module has been developed and incorporated into the CAM-Chem model to represent the processes affecting atmospheric mercury and its deposition over the globe. It includes the chemistry, emission, deposition, and transport processes for elemental, reactive, and particulate forms of mercury. The chemistry considers the oxidation of elemental mercury by ozone with temperature dependence, the oxidation by hydroxide ions, hydrogen peroxide and chlorine in gaseous phase, as well as the aqueous reduction and oxidation on mercury chemicals. The transport and deposition of mercury are determined using the approaches used for other chemicals in the CAM-Chem model. Mercury emissions are included based on published estimates for human-related, volcano eruption, and biomass burning sources, as well as the dynamic parameterizations for natural sources, including air-sea exchanges from global oceans, and land surfaces (soil, vegetation) and reemissions depending on the temperature, solar radiation and soil storage. The total emissions of mercury at the present climate condition is estimated to be 9600 Mg yr^{-1} over the globe, of which 2200, 2900, 3400, 600, and 500 Mg yr^{-1} are from respectively anthropogenic, land, ocean, biomass burning and volcano sources. The atmospheric lifetime of mercury against deposition is approximately 0.69 year in the absence of recycling from surface reemissions. In our model, the dynamic schemes for land and ocean emissions are simplified from previous dynamic models for point source emission, and then calibrated by the latest estimate on present global natural emissions based on observations. This solution not only considers the physical processes associated with natural emissions, but also includes the latest knowledge on it. Compared with the previous studies, both simplified schemes also save a lot of computation time for a global model. In addition, it

is the first time that reemission processes into the dynamic estimates of land and ocean emissions are considered relative to prior studies. In this way, there is no need to sacrifice the simulations of dry deposition to compensate for reemission processes. Although our approach appears to provide a good approximation of current knowledge on the reemission process, uncertainties remain that require further analysis.

The CAM-Chem/Hg model has been then evaluated relative to available measurements worldwide using meteorological conditions driven from the NCEP observational reanalysis. The evaluation includes both surface air TGM concentrations and annual total mercury wet depositions. They are compared with observations from 19 land sites that distribute evenly over the globe and 3 ocean cruise tracks for concentrations, and with 26 U.S. monitoring sites for depositions. For both quantities, the model captures the major characteristics of their geographic distributions and seasonal variations. As a result of these many analyses, we conclude that the CAM-Chem/Hg is one of, and possibly, the best modeling tools available to study the physical and chemical processes governing the emission, transport, transformation and deposition of atmospheric mercury. At the same time, we recognize that further limitations and uncertainties require further attention. In particular, improvements are needed to reduce the large underestimations of wet depositions near the coastal regions and of the concentrations in the middle atmospheric layers. For this underestimation, it may be associated with two potential issues. One is our poor understanding of the HG0/HgII redox chemistry including gaseous, aqueous and heterogeneous reactions; this could have an important effect on deposition patterns. The other is the wet deposition scheme, which

may need to be modified to better account for mercury attachment on other aerosols or for electrostatic adherence on droplets.

The sensitivity study on effects of domestic emissions versus transpacific transport of anthropogenic mercury emissions on the concentrations of mercury compounds in the United States shows that transpacific transport has significant influence on total mercury deposition over the western United States. On a national basis, 22% of total mercury deposition in the United States results from domestic anthropogenic sources, and only 9% are contributed by transpacific transport. However, the contributions to deposition on the western United States are comparable between domestic and transpacific sources. Domestic anthropogenic emissions are the dominant anthropogenic sources that contribute around 25% of total gaseous mercury concentrations on a national basis. The averaged percentage contribution to TGM concentrations from transpacific transport is only 7%. These analyses provide improved understanding of the present U.S. mercury concentrations and deposition, and the relationship between Asian and U.S. mercury pollution. However, another important issue is how will the U.S. mercury concentrations and this relationship likely to change in the coming decades. A comprehensive understanding through further research on this issue would help policy makers in considering effective strategies for mercury pollution.

Table 7.1 Reactions and rate constants used by the CAM-Chem Hg model.

Reactions	*Rate constant*	*Reference.*
Gaseous Reactions	Unit: $cm^3\ molec^{-1}\ s^{-1}$	
$Hg^0_{(g)} + O_{3(g)} \rightarrow 0.5HgP + 0.5RGM$	$2.11\times10^{-18}exp(-1256.5T^{-1})$	Gbor et al. [2006]
$Hg^0_{(g)} + H_2O_{2(g)} \rightarrow RGM$	8.5×10^{-19}	USEPA. [1997]
$Hg^0_{(g)} + Cl_{2(g)} \rightarrow RGM$	2.6×10^{-18}	Gbor et al. [2006]
$Hg^0_{(g)} + OH_{(g)} \rightarrow 0.5HgP + 0.5RGM$	7.7×10^{-14}	Gbor et al. [2006]
Aqueous Reactions	Unit: $m^{-1}s^{-1}$	
$Hg^0_{(aq)} + O_{3(aq)} \rightarrow Hg^{2+}_{(aq)} + products$	4.7×10^{7}	Munthe [1992]
$HgSO3 \rightarrow Hg^0_{(aq)} + products$	$T\ exp(31.971-12595T^{-1})$	Van Loon et al. [2000]
$Hg^{2+}_{(aq)} + HO_{2(aq)} \rightarrow Hg^0_{(aq)} + products$	1.1×10^{4}	Pehkonen & Lin [1998]
$Hg(OH)_{2(aq)} + hv \rightarrow Hg^0_{(aq)} + products$	6.0×10^{-7}	Xiao et al. [1994]
$Hg^0_{(aq)} + OH_{(aq)} \rightarrow Hg^{2+}_{(aq)} + products$	2.0×10^{9}	Lin & Pehkonen [1997]
$Hg^0_{(aq)} + HOCl_{(aq)} \rightarrow Hg^{2+}_{(aq)} + products$	2.09×10^{6}	Lin & Pehkonen [1998]
$Hg^0_{(aq)} + OCl^-_{(aq)} \rightarrow Hg^{2+}_{(aq)} + products$	1.99×10^{6}	Lin & Pehkonen [1998]

Table 7.2. CAM-Chem simulated 1999-2001 annual mean total mercury concentrations compared with measurements with varying periods at available land sites worldwide.

Observations				CAM-Chem/Hg ($ng\ m^{-3}$)
Site	**Period**	**Reference**[a]	**Concentration** ($ng\ m^{-3}$)	
Alert, Canada (82N, 62W)	1995–2002	[1]	1.55	1.43
Esther, Canada (52N, 110W)	1997–1999	[4]	1.69	1.15
Zeppelin, Norway (79N, 12E)	2000–2004	[2]	1.55	1.51
Pallas, Finland (67N, 24E)	1998–2002	[2]	1.34	1.57
Lista, Norway (58N, 6E)	2000–2003	[2]	1.68	1.63
Råö, Sweden (57N, 11E)	2001	[2]	1.66	1.67
Rörvik, Sweden (57N, 25E)	2001–2002	[2]	1.66	1.70
Zingst, Germany (54N, 12E)	2000	[2]	1.56	1.84
Mace Head, Ireland (54N, 10W)	1995–2001	[3]	1.75	1.79
Langenbrügge, Germany (52N,	2002	[2]	1.70	1.84
Cheeka Peak, Washington,	2001–2002	[5]	1.56	1.61
Detorit, United States (43N,	2003	[6]	2.2	1.9
Chongqing, China (29N, 106E)	2006-2007	[7]	6.7	4.9
Beijing, China (40N, 116E)	2005	[8]	4.9	3.9
Tokyo, Japan (35N, 135E)	2000-2001	[9]	2.80	2.54
New York, United States (42N,	2000-2003	[10]	2.3	1.93
Seoul, Korea (36N, 128E)	2003	[11]	5.0	4.7
Cape Point, South Africa (34S,	1998-2002	[12]	1.23	4.1
Neumayer, Antarctica (70S, 8W)	2000	[3]	1.06	1.26

a [1] Environmental Canada [2003]; [2] EMEP [2005]; [3] Ebinghaus et al. [2002]; [4] Kellerhals et al. [2003]; [5] Weiss-Penzias et al. [2003]; [6] Liu et al. [2007]; [7] Yang et al. [2008]; [8] Wang et al. [2007]; [9] Sakata and Marumoto [2002]; [10] Han et al. [2004]; [11] Kim et al. [2006]; [12] Baker et al. [2002].

Table 7.3. CAM-Chem modeled annual total mercury wet depositions as compared measurements at the selected monitoring sites of the NADP MDN.

Site	Location (Lat,Lon)	Observation	NADP	Model (1999-
A (FL11)	(25.39N,80.68W)	1998-2002	17.9	11.9
B(GA09)	(30.74N,82.13W)	1998-2002	12.3	12.5
C(GA40)	(33.93N,85.05W)	2001-2003	17.7	18.2
D(SC19)	(33.81N,80.78W)	1998-2002	12.7	15.9
E(NC42)	(35.74N,76.51W)	1998-2002	11.2	13.1
F(VA28)	(38.52N,78.43W)	2003-2005	13.2	14.7
G(PA47)	(39.99N,76.38W)	2003-2005	11.6	14.3
H(NY20)	(43.97N,74.22W)	2000-2002	9.1	12.1
I(ME98)	(44.38N,68.26W)	1998-2002	7.2	10.3
J(IN20)	(40.84N,85.46W)	2001-2003	12.2	12.3
K(WI22)	(43.07N,87.88W)	2003-2005	10.1	10.8
L(WI08)	(46.75N,91.61W)	1998-2002	7.7	9.2
M(MN23)	(46.25N,94.50W)	1998-2002	7.3	6.7
N(IL11)	(40.05N,88.37W)	1999-2002	9.3	10.1
O(KY10)	(37.13N,86.15W)	2003-2005	11.7	15.7
P(AL03)	(32.90N,87.25W)	2001-2003	13.6	14.2
Q(LA28)	(30.50N,90.38W)	1999-2002	15.8	13.3
R(TX21)	(32.38N,94.71W)	1998-2002	12.3	11.4
S(NM10)	(33.06N,107.29W)	1998-2002	4.1	4.7
T(OK99)	(35.75N,94.67W)	2003-2005	13.7	10.5
U(CO97)	(40.54N,106.68W)	1999-2002	6.8	5.7
V(MT05)	(48.51N,114.00W)	2004-2006	5.7	5.9
W(WA18)	(47.68N,122.26W)	1998-2002	6.2	10.4
X(OR10)	(44.21N,122.25W)	2003-2005	7.8	8.6
Y(CA72)	(37.43N,122.06W)	2000-2002	3.6	6.7
Z(CA97)	(39.82N,123.24W)	1998-2002	3.2	3.8

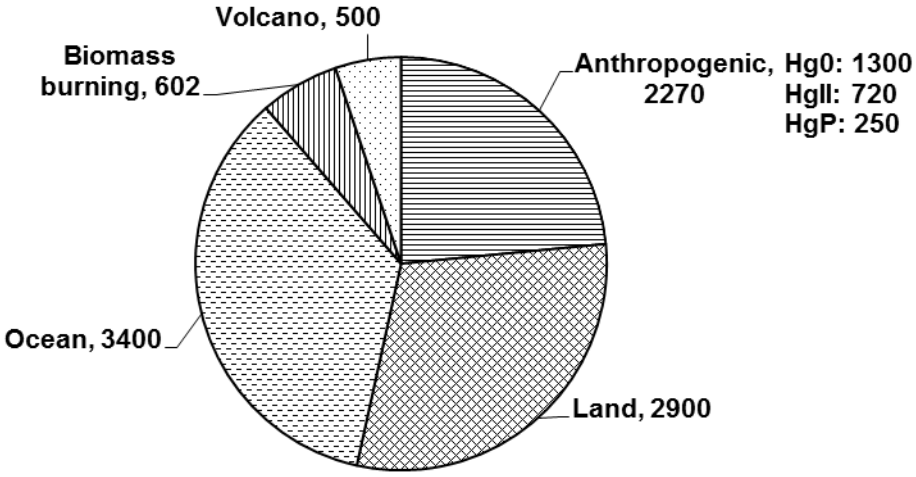

Figure 7.1. Estimated global total mercury emissions (Mg yr^{-1}) from different sources in 2000.

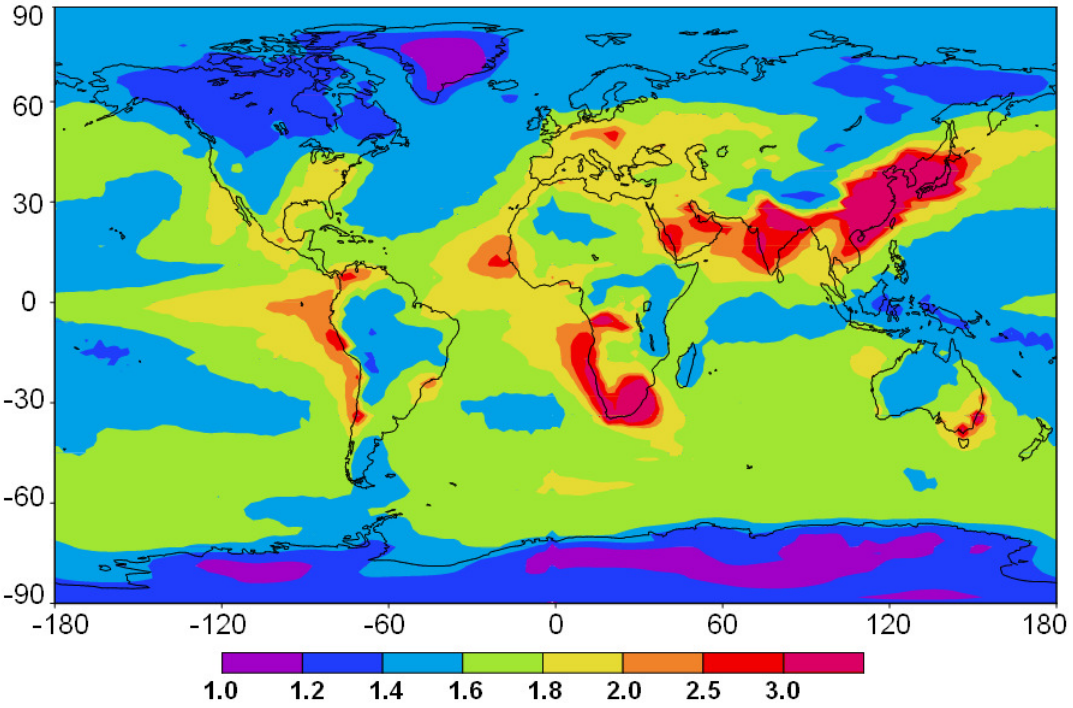

Figure 7.2. Annual mean surface TGM concentrations averaged in 1999-2001 derived by the CAM-Chem/Hg model.

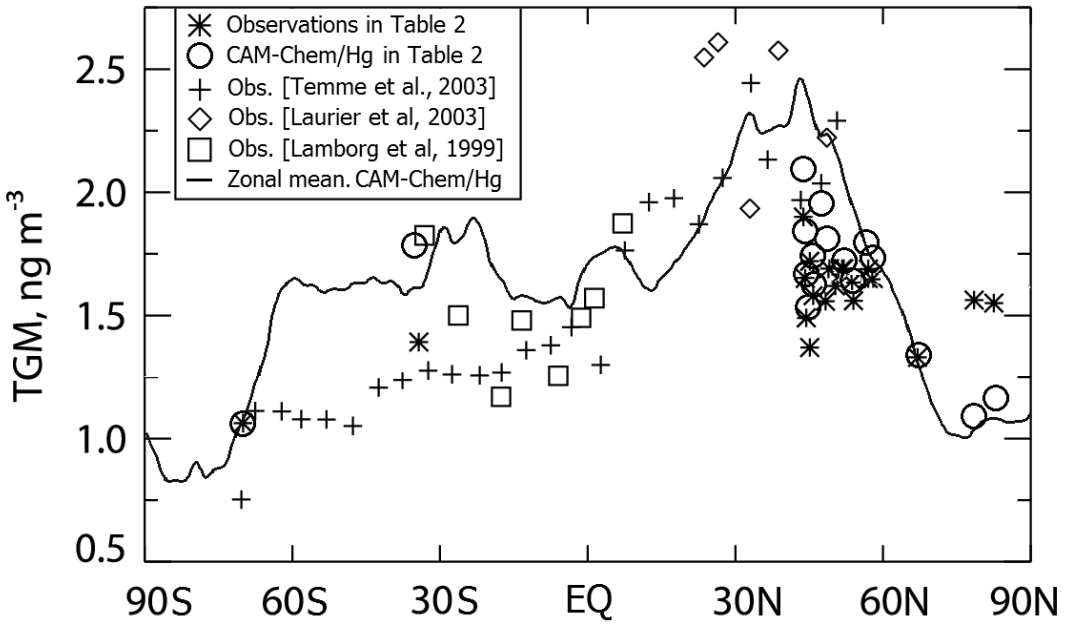

Figure 7.3. Variation of TGM surface concentrations with latitude. Zonally averaged and annual mean CAM-Chem/Hg model results (curve) are compared to observations (symbols) from previous studies. The observations on Land-based stations and

corresponding CAM-Chem/Hg values are from table 2. Reported measurements over the oceans are from Temme et al., [2003], Laurier et al., [2003] and Lamborg et al., [1999].

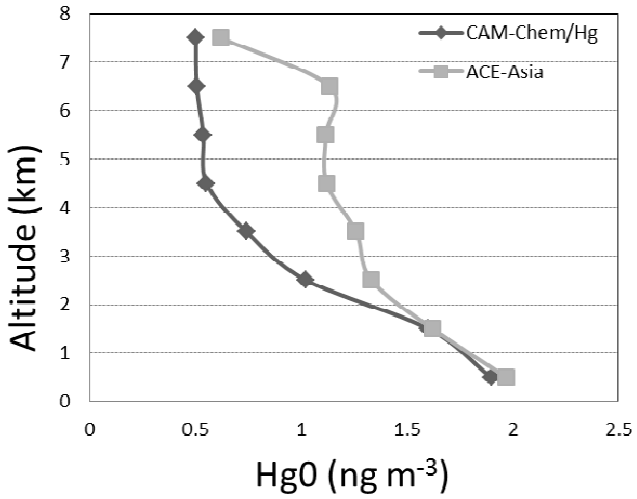

Figure 7.4. Vertical profile of Hg0 mixing ratios over southern Japan. Observations are from the ACE-Asia aircraft campaign during April-May 2001. The CAM-Chem result is averaged during the same period and over the same area.

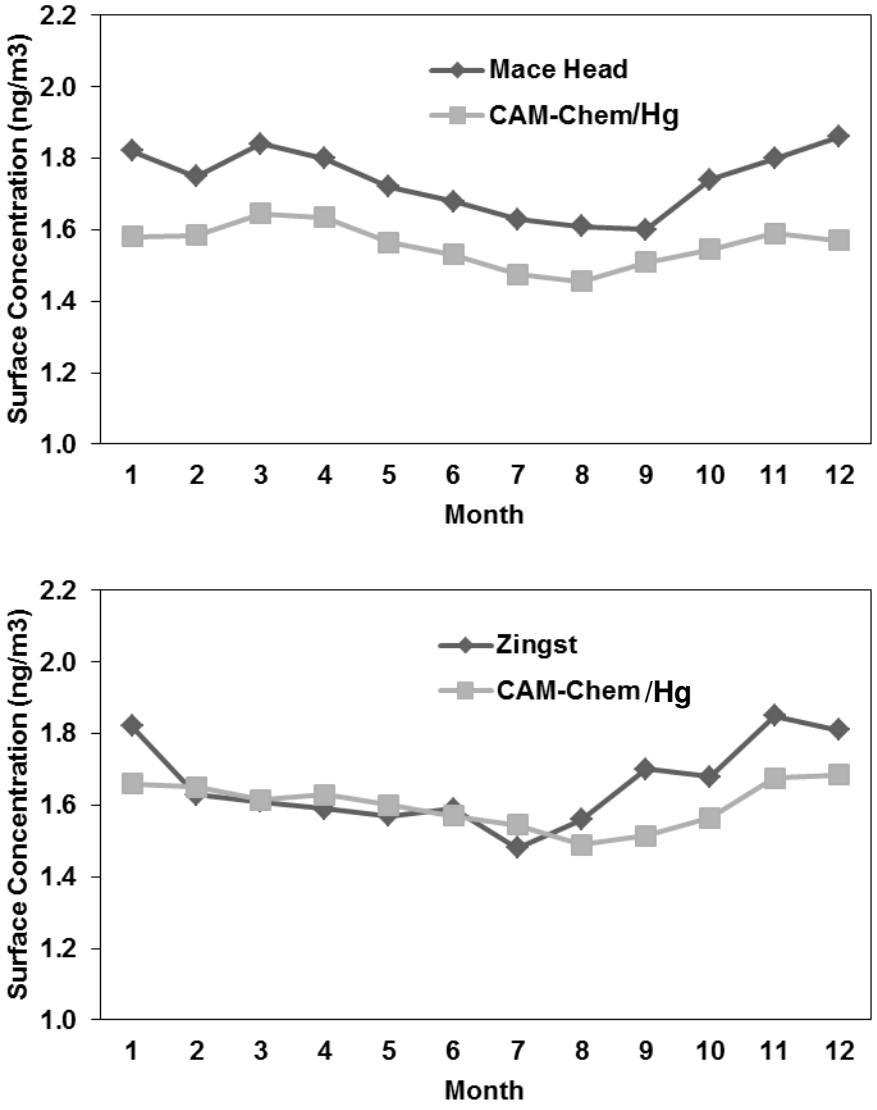

Figure 7.5. Seasonal variations of surface air TGM concentrations (ng m^{-3}) at coastal station: Mace Head, Ireland and Zingst, Germany. Shown are monthly means averaged in 1998-2004 for observations and 1999-2001 for the CAM-Chem/Hg.

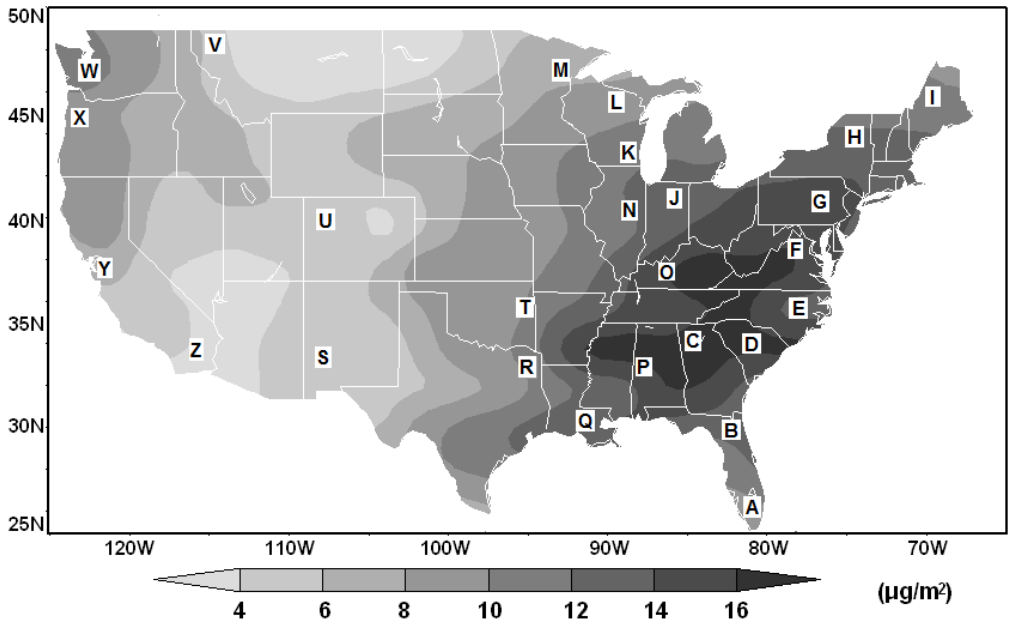

Figure 7.6. Annual total mercury wet deposition (µg m^{-2}) averaged during 1999-2001 as simulated by the CAM-Chem/Hg. Letters represent the MDN monitoring sites in Table 3.

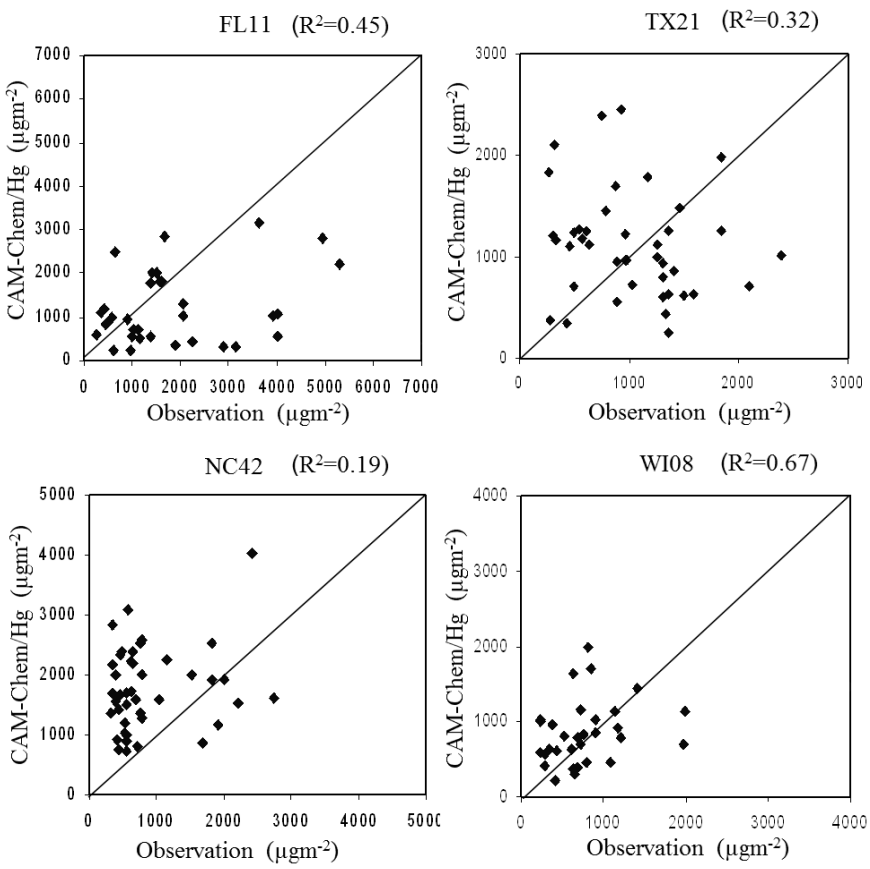

Figure 7.7. Scatter diagrams comparing modeled and measured monthly total mercury wet depositions during 1999-2001 at four MDN sites. Temporal correlation coefficients squared are also listed for each site.

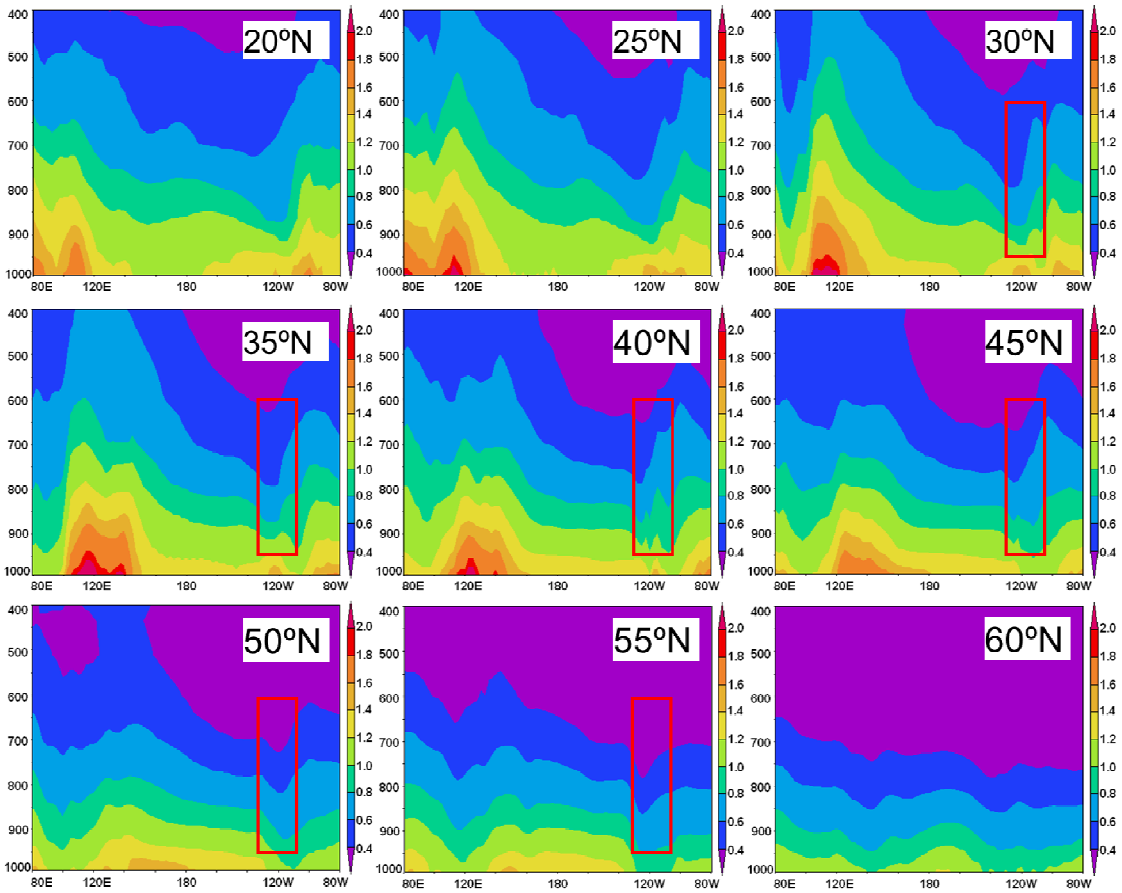

Figure 7.8. Latitude-pressure cross section for CAM-Chem/Hg simulated TGM concentrations. The red rectangle shows where the deposition may happen.

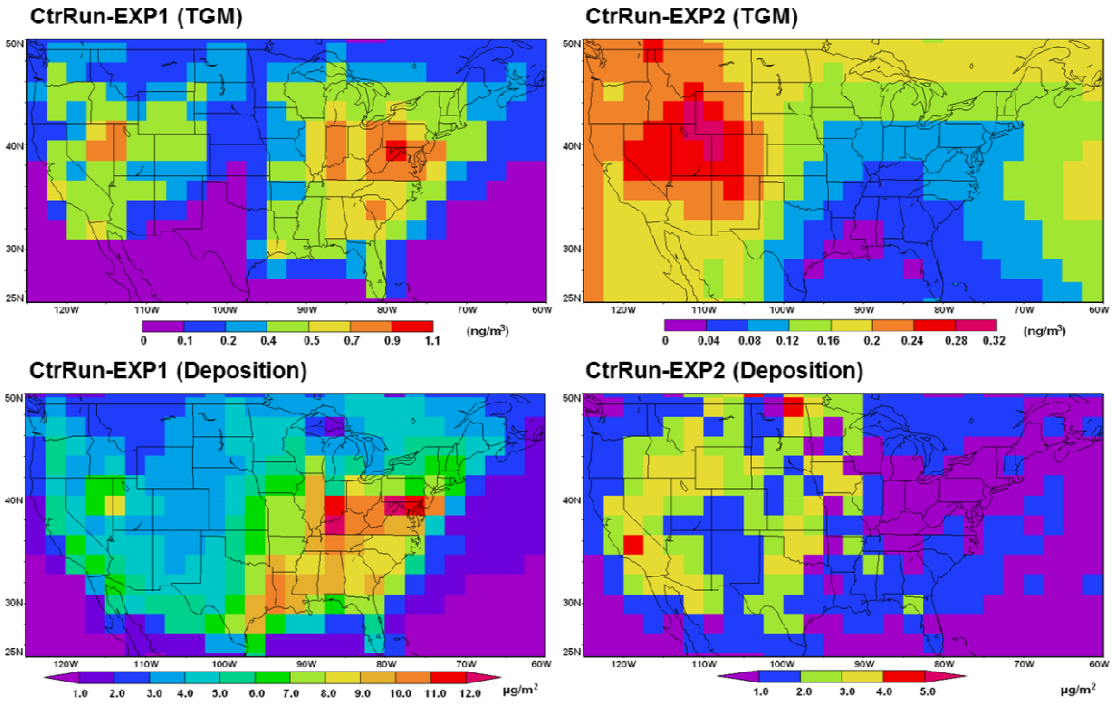

Figure 7.9. Sensitivity experiments for domestic versus international contributions to annual mean air concentration and deposition of U.S. mercury. CtrRun-Exp1 (TGM): Contributions of domestic anthropogenic emissions of mercury on TGM concentrations. CtrRun-Exp2 (TGM): Contributions of international anthropogenic emissions of mercury on TGM concentrations. CtrRun-Exp1 (Deposition): Contributions of domestic anthropogenic emissions of mercury on deposition of total mercury. CtrRun-Exp2 (Deposition): Contributions of international anthropogenic emissions of mercury on deposition of total mercury.

CHAPTER 8: EFFECTS OF 2000-2050 CHANGES IN CLIMATE AND EMISSIONS ON GLOBAL ATMOSPHERIC MERCURY POLLUTION AND ITS CONSEQUENCE ON THE UNITED STATES

8.1. Introduction

The toxic effects of mercury (Hg) have been a serious concern to governments and the scientific community. Much effort has been made to assess and monitor releases of mercury compounds and their effects on air quality [NADP, 1996; USEPA, 2006; UNEP, 2008]. Based on its toxicity and present pollution levels, controlling mercury emissions in the coming decades is a target for all nations [UNEP, 2008]. Projections of future levels of mercury are a key criterion to developing control strategies. Although many modeling studies have investigated past and present mercury in the atmosphere [Bullock et al., 2002; Selin et al., 2008; Lei et al., 2011], potential changes in future levels of atmospheric mercury compounds have not been examined.

Projections of future mercury effects on air quality need to consider the effects of potential changes in climate and emissions. Changes in climate alone will influence future atmospheric mercury levels and composition. Due to the low vapor point, the atmospheric lifetime and natural emissions of mercury are sensitive to changes in climate. Previous studies indicate that soil emission of mercury is affected by changes in temperature and solar radiation [Lindberg et al., 1998; Zhang et al., 2001]. Changes in the atmospheric general circulation may also change the pathway of atmospheric transport of mercury [Strode et al., 2007]. In addition, changes in emissions will also affect the atmospheric concentrations of mercury compounds. The records from glacial ice cores in

Wyoming [USGS, 2002] show that changes in emissions are the main factor driving atmospheric mercury concentration increases over hundreds of years in the past. Modeling studies of preindustrial cycles in atmospheric mercury indicate that industrial emissions of mercury have changed the composition of atmospheric mercury compounds [Selin et al., 2008].

Recent studies have shown that greenhouse gas emissions from human activities are the primary factor driving climate change over the last four decades [IPCC, 2001, 2007]. Through consideration of the uncertainties associated with future social and economic developments, IPCC has developed a series of future emissions scenarios for projecting the climate changes over this century [IPCC, 2001, 2007; IPCC SRES 2004]. Many studies of future air quality changes have used the IPCC climate scenarios to assess the climate change impacts and analyze uncertainties [e.g., Lin et al., 2008; Wu et al., 2008; Pye et al., 2009]. To consider the effects of climate change during the 2000 to 2050 period on mercury, this study uses projections for the future climate following the IPCC scenarios.

Future emissions of mercury compounds are influenced by potential changes in social development as well as the changes in climate. Mercury emitted into the atmosphere occurs both from anthropogenic and natural sources. Human-related emissions are closely associated with social and industrial developments. Anthropogenic emissions of global mercury are estimated to be 2190 Mg for the year 2000 [Pacyna et al., 2006]. Streets et al. [2009] projects the anthropogenic emissions of mercury to the year 2050 by considering different social development and energy use scenarios. In addition, some natural emissions, including land and ocean emissions, are affected by

climate. As a result, seasonal variations and spatial differences are very significant. These characteristics of natural emissions make simple scaling methods ineffective for future projections. On the other hand, as has been done by some models, the effects of climate change on natural emissions can be considered through dynamic modeling methods [Poissant and Casimir, 1998; Zhang et al. 2001; Wängberg et al., 2001; Selin et al., 2008; Lei et al., 2011]. This approach is also used here for the projection of natural emissions of mercury.

In this study, a global 3-D atmospheric mercury model, Community Atmospheric Model with mercury (CAM-Chem), is used to make an assessment of the effects of mercury on the U.S. for 2050. Three distinct climate/emissions pathways from the IPCC special report on Emission Scenarios (SRES) are considered, including the A1FI, A1B and B1 scenarios representing upper, middle and lower bounds of climate warming over the coming decades respectively. Projections of anthropogenic mercury emissions in 2050 are based on the energy use corresponding to the specific scenario, while natural emissions are projected through dynamic schemes for emission driven by future climate and environmental data. The following, first introduces the projection of future mercury emissions, then analyzes the U.S. mercury air pollution and uncertainties, and later discusses the effects of changes in climate and emissions.

8.2. Method

For this study, emissions of all chemical components used by the CAM-Chem model are projected to 2050. We first project emissions of chemicals other than mercury species from the present to 2050 following the IPCC Special Report on Emission

Scenarios, as we did for the future ozone study [Lei et al., 2011]. Then, anthropogenic emissions of mercury are projected to 2050 based on the energy use assumptions in the IPCC-SRES report [IPCC, 2001]. The projections follow the IPCC A1FI, A1B and B1 scenarios and use a method introduced by Streets et al. [2009]. Natural emissions from both land and ocean sources in 2050 are calculated using dynamic schemes built in the atmospheric mercury model [Lei et al., 2011]. Biomass burning in 2050 is also projected using a method introduced by Streets et al. [2009].

The CAM-Chem is driven by meteorological fields derived from the CCSM3 climate system model [Collins et al., 2006]. The meteorology fields derived for the present atmosphere with CCSM3 were archived with 6-hour temporal resolution, including winds, temperature, pressure, humidity and solar radiation. Simulations are performed with a 30 minute time step and a horizontal resolution of 1.9˚ x 2.5˚ with 26 vertical levels from the surface (1000 hPa) to 3-millibar level (~40 km altitude). Previous tests have demonstrated that roughly a 6 months' spin-up is enough for CAM-Chem to not be affected by initial conditions. In this study, each case was run for 5 years (2048–2050) following 1 year of model spin-up. Unless noted otherwise, all results discussed are based on 5-year averages. The modeled concentrations of mercury compounds were outputted at 1-hour intervals.

8.3. Projection of future Hg emissions

Emissions of mercury compounds for 2050 are derived in three ways based on the source type and dynamic emission approaches used in CAM-Chem.

8.3.1 Anthropogenic emissions

For the projections of anthropogenic emissions of mercury in 2050, we directly use the results for the A1B and B1 scenarios by Streets et al., [2009]. For the A1FI scenario, we project the mercury emissions using the same projection method that was used for the A1B and B1 scenarios as developed by Street et al. [2009] along with the energy use information in the IPCC SRES A1FI scenario [RIVM, 2001]. The A1FI scenario is characterized by the rapid increase in consumption of fossil fuel energy and economic growth. We assume that no significant advance is made over the reported Hg removal levels in the A1FI scenario. The rates of implementation of Flue Gas Desulphurization (FGD) by 2050 on coal-fired power plants for the A1 series scenarios are the same as referenced in RIVM [2001]. Of the factors that affect mercury emissions, the use of coal, oil and gas in 2050 under the A1FI scenario is assumed to increase much than under the A1B scenario. The final estimate of mercury emission amount in each IPCC SRES region is calculated based on the FGD and the estimated energy growth in RIVM [2001]. As introduced in Lei et al. [2011], we adopt the present (year 2000) anthropogenic emission of mercury directly from that prepared by Pacyna et al. [2006]. This is used as the base inventory to do the projection.

The resulting emissions inventories used in this study are summarized in Table 8.1. Global total Hg emissions are expected to increase in the future. The annual global mercury emission in 2050 is projected in the range of 2390-5990 Mg, an increase of 9 to 173% over the total emissions for the year 2000. The main factor affecting the emission is the increase in fossil fuel use, especially the increase projected for developing countries. Asia has the largest emission increase corresponding to its large population and increase in energy demand.

Figure 8.1 shows the projected mercury emissions over North America. The total mercury emissions in 2050 increase to 305.7 Mg/yr over North America under the A1FI scenario, 225.9 Mg/yr under the A1B scenario and decrease to 121.9 Mg/yr under the B1 scenario relative to the present value of 145.8 Mg/yr. The most significant characteristics are that the amount and ratio of reactive mercury (HgII) in the total mercury emissions will increase and the ratio of elemental mercury (Hg0) will decrease in 2050 under all future scenarios. The global shares of primary emitted mercury species are 67% Hg0, 25% HgII and 7% HgP at the present. They change in 2050 to 56% Hg0, 40% HgII and 4% HgP under the B1 scenario, to 47% Hg0, 49% HgII and 4% HgP under the A1B scenario, and to 49% Hg0, 43% HgII and 8% HgP under the A1FI scenario. This shift from Hg0 (reduced) to HgII (increased) may relatively reduce the long-range transport but significantly increase the local (wet) deposition of mercury.

8.3.2 Biomass burning and volcano emissions

Biomass burning is an important source in the global emissions inventories. The approach of Streets et al. [2009] is directly implemented here. Tropical forests, extra-tropical forests, savanna/grassland, and crop residue burning in fields are considered in the future emissions. The amounts of open biomass burned are adopted from IPCC [2001] forecasts, which are scenario-specific. However, biomass burning also includes natural wildfires, but the IPCC only considers those emissions that are directly associated with human activities. We use the managed forest projections and supplement them with estimates of wildfire emissions using the mature forest projections [IPCC, 2001]. Since the wildfire is a random event that is associated with the area of forest, we assume that

the rate of wildfire per unit area of forest is a constant [Streets et al., 2009]. As a result, changes in mature forest area over time are proportional to changes in wildfire emissions. The IPCC projections of grassland and crop residue burning (human activities) are also used. The global estimated total amounts mercury from biomass burning for 2000 is 600 Mg/yr. It is projected to be 670 Mg/yr in 2050 under the A1FI scenario, 570 Mg/yr in 2050 under the A1B scenario, and 447 Mg/yr in 2050 under the B1 scenario. These estimates are comparable with previous results on present emissions or future projection of mercury emission from biomass burning [Streets et al., 2001].

The volcanic emissions of mercury are estimated based on that of sulfur in the GEIA inventory using the ratio of Hg/SO_2 in volcanic emissions and SO_2 emissions [http://geiacenter.org]. A similar method is used by previous studies [Ferrara et al., 2000; Nriagu et al. 2003; Pyle and Mather, 2003]. Here, we used a unified Hg/SO_2 ratio of 1.5×10^{-7} for all volcanoes [Nriagu et al. 2003]. Present estimate of mercury emissions from volcanoes is around 500 Mg/yr. This value is considered a historical average for eruptions of active volcanoes and the slow emissions from non-erupting stable volcanoes [http://geiacenter.org], and is also considered to be applicable to future conditions.

8.3.3 Soil and Ocean emissions

For the projection of land emissions and ocean emissions, we used the dynamic schemes for land and ocean emissions of mercury developed in the CAM-Chem Hg module [Lei et al., 2011]. Two factors affect the future changes in land and ocean emissions. The first factor is climate change. The future land emissions depend on the skin temperature and available solar radiation, while the ocean emissions depend on the

surface wind and sea surface temperature. The other is changes in storage of mercury in the land and ocean reservoirs.

However, global mercury storage change is also related to the net deposition flux above the land and ocean. Anthropogenic and volcanic sources bring new mercury chemicals into the biogeochemical cycle of mercury. Therefore, the projections of these emissions contribute to the net mercury storage change. The latest estimate of present land mercury storage is around 240,000 Mg with a total deposition of 3260 Mg/yr and a total land emission of 2900 Mg/yr [Smith-Downey et al., 2010]. This suggests a net new mercury increase in the surface land reservoir of 360 Mg/yr, which take up 13% of total net mercury emissions (anthropogenic + volcanic: 2770 Mg/yr). Based on CAM-Chem simulations, an estimate of net increase in the atmospheric reservoir for the present atmosphere shows that around 1% of new emitted mercury will stay in the atmosphere. The other (86%) of the new mercury is deposited into the surface ocean. We assume that these ratios of the new mercury are maintained from 2000 to 2050. This relationship is used in the dynamic emission schemes in the CAM-Chem Hg model to calculate the future emission fluxes.

The land emission scheme is modified by considering the change in land mercury storage. The modified scheme is:

$$F_2 = F_1 \exp[-1.1\times10^4 (1/T_s - 1/T_0)] \exp[1.1\times10^3 (R_s - R_0)]\times C_i$$

where R_s is surface solar radiation and T_s is surface skin temperature. R_0 is the reference surface solar radiation with a value of 340 Wm^{-2}. T_0 is the reference surface temperature with a value of 288K. F_1 is the standard emission dataset. C_i is the enrichment factor following each scenario. C_i is calculated as following:

$$C_i = \frac{S_p + \alpha n(E_p + E_f)/2}{S_p}$$

where S_p is the present land storage of mercury (240,000 Mg). E_p is the present total new mercury emission amount. E_f is the projected new mercury emission amount. The value of α is is determined by the ratio of new mercury into the land reservoir. We assume that the net increase of new mercury follows a linear trend. The parameter n is the number of years relative to 2000. Here the value of n is 50.

The ocean emissions scheme is modified by considering the mercury concentration change in the ocean mixing layer. The modified simple model is:

$$F = K_w((C_w + m_i) - C_a / H')$$

where m_i is the scenario-specific change in mercury concentration in the ocean mixing layer based on present value. Other variables and calculations follow Lei et al. [2011]. As shown by Soerensen et al. [2010], 40% of the Hg in the ocean mixing layer is affected by the subsurface water. The change in the mercury exchange between the mixing layer and the subsurface water are neglected. 60% of the net deposition of new mercury will stay in the ocean mixing layer [Strode et al., 2007]. The m_i is calculated by following scheme:

$$m_i = \frac{60\% \beta n(E_p + E_f)/2}{71\% \times 4\pi R^2 \times d}$$

where β is the division ratio of new mercury into the surface ocean reservoir. It is estimated based on the present distribution of mercury deposition from anthropogenic sources. E_p is the present total new mercury emission amount. E_f is the projected new mercury emission amount, *n* is the number of years projected away from the present, and *R* is the radius of the Earth. The factor 71% accounts for the earth's surface covered by

oceans. The parameter d is the depth of ocean mixing layer. We set it to 50 meters as an average depth.

8.4. Global mercury pollution in 2050

Figure 8.2 shows the global annual mean surface concentrations of total gaseous mercury (TGM) for present and 2050 under the B1, A1B and A1FI scenarios. The concentration distribution of TGM follows the spatial distribution of industries. The result shows that the annual average TGM level has a little increase above the present level by 2050 under the B1 scenario in which the global total emission shows an increase in developing countries and decrease in developed countries. The temperature increase is around 1 °C. Temperature rise will accelerate the mercury cycle and lead to more land mercury emitted into the atmosphere. The concentration increase under the A1FI and A1B scenarios are very significant over global region. The concentration increase in Asia and Africa are very large. The averaged concentrations over Asian industrial regions are above 6.0 $\mu g/m^3$. The TGM concentrations over other parts of the world also shows an increase as a result of local emission increase and enhanced long range transport of mercury chemicals.

Figure 8.3 shows the zonal averaged surface TGM concentrations for present and 2050 under each scenario. Generally, present and future zonal averaged concentrations have a similar spatial pattern. The zonal average concentration peaks at mid-latitudes of the Northern Hemisphere, where industrial sources are largest. The average concentrations at mid-latitudes in the Southern Hemisphere are also larger than that in surrounding areas. This may be caused by the mining industry in the southern parts of

Africa. The estimated mercury concentration in 2050 under the A1FI scenario shows a significant rise (up to 4.7 $\mu g/m^3$) over middle and low latitude regions. The peak value is around twice as much as the present-day concentration. The peak value under the A1B scenario is around 0.5 $\mu g/m^3$ lower than the peak value under the A1FI scenario. The concentration change under the B1 scenario in the middle and low latitudes is up to 0.5 $\mu g/m^3$ higher above the present-day level. The concentration changes in high latitude regions are much smaller than changes in middle and low latitudes. At high latitudes of the Southern Hemisphere where less industry and human activities occur, the average concentration change is as low as 0.2 $\mu g/m^3$.

8.5. U.S. mercury effects on air quality

Figure 8.4 shows the annual average surface air concentrations of total gaseous mercury (TGM) for 2000 and 2050 under the B1, A1B and A1FI scenarios in the region of contiguous U.S. The TGM concentration distribution exhibits higher values in the coast area and the eastern U.S., where the mercury-related industries are centered. The results show that the annual average TGM levels will keep close to the present level by 2050 under the B1 scenario as a result of the compensating effects between the emission decrease and temperature increase around 1 □C. Emission increase in the neighboring countries may also contribute to the U.S. TGM concentration. By 2050 under the A1B scenario, the annual average TGM level is projected to rise, with increases up to 1.4 μg/m3 over the eastern U.S. The TGM level in 2050 under the A1FI scenario has largest increases up to 2.2 $\mu g/m^3$, as a response to the large increase in mercury emissions and serious change in climate under this scenario.

Figure 8.5 shows the simulated annual mean wet deposition of mercury in 2000 and 2050. Their spatial patterns are very close. Generally, the peak wet deposition region is the southeast, especially the coastal area of Georgia and South Carolina. The pattern is affected by the amount of precipitation and the atmospheric concentration of mercury. Present annual wet deposition of mercury is greater than 12 $\mu g/m^2$ in the eastern U.S. and around 4 $\mu g/m^2$ in the western U.S. By 2050, under the B1 scenario, the wet deposition only shows a 1-2 $\mu g/m^2$ increase over the eastern U.S., while there is little change in the western U.S. Under the A1B scenario, the Midwest has a wet deposition of 18-24 $\mu g/m^2$ which is as strong as the deposition in southeast U.S. by 2050. The increase in the eastern U.S. is around 6-12 $\mu g/m^2$, and it is around 2-4 $\mu g/m^2$ in the western U.S. The annual wet deposition in 2050 under the A1FI scenario increases around 10-14 $\mu g/m^2$ in the eastern U.S. and around 2-4 $\mu g/m^2$ in the western U.S.

8.6. Effects of changes in climate and anthropogenic emissions on U.S. mercury

In order to understand how the changes of climate and anthropogenic emissions individually contribute to the future atmospheric mercury concentration change, a sensitivity experiment that incorporates climate change only while keeping emission unchanged (i.e., the present-day level) is conducted under each scenario. Then, the difference between this experiment and the present-day run represents the effect of climate change only, while the difference between this experiment and the climate plus emission change run for 2050 depicts the effect of anthropogenic emission change.

For the projection of 2050 mercury effects considering both climate and anthropogenic emission changes, Figure 8.6 shows the simulated average mixing ratio of

annual mean surface mercury species over the continental U.S. for 2000 and 2050 under the B1, A1B and A1FI scenarios. The unit for mixing ratio of elemental mercury is 10^{-12} mol Hg/mol in following analysis, while the unit for reactive gaseous mercury and particulate mercury is 10^{-14} mol Hg/mol. The cylinder shows the averaged mixing ratio over the United States, and the line shows the range of uncertainty. As discussed in the previous section, the mixing ratio of each mercury species increased in 2050. Under the A1FI scenario, the increase is largest due to the large anthropogenic emission increase and the climate increase in temperature. Although elemental mercury is the main chemical form of mercury in the atmosphere, the relative mixing ratio increase rate is the largest under all three scenarios. This is resulted from the increase in precursor emissions of reactive gaseous mercury and accelerated oxidations of element mercury under a raising temperature.

Figure 8.7 shows the results for the sensitivity experiment of climate change only, where the anthropogenic emission and the land and ocean storages of mercury are all kept at the present-day level. Compared to the present-day mixing ratio of each mercury species, the differences between the three scenarios are small. Table 8.2 summarizes the changes of surface mixing ratios of Hg species over the U.S. in 2050 caused by climate change or anthropogenic emission change. The average temperature increase in 2050 under the B1, A1B, and A1FI scenarios are 1.0 ℃, 1.4 ℃ and 1.7 °□C, respectively. ΔHg shows the individual contribution of each factor on the average mercury species concentrations in 2050. The climate change individually contribute 0.26×10^{-12} mol Hg/mol under the B1 scenario, 0.39×10^{-12} mol Hg/mol under the A1B scenario and 0.49×10^{-12} mol Hg/mol under the A1FI scenario to the surface mixing ratio of elemental

mercury. The contributions to mixing ratio of reactive gaseous mercury are 0.41×10^{-14} mol Hg/mol under the B1 scenario, 0.66×10^{-14} mol Hg/mol under the A1B scenario and 1.07×10^{-14} mol Hg/mol under the A1FI scenario. The contributions to mixing ratio of particulate mercury are 0.37×10^{-14} mol Hg/mol under the B1 scenario, 0.59×10^{-14} mol Hg/mol under the A1B scenario and 0.93×10^{-14} mol Hg/mol under the A1FI scenario. The temperature increase leads to more emissions from land and ocean natural sources, as well as increasing the oxidation rate of elemental mercury. Therefore, both HgII and HgP show relatively higher increases in mixing ratio than that of Hg0.

The effect of anthropogenic emission change is calculated as the difference between the 2050 simulations of the climate plus emission changes and the climate change only. The anthropogenic emission change accounts for the emission increases due to land and ocean mercury storage changes, which mainly result from human activities. The emission decrease under the B1 scenario reduces the mixing ratio of elemental mercury has a decrease of 0.12×10^{-12} mol Hg/mol as a response to the emissions change. The mixing ratio of reactive gaseous mercury increased about 1.15×10^{-14} mol Hg/mol. The ratio of HgII to total emissions increased, resulting in a net emission increase in 2050 under the B1 scenario. The mixing ratio of particulate mercury in 2050 is reduced by 0.05×10^{-14} mol Hg/mol in response to the anthropogenic emissions changes. Under the A1B scenario, the change in composition of mercury emissions in 2050 results in a significant shift from elemental mercury to reactive gaseous mercury. The contribution of anthropogenic emission change to the mixing ratio of elemental mercury is about 0.42×10^{-12} mol Hg/mol. The contribution to HgII is around 2.13×10^{-14} mol Hg/mol. The contribution to HgP is around 0.41×10^{-14} mol Hg/mol. The contribution to HgII is much

higher than that in present. This trend continues in the A1FI case. Under the A1FI scenario, the contribution of anthropogenic emission changes to the mixing ratio of elemental mercury is about 0.55×10^{-12} mol Hg/mol, while it is 3.69×10^{-14} mol Hg/mol for HgII and 0.96×10^{-14} mol Hg/mol for HgP.

8.7. Discussion

We have investigated the effects of projected 2050 global changes in climate and emissions on atmospheric mercury effects on air quality in the United States by using a global atmospheric mercury model (CAM-Chem-Hg). Due to the changes in energy use, the developed countries show a slow increase or decrease in future mercury emission projections, while developing counties shows an increasing trend. The total mercury emissions are expected to increase by 2050. The total global anthropogenic mercury emissions in 2050 have a range between 2386.2 Mg/yr and 5983.7 Mg/yr. For the North America region, the total anthropogenic emission has a range between 121.9 Mg/yr and 305.7 Mg/yr. Under all scenarios, the ratio of elemental mercury in the emissions for 2050 decrease and the ratio of reactive gaseous mercury increase. Emissions from land and oceans in 2050 will increase due to an increase in the storage of mercury from net deposition of mercury. With projected changes in biomass burning and wildfires, the mercury emissions from biomass burning are estimated to be between 447 Mg/yr and 670 Mg/yr. This result implies that industrial development will seriously contribute to the global mercury pollution. Developing countries will be main contributors to in the coming decades. Therefore, controlling the use of industrial materials that contains

mercury compounds and improving technologies to reduce the release of mercury can effectively mitigate the mercury pollution.

For 2050, the zonal averaged surface total gaseous mercury (TGM) concentration over the Northern Hemisphere mid-latitude has a potential increase of 0.5-2.3 $\mu g/m^3$ above present levels. The zonal average of surface total gaseous mercury (TGM) concentration over the tropical and Southern Hemisphere mid-latitude regions increases by 0.5-1.2 $\mu g/m^3$. Changes of TGM concentrations at high latitude regions are relatively small. This indicates that clean areas such as Polar Regions in 2050 will have to face a higher risk of mercury pollution transported from the polluted regions than that in today.

The mercury effects on air quality in 2050 over the continental U.S. is examined with individual and combined effects of climate and emission changes. The climate change has a potential effect on the mixing ratio of atmospheric elemental mercury between $0.26\text{-}0.49\times10^{-12}$ mol Hg/mol, while the effect on mixing ratio of reactive gaseous mercury is around $0.41\text{-}1.07\times10^{-14}$ mol Hg/mol. Anthropogenic emissions changes have relatively larger effects on mercury species over the continental U.S. The potential effect on the mixing ratio of atmospheric elemental mercury is between -0.12 to 0.55×10^{-12} mol Hg/mol, while the effect on the mixing ratio of reactive gaseous mercury is around $1.15\text{-}3.69\times10^{-14}$ mol Hg/mol. The impact of emission change is relatively more significant than that of climate change on future mercury effects on air quality. As a result, the future U.S. TGM concentration may have a 2.1-4.0 $\mu g/m^2$'s increase in the eastern U.S. and around 1.4-3.0 $\mu g/m^2$'s increase on the western U.S. under the A1FI scenario. Under the lower emissions scenario, B1, the TGM concentration does not have a significant change. The effect of climate change and emissions increases in surrounding

areas is compensated for by domestic emissions decrease. This indicates that the change in climate will have a comparable effect to the changes in emissions on the U.S. mercury pollutions. Therefore, the situation for mercury pollution is more serious than that for other pollutants that may be mainly affected by changes in emissions. More concerns need to be put on monitoring the toxic mercury pollution.

We also note that wet deposition of mercury over the continental U.S. increases under all three scenarios. Precipitation change and increase of HgII concentration may result in the wet deposition increase. The annual wet deposition in 2050 may increases around 1-14 $\mu g/m^2$ in the eastern U.S. and around 0-4 $\mu g/m^2$ in the western U.S., depending on the projections in energy use. It is a very serious warning which implies more mercury from industrial emissions will be move into our water system. The water quality is expected to have a big challenge. Perhaps in 2050, a mercury removal treatment will be required in food and water production.

Table 8.1. Anthropogenic emissions of Hg for 2000 and in 2050 for each scenario and each world region (Mg/yr).

Scenario	North American	Asia & Oceania	Europe & Mid East	Africa	Central & South America	World
2000[(a)]	145.8	1305.9	247.8	398.4	92.1	2189.9
2050 A1FI	305.7	3307.1	861.3	789.2	720.4	5983.7
2050 A1B[(b)]	225.9	2970.0	676.5	509.6	437.6	4855.6
2050 B1[(b)]	121.9	1208.9	358.1	357.0	340.4	2386.2

(a) Results from Pacyna et al., 2006; (b) Projection results from Streets et al., 2009.

Table 8.2. Changes in surface mixing ratios of Hg species over the U.S. in 2050 resulting from climate change or anthropogenic emissions changes

Scenario	ΔT	Effect of Change in	Hg Species	ΔHg (unit[a,b])
B1	+1.0 □C	Climate (Climate2050 - Present)	Hg0	0.26
			HgII	0.41
			HgP	0.37
		Anthropogenic Emission (2050 - Climate2050)	Hg0	-0.12
			HgII	1.15
			HgP	-0.05
A1B	+1.4 □C	Climate (Climate2050 - Present)	Hg0	0.39
			HgII	0.66
			HgP	0.59
		Anthropogenic Emission (2050 - Climate2050)	Hg0	0.42
			HgII	2.13
			HgP	0.41
A1FI	+1.7 □C	Climate (Climate2050 - Present)	Hg0	0.49
			HgII	1.07
			HgP	0.93
		Anthropogenic Emission (2050 - Climate2050)	Hg0	0.55
			HgII	3.69
			HgP	0.96

ΔT: Temperature Change in 2050 above 2000

a: Hg0 in Unit of 10^{-12} mol Hg/mol.

b: HgII and HgP are in unit of 10^{-14} mol Hg/mol.

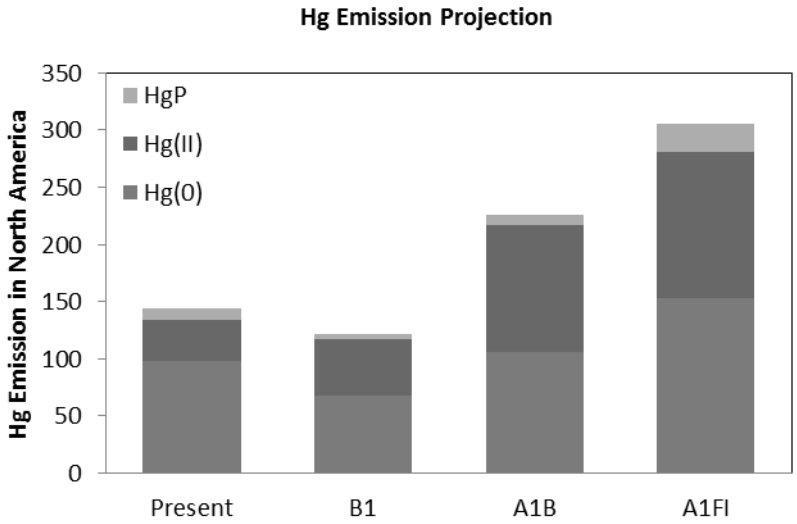

Figure 8.1. Ratios of various mercury chemicals in the 2000 and 2050 emissions inventories

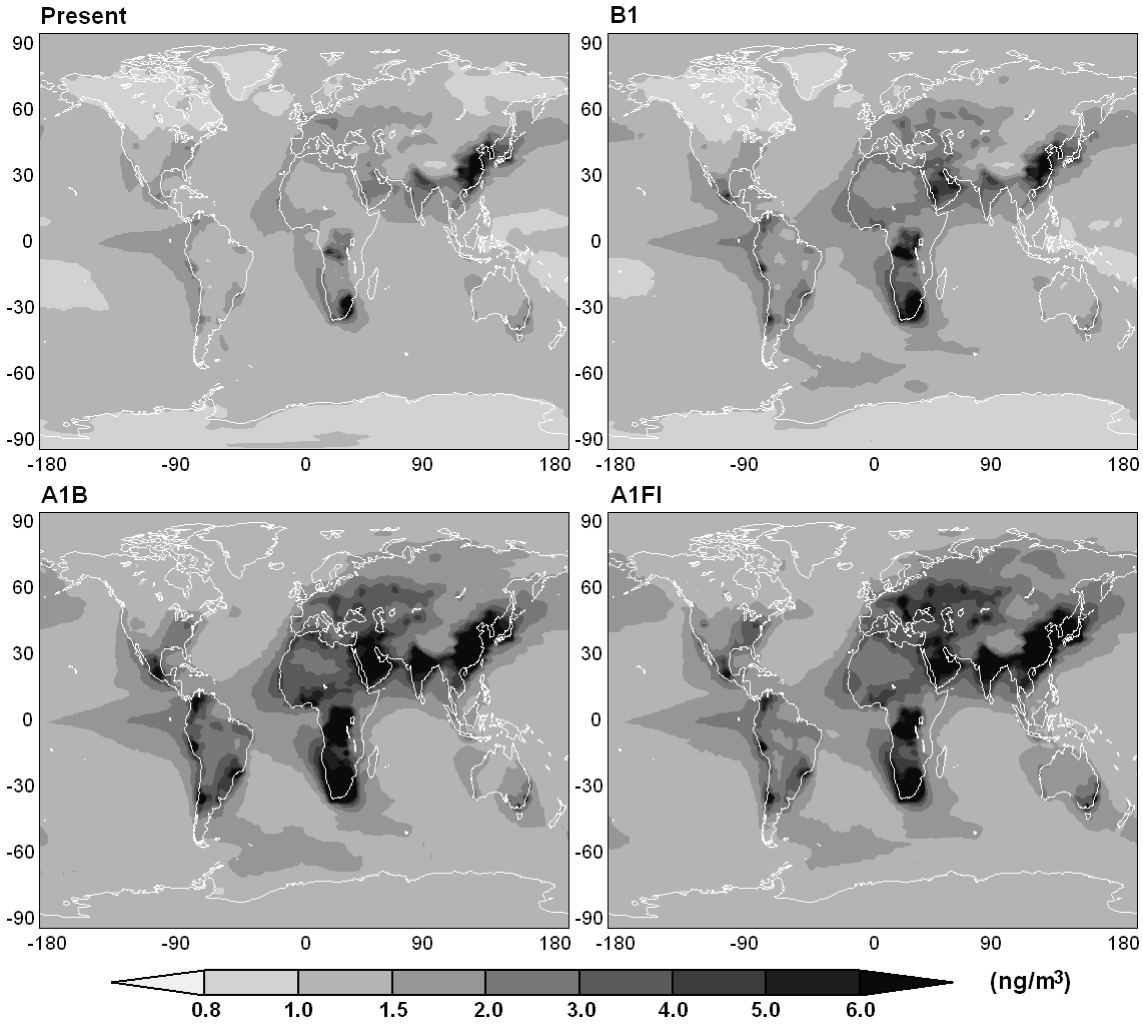

Figure 8.2. Annual mean of global surface mercury concentrations for 2000 and 2050 under the B1, A1B and A1FI scenarios as simulated by the CAM-Chem Hg model.

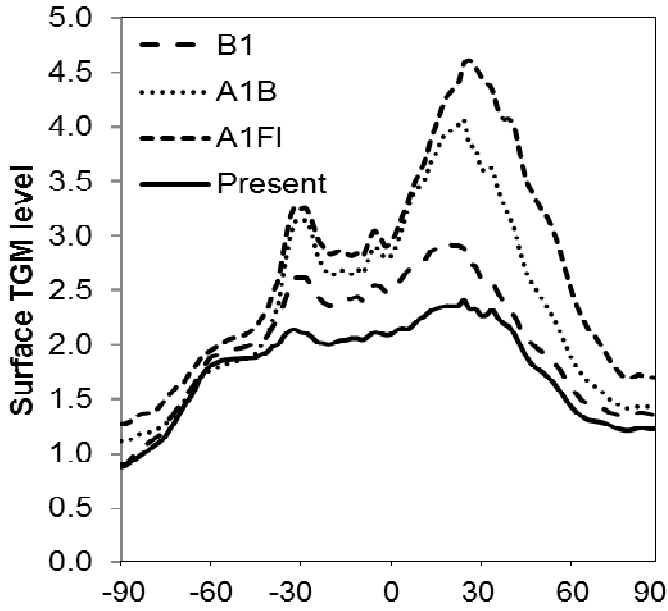

Figure 8.3. Zonal averaged surface TGM concentrations for 2000 and 2050 under the B1, A1B and A1FI scenarios as simulated by the CAM-Chem Hg model.

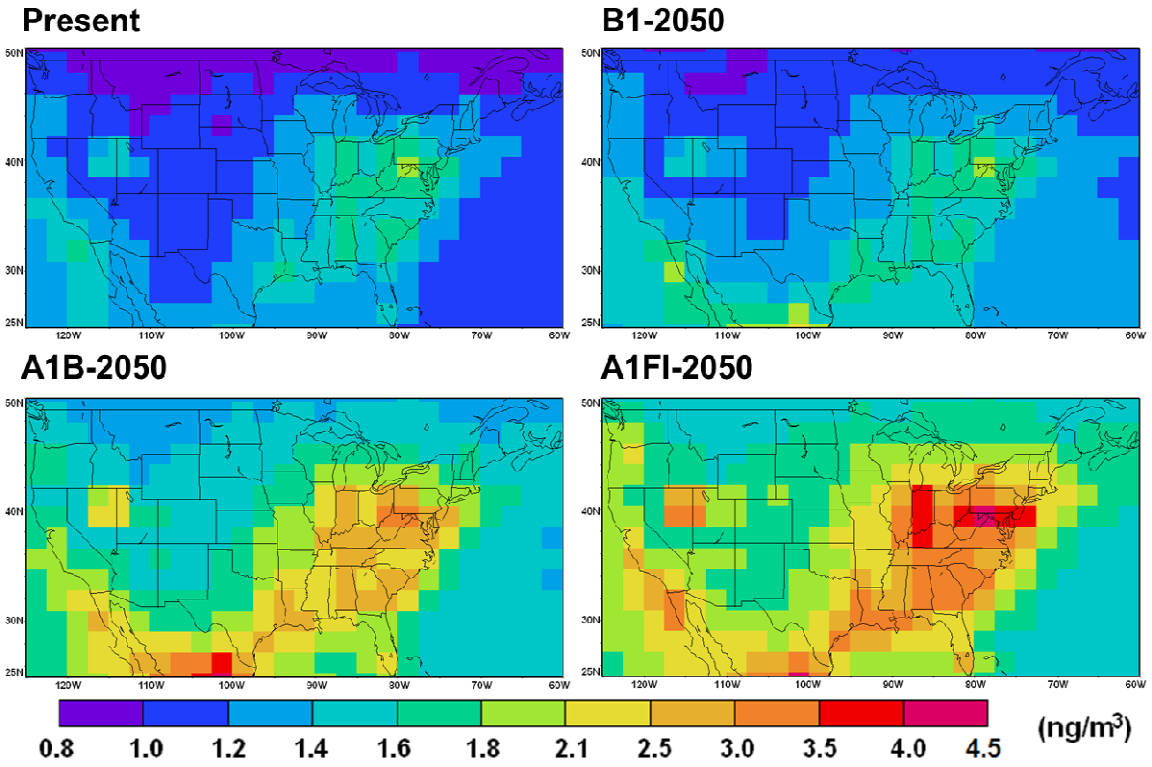

Figure 8.4. Annual mean of simulated surface TGM concentrations over the continental U.S. by CAM-Chem for 2000 and 2050 under the B1, A1B and A1FI scenarios.

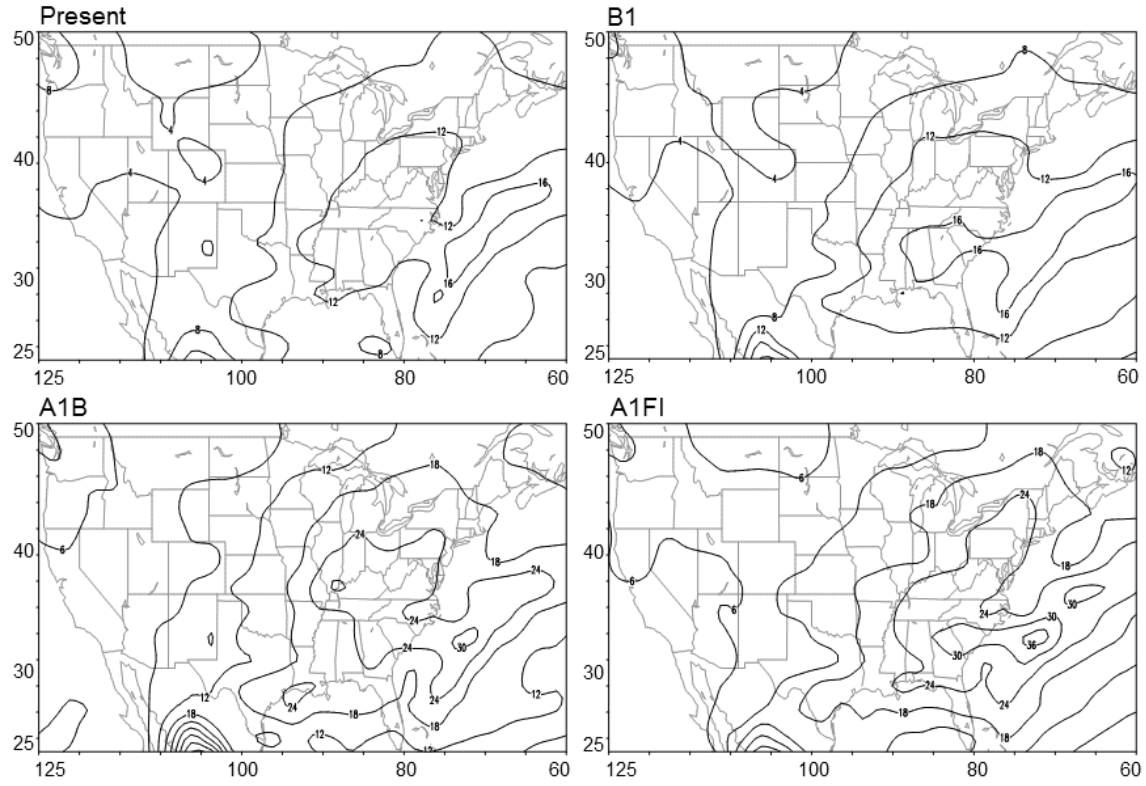

Figure 8.5. Simulated annual wet deposition in 2000 and 2050 under the B1, A1B, and A1FI scenarios. (Unit: $\mu g/m^2$)

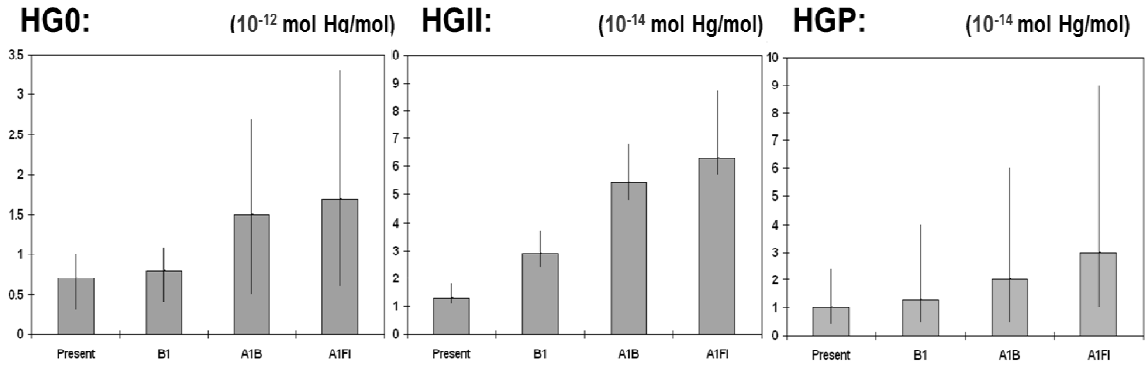

Figure 8.6. Simulated average mixing ratio of annual mean surface mercury species over the continental U.S. in 2000 and 2050 under the B1, A1B and A1FI scenarios (including both climate change and emission schanges)

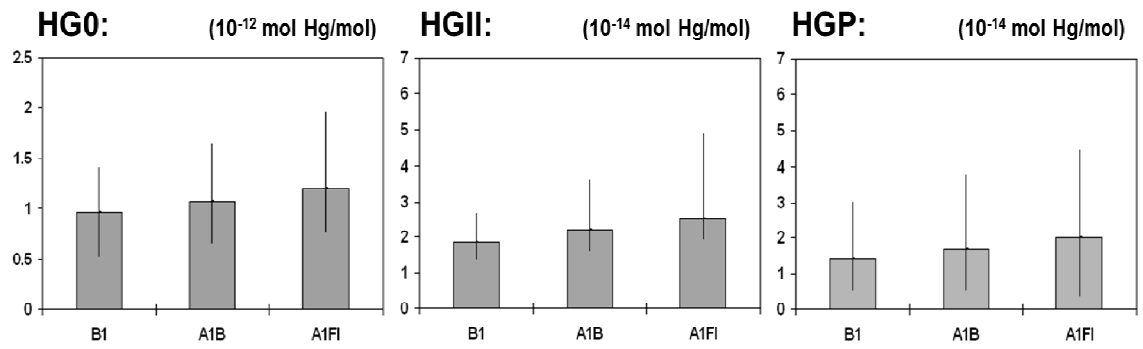

Figure 8.7. Simulated average mixing ratio of annual mean surface mercury species over the continental U.S. in 2050 under the B1, A1B and A1FI scenarios considering climate change effects only.

CHAPTER 9: CONCLUSION AND FUTURE WORK

Changes in global climate and pollutant emissions are very likely to continue in the coming decades driven by the human-related activities and natural fluctuations in climate system. These potential changes would have very important consequences on regional air quality over the contiguous United States due to their effects on atmospheric chemical and physical processes. To understand these effects, the present studies use the global Climate chemistry model, CAM-Chem version 3, to systematically assess potential changes in major air pollutants including surface ozone, particulate matter and mercury from the present (1998–2002) to the 2050 (2048–2052). The projections of future air quality consider changes in global climate, precursor emissions from anthropogenic and biogenic sources, and pollutant transport. Moreover, to evaluate the projection uncertainties resulting from different plausible trends of climate and emissions as a result of unknown human-related activities and climate variations, three IPCC SRES scenarios, A1FI, A1B and B1, are considered and compared to evaluate the resulting uncertainty in projecting future pollutant concentrations. To achieve a better understanding on the effect of mineral dust emissions on changes in future air quality especially the PM concentrations, a physical dust aerosol module is developed in the CAM-Chem model. In addition, a mercury module is also developed to simulate the atmospheric cycle of mercury and its consequences on the toxicity of U.S. air quality.

By incorporating all the modifications on CAM-Chem model and considering changes in global climate and anthropogenic emissions, the U.S. air quality is projected

to 2050. The results for future changes and concentrations of major pollutants are summarized in following paragraphs.

9.1 Ozone air quality

We investigate the effects of projected global changes in climate and human-related emissions for the year 2050 relative to 2000 for trends in the potential risk of hazardous ozone pollution episodes, which has not been examined in previous study. It is found that the projected changes in air temperature, precipitation, lighting, planetary boundary layer height and cyclone activities tend to intensify the associated extreme weather conditions that foster the risk of high ozone pollution episodes over many parts of the world. It is also found that the regional summertime daily 8-hour maximum surface ozone concentration in 2050 largely depends on changes in the anthropogenic emissions of ozone precursors. Our analysis on the frequency of "hazardous ozone days" in which the peak ozone concentration exceed the limit in the summer of 2050, based on 8 and 1-hour standards, show that under the a1b and b1 scenarios the risk of hazardous ozone pollution episodes will likely decrease in developed regions, but increase in developing regions. Under the a1fi scenario, the hazardous risks in all regions increase. The frequency of hazardous ozone days in summertime is derived to be 6-73 days for North America, 0-39 days for Europe, and 47-79 days for Asia under the 8-hour definition, and 0-57 for North America, 0-17 for Europe, and 4-59 for Asia under the 1-hour definition. The difference can be understood through statistical analysis of cumulative frequency distribution of daily peak ozone concentrations, which shows that the changes of ozone level are relatively more significant on the high value part.

In addition to the high ozone risk study, we also investigate the relative contributions of changes in local anthropogenic emissions (LE) versus changes in remote anthropogenic emissions (RE) on global surface ozone air quality in 2050 in order to better understand the origin of pollution change and provide more comprehensive reference for local air quality control than previous studies. We find that projected anthropogenic emissions changes under the A1FI scenario lead to an increase of 5-14 ppb in 2050 summertime daily 8 hour maximum (D8HM) ozone concentration over U.S., 48% of which is contributed by LE changes and the rest 52% is contributed by RE changes. For Europe, the change in local emissions contributes 62% of the surface ozone increase in 2050 summer, while 38% of the increase is attributed to remote emission change. For Asia, LE changes dominate the 2050 surface ozone change with an increase of 10-30 ppb on summertime D8HM ozone concentration. However, under the A1B and B1 scenarios, contributions from LE changes are much larger than that from RE changes over all three regions except the Asia under the B1 scenario, in which the RE changes contribute 31% of total change. The results indicate that for the United States and Europe, pollution control is a local issue under low global emission situations, while it becomes an international issue when fossil fuel use is rapidly increasing in the world. Due to the weak Euro-Asia transport, local emission increase seems to be the main problem for Asia's ozone air quality under all cases except the low emission scenario B1.

9.2 Particulate Matter air quality

Before examining the future changes in Particulate Matter (PM) air quality, a physical dust aerosol model that better consider the mineral dust process is developed and

incorporated into the CAM-Chem to reproduce the dust pollution over the globe. We developed previous wind erosion theory by Shao et al, by considering important physical processes including snow cover and frozen soil that have not been considered. The improved new dust emission theory can fit the requirements by simulations under all possible global soil/meteorology conditions. We also used the dynamic soil and vegetation information provided by community land surface model to consider the effect of climate change on surface environment and its projection on dust emission. Transport of dust is treated as aerosol size bins. Deposition is determined by size resolved particle and precipitation aerodynamics. As a result, this model has been developed into a state of art process-based atmospheric dust aerosol model that has better representative of natural dust processes than previous dust models. The main features of a model climatology generated from a 1998–2002 simulation were presented. The spatial and temporal patterns of the simulated atmospheric dust are then evaluated against the best available measurements worldwide. The evaluation includes both surface dust concentrations and annual total dust depositions. Surface concentrations are compared with observations from 16 sites in University of Miami Ocean Aerosol Network. Then the simulated mean annual dust deposition is compared with the reported observations of deposition from publications. For both quantities, the model captures the major characteristics of their geographic distributions and seasonal variations. The overall model performance is comparable to other published model results but it is able to capture dust effects not represented in previous studies. Therefore, the dust module in CAM-Chem can be used as a basic modeling tool to better understand the physical processes that govern the emission, transport, and deposition of atmospheric dust aerosols.

After successfully incorporating the mineral dust module, the CAM-Chem model is employed to project the 2050 Particulate matter levels in the United States and analyze the effect of climate change and anthropogenic emission change. It is the first-time projection of future total PM concentrations, which has not been studied due to the limitations in previous modeling tools that have not incorporated all components together. To ensure that the model provides a good representation of present-day PM pollution in the United States through comparisons of surface concentrations with U.S. EPA air quality system observations and CASTNET measurements, and surface composition with IMPROVE measurements. The comparisons show that CAM-Chem model can reproduce the spatial and temporal patterns of PM concentrations and the composition in the United States. As a result of individual factor, the effect of changes in climate during 2000-2050 on particulate matter is presented as increases in natural emissions including mineral dust and organic aerosols, and increase in the productivity of chemical reactions associated with secondary inorganic aerosols. It is projected to increase the levels of particulate matter in 2050 by 0-10 $\mu g/m^3$ for PM2.5 and 0-14 $\mu g/m^3$ for PM10 in the eastern and western US, but decrease PM2.5 by 0-6 $\mu g/m^3$ and 0-10 $\mu g/m^3$ for PM10 in the central United States. The seasonality of climate change effects is distinct with stronger effects in summer and weaker in winter. Simulations based on 2050 climate and emissions show that the changes in anthropogenic emissions decrease PM25 by 2-18 $\mu g/m^3$ and PM10 by 2-22 $\mu g/m^3$ relative to the climate change alone results. The seasonality of the extra changes in PM concentrations is indistinct. Changes in climate and emissions also affect the PM composition. As a result of changes in anthropogenic emissions, the percentages of inorganic aerosols and elemental carbon decrease in both

PM2.5 and PM10 by 2050. Organic aerosols are more affected by climate change than anthropogenic emission change, and the ratio of it in total PM increases following all three IPCC scenarios. Under the IPCC A1FI scenario, the percentages of mineral dust over the eastern and western US increased by 10%-20%. The magnitude of changes in mineral dust decreases under the A1B scenario, and becomes less than 2% under the B1 scenario.

In addition, we also examine the competition for ammonia between nitrate and sulfate aerosol formations. The role of this mechanism in aerosol concentration change has not been as completely analyzed in previous study. Sensitivity experiments with reduction of sulfate precursor emissions in CAM-Chem shows that changes in nitrate concentration linearly correlate to sulfate precursor reduction in winter. As a result, the nitrate concentration in winter shows a nonlinear correlation to precursor emission. Nitrate concentration changes in summer do not well linearly relate to changes in sulfate precursor emission, because of the effect of humidity and sulfate concentrations on nitrate aerosol formation. The concentration-precursor emission relationship for sulfate is not significantly affected by the competition with nitrate. Changes in sulfate concentrations show very good linear correlation with changes in precursor emissions in SOx emission reduction experiments and little correlation with changes in nitrate precursor emissions in NOx emission reduction experiments. The emission change experiment following the IPCC A1B emission change scenario shows that surface nitrate concentration in the major industrial region will increase by 2050, although the nitrate precursor emission will reduce to 63% of present-day level. The reduction in sulfate precursor emissions and increase in ammonia emissions leads to the converse change in

nitrate concentrations in response to its emission perturbations through the competition mechanism. That indicates the future emission control strategy may not effective to reduce the aerosol pollution in industrial regions.

9.3 Mercury effects on air quality

In order to better consider the mercury effects on air quality and effects of environmental factors on it, a mechanistic representation of the atmospheric mercury cycle is developed for the state-of-the-art global climate-chemistry model, CAM-Chem (Community Atmospheric Model with Chemistry). The model simulates the emission, transport, transformation and deposition of atmospheric mercury (Hg) in three forms: elemental mercury (Hg0), reactive mercury (HgII), and particulate mercury (HgP). Emissions of mercury include those from human, land, ocean, biomass burning and volcano related sources. Land emissions are calculated by a dynamic scheme that considers soil emissions, vegetation emissions and rapid reemission of deposited mercury. A simplified air-sea mercury exchange scheme is used to calculate emissions from the oceans. The chemistry mechanism includes the oxidation of Hg0 in gaseous phase by ozone with temperature dependence, OH, H_2O_2 and chlorine. Aqueous chemistry includes both oxidation and reduction of Hg0. Transport and deposition of mercury species are calculated through adapting the original formulations in CAM-Chem. The CAM-Chem model with mercury is driven by present meteorology to simulate the present mercury effects on air quality during the 1999-2001 period. Resulting surface concentrations of total gaseous mercury (TGM) are then compared with observations from worldwide sites. Simulated wet depositions of mercury over the continental United

States are compared to observations on 26 Mercury Deposition Network stations to test the wet deposition simulations. The evaluations of gaseous concentrations and wet deposition confirm a strong capability for the CAM-Chem mercury mechanism to simulate the atmospheric mercury cycle. The results also indicate that mercury pollution in East Asia and Southern Africa is very significant with TGM concentrations above 3.0 ng/m^3. The comparison to wet deposition indicates that wet deposition patterns of mercury are more affected by the spatial variability of precipitation. The sensitivity experiments show that 22% of total mercury deposition and 25% of TGM concentrations in the United States results from domestic anthropogenic sources, but only 9% of total mercury deposition and 7% of TGM concentrations are contributed by transpacific transport. However, the contributions of domestic and transpacific sources on the western United States levels of mercury are comparable.

Future changes in mercury effects on air quality have not been adequately understood in previous studies. To investigate the effects of 2000-2050 global change in climate and emissions on atmospheric mercury concentrations in the United States, the meteorology and mercury emissions including sources from anthropogenic, land, ocean, biomass burning and volcano are all projected to 2050. As a result, we find that the U.S. TGM concentration in 2050 may have a 2.1-4.0 $\mu g/m^2$'s increase on the eastern and around 1.4-3.0 $\mu g/m^2$'s increase on the western U.S. under the A1FI scenario. The potential changes in wet deposition under the A1FI scenario are around 10-14 $\mu g/m^2$ for the eastern U.S. and around 2-4 $\mu g/m^2$ for the western U.S. The increase of HgII in emissions tends to enhance the wet deposition. The TGM concentrations over the contiguous U.S. in 2050 under the B1 scenario are close to the observed present levels.

Effects of climate warming and emission increase in global range under the B1 scenario result in a domestic mercury emissions decrease. Through the analysis of individual effects, we also found that the effect of changes in anthropogenic emission contributes 32%-53% of the changes in future concentrations of mercury compounds, which is close to the ratio of 47%-68% contributed by the effects of climate change with associated natural emissions changes.

9.4 Future Works

Given the results presented in this thesis, three major issues are identified and worth addressing in the future, improving models to consider more processes that are important for air quality, considering the effect of changes in land use and surface environment on air quality change, and explore the change in risk of extreme air quality episodes.

9.4.1 Model development

Through this study, it is found that the projections of future air quality highly depend on the modeling scheme. Some biases are caused by the uncertainties in the modeling approach. One example is the simulations of wet depositions of mercury and mineral dust, which have problems in reproducing the strong wet deposition off the east coast of the United States. In addition, incorporating more chemical or physical processes is another important research area for model development. For example, mineral dust emissions and associated atmospheric effects can involve many physical and chemical processes. Mineral dust can affect the aqueous and heterogeneous reactions in clouds by

adding soluble chemicals into the cloud droplet. Mineral dust also reduces the alkalinity of the atmosphere through the reactions of soil particles with the acid chemicals in the atmosphere. It also increases the deposition of atmospheric pollutants through electrostatic adherence. A more advanced dust model is needed to consider these important processes.

9.4.2 Effect of changes in land use on air quality

The changes in land use and surface environment are expected to have significant effects on air quality. The land use change is an important factor affecting future emissions of mineral dust. The projection of changes in land use is not considered in this study, which may affect the analysis of dust. In addition, the biogenic emissions of organic carbon are also seriously affected by land use change. However, the projection of land use change is notoriously difficult. There remain many uncertain factors, including human activities, changes in agriculture, ecological transition etc. can result in land use change. Therefore, much effort is needed to address uncertainties and to improve projections of the change in future land use. After all, the effect of land use change on future air quality is an interesting topic to examine in the future studies.

9.4.3 Explore the risk of extreme pollution episodes

The most extreme pollution episodes are different from the high pollutant episodes in this study, and are associated with extreme meteorological conditions and/or extreme emissions episodes. These are difficult to project. However, the risk of extreme

pollution episodes rather than the prediction of a certain episode can be assessed. Further studies are needed to explore the understanding of such events.

Appendix A: Description of Physical Dust Aerosol Model

The Physical Dust Aerosol Model (PDAM) is developed based on Shao's soil erosion theory with consideration of the main physical processes associated with dust emission processes under various climate and surface conditions. To match the present air quality standards for aerosols, dust is divided into 4 size ranges. They are 0.1-1.0 μm, 1.0-2.5 μm, 2.5-10.0 μm and 10.0-40 μm. The soil particle-size distributions within groups are regarded as a composite of several lognormal distributions [Gomes et al., 1990; Chatenet et al., 1996]. In the model calculation, each size group is divided into 100 sub-groups to better considering the aerodynamic characteristics. To better interpret the model principles, physical equations and methods from Shao's book (Physics and Modeling of Wind Erosion, 2008) are summarized below.

A.1. Dust emission Scheme

The dust emission scheme consists of three components for computing threshold friction velocity, streamwise sediment transport and dust emission. This scheme is summarized below in this section for completeness.

A.1.1. Particle Size Distribution

A soil is characterized by its particle size distribution (mass probability density function), $p_s(d)$. The mass fraction of particles in the particle size interval $[d, d + \delta_d]$ is

given by $p_s(d)\ \delta_d$. This particle size distribution is a weighted average of $p_m(d)$ and $p_f(d)$, the minimally and fully dispersed parent soil particle size distribution, respectively:

$$p_s(d) = \gamma p_m(d) + (1-\gamma) p_f(d), \qquad (1)$$

where γ is the weight for $p_m(d)$ and (1 - γ) is that for $p_f(d)$. Both $p_m(d)$ and $p_f(d)$ can be determined through laboratory particle size analysis. There are two limiting cases for $p_s(d)$, namely,

$$p_s(d) \to p_m(d) \quad \text{weak erosion} \qquad (2)$$

$$p_s(d) \to p_f(d) \quad \text{strong erosion.} \qquad (3)$$

The choice of γ satisfies the requirements that

$$\gamma \to 1 \quad \text{weak erosion, } u_* \sim u_{*f} \qquad (4)$$

$$\gamma \to 0 \quad \text{strong erosion, } u_* \gg u_{*f}. \qquad (5)$$

where u_* is friction velocity and u_{*f} is threshold friction velocity (should be understood as the threshold friction velocity of the surface). A possible approximation for γ is

$$\gamma = e^{-k(u_* - u_{*f})^n}, \qquad (6)$$

with k and n being empirical coefficients that can be determined by fitting (6) to experimental data (k = 27.3 and n = 3 have been found). In this study, we used values k = 1 and n = 3, as k = 27.3 is probably too large [Shao et al., 2008].

A.1.2. Streamwise Sand Flux

We separate soil particles into sand and dust categories. This is done by introducing a critical particle size, d_c, which is the solution of

$$w_t(d_c) = \alpha_d \kappa u_*$$ (7)

where w_t is the particle terminal velocity, $\kappa = 0.4$ is the von Karman constant and α_d is an empirical parameter, commonly set to 0.5 to 1. The meaning of d_c is that particles smaller than d_c are easily dispersed in the atmosphere while particles larger than d_c are not. For $\alpha_d = 0.5$ and $u_* = 0.5$ ms^{-1}, d_c is around 35 μm.

The saltation of sand sized particles plays a critical role in the process of dust emission. For a given particle size, d_s, the streamwise saltation flux $\tilde{Q}$ can be calculated using

$$\tilde{Q}(d_s) = \begin{cases} \frac{c_o \rho u_*^3}{g}\left(1 - \frac{u_{*t}^2}{u_*^2}\right) & u_* \geq u_{*t} \\ 0 & u_* < u_{*t} \end{cases}$$ (8)

where c_o is a coefficient of order one, ρ is air density, g is acceleration due to gravity, u_* is friction velocity and u_{*t} is threshold friction velocity, a function of d_s. The calculation of u_{*t} will be described later. The streamwise saltation flux for all particle sizes can be estimated using

$$Q = \int_{d_1}^{d_2} \tilde{Q} p_s(d) \delta d$$ (9)

where d_1 and d_2 are the lower and upper size limits of particles in saltation. It is worthwhile to point out that (8) is originally derived for the so-called transport-limited saltation, i.e., saltation under the condition of unlimited supply of saltation material. Saltation under the condition of limited supply of saltation particles is called supply-limited saltation. Conceptually, (8) can be made applicable to supply-limited saltation by allowing u_{*t} to vary with surface conditions as saltation proceeds. For instance, $u_{*t} = \infty$ implies that the supply of saltation particles is zero. In the wind erosion scheme used in this study, u_{*t} is allowed to vary with surface conditions and hence, the supply-limited saltation has been partially considered. However, a satisfactory description of the evolution of u_{*t} during a wind erosion process is not yet possible.

A.1.3. Dust Emission

Three dust emission mechanisms are considered in the model:

(1). Aerodynamic entrainment: Dust particles can be lifted from the surface directly by aerodynamic forces. However, as the importance of gravity and aerodynamic forces diminishes for smaller particles and the interparticle cohesion becomes important, dust emission arising from direct aerodynamic lift is small in general;

(2). Saltation bombardment: As saltating particles (sand or aggregates) strike the surface, they cause localized impacts which are often strong enough to overcome the binding forces acting upon dust particles, leading to dust emission. The wind tunnel experiments of Shao et al. [2008] show that the dust emission rate caused by this mechanism is an order of magnitude larger than the aerodynamic entrainment; and

(3). Aggregates disintegration: Under natural conditions, dust particles often exist as dustcoats attached to sand grains in sandy soils or as aggregates in soils with a high clay content. During a weak wind erosion event, sand particles coated with dusts and clay aggregates behave as individuals and dust particles may not be released, while during a strong wind erosion event, dustcoats and soil aggregates may disintegrate resulting in increased dust emission. The importance of this mechanism is probably similar to that of saltation bombardment.

The dust emission rate related to these three mechanisms is formally expressed as

$$F = F_a + F_b + F_c \qquad (10)$$

In calculating F, we distinguish the dust emission in the absence of saltation from that in the presence of saltation, namely,

$$F = \begin{cases} F_a & \text{weak wind, no saltation} \\ F_b + F_c & \text{strong wind, with saltation} \end{cases} \qquad (11)$$

In modeling dust storms, the latter expression is used.

We divide dust particles into I size intervals, each with a mean value d_i (I = 1, …, I) and an increment Δd_i. As derived by Shao [2001], the emission of dust in the ith group generated by saltation bombardment and aggregates disintegration of particles of size d_s is given by

$$\tilde{F}(d_i, d_s) = c_Y \left[(1-\gamma) + \gamma \frac{p_m(d_i)}{p_f(d_i)} \right] \frac{\tilde{Q} g}{u_*^2 m} \left(\rho_b \eta_{fi} \Omega + \eta_{ci} m \right) \qquad (12)$$

where $c_Y = 1/7\ c_o$ is set to 0.05, ρ_b is soil bulk density, η_{fi} is the dust fraction given by

$$\eta_{fi} = \int_{d-\Delta d_i/2}^{d+\Delta d_i/2} p_f(d)\delta d, \qquad (13)$$

and η_{ci} is the dust fraction in aggregation given by

$$\eta_{ci} = \int_{d-\Delta d_i/2}^{d+\Delta d_i/2} \left[p_f(d) - p_m(d)\right]\delta d, \qquad (14)$$

$\Omega$is the volume removal (abrasion) caused by saltation and m is dust particle mass. As derived by Lu and Shao [1999], Ωassociated with a saltating particle of size ds with mass ms can be approximated by

$$\Omega \approx \frac{100u_*^2}{\beta^2}\left[0.24d_s + \frac{2.5u_*}{\beta}\right] \qquad (15)$$

with

$$\beta = \sqrt{2Sd_s/m_s}$$

and S being the soil drag force (force per unit area exerted by soil on a particle moving through it). S is considered as a property of the soil. Soft soils have smaller values of S than hard soils.

The emission of dust particles of size d_i caused by the saltation of all sand sized particles (sand plus aggregates) can be estimated as a weighted average

$$\breve{F}(d_i) = \int_{d_1}^{d_2} \bar{F}(d_i, d) p_s(d) \delta d. \qquad (16)$$

Note the integration is over the particle size range of saltating particles. Finally, the total dust emission is given by

$$F = \int_0^{d_c} \breve{F}(d) p_s(d) \delta d. \qquad (17)$$

where d_c is defined by (7). Note that the integration is over the size range of dust particles.

In this study, we concentrate on three particle size categories: d ≤2 μm; 2 < d ≤11 μm and 11 < d ≤22 μm. The dust fluxes for these different categories, F_1, F_2 and F_3 can be estimated by

$$F_1 = \int_0^{2\mu m} \breve{F}(d) p_s(d) \delta d \qquad (18)$$

$$F_2 = \int_{2\,\mu m}^{11\mu m} \breve{F}(d) p_s(d) \delta d \qquad (19)$$

$$F_3 = \int_{11\mu m}^{22\mu m} \breve{F}(d) p_s(d) \delta d \qquad (20)$$

The concentrations of dust corresponding to the three particle size groups will be denoted as c_1, c_2 and c_3, respectively.

A.2. Threshold Friction Velocity

The threshold friction velocity for the surface u_{*t}, depends on d_s and several factors including roughness frontal area index, λ, soil moisture, w, salt concentration in soil, s_c, etc. [Shao, 2000]. A pragmatic way of calculating u_{*t} is to express it in the following form

$$u_{*t}(d_s, \lambda, w, s_c, \ldots) = u_{*t0}(d_s) f_\lambda(\lambda) f_w(w) f_{sc}(s_c) f_{cr}(c_r) \qquad (21)$$

where $u_{*t0}(d_s)$ is the threshold friction velocity for sand particle of size d_s in the idealized situation when soil is dry, bare and free of salt and crust. In this study, $u_{*t0}(d_s)$ is calculated using the expression given by Shao and Lu [2000]:

$$u_{*t0}(d_s) = \sqrt{a_1\left(\sigma_p g d_s + \frac{a_2}{\rho d_s}\right)} \qquad (22)$$

where σ_p is particle-to-air density ratio. The coefficients $a_1 = 0.0123$ and $a_2 = 3 \times 10^{-4}$ kg s^{-2} are empirical coefficients obtained from fitting the above expression to wind tunnel observations.

The multiplicators f_λ, f_w, f_{sc} and f_{cr} are correction functions for surface roughness elements, soil moisture, salt concentration and crust, respectively. The first correction function has been derived based on conceptual analysis and wind tunnel data

$$f_\lambda = (1 - m_\gamma \sigma_\gamma \lambda)^{1/2} (1 + m_\gamma \beta_\gamma \lambda)^{1/2} \qquad (23)$$

According to Wyatt and Nickling [1997], β_r, σ_r and m_r are respectively 202, 1.45 and 0.16. The correction function f_w follows

$$f_w = \left[1 + A(\theta - \theta_r)^b\right]^{1/2} \qquad (24)$$

where θ is volumetric soil moisture. The air-dry soil moisture θ_r and the empirical coefficients A and b are soil type dependent. The correction function f_{sc} is basically of exponential form

$$f_{sc}(s_c) \propto exp(a_s s_c)$$

In this study, $f_{sc}(s_c)$ is set to 1, as no information of s_c is available. Gillette et al. [2001] have presented observational evidence for f_{cr}. However, the implementation of f_{cr} cannot be done readily, as the information for surface crust c_r is too difficult to obtain. Also f_{cr} is set to 1 in this study.

A.3. Dust Transport and Deposition

The treatment of dust transport and deposition is as described by Lu and Shao [2001]. Suppose the concentration for the ith particle size group is c_i, then the total dust concentration is

$$c_{tl} = \sum_{i=1}^{t} c_i.$$

The evolution of c_i obeys the conservation equation, written in the σ-coordinate system ($\sigma = p/p_s$, with p being atmospheric pressure and p_s being surface atmospheric pressure):

$$\frac{\partial p_s c_i}{\partial t}+\frac{\partial p_s u c_i}{\partial x}+\frac{\partial p_s v c_i}{\partial y}+\frac{\partial}{\partial \sigma} c_i\left(p_s \dot{\sigma}+g \rho w_{ti}\right)$$
$$=p_s \frac{\partial}{\partial x} K_{ph} \rho \frac{\partial c_i / \rho}{\partial x}+p_s \frac{\partial}{\partial y} K_{ph} \rho \frac{\partial c_i / \rho}{\partial y}$$
$$+\frac{g^2}{p_s} \frac{\partial}{\partial \sigma} K_{pz} \rho^3 \frac{\partial c_i / \rho}{\partial \sigma} \qquad (25)$$

with boundary conditions

$$c_i\left(p_s \dot{\sigma}+g \rho w_{ti}\right)-\frac{g^2}{p_s} K_{pz} \rho^3 \frac{\partial c_i / \rho}{\partial \sigma}=g \rho\left(F_i-F_{di}\right) \quad \text{for } \sigma=1$$
$$\frac{\partial c_i / \rho}{\partial \sigma}=0 \quad \text{for } \sigma=0 \qquad (26)$$

In the equations above, w_{ti} and F_{di} are the particle settling velocity and dust deposition rate for the ith particle size group, respectively; and u, v and $\dot{\sigma}$ are wind velocities. The horizontal particle diffusivity K_{ph} is assumed to be equal in the x and y directions. The vertical particle diffusivity K_{pz} is a function of particle size, estimated through a modification of the eddy diffusivity for neutral particles. The relationship between the eddy diffusivities for neutral and dust (heavy) particles follows the formulation of Csanady [1963]. Although there are more recent models on particle diffusivity, it can be shown that the Csanady model is sufficiently accurate for the purpose of this study and therefore has been used.

Dust particles are removed only by dry deposition at the surface. The deposition rate due to settling and turbulent diffusion is modeled as

$$F_{di}=c_{i0}\left(w_{ti}+v_{di}\right)$$

where c_{i0} is the value of c_i at surface. The dry deposition velocity, v_{di}, is parameterized following Raupach et al. [2001]. In general, the settling velocity w_t is a function of particle size, which can be estimated using

$$w_t(d) = \left(\frac{4\rho_p g d}{3\rho C_d (Re_t)} \right)^{1/2} \qquad (27)$$

where $Re_t = w_t\, d/\nu$ is particle Reynolds number at settling velocity (ν is kinematic viscosity) and the drag coefficient, C_d, is approximated calculated by

$$C_d(Re_t) = \frac{24}{Re_t}\left(1 + 0.15 Re_t^{0.687}\right).$$

The effective settling velocity for each particle size group is estimated by

$$w_{ti} = \frac{\int w_t(d) p_s(d) \delta d}{\int p_s(d) \delta d}$$

Equation (25) is solved by splitting the advective and diffusion terms. Advection is further split into horizontal and vertical terms. The horizontal advection term is treated using a multidimensional wave-propagation slope-limiter scheme which is second order accurate both in time and space [LeVeque, 1996]. It eliminates oscillations and maintains positivity, an important requirement for dust concentration. The vertical advection term is treated using the scheme of Bott [1989]. This scheme is positive definite but not monotonic. It is mass conserving and has very small numerical diffusion. Second order, area preserving polynomials are used inside the domain. These polynomials were derived

assuming variable grid spacing. The order of the polynomials is reduced to one near the domain boundary. The vertical diffusion is solved by using a fully implicit scheme and the algebraic equation system from the discretization is solved using the Thomas algorithm. Dust emission and dry deposition are computed together with the vertical diffusion.

Appendix B: Description of Mercury Emission Schemes

The mercury emission schemes used in this study are developed based on present studies on land and ocean emissions of mercury. Detailed descriptions of two schemes are introduced below:

B.1. Land emission scheme

Land sources include emissions from soil and vegetation, plus rapid reemissions of deposited mercury. Soil and vegetation contribute about 500-1800 Mg yr^{-1} [Lindqvist, 1991; Seigneur et al, 2001; Selin et al., 2007], while reemissions range in 260-1500 Mg yr^{-1} [Selin et al., 2008; Nicole et al., 2010], with their total estimate of 1100-3000 Mg yr^{-1}. Land emissions depend on both soil temperature [Lindberg et al., 1995; Poissant and Casimir, 1998] and surface solar radiation [Carpi and Lindberg, 1998; Zhang et al. 2001; Gustin et al., 2002]. Land mercury emissions are calculated using local temperature, solar flux, and estimated source distribution. The emission flux (F_1) is distributed over the globe according to the locations of mercury industries [Frank, 1999]. It is then adjusted using the relationship suggested by Zhang et al. [2001] and Poissant and Casimir [1998]:

$$F_2 = F_1 \exp[-1.1\times10^4 (1/T_s - 1/T_0)] \exp[1.1\times10^3 (R_s - R_0)]$$

where F_2 is the calculated land emission flux. R_s is the surface solar radiation flux and T_s is the local surface skin temperature. The reference value is 340 Wm^{-2} for R_0 and 288 K for T_0. The parameterization is subject to calibration using the 1995-2005 monthly mean R_s and T_s distributions from the NECP reanalysis to constrain the global annual total emission of 2900 Mg yr^{-1} estimated for 2000 [Nicole et al., 2010].

To consider the change in land storage of mercury and project the future changes, the scheme is modified based on the latest estimate of present mercury storage and projection of changes in anthropogenic emissions. Changes in global land mercury storage are related to the net deposition flux above the land and ocean. Anthropogenic and volcanic sources bring new mercury chemicals into the biogeochemical cycle of mercury. Therefore, the projections of these emissions contribute to the net mercury storage change. The latest estimate of present land mercury storage is around 240,000 Mg with a total deposition of 3260 Mg/yr and a total land emission of 2900 Mg/yr [Smith-Downey et al., 2010]. This suggests a net new mercury increase in the surface land reservoir of 360 Mg/yr; the land surface reservoir accounts for up to 13% of the total net mercury emissions (anthropogenic + volcanic: 2770 Mg/yr). Based on CAM-Chem simulations, an estimate of net increase in the atmospheric reservoir for the present atmosphere shows that around 1% of new emitted mercury will stay in the atmosphere. The other (86%) of the new mercury is deposited into the surface ocean. We assume that these ratios of the new mercury are maintained from 2000 to 2050. This relationship is used in the dynamic emission schemes in the CAM-Chem Hg model to calculate the future emission fluxes.

The land emission scheme is modified by considering the change in land mercury storage. The modified scheme is:

$$F_2 = F_1 \exp[-1.1\times10^4 (1/T_s - 1/T_0)] \exp[1.1\times10^3 (R_s - R_0)] \times C_i$$

where R_s is surface solar radiation and T_s is surface skin temperature. R_0 is the reference surface solar radiation with a value of 340 Wm^{-2}. T_0 is the reference surface temperature

with a value of 288K. F_1 is the standard emission dataset. C_i is the enrichment factor following each scenario. C_i is calculated as following:

$$C_i = \frac{S_p + \alpha n(E_p + E_f)/2}{S_p}$$

where S_p is the present land storage of mercury (240,000 Mg). E_p is the present total new mercury emission amount. E_f is the projected new mercury emission amount. The value of α is is determined by the ratio of new mercury into the land reservoir. We assume that the net increase of new mercury follows a linear trend. The parameter n is the number of years relative to 2000. Here the value of n is 50.

B.2. Ocean emission scheme

Ocean emissions are determined by a simplified air-sea exchange scheme that has been tested through field campaigns for good agreement with observations [Liss and Slater, 1974; Wängberg et al., 2001]. We estimate monthly mean mercury concentrations in surface oceans through the following scheme that also removes the dependence on the mercury storage in deep oceans:

$$F = K_w(C_w - C_a \quad H')$$

where F is the ocean emission flux of mercury; Kw is the gas transfer velocity of a species in the water-air interface based on the empirical relation of Wanninkhof [1992]:

$$Kw = 0.31u_{10}^2\left(\frac{S_{chg}}{600}\right)^{-0.5}$$

where ScHg is the Schmidt number of Hg and u10 is the wind speed at 10 m height. C_w and C_a are respectively the Hg0 concentration in the mixed-layer ocean (pg/L) and in the

surface atmosphere (ng/m^3). C_w is simplified by using the monthly mean concentration data [Soerensen et al., 2010], while C_a is determined by the atmospheric model.

H′ =[Hg]g/[Hg]aq

is the dimensionless Henry's-Law constant calculated at water temperatures (Tw) [Clever et al., 1985]:

$Log10(H)$= -1078/T+6.250

where H has the unit of Atm divided by molar fraction and T is the absolute temperature in Kelvin.

The ocean emissions scheme is modified by considering the mercury concentration change in the ocean mixing layer. The modified simple model is:

$$F = K_w((C_w + m_i) - C_a / H')$$

where m_i is the scenario-specific change in mercury concentration in the ocean mixing layer based on present value. Other variables and calculations are kept. As shown by Soerensen et al. [2010], 40% of the Hg in the ocean mixing layer is affected by the subsurface water. The change in the mercury exchange between the mixing layer and the subsurface water are neglected. 60% of the net deposition of new mercury will stay in the ocean mixing layer [Strode et al., 2007]. The m_i is calculated using

$$m_i = \frac{60\% \beta n(E_p + E_f)/2}{71\% \times 4\pi R^2 \times d}$$

where β is the division ratio of new mercury into the surface ocean reservoir. It is estimated based on the present distribution of mercury deposition from anthropogenic sources. E_p is the present total new mercury emission amount. E_f is the projected new

mercury emission amount, n is the number of years projected away from the present, and R is the radius of the Earth. The factor 71% accounts for the earth's surface covered by oceans. The parameter d is the depth of ocean mixing layer. We set it to 50 meters as an average depth.

References

Adams, B., A. White, and T. Lenton, 2004, An analysis of some diverse approaches to modeling terrestrial net primary productivity. Ecol. Modell., 177, 353–391.

Akimoto, H., 2003, Global air quality and pollution, Science, 302(5651), 1716–1719, doi:10.1126/science.1092666.

Amann, M., D. Derwent, B. Forsberg, O. Hanninen, F. Hurley, M. Krzyzanowski, F. de Leeuw, S. J. Liu, C. Mandin, J. Schneider, P. Schwarze, D. Simpson, 2008, Health risks of ozone from long-range transboundary air pollution. World Health Organization. Copenhagen, 93 p.

Baker, P., Brunke, E., Slemr, F., and Crouch, A., 2002, Atmospheric mercury measurements at Cape Point, South Africa, Atmos. Environ., 36, 2459–2465.

Bergan, T., L. Gallardo, and H. Rodhe, 1999, Mercury in the global troposphere: A three-dimensional model study, Atmos. Environ., 33, 1575–1585.

Bertschi, I. T., and D. A. Jaffe, 2005, Long-range transport of ozone, carbon monoxide, and aerosols to the NE Pacific troposphere during the summer of 2003, Observations of smoke plumes from Asian boreal fires, J. Geophys. Res., 110, D05303, doi:10.1029/2004JD005135.

Bullock, O., and Brehme, K., 2002, Atmospheric mercury simulation using the CMAQ model: formulation description and analysis of wet deposition results, Atmospheric Environment 36 (2002), pp. 2135–2146.

Bullock, O., Atkinson, D., Braverman, T., Civerolo, K., Dastoor, A., Davignon, D., Ku, J-.Y., Lohman, K., Myers, T.C., Park, R.J., Seigneur, C., Selin, N.E., Sistla, G., and Vijayaraghavan, K., 2008, The North American Mercury Model Intercomparison Study (NAMMIS): Study description and model-to-model comparisons. Journal of Geophysical Research 113, D17310, doi:10.1029/2008JD009803.

Bullock, O., Atkinson, D., Braverman, T., Civerolo, K., Dastoor, A., Davignon, D., Ku, J.-Y., Lohman, K., Myers, T. C., Park, R. J., Seigneur, C., Selin, N. E., Sistla, G., and Vijayaraghavan, K., 2009, An analysis of simulated wet deposition of mercury from the North American Mercury Model Intercomparison Study, J. Geophys. Res., 114, D08301, doi:10.1029/2008JD011224.

Brasseur, G. P., J. T. Kiehl, J.-F. Müller, T. Schneider, C. Granier, X. X. Tie, and D. Hauglustaine, 1998, Past and future changes in global tropospheric ozone: Impact on radiative forcing, Geophys. Res. Lett., 25, 3807–3810.

Calhoun, J. A. and E. Prestbo, 2001, Kinetic study of the gas phase oxidation of elemental mercury by molecular chlorine. Report available from Fron tier Geosciences, Inc., 414 Pon tius Av e nue N., Se at tle, WA 98109.

Calvert, J. and Lindberg, S., 2005, Mechanisms of mercury removal by O3 and OH in the atmosphere, Atmos. Environ., 39, 3355–3367, doi:10.1016/j.atmosenv.2005.01.055.

Carpi, A., and S. E. Lindberg, 1998, Application of a Teflon (TM) dynamic flux chamber for quantifying soil mercury flux: Tests and results over background soil, Atmos. Environ., 32(5), 873– 882.

Clean Air Act Amendments of 1990, 1992, Pub.L. 101-549, 104 Stat. 2399, 1990-11-15.

Clever, H.L., Johnson, S.A., and Derrick, A.E., 1985, The solubility of mercury and some sparingly soluble mercury salts in water and aqueous electrolyte solutions, J. Phys. Chem. Ref. Data 14, p. 631.

Collins, W. D., P. J. Rasch, B. A. Boville, J. J. Hack, J. R. McCaa, D. L. Williamson, B. P. Briegleb, C. M. Bitz, S.-J. Lin, and M. Zhang, 2006a, The Community Climate System Model Version 3 (CCSM3), J. Clim., 19, 2122–2143, doi:10.1175/JCLI3761.1.

Collins, W. D., P. J. Rasch, B. A. Boville, J. J. Hack, J. R. McCaa, D. L. Williamson, B. P. Briegleb, C. M. Bitz, S.-J. Lin, and M. Zhang, 2006b, The formulation and atmospheric simulation of the Community Atmosphere Model Version 3 (CAM3), J. Clim., 19, 2144–2161, doi:10.1175/JCLI3760.1.

Dairaku Koji, Seita Emori, and Hironori Higashi, 2008, Potential Changes in Extreme Events Under Global Climate Change, Journal of Disaster Research Vol.3 No.1.

Dawson, J. P., P. J. Adams, and S. N. Pandis, 2007, Sensitivity of ozone to summertime climate in the eastern USA: A modeling case study. Atmos. Environ., 41, 1494–1511.

Ding Ruiqiang，L.I. Jianping，and H.A .Kyung-Ja，2008，Decadal change of January and July persistence of monthly mean 500 hPa geopotential height anomalies，Geophysical Research Letters，Vol.35, L15702, doi:10.1029/2008GL034137.

Duncan, B.N., and I. Bey 2004, A modeling study of export pathways of pollution from Europe: Seasonal and Interannual variations (1987-1997), J. Geophys. Res., 109, D08301, doi:10.1029/2003JD004079.

Ebinghaus, R., H. H. Kock, C. Temme, J. W. Einax, A. G. Lowe, A. Richter, J. P. Burrows, and W. H. Schroeder, 2002, Antarctic springtime depletion of atmospheric mercury, Environ. Sci. Technol., 36, 1238– 1244

Emmons, L. K., Walters, S., Hess, P. G., Lamarque, J.-F., Pfister, G. G., Fillmore, D., Granier, C., Guenther, A., Kinnison, D., Laepple, T., Orlando, J., Tie, X., Tyndall, G., Wiedinmyer, C., Baughcum, S. L., Kloster, S., 2010, Description and evaluation of the Model for Ozone and Related chemical Tracers, version 4 (MOZART-4), Geosci. Model Dev., 3, 43-67, doi:10.5194/gmd-3-43-2010.

European Environment Agency (EEA), 2003, EEA Annual report 2002 and Environmental statement 2003.

European Environment Agency (EEA), 2010, EEA Annual report 2009 and Environmental statement 2010.

Ferrara, R., Mazzolai, B., Lanzillotta, E., Nucaro, E., and Pirrone, N., 2000, Volcanoes as emission sources of atmospheric mercury in the Mediterranean basin, The Science of the Total Environment, 259, 115-121.

Fiore, A. M., D. J. Jacob, I. Bey, R. M. Yantosca, B. D. Field, A. C. Fusco, and J. G. Wilkinson, 2002, Background ozone over the United States in summer: Origin, trend,

and contribution to pollution episodes, J. Geophys. Res., 107(D15), 4275, doi:10.1029/2001JD000982.

Fiore, A. M., L. W. Horowitz, D. W. Purves, H. Levy II, M. J. Evans, Y. Wang, Q. Li, and R. M. Yantosca, 2005, Evaluating the contribution of changes in isoprene emissions to surface ozone trends over the eastern United States, J. Geophys. Res., 110, D12303, doi:10.1029/2004JD005485.

Frank, D. G., 1999, Mineral Resource Data System (MRDS) data in ArcView Shape File Format, for Spatial Data Delivery Project, http://webgis.wr.usgs.gov/globalgis/metadata_qr/metadata%5Core_deposits.htm, U.S. Geol. Surv., Spokane, Wash.

Friedli, H.R., Radke, L.F., Prescott, R.,Li, P., Woo, J.-H., Carmichael, G.R., 2004, Mercury in the atmosphere around Japan, Korea and China as observed during the 2001 ACE Asia field campaign: measurements, distributions, sources, and implications. Journal of Geophysical Research 109, D19 S25.

Fiore, A. M., D. J. Jacob, I. Bey, R. M. Yantosca, B. D. Field, A. C. Fusco, and J. G.Wilkinson, 2002a, Background ozone over the United States in summer: Origin, trend, and contribution to pollution episodes, J. Geophys. Res., 107(D15), 4275, doi:10.1029/2001JD000982.

Fiore, A. M., D. J. Jacob, B. D. Field, D. G. Streets, S. D. Fernandes, and C. Jang, 2002b, Linking ozone pollution and climate change: The case for controlling methane, Geophys. Res. Lett., 29(19), 1919, doi:10.1029/2002GL015601.

Fusco, A.C., Logan, J.A., 2003. Analysis of 1970–1995 trends in tropospheric ozone at Northern Hemisphere midlatitudes with the GEOS-CHEM model. Journal of Geophysical Research 108 (D15), ACH 4-1–ACH 4-25.

Gbor, P. K., D. Wen, F. Meng, F. Yang, B. Zhang and J. J, 2006, Sloan, Improved model for mercury emission, transport and deposition, Atmos. Environ., 40, (5), 973-983.

Giorgi, F., and W.L. Chameides, 1985, The rainout parameterization in a photochemical model. Journal of Geophysical Research, 90, 7872-7880.

Godowitch, J.M., C. Hogrefe, S.T. Rao, 2008, Diagnostic analyses of regional air quality model: Changes in modeled processes affecting ozone and chemical-transport indicators from NOx point source emission reductions. Journal of Geophysical Research,113, D19303, doi:10.1029/2007JD009537.

Granier C., Guenther A., Lamarque J., Mieville A., Muller J., Olivier J., Orlando J., Peters J., Petron G., Tyndall G. & Wallens S., 2005, POET, a database of surface emissions of ozone precursors, techreport, available on the internet at: http://www.aero.jussieu.fr/projet/ACCENT/POET.php.

Guenther, A., T. Karl, P. Harley, C. Wiedinmyer, P. I. Palmer, and C. Geron, 2006, Estimates of global terrestrial isoprene emissions using MEGAN (Model of Emissions of Gases and Aerosols from Nature), Atmos. Chem. Phys., 6(11), 3181-3210.

Gustin, M. S., H. Biester, and C. S. Kim, 2002, Investigation of the lightenhanced emission of mercury from naturally enriched substrates, Atmos. Environ., 36(20), 3241– 3254.

Green Facts. 2011. Ozone. Downloaded from http://www.greenfacts.org/en/index.htm on May 24, 2011.

Guenther, A., 1997, Seasonal and spatial variations in natural volatile organic compound emissions. Ecol. Appl., 7, 34–45.

Hauglustaine, D. A., J. Lathière, S. Szopa, and G. A. Folberth, 2005, Future tropospheric ozone simulated with a climate-chemistry-biosphere model, Geophys. Res. Lett., 32, L24807, doi:10.1029/2005GL024031.

Hauglustaine, D. A., and G. P. Brasseur, 2001, Evolution of tropospheric ozone under anthropogenic activities and associated radiative forcing of climate, J. Geophys. Res., 106, 32,337–32,360.[AGU]

Hayhoe, K., VanDorn, J., Croley, T., Schlegal, N., Wuebbles, D., 2010, Regional climate change projections for Chicago and the US Great Lakes, Journal of Great Lakes Research, Volume 36, Pages 7-21

Hall, B., 1995, The gas phase oxidation of elemental mercury by ozone, Water Air Soil Pollut., 80, 301– 315.

Han, Y.J., Holsen, T.M., Lai, S.O, Hopke, P.K., Yi, S.M., Liu, W., Pagano, J., Falanga, L., Milligan, M., Andolina, C., 2004, Atmospheric gaseous mercury concentrations in New York State: relationships with meteorological data and other pollutants. Atmospheric Environment 38, 6431-6446.

Hang Lei, Zhaohui Lin, Jianhua Sun, 2005, An improved dust storm numerical simulation system and its experiments in north China <in Chinese> Climate and Environmental Research, 10 (9).

Heald, C. L., Henze, D. K., Horowitz, L. W., Feddema, J., Lamarque, J.-F., Guenther, A., Hess, P. G., Vitt, F., Seinfeld, J. H., Goldstein, A. H., Fung, I., 2008, Predicted change in global secondary organic aerosol concentrations in response to future climate, emissions, and land use change, J. Geophys. Res., 113, D05211, doi:10.1029/2007JD009092.

Hemispheric Transport of Air Pollution, 2007, Air Pollution Studies No. 16

Holloway, T., A. Fiore, and M. G. Hastings, 2003, Intercontinental transport of air pollution: Will emerging science lead to a new hemispheric treaty?, Environ. Sci. Technol., 37, 4535–4542.

Holmes, C., Jacob, D., and Yang, X., 2006, Global lifetime of elemental mercury against oxidation by atomic bromine in the free troposphere, Geophys. Res. Lett., 33, L20808, doi:10.1029/2006GL027176.

Hogrefe, C., and Coauthors, 2004, Simulating changes in regional air pollution over the eastern United States due to changes in global and regional climate and emissions. J. Geophys. Res., 109, D22301, doi:10.1029/2004JD004690.

Horowitz, W., Walters, S., Mauzerall, L., Emmons, Louisa K., Rasch, J., Granier, C., Tie, X., Lamarque, J., Schultz, G., Tyndall, S., 2003, A global simulation of tropospheric ozone and related tracers: Description and evaluation of MOZART, version 2, J. Geophys. Res., 108(D24), 4784, doi:10.1029/2002JD002853.

Hudman, R. C., 2004, Ozone production in transpacific Asian pollution plumes and implications for ozone air quality in California, J. Geophys. Res., 109, D23S10, doi:10.1029/2004JD004974.

Intergovernmental Panel on Climate Change (IPCC), 2001, Atmospheric chemistry and greenhouse gases, in Climate Change 2001, The Scientific Basis, edited by J. T. Houghton et al., pp. 239–288, Cambridge Univ. Press, New York.

Intergovernmental Panel on Climate Change (IPCC), 2007, IPCC Fourth Assessment Report: Climate Change 2007 (AR4)., Cambridge, United Kingdom and New York, NY, USA.: Cambridge University Press. Retrieved 2011-06-14.

Jacob, D. J., J. A. Logan, and P. P. Murti, 1999, Effect of rising Asian emissions on surface ozone in the United States, Geophys. Res. Lett., 26, 2175–2178, doi:10.1029/1999GL900450.

Jacob, D. J., Darrell A. Winner, 2008, Effect of climate change on air quality, Atmospheric Environment, Volume 43, Issue 1, January 2009, Pages 51-63

Jaeglé, L., D. A. Jaffe, H. U. Price, P. Weiss-Penzias, P. I. Palmer, M. J. Evans, D. J. Jacob, and I. Bey, 2003, Sources and budgets for CO and O3 in the northeastern Pacific during the spring of 2001: Results from the PHOBEA-II Experiment, J. Geophys. Res., 108(D20), 8802, doi:10.1029/2002JD003121.

Jaffe, D., 1999, Transport of Asian air pollution to North America, Geophys. Res. Lett., 26, 714–771.

Kunkel, K. E., H.-C. Huang, X.-Z. Liang, J.-T. Lin, D. J. Wuebbles, Z. Tao, A. Williams, M. Caughey, J. Zhu, and K. Hayhoe, 2008, Sensitivity of future ozone concentrations in the Northeast U.S. to regional climate change, Mitigation and Adaptation Strategies for Global Change, 13 (5-6), 597-606, doi:10.1007/s11027-007-9137-y.

Kanamitsu, M., W. Ebisuzaki, J. Woollen, S.-K. Yang, J.J. Hnilo, M. Fiorino, and G.L. Potter, 2002, The NCEP-DOE AMIP-II reanalysis (R-2). Bull. Amer. Meteor. Soc., 83, 1631-1643.

Katragkou E, Zanis P, Tegoulias I, Melas D, Kioutsioukis I, Króger BC, Huszar P, Halenka T, Rauscher S, 2010, "Decadal regional air quality simulations over Europe in present climate: Near surface ozone sensitivity to external meteorological forcing", Atmospheric Chemistry and Physics, 10: 11805-11821.

Kellerhals, M., S. Beauchamp, W. Belzer, P. Blanchard, F. Froude, B. Harvey, K. McDonald, M. Pilote, L. Poissant, K. Puckett, B. Schroeder, A. Steffen, and R. Tordon., 2003, Temporal and spatial variability of total gaseous mercury in Canada: Results from the Canadian Atmospheric Mercury Measurement Network (CAMNet), Atmos. Environ., 37, 1003–1011.

Kim, S., Han, Y., Holsen, T.M., Yi, S., 2009. Characteristic of atmospheric speciated mercury concentrations (TGM, Hg(II), and Hg(p)) in Seoul, Korea. Atmospheric Environment 43, 3267 - 3274.

Koffi, B., Szopa, S., Cozic, A., Hauglustaine, D., and van Velthoven, P., 2010, Present and future impact of aircraft, road traffic and shipping emissions on global tropospheric ozone, Atmos. Chem. Phys., 10, 11681-11705, doi:10.5194/acp-10-11681-2010.

Kunkel, K. E., H.-C. Huang, X.-Z. Liang, J.-T. Lin, D. J. Wuebbles, Z. Tao, A. Williams, M. Caughey, J. Zhu, and K. Hayhoe, 2008, Sensitivity of future ozone concentrations in the Northeast U.S. to regional climate change, Mitigation and Adaptation Strategies for Global Change, 13 (5-6), 597-606, doi:10.1007/s11027-007-9137-y.

Kunkel, Kenneth E., Xin-Zhong Liang, Jinhong Zhu, 2010, Regional Climate Model Projections and Uncertainties of U.S. Summer Heat Waves. J. Climate, 23, 4447–4458.

Kock, H.H., Bieber, E., Ebinghaus, Spain, T.G. and Thees, B., 2005, Comparison of long-term trends and seasonal variation of atmospheric mercury concentrations at two European coastal monitoring stations Mace Head, Ireland and Zingst, Germany, Atmospheric Environment 39, pp. 7549–7556.

Lamarque, J.-F., P. Hess, L. Emmons, L. Buja, W. Washington, and C. Granier, 2005, Tropospheric ozone evolution between 1890 and 1990. J. Geophys. Res., 110, D08304, doi:10.1029/2004JD005537.

Lamarque, J. F., 2008, Simulated lower stratospheric trends between 1970 and 2005: Identifying the role of climate and composition changes, Journal of Geophysical Research-Atmospheres, 113(D12), 19.

Lamarque, J.-F., Emmons, L. K., Hess, P. G., Kinnison, D. E., Tilmes, S., Vitt, F., Heald, C. L., Holland, E. A., Lauritzen, P. H., Neu, J., Orlando, J. J., Rasch, P., and Tyndall, G. , 2011, CAM-chem: description and evaluation of interactive atmospheric chemistry in CESM, Geosci. Model Dev. Discuss., 4, 2199-2278, doi:10.5194/gmdd-4-2199-2011.

Lamborg, C., Rolfhus, K., Fitzgerald, W., and Kim, G., 1999, The atmospheric cycling and air-sea exchange of mercury species in the South and equatorial Atlantic Ocean, Deep-sea Research II, 46, 957–977.

Lamborg, C. H., W. F. Fitzgerald, A. W. H. Damman, J. M. Benoit, P. H. Balcom, and D. R. Engstrom, 2002, Modern and historic atmospheric mercury fluxes in both hemispheres: Global and regional mercury cycling implications, Global Biogeochem. Cycles, 16(4), 1104, doi:10.1029/2001GB001847.

Laurier, F., Mason, R., Whalin, L., and Kato, S., 2003, Reactive gaseous mercury formation in the North Pacific Ocean's marine boundary layer: A potential role of halogen chemistry, J. Geophys. Res., 108, 4529, doi:10.1029/2003JD003625.

Lawrence, M. G., 2003, Global chemical weather forecasts for field campaign planning: Predictions and observations of large scale features during MINOS, CONTRACE and INDOEX, Atmos. Chem. Phys., 3, 267– 289.

Leung RL, Gustafson WI Jr., 2005, Potential regional climate change and implications to US air quality Geophys Res Lett 32(16).

Li, Q., Jaeglé, L., 2002, Transatlantic transport of pollution and its effects on surface ozone in Europe and North America, J. Geophys. Res., 107(D13), 4166, doi:10.1029/2001JD001422.

Liang, X.-Z., L. Li, K.E. Kunkel, M. Ting, and J.X.L. Wang, 2004, Regional climate model simulation of U.S. precipitation during 1982-2002. Part 1: Annual cycle. J. Climate, 17, 3510-3528.

Lin C.-J. and S.O. Pehkonen, 1997, Aqueous free radical chemistry of mercury in the presence of iron oxides and ambient aerosol. Atmospheric Environment, v.31, pp.4125-4137.

Lin, C.-J., Pehkonen, S.O., 1999. The chemistry of atmospheric mercury: a review. Atmospheric Environment 33, 2067–2079.

Lin, C.-J., P. Pongprueksa, S. E. Lindberg, S. O. Pehkonen, D. Byun, and C. Jang, 2006, Scientific uncertainties in atmospheric mercury models. I: Model science evaluation, Atmos. Environ., 40, 2911 – 2928.

Lin, J.-T., X.-Z. Liang, and D. J. Wuebbles, 2008, Effects of intercontinental transport on surface ozone over the United States: Present and future assessment with a global model, Geophys. Res. Lett, 35, L02805, doi:10.1029/2007GL031415.

Lin, X., and Y. Tao, 2003, A numerical modeling study on regional mercury budget for eastern North America. Atmos. Chem. Phys., 3, 535–548.

Lindberg, S. E., K. H. Kim, T. P. Meyers, and J. G. Owens, 1995, Micrometeorological gradient approach for quantifying air-surface exchange of mercury vapor: Tests over contaminated soils, Environ. Sci. Technol., 29(1), 126–135.

Lindqvist, O., 1991, Mercury in the Swedish environment: Recent research on causes, consequences and corrective methods, Water Air Soil Pollut., 55, xi – 261.

Liu, H., Jacob, D., Bey, I., and Yantosca, R., 2001, Constraints from Pb-210 and Be-7 on wet deposition and transport in a global threedimensional chemical tracer model driven by assimilated meteorological fields, J. Geophys. Res., 106, 12109–12128.

Liu, B., Keeler, G.J., Dvonch, J.T., Barres, J.A., Lynam, M.M., Marsik, F.J., Morgan, J.T., 2007. Temporal variability of mercury speciation in urban air. Atmospheric Environment 41, 1911 - 1923.

Liss, P. S., and Slater, P., G., 1974, Flux of gases across the airsea interface, Nature, 247, 181-184.

Lin, J.-T., X.-Z. Liang, and D. J. Wuebbles, 2008a, Effects of intercontinental transport on surface ozone over the United States: Present and future assessment with a global model, Geophys. Res. Lett, 35, L02805, doi:10.1029/2007GL031415.

Lin, J.-T., K. O. Patten, X.-Z. Liang, and D. J. Wuebbles, 2008b, Effects of future climate and biogenic emissions changes on surface ozone over the United States and China, J. Appl. Meteor, 47(7), 1888-1909, doi: 10.1175/2007JAMC1681.

Lionello, P., U. Boldrin and F. Giorgi, 2008, Cyclone climatology over Europe from a regional climate change simulation. Climate Dynamics, 30, 657-671.

Lionello P., M.B.Galati, E.Elvini, 2010, Extreme storm surge and wind wave climate scenario simulations at the Venetian littoral Phys. Chem. Earth 10.1016/j.pce.2010.04.001

Manders AMM , Schaap M , Jozwicka M , Arkel F van , Weijers E , Matthijsen J, 2009, The contribution of sea salt to PM10 and PM2.5 in the Netherlands, Netherlands Environmental Assessment Agency.

Mason, R. and Sheu, G., 2002, Role of the ocean in the global mercury cycle, Global Biogeochem. Cy., 16, 1093, doi:10.1029/2001GB001440.

Mickley, L. J., D. J. Jacob, B. D. Field, and D. Rind, 2004, Effects of future climate change on regional air pollution episodes in the United States, Geophys. Res. Lett., 31, L24103, doi:10.1029/2004GL021216.

Munthe, J., 1992, Aqueous oxidation of elemental Hg by O3. Atmospheric Environment, 26A (1992), pp. 1461–1468.

Murazaki, K., and P. Hess, 2006, How does climate change contribute to surface ozone change over the United States?, J. Geophys. Res., 111, D05301, doi:10.1029/2005JD005873.

National Atmospheric Deposition Program (NADP), 2008, Annual data summaries, http://nadp.sws.uiuc.edu/lib/dataReports.aspx.

Newell, R. E., and M. J. Evans, 2000, Seasonal changes in pollutant transport to the North Pacific: The relative importance of Asian and European sources, Geophys. Res. Lett. 27, 2509-2512.

Nriagu, J. and Becker, C., 2003, Volcanic emissions of mercury to the atmosphere: global and regional inventories, The Science of The Total Environment, 304, 3 - 12.

Olivier, J.G.J., J.J.M. Berdowski, J.A.H.W. Peters, J. Bakker, A.J.H. Visschedijk and J.P.J. Bloos, 2001, Applications of EDGAR. Including a description of EDGAR V3.0: reference database with trend data for 1970-1995. RIVM, Bilthoven, report no. 773301 001 / NRP report 410200 051. ISBN 90-5851-077-8.

Olivier J., J. Peters, C. Granier, G. Petron, J.F. Muller, and S. Wallens: Present and future surface emissions of atmospheric compounds, POET report no 2, EU project EVK2-1999-00011, 2003.

Pacyna, E. G., J. M. Pacyna, F. Steenhuisen, and S. Wilson, 2005, Global anthropogenic mercury emission inventory for 2000, Atmos. Environ., 40(22), 4048– 4063.

Pacyna, E. G., J. M. Pacyna, F. Steenhuisen, and S. Wilson, 2006, Global anthropogenic mercury emission inventory for 2000, Atmos. Environ., 40(22), 4048– 4063.

Pal, B. and P. A. Ariya, 2004, Studies of ozone initiated re actions of gaseous mercury: kinetics, product studies and atmospheric implications. Phys. Chem. Chem. Phys., 6, 572- 579, doi: 10.1039/b311150d.

Parrish, D. D., Y. Kondo, O. R. Cooper, C. A. Brock, D. A. Jaffe, M. Trainer, T. Ogawa, G. Hübler, and F. C. Fehsenfeld, 2004, Intercontinental Transport and Chemical Transformation 2002 (ITCT 2K2) and Pacific Exploration of Asian Continental Emission (PEACE) experiments: An overview of the 2002 winter and spring intensives, J. Geophys. Res., 109, D23S01, doi:10.1029/2004JD004980.

Park, R. J., Jacob, D. J., Kumar, N., and Yantosca, R. M.: Regional visibility statistics in the United States: Natural and transboundary pollution influences, and implications for the Regional Haze Rule, Atmos. Environ., 40, 5405–5423, 2006.

Peng R., Dominici F., Pastor-Barriuso R., Zeger S., Samet J., 2005, "Seasonal analyses of air pollution and mortality in 100 U.S. cities," American Journal of Epidemiology, 161 (6), 585–594. doi:10.1093/aje/kwi075

Pickering, K. E., Y. Wang, W. Tao, C. Price, and J. Mu¨ ller,1998, Vertical distributions of lightning NOx for use in regional and global chemical transport models, J. Geophys. Res., 103, 31,203–31,216.

Pehkonen, S. and Lin, C., 1998, Aqueous photochemistry of mercury withorganic acids, J. Air Waste Manage., 48, 144–150.

Pfister, G.G., L.K. Emmons, P.G. Hess and J. Lamarque, 2008, Contribution of isoprene to chemical budgets: a model tracer study with the NCAR CTM MOZART-4, Journal of Geophysical Research. D. Atmospheres 113.

Pleijel, K. and Munthe, J., 1995, Modeling the Atmospheric Mercury Cycle - Chemistry in Fog Droplets. Atmos. Environ. 29: 1441–1457.

Poissant, L., and A. Casimir, 1998, Water-air and soil-air exchange rate of total gaseous mercury measured at background sites, Atmos. Environ., 32(5), 883– 893.

Pochanart, P., H. Akimoto, Y. Kajii, V. M. Potemkin, T. V. Khodzher, 2003, Regional background ozone and carbon monoxide variations in remote Siberia/East Asia, J. Geophys. Res. 108, 4028.

Potosnak, M., 2002, Effects of growth carbon dioxide concentration on isoprene emissions from plants, doctoral thesis, 140 pp., Columbia Univ., New York.

Potosnak, M., 2002, Effects of growth carbon dioxide concentration on isoprene emissions from plants. Ph.D. thesis, Columbia University, 140 pp.

Prather, M., 2003, Fresh air in the 21st century?, Geophys. Res. Lett., 30(2), 1100, doi:10.1029/2002GL016285.

Price, C., J. Penner, and M. Prather, 1997, NOx from lightning: 1. Globaldistribution based on lightning physics, J. Geophys. Res., 102, 5929–5941, doi:10.1029/96JD03504.

Pye, H. O. T., H. Liao, S. Wu, L. J. Mickley, D. J.Jacob, D. K. Henze, and J. H. Seinfeld, 2009, Effect of changes in climate and emissions on future sulfate-nitrate-ammonium aerosol levels in the United States, J. Geophys. Res., 114, D01205.

Pyle, D. M. and Mather, T. A., 2003, The importance of volcanic emissions for the global atmospheric mercury cycle, Atmospheric Environment, 37, 5115 - 5124.

Racherla, P. N., and P. J. Adams, 2006, Sensitivity of global tropospheric ozone and fine particulate matter concentrations to climate change. J. Geophys. Res., 111, D24103, doi:10.1029/2005JD006939.

RIVM, 2001, The IMAGE 2.2 implementation of the SRES scenarios, A comprehensive analysis of emissions, climate change and impacts in the 21st century, RIVM CD-ROM publication 481508018. Bilthoven, the Netherlands, National Institute for Public Health and the Environment.

Rosenberg S, Vedlitz, V., Cowman, D., Zahran, S., 2009, Climate change: a profile of US climate scientists' perspectives, Climatic Change, DOI 10.1007/s10584-009-9709-9.

Sakata, M. and K. Marumoto, 2002, Formation of atmospheric particulate mercury in the Tokyo metropolitan area. Atmos. Environ., 36, 239–246.

Schroeder, W.H. and Munthe, J., 1998, Atmospheric mercury - An overview. Atmos. Environ. 32: 809–822.

Seigneur, C., K. Vijayaraghavan, K. Lohman, P. Karamchandani, and C. Scott, 2004, Global source attribution for mercury deposition in the United States, Environ. Sci. Technol., 38, 555–569.

Seigneur, S., P. Karamchandani, K. Lohman, and K. Vijayaraghavan, 2001, Multiscale modeling of the atmospheric fate and transport of mercury, J. Geophys. Res., 106, 27,795–27,809.

Strode, S., L. Jaeglé, N. E. Selin, D. J. Jacob, R. J. Park, R. M. Yantosca, R. P. Mason, and F. Slemr, 2007, Air-sea exchange in the global mercury cycle, Global Biogeochem. Cycles, 21, GB1017, doi:10.1029/2006GB002766.[AGU]

Selin, N. E., Jacob, D. J., Park, R. J., Yantosca, R. M., Strode, S., Jaegl´e, L., and Jaffe, D., 2007, Chemical cycling and deposition of atmospheric mercury: Global constraints from observations, J. Geophys. Res., 112, 1–14, doi:10.1029/2006JD007450.

Selin, N. E., Jacob, D. J., Yantosca, R. M., Strode, S., Jaegl´e, L., and Sunderland, E. M., 2008, Global 3-D land-ocean-atmosphere model for mercury: Present-day versus preindustrial cycles and anthropogenic enrichment factors for deposition, Global Biogeochem. Cyc., 22, 1–13, doi:10.1029/2007GB003040.

Seigneur, S., P. Karamchandani, K. Lohman, and K. Vijayaraghavan, 2001, Multiscale modeling of the atmospheric fate and transport of mercury, J. Geophys. Res., 106, 27,795–27,809.

Shia, R.-L., C. Seigneur, P. Pai, M. Ko, and N. D. Sze, 1999, Global simulation of atmospheric mercury concentrations and deposition fluxes, J. Geophys. Res., 104, 23,747– 23,760.

Shao, Y., 2008, Physics and Modelling of Wind Erosion. Springer Verlag, 2nd edition.

Shao, Y., E. J. Jung and L. M. Leslie, 2002, Numerical prediction of Northeast Asian dust storms using an integrated wind erosion modeling system. J. Geophys. Res., 107, 4814.

Shao, Y., 2004, Simplification of a Dust Emission Scheme and Comparison with Data. J. Geophysical Res. 109, D10202, doi:10.1029/2003JD004372.

Shao, Y., 2000, Physics and Modelling of Wind Erosion. Kluwer Academic Publishers, 393pp. (Springer Verlag, 2nd edition, 2008)

Sillman, S., and P. J. Samson, 1995, Impact of temperature on oxidant photochemistry in urban, polluted rural and remote environments. J. Geophys. Res., 100, 11 497–11 508.

Sillman, S., F. Marsik, K. I. Al-Wali, G. J. Keeler, and M. S. Landis, 2005, Models for the formation and transport of reactive mercury: Results for Florida, the northeastern U.S. and the Atlantic Ocean, paper presented at Fifth Air Quality Conference: Mercury, Trace Elements, SO3 and Particulate Matter, Energy and Environ. Res. Cent., Arlington, Va.

Smith-Downey, N.V., Sunderland, E.M., and Jacob, D.J., 2010, Anthropogenic impacts on global storage and emissions of mercury from terrestrial soils: insights from a new global model , J. Geophys. Res., 115, G03008.

Soerensen, A.L., H. Skov, D.J. Jacob, B.T. Soerensen, and M.S. Johnson, 2010, Global concentrations of gaseous elemental mercury and reactive gaseous mercury in the marine boundary layer, Environ. Sci. Technol., 44, 7,425-7,430.

Solberg, S., Bergstrøm, R., Langner, J., Laurila, T., and Lindskog, A., 2005, Changes in Nordic surface ozone episodes due to European emission reductions in the 1990s, Atmospheric Environment 39 2005, pp. 179–192.

Solberg Sverre, Robert Bergström, Joakim Langner, Tuomas Laurila, Anne Lindskog., 2005., Changes in Nordic surface ozone episodes due to European emission reductions in the 1990s., Atmospheric Environment, Volume 39, Issue 1, January 2005, Pages 179-192

Sommar, J., K. Ga°rdfeldt, D. Stro¨mberg, and X. Feng, 2001, A kinetic study of the gas-phase reaction between the hydroxyl radical and atomic mercury, Atmos. Environ., 35, 3049–3054.

Streets, D. G., Hao, J., Wu, Y., Jiang, J., Chan, M., Tian, H., and Feng, X., 2005, Anthropogenic mercury emissions in China, Atmos. Environ., 39, 7789–7806.

Streets, D., Zhang, Q., and Wu, Y., 2009, Projections of global mercury emissions in 2050, Environ. Sci. Technol., 43, 2983–2988, doi:10.1021/es802474j.

Stevenson, D. S., C. E. Johnson, W. J. Collins, R. G. Derwent, and J. M. Edwards, 2000, Future estimates of tropospheric ozone radiative forcing and methane turnover: The impact of climate change, Geophys. Res. Lett., 27, 2073–2076.

Streets, D.G., Waldhoff, S.T., 2000. Present and future emissions of air pollutants in China: SO2, NOx, and CO. Atmospheric Environment 34, 363–374.

Streets, D. G., T. C. Bond, T. Lee, and C. Jang, 2004, On the future of carbonaceous aerosol emissions, J. Geophys. Res., 109, D24212, doi:10.1029/2004JD004902.

Stohl, A. and Trickl, T., 1999, A textbook example of long-range transport: Simultaneous observation of ozone maxima of stratospheric and NorthAmerican origin in the free troposphere over Europe, J. Geophys. Res., 104, 30445–30462.

Stohl, A., Forster, C., Eckhart, S., Spichtinger, N., Huntrieser, H., Heland, J., Schlager, H., Wilhelm, S., Arnold, F., and Cooper, O., 2003, A backward modeling study of intercontinental pollution transport using aircraft measurements, J. Geophys. Res., 108, D12, doi:10.1029/2002JD002862.

Stull, R., 1997, An Introduction to Boundary Layer Meteorology, Kluwer Acad., Dordrecht, Netherlands.

Tan, Q., Chameides,W. L., Streets, D.,Wang, T., Xu, J., Bergin, M., and Woo, J. , 2004, An evaluation of TRACE-P emission inventories from China using a regional model and chemical measurements, J. Geophys. Res., 109(D22), D22305, doi:10.1029/2004JD005071.

Tao, Z., A. Williams, H.-C. Huang, M. Caughey, and X.-Z. Liang, 2007, Sensitivity of U. S. surface ozone to future emissions and climate changes, Geophys. Res. Lett., 34, L08811, doi:10.1029/2007GL029455.

Temme, C., Einax, J., Ebinghaus, R., and Schroeder, W., 2003, Measurements of atmospheric mercury species at a coastal site in the Antarctic and over the South Atlantic Ocean during polar summer, Environ. Sci. Technol., 37, 22–31.

Temme, C., Ebinghaus, R., Schwerin, A., Bieber, E., 2006, Field intercomparison of mercury measurements in ambient air and precipitation within EMEP. Presentation at the Eighth International Conference on Mercury as a Global Pollutant, Madison, WI, August 8–11.

Tie, X., Brasseur, G., Emmons, L., Horowitz, L., and Kinnison, D., 2001, Effects of aerosols on tropospheric oxidants: A global model study, J. Geophys. Res. 106, 22931–22964.

Tie, X., S. Madronich, S. Walters, D. P. Edwards, P. Ginoux, N. Mahowald, R. Y. Zhang, C. Lou, and G. Brasseur, 2005, Assessment of the global impact of aerosols on tropospheric oxidants, J. Geophys. Res., 110, D03204, doi:10.1029/2004JD005359.

Tie, X., and Coauthors, 2006, Chemical characterization of air pollution in Eastern China and the Eastern United States. Atmos. Environ., 40, 2607–2625.

U.S. Environmental Protection Agency (EPA), 2008a, National Ambient Air Quality Standards (NAAQS).

U.S. Environmental Protection Agency (EPA), 2008b, Our Nation's Air - Status and Trends through 2008.

U.S. Environmental Protection Agency (EPA), 2008, National Ambient Air Quality Standards (NAAQS).

US EPA, 1997, Mercury Study Report to Congress. Fate and Transport of Mercury in the Environment, Vol. III. EPA-452/R-97-005, US Environmental Protection Agency, US Government Printing Office, Washington, DC.

Van der Werf, G. R., Randerson, J. T., Giglio, L., Collatz, G. J., Kasibhatla, P. S., and Arellano Jr., A. F., 2006, Interannual variability in global biomass burning emissions from 1997 to 2004, Atmos. Chem. Phys., 6, 3423–3441, doi:10.5194/acp-6-3423-2006.

Van Loon, L., E. Mader, and S. Scott, Reduction of the aqueous mercuric ion by sulfite, 2000, UV spectrum of HgSO3 and its intramolecular redox reaction. Journal of Physical Chemistry. 104, 1621-1626.

Wild O., P. Pochanart and H. Akimoto, 2004, Trans-Eurasian transport of ozone and its precursors, J. Geophys. Res., 109, D11302, doi:10.1029/2003JD004501.

Wilkening, K. E., L. A. Barrie, and M. Engle, 2000, Trans-Pacific air pollution, Science, 290(5489), 65–67, doi:10.1126/science.290.5489.65.

Wang, T., Cheung, V.T.F., Li, Y.S., Anson, M., 2001, Ozone and related gaseous pollutants in the boundary layer of eastern china: overview of the recent measurements at a rural site. Geophysical Research Letters 28, 2373–2376.

Wang, H., L. Zhou, and X. Tang, 2006, Ozone concentrations in rural regions of the Yangtze Delta in China. J. Atmos. Chem., 54, 255–265, doi:10.1007/s10874-006-9024-z.

Wu, S., L. J. Mickley, D. J. Jacob, D. Rind, and D. G. Streets, 2008a, Effects of 2000–2050 changes in climate and emissions on global tropospheric ozone and the policy-relevant background surface ozone in the United States, J. Geophys. Res., 113, D18312, doi:10.1029/2007JD009639.

Wu, S., L. J. Mickley, E. M. Leibensperger, D. J. Jacob, D. Rind, and D. G. Streets, 2008b, Effects of 2000–2050 global change on ozone air quality in the United States, J. Geophys. Res., 113, D06302, doi:10.1029/2007JD008917.

Wu, S., B.N. Duncan, D.J. Jacob, A.M. Fiore and O. Wild, 2009, Chemical nonlinearities in relating intercontinental ozone pollution to anthropogenic emissions, Geophys. Res. Lett., 36, L05806.

Wang, Y., D. J. Jacob, and J. A. Logan, 1998, Global simulation of tropospheric O3-NOx-hydrocarbon chemistry: 1. Model formulation, J. Geophys. Res., 103, 10,713–10,726.

Wang, Z.W., Zhang, X.S., Chen, Z.S., Zhang, Y., 2006, Mercury concentrations in size - fractionated airborne particles at urban and suburban sites in Beijing, China. Atmospheric Environment 40, 2194 - 2201.

Wamsley, J.L. and M.L. Wesley, 1996, Modification of coded parameterizations of surface resistances to gaseous dry deposition, Atmos. Environ., 30, 1181-1188.

Wa¨ngberg, I., S. Schmolke, P. Schager, J. Munthe, R. Ebinghaus, and A. Iverfeldt, 2001, Estimates of air-sea exchange of mercury in the Baltic Sea, Atmos. Environ., 35(32), 5477– 5484.

Weiss-Penzias, P., D. A. Jaffe, A. McClintick, E. M. Prestbo, and M. S. Landis, 2003, Gaseous elemental mercury in the marine boundary layer: Evidence for rapid removal in anthropogenic pollution, Environ. Sci. Technol., 37, 3755–3763.

Wesley, M. L., 1989, Parameterizations of surface resistances to gaseous dry deposition in regional scale numerical models, Atmos. Environ., 23, 1293-1304.

Wesley, M. L., and B. B. Hicks, 2000, A review of the current status of knowledge on dry deposition, Atmos. Environ., 34, 2261-2282.

Witt, M., Mather, T., Baker, A., De Hoog, J. and Pyle, D., 2010, Atmospheric trace metals over the south-west Indian Ocean: Total gaseous mercury, aerosol trace metal concentrations and lead isotope ratios. Marine Chemistry, doi:10.1016/j.marchem.2010.02.005.

Wuebbles, D. J., K. O. Patten, M. T. Johnson, and R. Kotamarthi, 2001, New methodology for Ozone Depletion Potentials of short-lived compounds: n-Propyl bromide as an example, J. Geophys. Res., 106, 14,551–14,572.

Wuebbles, D. J., H. Lei, and J.-T. Lin, 2007, Intercontinental transport of aerosols and photochemical oxidants from Asia and its consequences, Environmental Pollution, 150(1), 65-84.

Wylie, Donald, Darren L. Jackson, W. Paul Menzel, John J. Bates, 2005, Trends in Global Cloud Cover in Two Decades of HIRS Observations. J. Climate, 18, 3021–3031.

Xiao, X., Yang, X., Miller, D., Helble, J., and Carley, R., 1994, A regional scale modeling study of atmospheric transport and transformation of mercury. II. Simulation results for the northeast United States. Atmospheric Environment, 34, pp. 4945–4955.

Yang Y, Chen H, Wang D, 2009, Spatial and temporal distribution of gaseous elemental mercury in Chongqing, China. Environ Monit Assess 156:479–489.

Yienger, J.J., Galanter, M., Holloway, T.A., Phadinx, M.J., Guttikunda, S.K., Carmichael, G.R., Moxim, W.J. and Levy ll, H., 2000, The episodic nature of air pollution transport from Asia to North America. Journal of Geophysical Research 105 26, pp. 931–945.

Zhu, C., B. Wang, and W. Qian, 2008, Why do dust storms decrease in northern China concurrently with the recent global warming?, Geophys. Res. Lett., 35, L18702, doi:10.1029/2008GL034886.

Zhang, H., S. E. Lindberg, F. J. Marsik, and G. J. Keeler, 2001, Mercury air/surface exchange kinetics of background soils of the Tahquamenon River watershed in the Michigan Upper Peninsula, Water Air Soil Pollut., 126(1– 2), 151– 169.

Zhang, L., Padro, and Walmsley, 1996, A multi-layer model vs single-layer models and observed O_3 dry deposition velocities, Atmos. Environ., 30, 339345.

Zender, C.S., Bian, H., Newman, D., 2003, The mineral dust entrainment and deposition (DEAD) model: description and 1990s dust climatology. Journal of Geophysical Research 108 (D14), 4416.

Zlatev, J. Fenger, L. Mortensen, 1996, Relationships between emission sources and excess ozone concentrations., Computers & Mathematics with Applications, Volume 32, Issue 11, Pages 101-123

Zhao, C. S., X. Tie, G. L. Wang, Y. Qin, and P. C. Yang, 2006, Analysis of air quality in eastern China and its interaction with other regions of the world, J. Atmos. Chem., 55, 189–204, doi:10.1007/s10874-006-9022-1.

Zobler, L, 1999, Global Soil Types, 1-Degree Grid Data set. Oak Ridge National Laboratory Distributed Active Archive Center, Oak Ridge, TE, U.S.A.